Understanding Haemodynamic Changes Surrounding Epileptic Events in Children

Elhum Anahit Shamshiri

Thesis submitted for the degree of

Doctor of Philosophy

of

University College London.

Developmental Imaging and Biophysics Section

University College London

02 March 2017

Declaration

I, Elhum Shamshiri, confirm that the work presented in this thesis is my own. Where information has been derived from other sources, I confirm that this has been indicated in the thesis.

Elhum Shamshiri

Abstract

The interrelationship between cerebral haemodynamics and epileptic activity has been the subject of study for over 100 years. The overall goal of this PhD is to use and develop multimodal imaging to better understand this relationship in a paediatric population. This has important implications for the localisation of epileptic activity that can aid pre-surgical evaluation and seizure detection.

The benefit of interictal epileptiform discharge (IED) suppression in clinical treatment is under debate, considering little is known about their impact on cognitive function. By applying EEG-fMRI, it was found that transient effects of IEDs were responsible for connectivity differences between patients and controls, showing the widespread impact of IEDs on BOLD signal and suggesting the importance of IED suppression for normal functional connectivity.

Haemodynamic changes may occur prior to epileptic event onset. Therefore we evaluated the response function (HRF) to IEDs in paediatric focal epilepsy patients, as an HRF was created from simultaneous EEG-fMRI data and found to be beneficial in the delineation of epileptic foci. However, the underlying neurovascular changes seen in this altered HRF still needed to be explored. Therefore EEG-NIRS was utilised to interpret the mechanistic changes found in BOLD during IEDs. NIRS provides the added information of concentration changes of both –oxy and –deoxy haemoglobin rather than relative changes in deoxyhaemoglobin. To perform these experiments a new optode holder applicable to the clinical environment had to be made and tested for efficacy. The best design was a flexible optode grid, as it required no interference with the standard clinical protocol.

Once tested in patients, EEG-NIRS found pre-ictal/pre-IED increases in oxygen saturation and oxyhaemoglobin concentrations, thereby corroborating with prior haemodynamic changes seen in EEG-fMRI.

Therefore, by utilizing both EEG-fMRI and EEG-NIRS a greater understanding of the haemodynamic changes surrounding epileptic events in children can be obtained.

Acknowledgements

I would like to express my sincere gratitude to my supervisors, Doctor David Carmichael for his guidance which helped me throughout my PhD as well as through the writing of this thesis, and Professor Helen Cross for all of the help and support she has given me. I would also like to thank Alan Worley for all the good advice he has given me and always having his door open for a discussion.

I would also like to thank my co-workers Tim Tierney, Doctor Maria Centeno, and Suejen Perani for their guidance and encouragement that made working at the Institute of Child Health a rewarding (and fun) experience.

From the staff at Great Ormond Street Hospital I would like to thank Charlotte Wilkinson for her help and never-ending patience, which I am very grateful for. I would also like to thank Kelly St Pier for her knowledge and guidance throughout my PhD, and her willingness to teach me about working in the clinical realm. I would also like to thank the telemetry team, including Emma Dean, Rui Silva, and Arjel Lejarde for their support and making my work at the hospital an exciting and inviting place to be. I would also like to thank Dil Hair for his support and encouragement. Furthermore I would like to thank all of the radiographers in the MR department. In particular I would like to thank Jessica Cooper and Tina Banks for all of their help and hard work, as without their patience and support this would not have been possible.

From the University College London Medical Physics Department, I would like to thank Doctor Ilias Tachtsidis for his willingness to work with such an interdisciplinary team to apply optical imaging in the clinical realm, and introducing me to the field of Near Infrared Spectroscopy.

I would also like to thank my family who have been extremely supportive throughout the entire PhD, even from afar. I would especially like to thank my mother, who has always been there for me and whose strength and intellect I aspire to live up to.

Papers and Abstracts

Directly arising from this Thesis

Papers

Shamshiri EA, Tierney TM, Centeno M, St Pier K, Pressler RM, Sharp DJ, Perani S, Cross JH, Carmichael DW (2016): Interictal activity is an important contributor to abnormal intrinsic network connectivity in paediatric focal epilepsy. Hum Brain Mapp 236:221–236.

Publications related to the work in this thesis

Centeno M., Tierney T.M., Perani S., Shamshiri E.A., St Pier K., Wilkinson C., Konn D., Banks T., Vulliemoz S., Lemieux L., Pressler R.M., Clark C.A., Cross J.H., Carmichael D.W. (2016). Optimising EEG-fMRI for localisation of focal epilepsy in children. PLoS One 11: e0149048.

Tierney T.M., Weiss-Croft L.J., Centeno M., Shamshiri E.A., Perani S., Baldeweg T., Clark C.A., Carmichael D.W. (2016). FIACH: A biophysical model for automatic retrospective noise control in fMRI. Neuroimage 124: 1009-10020.

Abstracts

Shamshiri E., Centeno M., St Pier K., Perani S., Cross J.H., Carmichael D.W. (2014, May). Failure of connectivity modulation during an attentional task in children with epilepsy is not explained fully by interictal activity. Poster presented at the annual meeting of International Society for Magnetic Resonance in Medicine, Milan, Italy.

Shamshiri E., Centeno M., Tierney T., St Pier K., Perani S., Cross J.H., Carmichael D.W. (2014, June). An investigation of the role of interictal activity on a natural stimulus in children with epilepsy. Poster presented at the annual meeting of Organization for Human Brain Mapping, Hamburg, Germany.

Shamshiri E.A., Centeno M., Tierney T.M., St Pier K., Pressler R., Perani S., Cross J.H., Carmichael D.W. (2014, December). Investigating the role of interictal activity

during a natural stimulus presentation in children with epilepsy. Poster presented at the annual meeting of Brain Modes, London, United Kingdom.

Shamshiri E.A., Centeno M., Tierney T.M., St Pier K., Pressler R., Perani S., Cross J.H., Carmichael D.W. (2015, May). Investigating the role of interictal activity during a natural stimulus presentation in children with focal epilepsy. Poster presented at the annual meeting of International Society for Magnetic Resonance in Medicine, Toronto, Canada.

Shamshiri E.A., Centeno M., Tierney T.M., St Pier K., Pressler R., Perani S., Cross J.H., Carmichael, D.W. (2015, June). Investigating the role of interictal activity during a natural stimulus presentation in children with focal epilepsy. Poster presented at the annual meeting of Organization for Human Brain Mapping, Toronto, Canada.

Shamshiri E.A., Centeno M., Tierney T.M., St Pier K., Pressler R., Perani S., Cross J.H., Carmichael, D.W. (2015, September). Assessing the impact of interictal discharges on resting state network connectivity in focal epilepsy using EEG-fMRI and a natural stimulus task. Talk presented at the annual meeting of International Epilepsy Congress, Istanbul, Turkey.

Table of Contents

Declaration 2

Abstract 3

Acknowledgements 4

Papers and Abstracts 5

Table of Contents 7

Table of Figures 12

Table of Tables 15

Table of Abbreviations 16

Chapter 1 General Introduction 20

1.1 Epilepsy 20

1.1.1 Neurophysiology and Neurochemistry of Cortical Neurons 20

1.2 Vascular and Physiological Relationships 27

1.2.1 Vasculature 27

1.2.2 Cerebral Autoregulation 28

1.2.3 Metabolic, Vascular, and Neuronal Coupling 29

1.3 Neuroimaging 34

1.3.1 Electroencephalography 34

1.3.2 Magnetic Resonance Imaging 36

1.3.3 Combining EEG and fMRI 46

1.3.4 Near Infrared Spectroscopy 47

1.3.5 Combining EEG and NIRS 52

1.4 Objectives 52

Chapter 2 Interictal Activity Contributes to Abnormal Connectivity in Paediatric Focal Epilepsy 54

2.1 Abstract 54
2.2 Objectives 55
2.3 Introduction 55
2.4 Methods 58
2.4.1 Subjects 58
2.4.2 Data Acquisition 62
2.4.3 Paradigm 62
2.4.4 Data Processing 63
2.4.5 Controlling for the Effect of IEDs 63
2.4.6 Statistical Analysis 64
2.5 Results 70
2.5.1 Network More Activated by Waiting 70
2.5.2 Network More Activated by Video 71
2.5.3 Functional Connectivity 72
2.6 Discussion 76
2.6.1 Summary 76
2.6.2 Importance of IEDs and Compromised Network Connectivity 76
2.6.3 Transient and Non-Transient Effects of IEDs 77
2.6.4 The Impact of Drug Load on Patient Task Response 79
2.6.5 Clinical Implications 79
2.6.6 Seizures and IEDs 81
2.6.7 Future Works 81
Chapter 3 Finite Impulse Response and Quantifying the fMRI Response to Epileptic Spikes 82
3.1 Abstract 82
3.2 Objectives 83
3.3 Introduction 83

3.4 Methods 85
3.4.1 Participants 85
3.4.2 Data Acquisition 89
3.4.3 Data Processing 89
3.4.4 Finite Impulse Response Deconvolution 90
3.4.5 Simulation 91
3.4.6 Training the IED Basis Set 92
3.4.7 Testing the IED Basis Set 93
3.5 Results 98
3.5.1 Simulations 98
3.5.2 Training the IED Basis Set 102
3.5.3 Testing the IED Basis Set 110
3.6 Discussion 124
3.6.1 Simulations 124
3.6.2 Smooth FIR Deconvolution 124
3.6.3 Testing the IED-HRF Basis Set 125
3.6.4 Issues with Reporting the Global Maxima 126
3.6.5 Possible Reasons for Early Haemodynamic Change 126
3.6.6 Limitations 128
3.6.7 Future Work 128
3.7 Conclusions 129
Chapter 4 NIRS Optode Holder Design and Construction 130
4.1 Abstract 130
4.2 Objectives 131
4.3 Introduction 131
4.4 Methods 133
4.4.1 Data Acquisition 135

4.4.2 Data Processing 145
4.5 Results 146
4.5.1 Cap Design on Healthy Adults 146
4.5.2 Flexible Optode Design Pilot on Healthy Adults 148
4.6 Discussion 153
Chapter 5 EEG-NIRS Recordings in Paediatric Epilepsy Patients during EEG Video-Telemetry 155
5.1 Abstract 155
5.2 Objectives 155
5.3 Introduction 156
5.4 Methods 158
5.4.1 Patients 158
5.4.2 Data Acquisition: 158
5.4.3 Data Analysis 159
5.5 Results 160
5.5.1 Patients with Seizures 163
5.5.2 Patients with Interictal Epileptiform Discharges 170
5.6 Discussion 172
5.6.1 Haemodynamic Changes Related to Seizures 172
5.6.2 Haemodynamic Changes Related to Interictal Epileptiform Discharges 173
5.6.3 Deoxyhaemoglobin and Meeting Metabolic Demands of the Seizure Focus 174
5.6.4 Haemodynamics Contralateral to the Seizure Focus 176
5.6.5 Limitations 176
5.6.6 Future Work 176
5.6.7 Conclusion 177
Chapter 6 Laser Doppler Flowmetry in Surgical Paediatric Epilepsy Patients 178

6.1 Abstract 178
6.2 Objectives 178
6.3 Introduction 179
6.3.1 Historical Laser Doppler Design 181
6.3.2 Current Laser Doppler Design 183
6.4 Results 184
6.4.1 Historical Laser Doppler Data 185
6.4.2 Current Laser Doppler Data in Humans 187
6.5 Discussion 187
Chapter 7 Discussion 188
7.1 Objectives and General Summary of Results 188
7.1.1 Network Connectivity Reductions are Due to IEDs 188
7.1.2 FIR and Quantifying the fMRI Response to Epileptic Spikes 189
7.1.3 NIRS Identifying Oxygenation Changes in Seizure Focus 190
7.1.4 The Potential for Invasive Blood Flow Measurements 191
7.2 Summary 192
Chapter 8 Appendix 193
8.1 Connectivity Networks and the Effect of IEDs 193
8.2 Principal Components Analysis 213
References 214

Table of Figures

Figure 1.1 Action potentials and neurotransmitter release 21
Figure 1.2 Pharmacological agents regulating glutamate and GABA 23
Figure 1.3 Representation of intracellular and extracellular paroxysmal depolarisation shift during ictal and inter-ictal periods 25
Figure 1.4 Illustration of blood flow from arteries to veins 28
Figure 1.5 Flexibility of cerebral autoregulation. 29
Figure 1.6 Overview of the meninges 33
Figure 1.7 Astrocytes: the connecting link between blood vessels and neurons 33
Figure 1.8 Summation of dipoles and the physiological basis of EEG 35
Figure 1.9 T1 Relaxation 38
Figure 1.10 T2 Relaxation 38
Figure 1.11 G_x gradient: frequency encoding in the x-direction 39
Figure 1.12 Magnetic field flux for paramagnetic and diamagnetic mediums 41
Figure 1.13 Modelling an fMRI task using the haemodynamic response function 43
Figure 1.14 Fixed HRF models 45
Figure 1.15 Physiological underpinning of the HRF 46
Figure 1.16 Extinction curves for absorbers found in tissue 48
Figure 1.17 Illustration of NIRS cerebral penetration 51
Figure 2.1 Task paradigm 63
Figure 2.2 Overview of analysis approach 65
Figure 2.3 Task response 71
Figure 2.4 Functional connectivity 74
Figure 2.5 Changes in patient functional connectivity associated with IEDs 75
Figure 3.1 Methods for training the basis set 96
Figure 3.2 Methods for testing the basis set 97
Figure 3.3 Smoothness optimisation simulation comparing standard and smooth FIR 98
Figure 3.4 Example of Gibbs phenomenon. 100
Figure 3.5 Extracted responses for both standard and smooth FIRs 101
Figure 3.6 Time course of original data 101
Figure 3.7 PCA Components 103

Figure 3.8 GLM Comparison for patients included in training the IED-HRF basis set 109
Figure 3.9 Post-surgical patients: testing the IED basis set on the concordant cluster 111
Figure 3.10 Comparison for patients included in testing the IED-HRF basis set 123
Figure 4.1 Summary of tasks performed to test efficacy of both cap and flexible grid designs 134
Figure 4.2 Flowchart of methodological steps taken for the cap and flexible grid designs 134
Figure 4.3 EEG electrode placement used for simultaneous EEG-NIRS 135
Figure 4.4 NIRS optode placement for motor task in simultaneous EEG-NIRS 137
Figure 4.5 CAD drawing of optode holder used in cap design 138
Figure 4.6 Recording conditions for the pilot NIRS cap design 139
Figure 4.7 Testing variations of the flexible grid design 141
Figure 4.8 CAD drawing of optode holder used in flexible grid design 143
Figure 4.9 Recording paradigm for healthy adult controls in pilot data 144
Figure 4.10 Steps for NIRS grid preparation 144
Figure 4.11 Example of NIRS grid placement during motor task 145
Figure 4.12 Changes in haemoglobin during finger-tapping task using cap design 147
Figure 4.13 Changes in haemoglobin during maths task: forehead recordings 148
Figure 4.14 Haemoglobin concentration changes during blood occlusion 149
Figure 4.15 Average change in oxyhaemoglobin for all healthy subjects during finger-tapping motor task 150
Figure 4.16 Average change in deoxyhaemoglobin for all healthy subjects during finger-tapping motor task 151
Figure 4.17 Significant differences in oxyhaemoglobin in healthy adults during finger-tapping motor task 152
Figure 4.18 Significant differences in oxyhaemoglobin in healthy adults during finger-tapping motor task 153
Figure 4.19 Pro/Con list of optode holder designs 154
Figure 5.1 EEG-NIRS changes at 40sec window surrounding seizure event: Patient #1 164
Figure 5.2 NIRS changes at 10min window surrounding seizure event: Patient #1 165

Figure 5.3 EEG-NIRS changes at 40sec window surrounding seizure event: Patient #2 166
Figure 5.4 NIRS changes at 10min window surrounding seizure event: Patient #2 167
Figure 5.5 EEG-NIRS changes at 40sec window surrounding seizure event: Patient #3 168
Figure 5.6 NIRS changes at 10min window surrounding seizure event: Patient #3 169
Figure 5.7 Patients: EEG and NIRS changes for IED events 171
Figure 6.1 Laser Doppler measures the microvascular blood flow in capillaries 179
Figure 6.2 Historical LD-iEEG grid 182
Figure 6.3 Historical data: Patient #1 LD-iEEG grid placement 182
Figure 6.4 Historical data: Patient #2 LD-iEEG grid placement 183
Figure 6.5 Modern Laser Doppler-iEEG strip design 184
Figure 6.6 Historical Data: Patient #1 LD-iEEG recording 186
Figure 8.1 Spatial Definition for ROI determining Effect of Clinical Variables 198
Figure 8.2 Network overlays of the General Linear Model 199
Figure 8.3 Network overlays of the functional connectivity map 206
Figure 8.4 Principal components characterised as noise 213

Table of Tables

Table 2.1 Patient Information: EEG-fMRI Connectivity 59
Table 2.2. Seed middle cingulate functional connectivity controls > patients 73
Table 2.3. Seed right fusiform functional connectivity controls > patients 74
Table 3.1 Patient Information: EEG-fMRI haemodynamics 86
Table 3.2 Patients included in training the basis set 104
Table 3.3 Concordant Cluster 109
Table 3.4 Global Maxima 109
Table 3.5 Post-surgical patients included in testing the basis set: Concordant Cluster 113
Table 3.6 Lesion patients included in testing the basis set: Concordant Cluster 115
Table 3.7 Post-surgical patients included in testing the basis set: Global Maxima . 118
Table 3.8 Lesion patients included in testing the basis set: Global Maxima 120
Table 3.9 Concordant Cluster 123
Table 3.10 Global Maxima 123
Table 4.1 Testing optode holders: Holder dimensions 142
Table 4.2 Testing optode holders: Iterations 142
Table 5.1 Patient information sheet: EEG-NIRS 162
Table 8.1 Group Activations for ‘Wait’ > ‘Video’ 193
Table 8.2 Group Activations for ‘Video’ > ‘Wait’ 195
Table 8.3 Paired t-test for FC Controlling vs Not Controlling for IEDs 196
Table 8.4 Control Network Overlap with Previous Studies: GLM 200
Table 8.5 Patient Network Overlap with Previous Studies: GLM 202
Table 8.6 Group Difference Network Overlap with Previous Studies: GLM 204
Table 8.7 Control Network Overlap with Previous Studies: FC 207
Table 8.8 Patient Network Overlap with Previous Studies: FC 209
Table 8.9 Group Difference Network Overlap with Previous Studies: FC 211

Table of Abbreviations

AAL	Automated Anatomical Labelling
AED	Anti-Epileptic Medication
AMPA	Alpha-Amino-3-Hydroxy-5-Methyl-4-Isoxazole Propionic Acid
BOLD	Blood Oxygen Level Dependent
Ca^{2+}	Calcium
CBF	Cerebral Blood Flow
CBV	Cerebral Blood Volume
CBZ	Carbamazepine
cHRF	Canonical Haemodynamic Response Function
Cl^-	Chloride
CLBZ	Clobazam
$CMRO_2$	Cerebral Metabolic Rate of Oxygen
CO_2	Carbon Dioxide
CSF	Cerebral Spinal Fluid
dACC	dorsal Anterior Cingulate Cortex
DBS	Deep Brain Simulation
deoxyHb	Deoxyhaemoglobin
DMN	Default Mode Network
DNET	Dysembryoplastic Neuroepithelial Tumour
ECN	Executive Control Network
EEG	Electroencephalography
EEG-fMRI	Electroencephalography-functional Magnetic Resonance Imaging
EEG-NIRS	Electroencephalography-Near Infrared Spectroscopy
EPI	Echo Planar Imaging
EPSP	Excitatory Post-Synaptic Potential
ESI	Electrical Source Imaging
FCD	Focal Cortical Dysplasia
FDA	Federal Drug Administration (United States of America)

FIACH	Functional Image Artefact Correction Heuristic
FIR	Finite Impulse Response
fMRI	Functional Magnetic Resonance Imaging
FOV	Field of View
Fp	Fronto-Parietal
FSIQ	Full Scale Intelligence Quotient
FWE	Family Wise Error
FWHM	Full Width at Half Maximum
GAB	Gabapentin
GABA	Gamma-AminoButyric Acid
GLM	General Linear Model
GOSH	Great Ormond Street Hospital
HbDiff	Haemoglobin Difference
HbT	Total Haemoglobin
HRF	Haemodynamic Response Function
ICN	Intrinsic Connectivity Network
IED	Interictal Epileptiform Discharge
IED-HRF	Interictal Epileptiform Discharge Haemodynamic Response Function
iEEG	Intracranial Electroencephalography
IPSP	Inhibitory Post-Synaptic Potential
IQ	Intelligence Quotient
K^+	Potassium
L	Left
LCM	Lacosamide
LD	Laser Doppler
LD-iEEG	Laser Doppler-intracranial Electroencephalography
LTG	Lamotrigine
LVT	Levetiracetam
M	Magnetisation
MBLL	Modified Beer Lambert Law
MEG	Magnetoencephalography
MNI	Montreal Neurological Institute
MR	Magnetic Resonance
MRI	Magnetic Resonance Imaging

NA	Not Applicable
Na^+	Sodium
NIRS	Near Infrared Spectroscopy
NMDA	N-Methyl-D-Aspartate
O_2	Oxygen
OD	Optical Density
OXC	Oxcarbazepine
oxyHb	Oxyhaemoglobin
PCA	Principal Component Analysis
PDS	Paroxysmal Depolarisation Shift
PET	Positron Emission Tomography
PGB	Pregabalin
PMP	Perampanel
PSP	Post-Synaptic Potential
PU	Perfusion Units
R	Right
RF	Radio Frequency
RFT	Random Field Theory
RS	Resting State
RUF	Rufinamide
SAR	Specific Absorption Rate
sFIR	Smooth Finite Impulse Response
SN	Salience Network
SNR	Signal to Noise Ratio
SOZ	Seizure Onset Zone
SPECT	Single Photon Emission Computed Tomography
SPM	Statistical Parametric Map
T	Tesla
TE	Echo Time
TMS	Transcranial Magnetic Stimulation
TP	Time Point
TPM	Topiramate
TR	Repetition Time
TS	Temporal Sclerosis

UK	United Kingdom
VPA	Valproate
VSD	Voltage-Sensitive Dye
WASI	Wechsler Abbreviated Scale of Intelligence
WISC	Weschler Intelligence Scale for Children
ZNS	Zonisamide

Chapter 1 General Introduction

1.1 Epilepsy

Epilepsy is a common symptom and affects about 1% of children (Harrison et al., 1976; Hauser et al., 1991) with a very high incidence rate in early childhood and a relative decrease in adolescence (Everitt et al., 1998). It is defined as the recurrent clinical manifestation of abnormal and excessive discharges of local cortical neurons in the grey matter (Fisher et al., 2014). However, an isolated seizure cannot be referred to as epilepsy. Epilepsy is generally diagnosed based on behavioural symptoms and can be confirmed via electroencephalography (EEG).

The majority of patients become seizure-free after medication, however up to 25% of affected children are drug-resistant. These drug-resistant patients are often referred for a series of neuroimaging tests (such as EEG video-telemetry, fMRI, SPECT, and PET imaging) to determine the possibility of surgical resection of the seizure focus to improve seizure burden. Therefore, the need for accurate localising tools is crucial.

Epilepsy results from abnormal hyperexcitable and hypersynchronous neuronal activity (Engel et al., 2008). It has many sources varying from structural brain damage, to genetic (Vadlamudi et al., 2003). Broadly, seizures can be classified into two types: focal (localised to one hemisphere) and generalised (activity in both hemispheres). However, the possible progression from focal to bilateral tonic-clonic seizures prompted debates concerning seizure reclassification. The final decision sustained the bimodal classification scheme for ease of use in communicating clinical care, teaching, and research (Fisher et al., 2016).

The mechanisms underlying seizures and the origin of hyper-excitability of neuronal networks have yet to be determined, however there is some understanding of the neurophysiological and neurochemical factors governing this pathological activity.

1.1.1 Neurophysiology and Neurochemistry of Cortical Neurons

The cortex is comprised of two classes of neurons (Bromfield et al., 2006), the first being principal neurons (also called ‘projection’ neurons), which send information to

distant areas of the brain and generally form excitatory synapses on post-synaptic neurons. The second class of neurons are interneurons, which contrary to principal neurons, send information locally and form inhibitory synapses on either principal cells or other inhibitory neurons. This network organisation allows for feed-forward inhibition (interneurons inhibiting projection cells) and feed-back inhibition (projection cells activating interneurons, which in turn inhibit projection cells) thereby controlling network excitability.

Neuronal communication is governed by action potentials. An action potential occurs by depolarisation of the intra-cellular membrane which becomes less negative due to shifts in ion concentration from extracellular to intracellular space. When an action potential occurs, the membrane depolarisation propagates down the axon (see Figure 1.1) opening the voltage-gated calcium channels at the axon terminals, and thus releasing the neurotransmitters from their vesicles into the synaptic cleft and finally transfers to the post synaptic membrane in the next nearby cell. Depolarisation can occur due to excitatory synaptic neurotransmission, decreased inhibitory neurotransmission (inhibiting the inhibitor), or altering the state of voltage-gated ion channels.

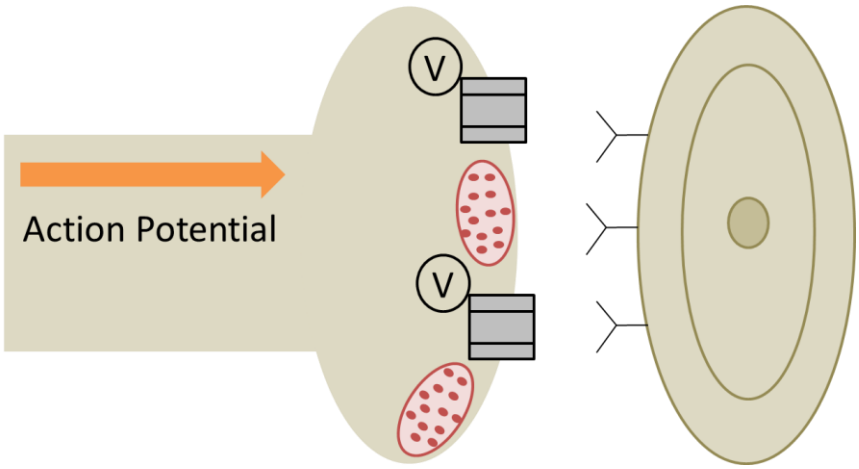

Figure 1.1 Action potentials and neurotransmitter release
This illustration depicts the movement of the action potential from the presynaptic neuron (left) to the postsynaptic neuron (right). The propagation of the membrane depolarisation is illustrated by an orange arrow. When the action potential reaches the axon terminals, the voltage-gated calcium channels (voltage-gated indicated by the letter 'V'; calcium channels illustrated by grey boxes) opens, this initiates the

release of neurotransmitters (red circles) within the vesicles (pink circles). The neurotransmitters subsequently attach to receptors ('Y' shaped symbol) of the postsynaptic neuron and incur an electrical change dependent on the neurotransmitter released.

The primary neurotransmitters in the brain are glutamate, GABA (Gamma-AminoButyric Acid), acetylcholine, norepinephrine, dopamine, serotonin, and histamine. However there are two neurotransmitters typically considered to be critical to seizure control: glutamate and GABA.

Glutamate is the major excitatory neurotransmitter in the cortex. There are several subtypes of glutamate receptors including AMPA (Alpha-Amino-3-Hydroxy-5-Methyl-4-Isoxazole Propionic Acid) and NMDA (N-Methyl-D-Aspartate) receptors, both of which produce an influx of Na^+ ions in the post-synaptic neuron when activated (see Figure 1.2 in red). This contributes to cell depolarisation and subsequent action potentials. Previous animal models have shown that NMDA and AMPA induce seizure activity (Yamaguchi et al., 1993; Rogawski et al., 1996; Rogawski et al., 2011) whereas their antagonists suppress seizure activity. Such antagonists can be used as antiepileptic medication such as lamotrigine and topiramate.

Contrary to glutamate, GABA is the major inhibitory neurotransmitter in the adult brain. It has two major receptor subtypes: $GABA_A$ and $GABA_B$. $GABA_A$ receptors are found post-synaptically and are permeable to Cl^- ions. Chloride ions hyperpolarise the cell membrane thereby inhibiting action potentials (see Figure 1.2 in purple). Pharmacological agents take advantage of this phenomenon by using $GABA_A$ agonists in suppressing seizures including valproate, vigabatrine, diazepam, and phenobarbital. These medications either interfere with the transporter function (valproate and vigabatrine) or act through the GABA receptor sites inducing the release of Cl^- ions into the post-synaptic cell (phenobarbital and diazepam). $GABA_B$ receptors are similar to $GABA_A$ in that both are inhibitory, but $GABA_B$ is found pre-synaptically and is associated with a secondary release of K^+ ions, leaving the cell and prompting hyperpolarisation. Previous studies have also suggested that agonists of $GABA_B$ can exacerbate seizure activity in absence and temporal lobe epilepsies

(Caddick et al., 1996) however the mechanisms behind this occurrence have yet to be determined. Furthermore, $GABA_A$ has been reported to act as an excitatory neurotransmitter in neonates (LoTurco et al., 1995), thereby adding an extra layer of complexity in interpreting the interaction of seizures and age-dependent neurotransmitter behaviour.

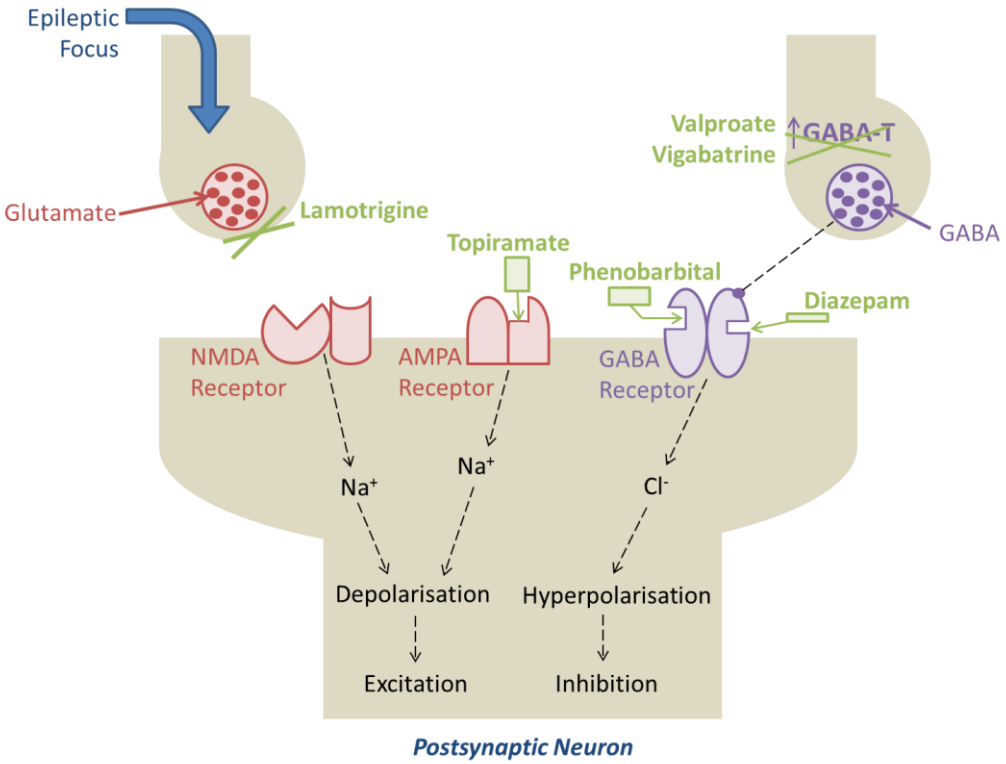

Figure 1.2 Pharmacological agents regulating glutamate and GABA
An illustration of the presynaptic (top left, top right) and postsynaptic (middle bottom) neurons and their role in preventing the propagation of neuronal activity from the epileptic focus (blue arrow) via antiepileptic drugs (AEDs; illustrated in green). Glutamate (red circles; presynaptic) is an excitatory neurotransmitter, and its release discharges Na^+ ions into the postsynaptic cell, thus increasing the likelihood of depolarisation and excitation. Therefore both lamotrigine and topiramate prevent the neurotransmitters from attaching to their postsynaptic receptors (red blocks; postsynaptic) by blocking the release of glutamate presynaptically (lamotrigine) or blocking the postsynaptic receptor to prevent attachment (topiramate). In contrast, GABA (purple circles; presynaptic) acts as an inhibitor, and its release discharges Cl^- ions thus increasing the chance of hyperpolarisation and inhibition in the postsynaptic neuron. Many AEDs act upon

GABA, including phenobarbital, diazepam, valproate, and vigabatrine. Phenobarbital and diazepam attach to the postsynaptic GABA receptors, initiating an increase in Cl^- into the postsynaptic neuron. Similarly, Valproate and vigabatrine increase the Cl^- ions in the postsynaptic cell by blocking the reuptake of GABA in the synaptic cleft via GABA-T (GABA transaminase). These are just a few examples of how pharmacological agents aid in preventing the propagation of action potentials from the epileptic focus.

Many pharmacological agents attempt to reduce the likelihood of an action potential and prevent the progression through neuronal networks. The continuous burst of action potentials characteristic of epilepsy is known as the paroxysmal depolarising shift (PDS) (see Figure 1.3, top panel). PDS requires large and sustained depolarisations that occur synchronously within a large population of neurons (Holmes et al., 2001). However, during this prolonged depolarisation there is no intervening repolarisation, as is normal in excitatory post-synaptic potential (EPSP). Additionally, the duration of this depolarisation is much longer than normal, ranging from 10-16ms in a normal EPSP to 100-200ms in PDS (Holmes et al., 2001).

The neurochemical manifestation of PDS (Holmes et al., 2001) begins with the opening of AMPA channels releasing Na^+ into the cell causing depolarisation (see Figure 1.3, bottom panel). This is followed by the opening of the NMDA channels, allowing both Na^+ and Ca^{2+} to enter the cell membrane, further depolarising the cell. The next step is hyperpolarisation, which occurs due to the opening of K^+ channels and the activation of GABA permitting the efflux of K^+ and influx of Cl^- ions. The role of voltage-gated K^+, Na^+, Ca^+ and GABA receptors in initiating PDS has led many researchers to probe genetic mutations associated with these channels and their subsequent relationship to different epilepsies.

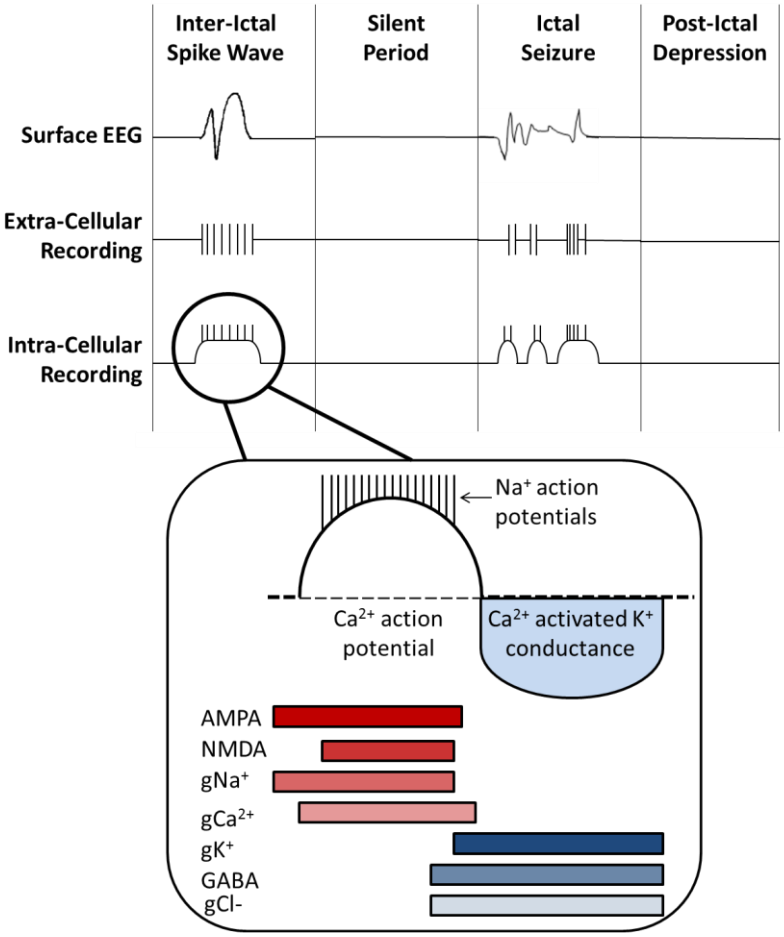

Figure 1.3 Representation of intracellular and extracellular paroxysmal depolarisation shift during ictal and inter-ictal periods

The top panel illustrates the representation of ictal and inter-ictal periods in surface EEG (top row), extra-cellular recordings (middle row), and intra-cellular recordings (bottom row). Interictal spike waves traditionally seen on surface EEG have an associated cellular response with prolonged depolarisations, illustrated by black lines, defining sudden voltage change. Cellular activity seen during the ictal states is similar with more frequent depolarisations and rhythmic activity on surface EEG. The prolonged depolarisation is more clearly seen intra-cellularly, with no intervening repolarisation. The neurochemical processes of paroxysmal depolarisation shift (PDS) in an interictal state are highlighted in the bottom panel. The first step is depolarisation (highlighted in red): PDS starts with an initial opening of AMPA channels releasing Na^+ intracellularly. A subsequent opening of NMDA channels further depolarises the cell with increases in Na^+ and Ca^{2+}. After this prolonged depolarisation, there is a second hyperpolarisation phase (highlighted in blue): initiated by the efflux of K^+ due to Ca^{2+} activated channels and the influx of Cl^- due to the opening of GABA channels.

Genetic mutations associated with sodium channels (Escayg et al., 2000; Spampanato et al., 2001; Heron et al., 2002; Lossin et al., 2003; Berkovic et al., 2004), calcium channels (Vitko et al., 2005), potassium channels (Zuberi et al. 1999; Eunson et al., 2000), and $GABA_A$ receptors have triggered generalised epilepsy with febrile seizures, childhood absence epilepsy, focal onset epilepsy, and juvenile myoclonic epilepsy respectively. Though there has been much progress in genetics research in epilepsy patients, there is still much to learn. Genes that are currently discussed as susceptibility factors could account for only a fraction of genetic contributions (Turnbull et al., 2005; Engel et al., 2008; Thomas and Berkovic, 2014).

There are three main theories as to why regions of the epileptogenic cortex become hyperexcitable. The first theory assumes a selective loss of interneurons provoking hyper-excitability. Treatment under this theory involves interneuron transplantation (Mathern et al., 1995; Colasante et al., 2015; Chohan et al., 2016). Another theory proposes synaptic reorganisation as the cause of hyper-excitability, such as 'sprouting' of excitatory axons following injury (Babb and Brown, 1987). Sprouting increases the number of connections and the extent of its neuronal excitation in the altered neuronal network. Finally, the loss of excitatory neurons that would normally activate inhibitory neurons can also cause a shift in excitability (Sloviter et al., 2003). This is also called the 'dormant basket cell' hypothesis, as basket cells are a type of inhibitory neuron that remains dormant until activated by an excitatory neuron (ie: mossy cell). However it is important to note that seizures affect an overall hierarchy of brain architecture, from the single neuron level to the epileptogenic networks.

A macroscopic epileptogenic network can comprise of multiple brain regions (nodes) that are involved in the generation of epileptic activity (Spencer, 2002). The connectivity between those nodes determines the pattern of network activity for both focal and generalised epilepsies. Furthermore, these abnormal functional connections not only influence epileptogenic networks (Iannotti et al., 2016), but also permeate fMRI resting state networks (Centeno and Carmichael, 2014) indicating IED's extensive impact on overall brain connectivity. The multi-nodal characteristic of epileptogenic networks can also be demonstrated at a cellular level using voltage-sensitive dye (VSD) imaging, where multidirectional waves of membrane potential

cause network change to accompany seizures (Ma et al., 2013). Therefore, epilepsy can be defined as a network disease (Centeno and Carmichael, 2014; Laufs et al., 2014), in which seizures arise as a result of changes in network structure, not necessarily provoked by a single focal pathologic brain region (Terry et al., 2012). If or how the interactions at the level of neurons translate to macroscopic network synchrony has yet to be fully understood.

The predominant abnormality characterizing epileptic activity is an excess of neuronal firing within an epileptogenic network, but there are other biological abnormalities that are coupled with seizure activity including changes in blood oxygenation and flow. Seizures and inter-ictal activity can be altered by many factors such as sleep, hormone levels, or brain maturation. This indicates that the brain state as defined by its connectivity and excitability has a significant impact on the generation of epileptic activity.

1.2 Vascular and Physiological Relationships

1.2.1 Vasculature

The normal regulation of cerebral blood supply is transported through a continuous vessel system in the body. Arteries carry blood away from the heart while veins carry blood to the heart thereby allowing oxygenated and deoxygenated blood to travel through the body. Capillaries then join arteries to veins and carry blood to tissue and exchange nutrients locally. They are small vessels, generally less than 4-5μm in width (Mraovitch and Sercombe, 1996), with a tissue wall consisting of a single layer of flat transparent cells called tunica intima. In contrast, arteries and veins have three tissue layers including the tunica intima as well as the tunica media and tunica adventitia (see Figure 1.4). The restrictive size of the capillary allows for only one blood cell to travel through in single file.

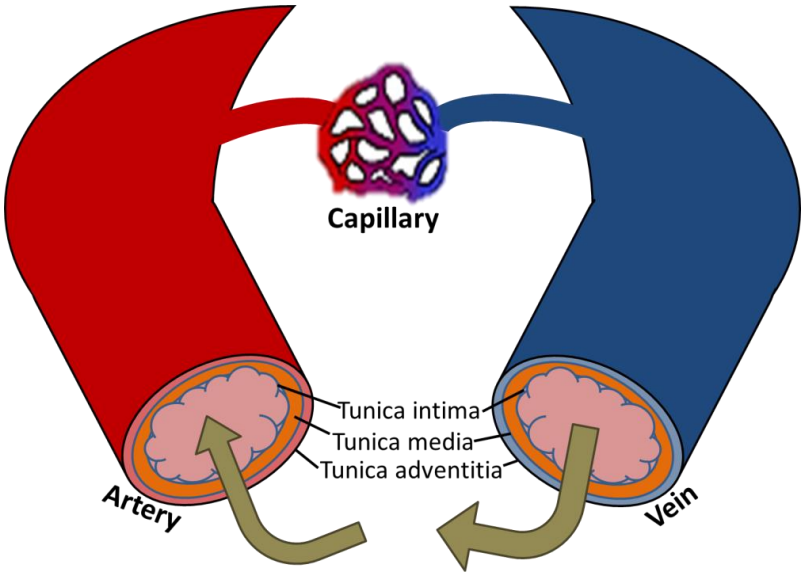

Figure 1.4 Illustration of blood flow from arteries to veins
Arteries carry oxygenated blood away from the heart while veins carrying deoxygenated blood to the heart. Both arteries and veins consist of three layers called the tunica intima, tunica media, and tunica adventitia. Capillaries are connected to both arteries and veins and perfuse the tissue with nutrients.

1.2.2 Cerebral Autoregulation

Vascular beds control blood flow through autoregulation. Autoregulation is the ability of cerebral vessels to maintain a constant blood flow when there is a change in perfusion pressure (Mraovitch and Sercombe, 1996). The necessity of functioning cerebral autoregulation is critical. The failure of cerebral circulation within a time period as short as 5 minutes can result in death of nerve cells. Also, the brain comprises only 2-3% of total body weight but receives 15% of cardiac output and consumes 20% of oxygen (and 25% of blood glucose), indicating the continuous need for systematic blood flow to the brain (Harper and Jennett, 1990).

Though autoregulation is very flexible, there are limitations. For example, when the mean arterial blood pressure is above 150mmHg autoregulation is unable to function and a forced dilation of vessels occurs as a result, leading to cerebral oedema (Harper and Jennett, 1990). In the reversed case, extreme low values can cause cerebral hypoxia (see Figure 1.5). Additionally, autoregulation can be compromised in many neurological disorders including stroke (Jaeger et al., 2012), traumatic brain injury (Figaji et al., 2009), and epilepsy (Heiss, 1979; Penfield, 1939). The complete

understanding of autoregulation in epilepsy has yet to be determined. However previous research has indicated marked increases in cerebral blood flow during seizures (Heiss, 1979; Penfield, 1939) beyond the range of normal autoregulation.

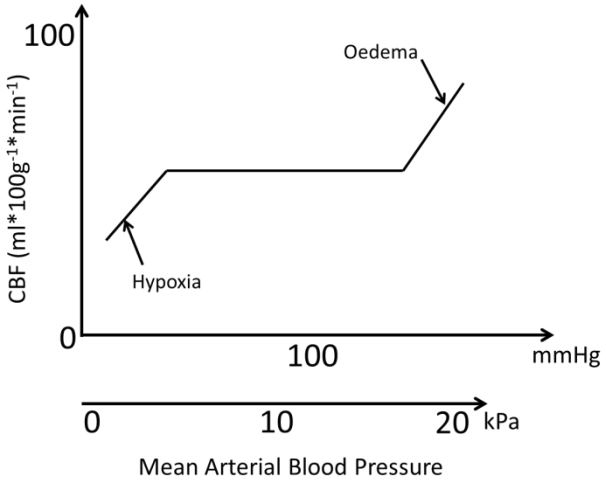

Figure 1.5 Flexibility of cerebral autoregulation.
Autoregulation is the process by which cerebral blood flow is maintained at an appropriate mean arterial blood pressure between 50-150mmHg. A deficit of tissue oxygenation can occur at <50mmHg resulting in hypoxia. The converse can also occur at >150mmHg with a cerebral oedema which can lead to increased intracranial pressure.

The mechanisms of cerebral autoregulation in response to external stimuli (e.g., a flickering checkerboard) or internal stimuli (e.g., epileptic spikes) are the basis for many neuroimaging techniques. This includes the physiological relationship between cerebral blood flow (CBF), cerebral blood volume (CBV), and cerebral metabolic rate of oxygen consumption ($CMRO_2$).

1.2.3 Metabolic, Vascular, and Neuronal Coupling

1.2.3.1 Metabolic-Vascular Coupling

An increase in neuronal activity results in a haemodynamic response allowing oxygen and glucose to be delivered to brain tissue. The haemodynamic response is defined by the interactions between CBF, CBV, and $CMRO_2$. CBF and CBV have a steady-state relationship that can be defined by Equation 1.1. The CBF increase after neuronal activity is caused by a relaxation of the smooth muscles in the arterioles.

$$v = f^{\propto}$$ ***Equation 1.1***

Where v=cerebral blood volume (CBV), f=cerebral blood flow (CBF), and $\propto = 0.4$ (Grubb et al., 1974).

This increase in relaxation subsequently triggers a decrease in arteriolar resistance allowing more blood through the circulatory system, and thus decreasing the pressure in arterioles (and increasing the pressure in capillaries and veins). CBF and CBV are highly related because the increased pressure in capillaries and veins forces vessel expansion and thus an increase in CBV. However, developmental differences can be seen in varying age groups. The normal CBF reported in healthy adults can range from 40-60ml/100g/min in grey matter to 10-30ml/100g/min in white matter (Grubb et al., 1974). In contrast to CBV values which range from 0.04-0.06ml/ml and 0.01-0.03ml/ml in grey and white matter respectively (Herold et al., 1986; Grubb et al., 1978; Donahue et al., 2010). Paediatric groups can have a much wider range of values (Hales et al., 2014), underlining the importance of studies focusing on haemodynamics in the developing brain.

The relationship between $CMRO_2$ is slightly more complex in that it is defined by multiple physiological variables including the net oxygen extraction fraction (E), the arterial oxygen concentration (C_a), and CBF (see Equation 1.2). During a baseline state the relationship between CBF and $CMRO_2$ is roughly linear (see Equation 1.3) with previous studies defining the slope as n=2-3 (Davis et al., 1998; Hoge et al., 1999; Kastrup et al., 2002; Marrett and Gjedde, 1997; Seitz and Roland, 1992). These values indicate an increase in CBF which surpasses that of $CMRO_2$ producing a decrease in E, the amount of oxygen extracted by the tissue from the blood. The oxygen limitation model provides an explanation for this imbalance between CBF and $CMRO_2$.

$$\boldsymbol{CMRO_2 = E \cdot C_a \cdot CBF}$$ ***Equation 1.2***

$$n = \frac{\frac{\Delta CBF}{CBF_0}}{\frac{\Delta CMRO_2}{CMRO_{2_0}}} = \frac{f-1}{m-1}$$ *Equation 1.3*

Where the baseline values for both CBF and $CMRO_2$ are denoted with the subscript "0" and concentration changes are denoted with delta. Therefore f and m are CBF and $CMRO_2$ normalised to baseline respectively.

The oxygen limitation model (Buxton and Frank, 1997; Hyder et al., 1998; Buxton et al., 2002) provides a sensible explanation for the disparity between oxygen delivery and oxygen utilisation accompanying neuronal activation. The overall goal of the oxygen limitation model is to transport oxygen from the capillaries to the mitochondria where there is a net increase of $CMRO_2$ (with the assumption of absence of capillary recruitment). This model states that an increase in oxygen metabolism can only be achieved through an increase in pO_2 in the blood vessels supported by the increase in CBF. However, because O_2 metabolism is restricted by the rate of transport out of the capillaries, a larger increase in CBF is required in comparison to $CMRO_2$ (Buxton and Frank, 1997). This phenomenon describes the metabolic-vascular coupling associated with neuronal stimulation but does not describe the physiological mechanisms involved in neuronal activity. To further explore this relationship, an understanding of neurovascular coupling is essential.

1.2.3.2 Neurovascular Coupling

The interdependent relationship between vascular circulation and neuronal activity is defined as neurovascular coupling. At baseline, cerebrovascular autoregulation takes place in the form of arterial relaxation or constriction during decreases and increases in arterial pressure respectively. However changes in neuronal activity deviating from baseline are coupled with local increases in CBF (Roy and Sherrington, 1890). This phenomenon is referred to as functional hyperaemia. Many hypotheses were developed to explain functional hyperaemia, however the most popular of which recognises the involvement of interneurons and glial cells (specifically astrocytes).

Oxygenated blood is delivered through arterioles in the cerebral cortex located in the pia mater (see Figure 1.6). As described previously arterioles are connected to

capillaries (see Figure 1.4) which deliver blood to the surrounding tissue. The connecting link between blood vessels and the neurons is thought to stem from glial cells (Zonta et al., 2003) whose end feet lay on local capillaries (see Figure 1.7). The local proximity of astrocytes to both blood vessels and neurons allows them to facilitate communication between them. When the presynaptic neuron releases neurotransmitters (i.e., glutamate) across the post-synaptic cleft to reach the postsynaptic neuron, astrocytes detect the local neurotransmitter release. This causes intracellular Ca^{2+} propagation across the astrocyte. Subsequently the terminal end feet of the astrocyte release vasodilating (or vasoconstricting) transmitters to proximal arterioles, such dilating (or constricting) vessels nearby. Interneurons might also play a role, as they are proximal to blood vessels and can release vasoactive factors during neuronal activity (Cauli et al., 2004). The benefit of this hypothesis is that it accounts for the rapid and spatially specific CBF changes occurring with neuronal activity.

Other theories regarding functional hyperaemia refer to feed-back and feed-forward mechanisms. The feed-back process requires an initial recognition of energy deficit caused by increased neuronal activity that triggers increases in CBF. However, the hypoxic/hypoglycaemic deficit following stimulation are transient and of low magnitude, making it unlikely to be the sole driving force of CBF changes in areas of local neuronal activity (Shmuel, 2010). In contrast, the feed-forward mechanism involves the additive effect of several vasoactive mediators involved in neurotransmitter-related signalling such as ions, neurotransmitters, and neuromodulators (Edvinsson and Krause 2002; Hamel 2004). Nevertheless, under this model the breakdown of one of these mediators would not disrupt the CBF response, thereby indicating a multi-route system (Iadecola 2004).

The role of neurovascular coupling in epilepsy remains largely unknown however some physiological mechanisms have been identified in causing seizure activity. Interictal and ictal activity increase local metabolic demand due to PDS, and thus require a corresponding increase in regional CBF to sustain nutrient supply. The epilepsy-induced functional hyperaemia can therefore be used in functional neuroimaging, as a rise in local CBF results in increased oxygenated haemoglobin and a rise in blood oxygen level dependent signal. Therefore, the above models for

metabolic, vascular, and neuronal coupling provide a basis for quantitative interpretation of functional magnetic resonance imaging, especially in regards to changes in CBF and changes in neuronal activity.

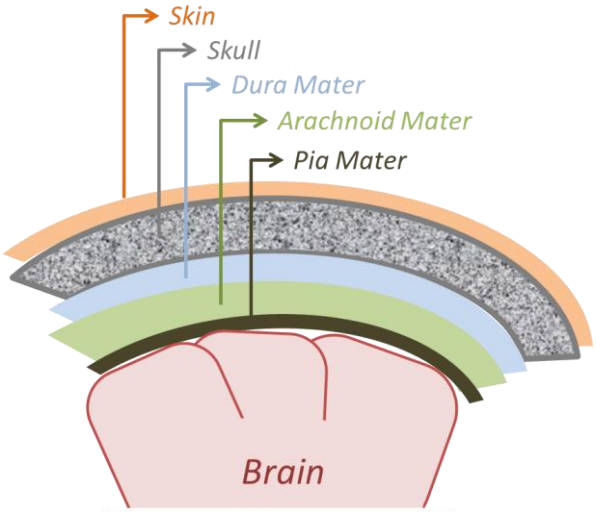

Figure 1.6 Overview of the meninges

The human brain is enveloped by multiple layers. The first two external layers are the skin (orange) and skull (grey) which provide a protective surface. The meninges include the dura mater (blue), arachnoid mater (green) and pia mater (brown). The dura mater is thick and durable and contains large blood vessels. The arachnoid mater has a web-like structure that is thin and transparent. The pia mater is a thin sheet that covers the brain and has capillaries that nourish the brain tissue underneath.

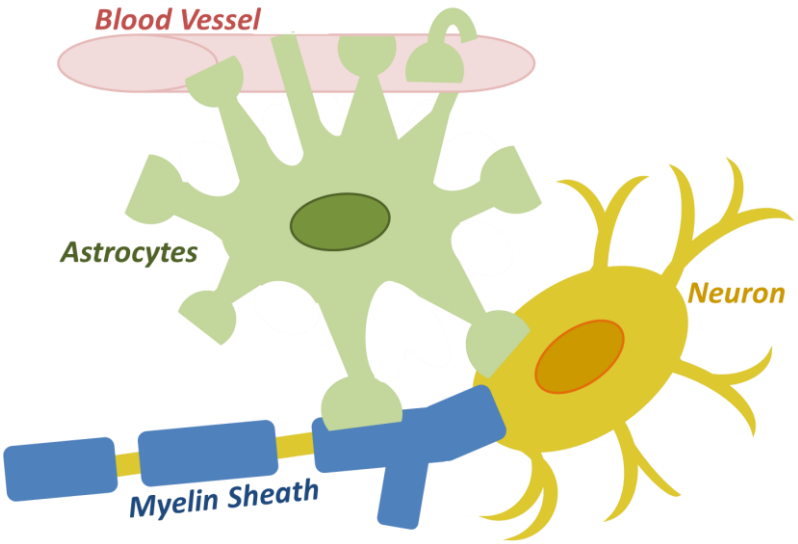

Figure 1.7 Astrocytes: the connecting link between blood vessels and neurons

Astrocytes (seen in green; can be identified by their star-like appearance) are believed to have a role in cerebral microcirculation as they are a physical bridge between neurons (yellow) and blood vessels (red).

1.3 Neuroimaging

Neuroimaging can be widely split into two modalities in the context of this thesis. One which measures electrophysiology (such as EEG) and another focused on measuring haemodynamics and metabolism (such as fMRI and NIRS).

EEG can directly measure the electrical fluctuations from a population of neurons while other techniques, such as fMRI, indirectly record changes in neuronal function by exploiting the metabolic changes following periods of neural activity. Ideally these techniques will be performed non-invasively to reduce any possible discomfort or risk of infection.

1.3.1 Electroencephalography

Electroencephalography (EEG) is frequently used in the diagnoses of epilepsy. It measures the electrical potentials of cortical neuronal dendrites near the surface of the scalp (Lopes da Silva, 2010). EEG electrodes are typically placed on the scalp according to the internationally recognised 10-20 system. The 10-20 system requires adjacent electrodes to have a separation of either 10% or 20% of the total distance from the nasion to the inion (Hughes, 1994). This allows for standardised measurements for studies within subjects (e.g.: recording EEG on different days, or in different centres) as well as between subjects.

The physiological basis of the EEG signal relies on the structure of the pyramidal cells within the cortical surface (Lopes da Silva and van Rotterdam, 2005; Olejniczak, 2006). These cells tend to share the same orientation and polarity and can be activated in synchrony. Neuronal synchrony is necessary as electrodes cannot detect the small magnitude changes emerging from a single neuron. If neuronal activations occur in synchrony, a group of coordinated postsynaptic potentials must occur. Post-synaptic potentials (PSPs) are electrical changes in membrane potential

that can contribute to the occurrence of an action potential, depending on whether the PSP is excitatory (EPSP) or inhibitory (IPSP) (Shmuel, 2010).

When this stimulus occurs, an excitatory signal allows positively charged ions to move through the cellular membrane into an area called the 'sink' where the ions are dumped from the presynaptic cells into the postsynaptic (Nicholson, 1973). As these positively charged ions are moving from the dendrites towards the cell body, the local extracellular region of the synapse will be slightly negative (see Figure 1.8). Once these positively charged ions reach the cell body and basal dendrites, the ions rush out of the cell membrane at a site referred to as the 'source' (Nicholson, 1973). The region surrounding the source has a slight positive charge in the extracellular space, making the cell oppositely charged at both ends (negative at the dendrites, positive at the axon). This phenomenon is referred to as a dipole, and it is the summation of these dipoles that generate the EEG signal (Niedermeyer et al., 2005; Speckmann et al., 2005).

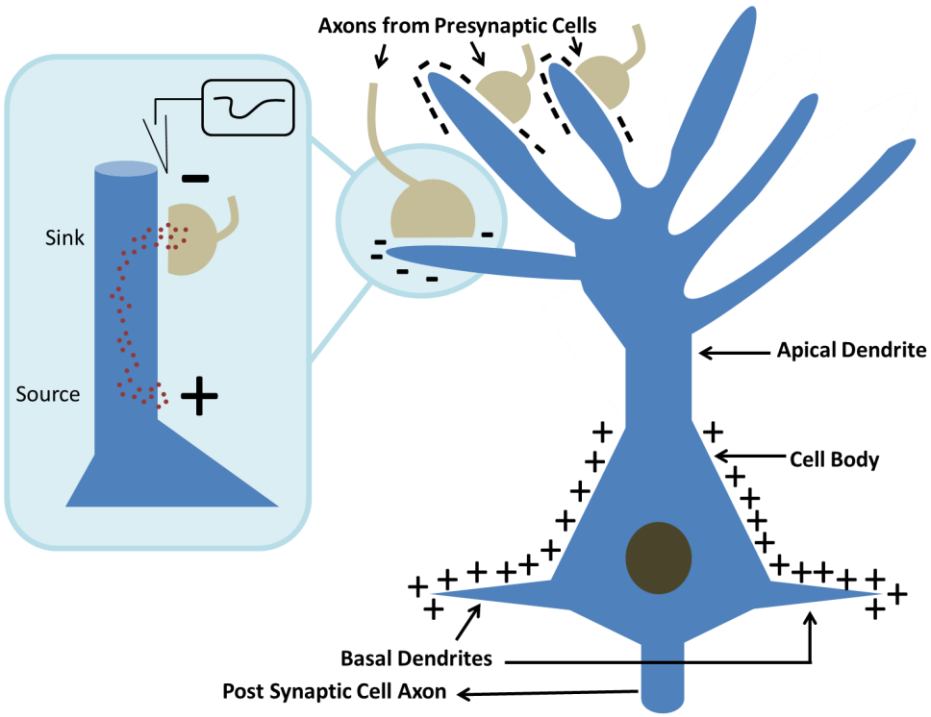

Figure 1.8 Summation of dipoles and the physiological basis of EEG
After an excitatory signal synapses on to the apical dendrite of the pyramidal cell (see right panel), an extracellular dipole is generated where the region surrounding the synapse becomes more negative and the positively charged ions move down to the cell body and basal dendrites. The positively charged ions then rush out of the

cellular membrane making the local extracellular region more positive. Therefore, an extracellular dipole is generated at the sink (site of the synapse) and the source (where the ions exit the cell membrane) with negative and positive charges respectively (see left panel). The summation of these pyramidal dipoles is the source of EEG signal.

EEG has the benefit of directly measuring changes in neuronal activity with high temporal resolution. For this reason it is used for the diagnoses of epilepsy. Unfortunately, the scalp EEG can only acquire signals from nearby sources. It is thought to penetrate around 6 cm^2 of cortex (Cooper et al., 1965), but this only includes surface gyri, as cortical dipoles within sulci tend to cancel each other out. Therefore, EEG recordings have high temporal resolution, but are limited with spatial localisations. Contrary to EEG, functional magnetic resonance imaging has poor temporal resolution but high spatial resolution that can capture activity on the millimetre scale (Laufs, 2012; Lemieux et al., 2001; Turner et al., 1998). To obtain both, previous studies have used simultaneous EEG-fMRI in order to better categorise the seizure onset zone (Centeno et al., 2016). Therefore, by combining these two techniques, we are aiming to substitute one method's deficiencies with another's strengths. Simultaneous EEG-fMRI will be further discussed in Chapter 2 and Chapter 3.

1.3.2 Magnetic Resonance Imaging

Magnetic Resonance Imaging (MRI) allows for non-invasive observations of tissue morphology using radiofrequency pulses and magnetic fields. The signal from MRI is due to the magnetic moment of the hydrogen nucleus (proton) which itself is due to the quantum property known as spin. The high concentration of hydrogen nuclei in the body (particularly in water and fat) make it ideal for study (Bloembergen et al., 1947). It is possible to observe a signal from other nuclei such as phosphorous and carbon isotopes (Novotny, 1995), however their low concentration in the body makes imaging challenging.

Once the sample is exposed to a strong static magnetic field (B_0), an almost equal number of spins align parallel to the field as they do antiparallel. However there is a slight excess parallel to the field as opposed to against it, due to its lower energy

state, which leads to a net moment. The subsequent summation of the magnetic moments gives rise to a net magnetic moment per unit volume. This magnetic moment per unit volume is referred to as magnetisation (M). A magnetic field applied at the Larmor frequency orthogonal to B_0 (63.87MHz at 1.5T; see Equation 1.4) tips the magnetisation vector away from B_0. This is termed the radiofrequency (RF) pulse. The frequency required for the RF pulse (ω) is determined by the gyromagnetic ratio (γ) constant and the magnetic field (B_0) (see Equation 1.4).

$$\boldsymbol{\omega = \gamma B_0} \qquad \textit{Equation 1.4}$$

The magnetisation that has been tipped into the transverse plane then precesses at the Larmor frequency. This precessing magnetisation will induce a voltage in a nearby receiver due to magnetic induction (in accordance with Faraday's law); this is the signal we measure in MRI. This effect was originally demonstrated by Bloch (1946) and Purcell et al. (1946) and has since been the used as the basis for modern neuroimaging methods.

1.3.2.1 Relaxation

The use of an RF pulse disturbs the equilibrium state of the magnetisation. In order for the magnetisation to return to its equilibrium state the process of relaxation must occur. There are two forms of relaxation that occur simultaneously. One is called longitudinal relaxation (T1), which causes the component of the magnetisation parallel to B_0 to recover (Figure 1.9) following an RF pulse. The second form of relaxation is the transverse relaxation time (T2), which is the loss of phase coherence of the component of magnetisation perpendicular to the magnetic field (see Figure 1.10) which causes this component of the magnetisation to return to its equilibrium value of zero. Both T1 and T2 are sensitive to their molecular environment which is different between tissue types. For example at 3T the T1 of white matter, grey matter, and CSF is approximately 850ms, 1300ms, and 4500ms respectively (Wansapura et al., 1999). Thus, T1 weighted images are commonly used to achieve contrast between these tissues. T2 weighted images also have a distinction between tissue types: 80ms for white matter and 110ms for grey matter. However CSF values are around 2000ms making differences between CSF and brain tissue easily

distinguishable from fluid compartments (Wansapura et al. 1999). Therefore, T2 weighted images can be used as a means for lesion detection.

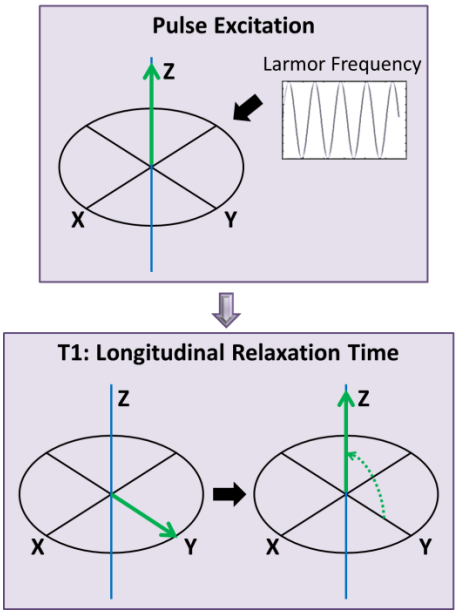

Figure 1.9 T1 Relaxation

T1 (or longitudinal) relaxation time determines the time it takes for net magnetisation to return to its equilibrium position along the magnetic field. After the initial RF pulse at the Larmor frequency (top panel), the magnetisation tilts from Z to Y (bottom panel, left). The time it takes to return to equilibrium (bottom panel, right) is determined by the T1 relaxation time.

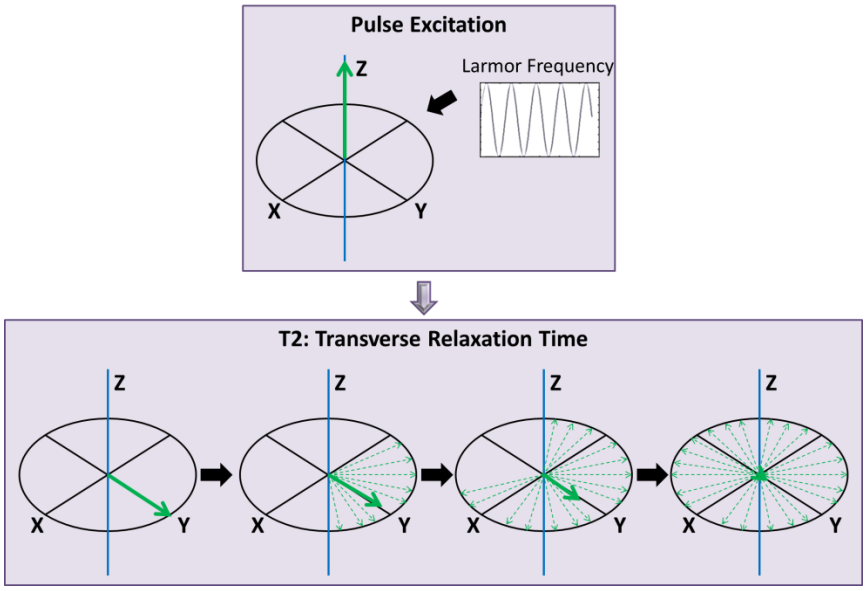

Figure 1.10 T2 Relaxation

Similar to T1 relaxation time, T2 (or transverse) relaxation time starts with the initial RF pulse in the Larmor frequency (top panel). After which, the magnetisation is in-phase within the X Y plane. In time there is a loss of phase coherence (bottom panel far left to bottom panel far right) resulting in signal decay.

1.3.2.2 Gradients

In order to obtain images in 3D space, spatial encoding of the MR signal is required in three orthogonal directions which we define here as x, y, and z using linear magnetic field gradients. The first to use linear magnetic field gradients was Lauterbur et al. (1973). The gradient in the x-direction (G_x) is referred to as the read gradient and performs the frequency encoding. During acquisition with Gx, the frequency of precession increases linearly along the x-direction making nuclei precession dependent on the position in the brain (see Figure 1.11). Therefore, magnetisation position can be determined based on frequency using the Fourier transform. The precessional frequencies in the y-direction is determined by the phase encoding (PE) gradient, which refers to the signal phase shift along the y direction by the application of successive PE gradients (G_y) with different amplitude. The third gradient (G_z) is referred to as the slice selective gradient and here occurs in the z-direction. G_z is similar to the frequency encoding gradient as it changes the precessional frequency along z. The difference is that a frequency selective RF pulse is utilised to excite only one slice at a time. With these three gradients Gx, Gy, and Gz it is possible to obtain 3D images. Note that while this description for simplicity limits read, phase and slice to being x,y and z directions the spatial encoding can be applied in any arbitrary direction in practice.

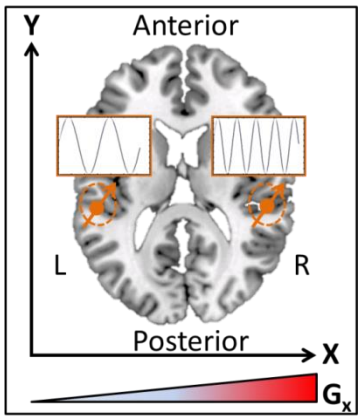

Figure 1.11 G_x gradient: frequency encoding in the x-direction

Precession frequency changes linearly across space in the x-direction, as illustrated by the bottom scale (higher frequencies in red and lower frequencies in blue). Therefore magnetisation position can be determined based on frequency. The magnetisations rotate (orange arrows) at a frequency dependent on the magnetic field.

1.3.2.3 T2*

We have previously said that relaxation in the transverse plane is dictated by T2. However, after an RF pulse the signal can decay much faster than T2 would predict. This effective relaxation time is referred to as T2*. This is because the addition of background (constant) magnetic field inhomogeneities causes faster loss of phase coherence. For example, the presence of paramagnetic biological substances such as deoxyhaemoglobin increases the magnetic susceptibility in an area, creating local magnetic fields and contributing to the loss of phase coherence. These field inhomogeneities can be captured by a time constant called T2'. The relationship between T2*, T2, and T2' is as follows:

$$\frac{\mathbf{1}}{\boldsymbol{T2^*}} = \frac{\mathbf{1}}{\boldsymbol{T2}} + \frac{\mathbf{1}}{\boldsymbol{T2'}} \qquad \textit{Equation 1.5}$$

This increased loss of phase coherence may at first seem undesirable. However, it now means the images we create (as described in the previous section) are sensitive to changes in susceptibility. We know that as oxygenation changes so does susceptibility. This effect can be harnessed to study human brain function as changes in neural activity are associated with changes in oxygenation (see section 1.2). This forms the basis of a technique used by neuroscientists to study brain function called functional Magnetic Resonance Imaging (fMRI).

1.3.2.4 Functional Magnetic Resonance Imaging

The theoretical basis of fMRI was first described by Ogawa et al. (1990). He referred to the oxygenation dependence on the MRI signal as Blood Oxygenation Level Dependent (BOLD). Essentially Ogawa et al. (1990) illustrated the different magnetic properties associated with -oxy and –deoxy haemoglobin could be interrogated using MRI. Deoxyhaemoglobin is paramagnetic (slightly attracts the local magnetic field) (see Figure 1.12 left panel) while both oxyhaemoglobin and

brain tissue are diamagnetic (slightly repels the local magnetic field) (see Figure 1.12 right panel). During rest, blood concentration is more paramagnetic, thereby causing local field inhomogeneities. Consequently, inhomogeneities in the local magnetic field decrease the MRI signal. However, when neuronal activity prompts the increase of oxyhaemoglobin within a brain region, local field inhomogeneities are reduced causing a temporary increase in signal amplitude. This signal change is known as the BOLD effect, and is representative of neuronal activation. Therefore BOLD-fMRI is an indirect measure of neuronal activity with the added benefit of being non-invasive and having high spatial resolution.

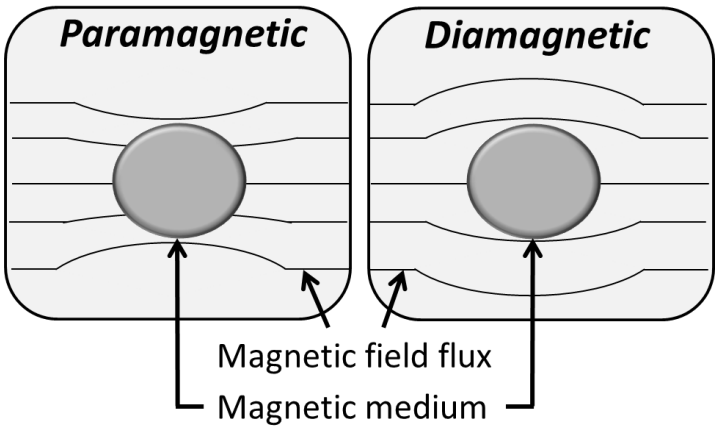

Figure 1.12 Magnetic field flux for paramagnetic and diamagnetic mediums
Magnetic flux changes are dependent of the magnetic property of the medium (circle) and whether it is paramagnetic (left) which attracts the local magnetic field, or diamagnetic (right) which repels the local magnetic field.

1.3.2.5 From Neurons to Networks

FMRI indirectly records neuronal activity at a macroscopic level however the neuronal origin of the underlying BOLD signal is still not completely known (Murta et al., 2015). In general, there are two main forms of neuronal activation 1) synaptic activation which represents slow changes in membrane potential (such as IPSPs and EPSPs) and 2) action potentials which are fast responses in membrane depolarisation (Lopes da Silva, 2010). Previous work shows that BOLD signal better reflects synaptic activity than action potentials (Thomsen et al., 2004). This is consistent with calculations of the energy budget of the cortex that are higher in synaptic activity, thus consuming more ATP and oxygen than action potentials (Hall et al., 2016). The impact of synaptic activity on blood volume, blood flow, and oxygenation is

subsequently measured by the BOLD signal. As previously stated, these neurovascular changes can be attributed to a feed-forward mechanism via astrocyte mediation (Rothman et al., 2003; Zonta et al., 2003). However the neurovascular coupling is less well determined in epilepsy and it is possible that interictal and ictal BOLD changes are generated by different neuronal populations and network mechanisms (De Curtis and Avanzini, 2001) thereby modifying the physiological interpretation of BOLD signal. Therefore, it is important to disentangle the effects of both IEDs and seizures on haemodynamics.

The above considers epilepsy, neuronal activity and its measurement via haemodynamic responses at a micro-meso scale. However, focal epilepsy is increasingly considered to be a network disease and the interaction between widespread brain regions can manifest in network abnormalities in epileptogenic (Iannotti et al., 2016) and resting state networks, which have previously been associated with cognitive performance (Widjaja et al., 2013; Ibrahim et al., 2014). Therefore, fMRI can be used to measure the effect of epilepsy at this scale.

FMRI can be used to measure functional connectivity. Functional connectivity studies have shown the brain is organised into intrinsic connectivity networks (ICNs), each network is defined by strong correlations between nodes within the network. These networks can be found by extracting them from fMRI during rest (Smith et al., 2009). ICNs have frequently been found to be compromised in patients with epilepsy as demonstrated across many resting state fMRI (RS-fMRI) studies (Waites et al., 2006; Zhang et al., 2009; Haneef et al., 2012; Centeno and Carmichael, 2014). However, the influence of epileptic activity on these networks has yet to be fully examined, thus prompting the need for simultaneous recordings of EEG-fMRI (see Chapter 2).

1.3.2.6 fMRI Analysis Methodology

When creating a BOLD fMRI model the objective is to map a spatial response to a stimulus. To do so, knowledge of the brain's BOLD response to the stimulus is required. The function to describe this haemodynamic response is termed the haemodynamic response function (HRF), and is used in predicting the fMRI response to stimuli. In order to do this, one needs to perform a linear convolution

between the input paradigm and the haemodynamic response function (HRF) (see Figure 1.13). The HRF represents the haemodynamics of a neuronal response to a stimulus and lasts approximately 30 seconds from event onset to the return to baseline (Friston et al., 1994; Friston et al., 1998). The HRF can be represented in a multitude of ways and a standardized model has yet to be decided upon, but the simplest and most commonly used design is the canonical HRF (see Equation 1.6). As an attempt to account for possible variability, the spatial and temporal derivatives can also be applied to the canonical model.

Other types of HRFs include the gamma (see Equation 1.7) and Glover functions (see Equation 1.8). All of which represent a 'fixed' model approach. Additionally, all three models described (canonical, gamma, and Glover) have a very similar shape, as illustrated in Figure 1.14. This is mainly due to the physiological parameters that govern the BOLD response.

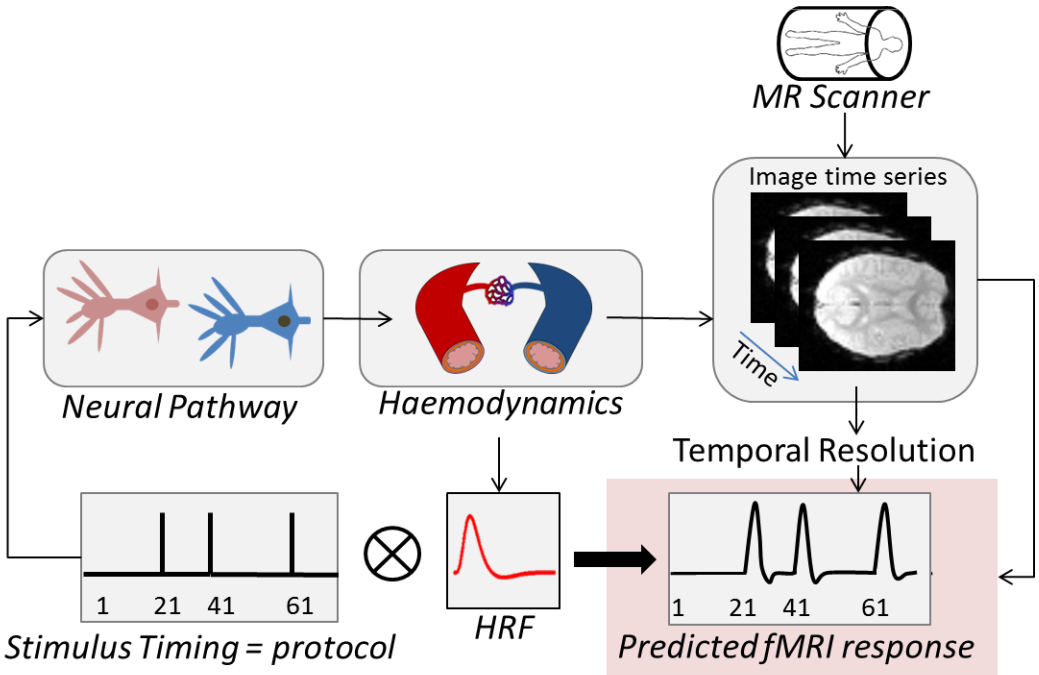

Figure 1.13 Modelling an fMRI task using the haemodynamic response function
The activity of the neural pathway (top left) has corresponding changes in haemodynamics (top middle), which can then be detected in the BOLD image time series extracted from fMRI (top right). The stimulus protocol (bottom left) of an fMRI experiment initiates neuronal activity with a corresponding change in haemodynamics represented by the haemodynamic response function (HRF) (bottom

middle). Finally, the convolution of the stimulus and the HRF gives a predicted BOLD fMRI response to the stimulus (bottom right).

$$\boldsymbol{h_{canonical}(t) = \frac{l_1 h_1 \times t^{(h_1-1)} \times e^{-l_1 t}}{\gamma(h_1)} - c \times \frac{l_2 h_2 \times t^{(h_2-1)} \times e^{-l_2 t}}{\gamma(h_2)}} \qquad \textbf{Equation 1.6}$$

Where t is the time in seconds and $\gamma(h)$is the standard gamma-variate. $l_1 = l_2 = 1$, $h_1 = 6$, $h_2 = 16$.

$$\boldsymbol{h_{gamma}(t) = \left(\frac{t}{bc}\right)^{b} \times e^{b-\frac{t}{c}}} \qquad \textbf{Equation 1.7}$$

Where t is time (seconds), b = 8.6, and c = 0.547. Variables 'b' and 'c' must be estimated from the dataset parameters, in this case visual flash stimuli (Cohen, 1997).

$$\boldsymbol{h_{glover}(t) = \left(\frac{t}{d_1}\right)^{a_1} \times e^{-\left(\frac{t-d_1}{b_1}\right)} - c \times \left(\frac{t}{d_2}\right)^{a_2} e^{-\left(\frac{t-d_2}{b_2}\right)}} \qquad \textbf{Equation 1.8}$$

Where t is time (seconds), $a_1 = 6$, $a_2 = 12$, $b_1 = b_2 = 0.9$, $c = 0.35$. The parameters a_1, a_2, b_1, b_2, and c are taken from auditory stimulus datasets (Glover, 1999; Worsley et al., 2002).

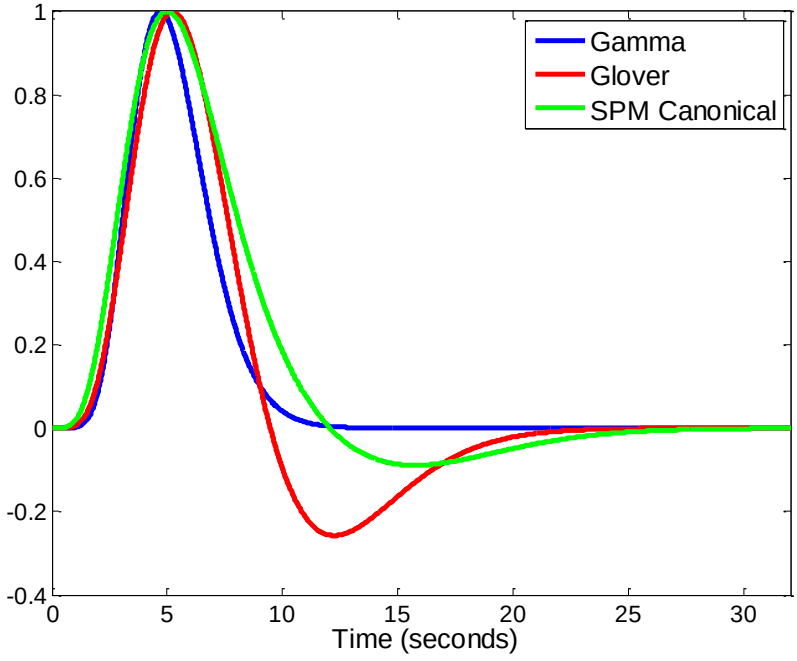

Figure 1.14 Fixed HRF models
Illustration of fixed model HRFs, including gamma (blue), Glover (red), and the SPM canonical (green).

The physiological response of the HRF can be subdivided into two subsections of large overshoot and mild undershoot, however it should be noted that the initial dip has not been consistently seen in fMRI experiments, which is why it is not depicted in Figure 1.14. However it has been reported in animal studies as well as in high field strengths (Frostig et al., 1990; Buxton, 2001; Yacoub et al., 2001).

Once the initial neuronal activation occurs there is an increase in the cerebral metabolic rate of oxygen consumption ($CMRO_2$). 1) The consumption of oxygen leads to higher rates of deoxyhaemoglobin and thus lowers the signal due to field inhomogeneities, causing the initial dip. 2) The signal quickly recovers due to a rapid increase in cerebral blood volume (CBV) and subsequent increase of cerebral blood flow (CBF) results in an overshoot (Shen et al., 2008). Though the CBV and CBF have opposing effects, in that CBV increases the concentration of deoxyhaemoglobin while CBF increases the concentration of oxyhaemoglobin, the dramatic increase in CBF trumps the opposing effects of both $CMRO_2$ and CBV, thus contributing to the large overshoot in the HRF. Finally, 3) the HRF has a small undershoot approximately 10 seconds prior to 4) returning to baseline due to the lagging CBV relaxation time (see Figure 1.15).

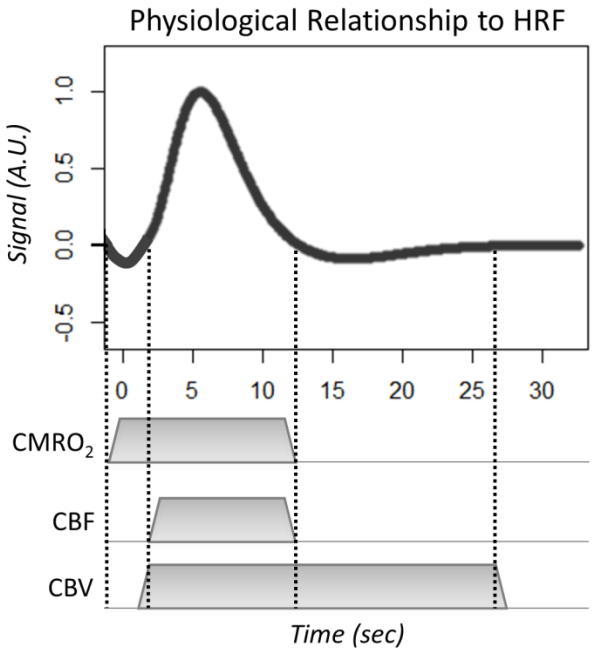

Figure 1.15 Physiological underpinning of the HRF
The initial increase in $CMRO_2$ can cause a slight dip in the haemodynamic response due to the oxygen consumption, resulting in an increase in deoxyhaemoglobin. A subsequent rise in the signal is caused by a large amount of CBF that overpowers the $CMRO_2$ and CBV increases. However, once the increase in CBF subsides, there is a continuation of CBV increases resulting in a slight undershoot prior to returning to baseline.

The general physiology behind the HRF is well defined, but the mechanisms initiating changes in blood flow in response to neuronal activity is still unclear even for healthy cortex although in primary sensory cortices this has been relatively well characterised (Logothetis et al. 2001). However BOLD contrast is fuelled by a variety of sources with few observables (Donahue et al., 2016), making it difficult to define the concentration changes specifically attributed to either –oxy or –deoxy haemoglobin. In this respect, other neuroimaging techniques such as near infrared spectroscopy are more specific.

1.3.3 Combining EEG and fMRI

As described previously, fMRI is a neuroimaging technique with high spatial resolution, which is particularly useful for patients with epilepsy as pre-surgical evaluation requires localisation of the epileptogenic cortex. However, fMRI has low

temporal resolution, which is imperative as epileptic activity can occur in the range of milliseconds. EEG has the opposite problem, in that it has low spatial resolution but high temporal resolution, therefore the simultaneous use of EEG can allow for the acquisition of data that has high spatial-temporal resolution thereby making it possible to record EEG-fMRI for mapping haemodynamic changes related to epileptic events (Ives et al., 1993; Lemieux et al., 2001).

1.3.4 Near Infrared Spectroscopy

Similar to fMRI, Near Infrared Spectroscopy (NIRS) takes advantage of neurovascular coupling between blood oxygenation and neuronal activation to indirectly measure changes in the brain's response to internal or external stimuli. It does so by utilizing the sensitivity of haemoglobin to near infrared light, which can determine changes in –oxy and –deoxy haemoglobin concentrations. NIRS has been used in various clinical populations ranging from those with metabolic diseases such as diabetes (Brown et al., 2005), to psychiatric disorders such as schizophrenia (Koike et al., 2013), to neurological diseases such as epilepsy (Wallois et al., 2010).

NIRS is a fairly new technique with increasing popularity, especially in childhood developmental studies (Gervain et al., 2011). However, most of this work is done on either infants or adults, with an age gap surrounding toddler to teenage years. Infants are well-suited for NIRS recordings as they have significantly thinner skin/skull compared to older children and adults, producing a threefold increase in the depth of light penetration. Many studies have also looked at adult epilepsy populations (Sokol et al., 2000; Buchheim et al., 2004; Slone et al., 2012) however NIR light penetration is only able to reach superficial cortices in adults, constraining the spatial and patient foci range of studies conducted. This limitation is due to the interaction of NIR with brain tissue.

Light in the near infrared range is between 700-1000nm and is strongly attenuated in tissue. Therefore it cannot penetrate more than ~1cm in adult brains. Light attenuation occurs when the transmitted light is less than the incident light after passing through a medium and is determined by two optical properties: absorption and scatter.

Absorption is dependent on the wavelength of light and the molar extinction coefficient of the medium illuminated. The near-infrared range of the spectrum is ideal in that it allows for intervening tissues (ie: skin and bone) to be rendered transparent to light at these wavelengths, allowing absorption of oxyhaemoglobin (oxyHb) and deoxyhaemoglobin (deoxyHb). Chromophores such as haemoglobin have specific extinction coefficients for their oxygenated and deoxygenated states (seen **Error! Reference source not found.** left panel). The isobestic point (where the extinction coefficients of oxyHb and deoxyHb are equal) can be seen at 800nm. However between the range of 650-950nm both forms of haemoglobin are clearly distinguishable. Therefore, in order to measure changes in different haemoglobin concentrations, NIRS utilizes two wavelengths: one sensitive to oxyHb and one sensitive to deoxyHb.

However, there are compounds other than oxyHb and deoxyHb that can be absorbed by near-infrared light. These tissue absorbers include: water, lipids, melanin, and cytochrome c oxidase. As seen in **Error! Reference source not found.**, some of these chromophores overlap in their absorption spectra with haemoglobin, however many of these chromophores (such as water, lipids, and melanin) do not change rapidly over time and do not influence measurements of haemoglobin concentration changes.

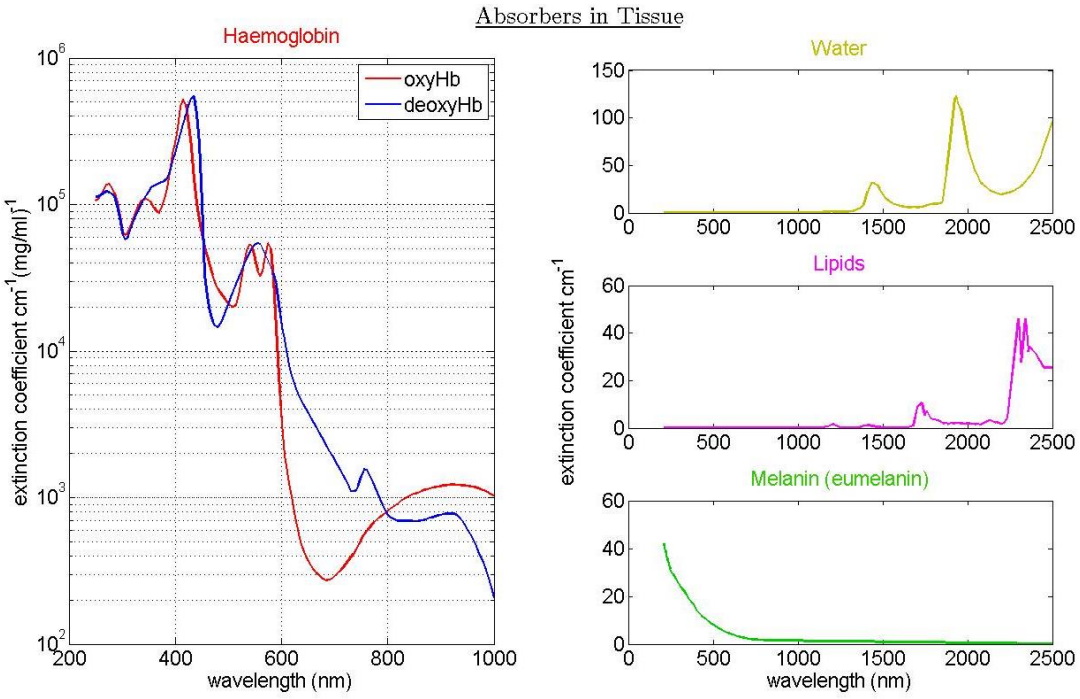

Figure 1.16 Extinction curves for absorbers found in tissue
Haemoglobin extinction coefficient for oxyhaemoglobin (in red) and deoxyhaemoglobin (in blue) can be seen in the left panel (Prahl et al., 1999). The extinction coefficients of other tissue absorbers include water (Palmer et al., 1974; Pope et al., 1997), lipids (Altshuler et al., 2003; van Veen et al., 2004), and melanin (Sarna et al., 1988), which are all considered stationary and therefore do not influence concentration changes of haemoglobin. Furthermore, the wavelength at which NIRS is being tested (780nm for deoxyhaemoglobin in blue; 830nm for oxyhaemoglobin in red) is not within the range of water (yellow), lipids (pink), or melanin (green).

On the other hand, changes in cytochrome c oxidase is of considerable interest as it represents cell metabolism and oxygen availability at the cellular level however the concentration of cytochrome c oxidase in living tissue is at least an order of magnitude below that of haemoglobin (Sato et al., 1976; Van Kuilenburg et al., 1991), thereby making it more difficult to measure. However, the difficulty in precise quantitative interpretation of this chromophore has motivated current research in this area (Banaji et al., 2010; Bale et al., 2014).

Though not absorbing, both the skin and skull can prove to be highly scattering. Therefore, the essential points of consideration in NIRS imaging are the absorption of light and light scattering media.

The original Beer-Lambert Law (see Equation 1.9) is modified in order to account for interference from biological matter between the scalp and the cerebrum.

Scattering has been accounted for by the modified Beer-Lambert Law (see Equation 1.10), which measures this loss of attenuation due to scatter and absorption (measured in Optical Density - OD units).

$$\boldsymbol{A = -log\left(\frac{I}{I_0}\right) = c \times \Sigma_{\lambda} \times l}$$ ***Equation 1.9***

Where A = absorbance, I is the intensity of transmitted light (after it hits the medium), I_0 is the intensity of incident light (before hitting the medium), c = concentration, ε_λ = molar extinction coefficient of wavelength λ, and l is the distance that light travels in the medium. The modified Beer-Lambert law (Equation 1.10) describes the attenuation of light that is absorbed, scattered and transmitted through to detector optodes.

$$-\boldsymbol{log}\left(\frac{\boldsymbol{I}}{\boldsymbol{I_0}}\right) = (\boldsymbol{c} \times \boldsymbol{\Sigma_\lambda} \times \boldsymbol{l} \times \boldsymbol{DPF}) + \boldsymbol{G} \qquad \textit{Equation 1.10}$$

Where DPF stands for Differential Pathlength Factor, which accounts for trajectory of light in biological matter due to scattering (see Delpy et al., 1988 for more information), and G is the measurement geometry and scattering coefficient (constant). Therefore, the changes in concentration can be calculated by Equation 1.11:

$$\boldsymbol{\Delta A} = \left(\left(\Delta \boldsymbol{c_{oxy}} \times \boldsymbol{\varepsilon_{\lambda_{oxy}}}\right) + \left(\boldsymbol{\Delta c_{deoxy}} \times \boldsymbol{\varepsilon_{\lambda_{deoxy}}}\right)\right) \times \boldsymbol{l} \times \boldsymbol{DPF} \qquad \textit{Equation 1.11}$$

Both BOLD and NIRS deduce neural activity based on changes in the oxygenation of haemoglobin.

The distance at which the light travels through the brain depends on the optode separation on the surface of the scalp. The trajectory of source pairing follows a banana-shape through the cerebrum (see **Error! Reference source not found.**7). Expanding the length between inter-optode distances provides a deeper cortical neuronal range of activity, but also decreases spatial resolution. Interestingly, newborns have a wider range of penetration due to their thin scalp tissue. Therefore an inter-optode distance of 3cm would provide a newborn penetration of 10-15mm into the cortex, while the average adult would only have 3-5mm penetration with the same inter-optode distance (Gervain et al., 2011). Accordingly, there are differences throughout development produced dominantly by scalp thickening and hair growth acquired with aging.

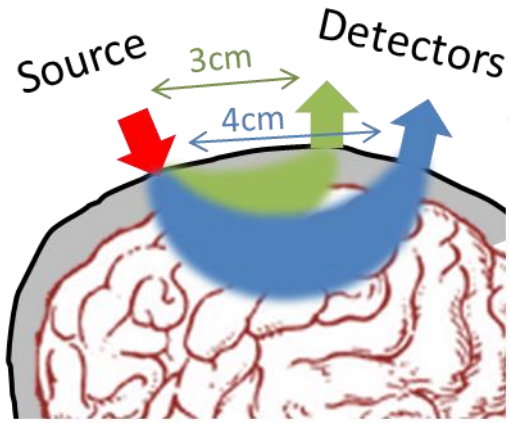

Figure 1.17 Illustration of NIRS cerebral penetration
The further away you place the source from the detector the deeper the penetration. However the cost of this is spatial specificity.

The combined knowledge on the behaviour of both oxygenated haemoglobin and blood flow from all three neuroimaging techniques can provide a better understanding of the shape and temporal dynamics of local blood supply during seizures. The aim of using a combination of techniques is to provide an accurate representation of the HRF while simultaneously determining whether haemodynamic changes can precede epileptic activity.

Overall, NIRS measurements in oxyHb and deoxyHb can prove to be highly advantageous for future recordings in clinical populations due to its non-invasive nature and high temporal resolution. Neurovascular coupling can assume changes in neuronal activity, which is imperative in understanding the effects of local and network level epileptic activity on haemodynamics. The effect of epileptic activity on cognitive networks is particularly interesting considering that epilepsy is a network disease, affecting multiple brain nodes within an epileptogenic network (Centeno and Carmichael, 2014). However, there are still issues in noise control that need to be addressed before NIRS is immersed into the clinical realm, especially in paediatric epilepsy patients where problems in motion artefact and compliance are likely. Other neuroimaging techniques such as BOLD could be used to further understand the effects of epileptic activity.

1.3.5 Combining EEG and NIRS

The combination of EEG and NIRS allows for the quantitative study of neurovascular coupling (Giacometti and Diamond, 2013) between electrical and haemodynamic changes in response to epileptic events. As both techniques share high temporal resolution (EEG on the order of 1000Hz and NIRS at 10Hz), this enables the examination of more subtle haemodynamic features which cannot be measured by fMRI due to its lower temporal resolution (0.5Hz). This, along with the portable nature of both EEG and NIRS techniques makes using simultaneous EEG-fMRI highly beneficial.

1.4 Objectives

The purpose of this thesis is to understand the response associated with, and impact of, epileptic events in children on regional haemodynamic changes in the brain. To achieve this aim, a variety of neuroimaging techniques will be used to better understand the impact of epileptic events on brain activity. This thesis is focused on paediatric focal epilepsy patients being evaluated for epilepsy surgery and so the results are expected to have relevance for the treatment and evaluation of these patients. In the following chapters different aspects of this general theme will be addressed through the use of simultaneous multi-modal imaging such as EEG-fMRI and EEG-NIRS.

One aspect that has not been well characterised is the relationship between ongoing 'normal' brain activity and epileptic discharges. Cognitive function has been linked to network integrity, which is the strong correlation found between nodes within a cognitive network (Fox et al., 2005). Patients with epilepsy have displayed compromised brain connectivity however the impact of IEDs on connectivity is unknown (Centeno and Carmichael, 2014). As epilepsy is increasingly being referred to as a network disease, it is the goal of Chapter 2 to determine the contribution of IEDs to abnormal connectivity using EEG-fMRI.

A second aspect that remains uncertain is the relationship between haemodynamic 'responses' and epileptic events. Previous EEG-fMRI studies have suggested a haemodynamic change prior to electrical events, which may reflect a more localised

event than the spike itself (Jacobs et al., 2009); however results are inconsistent. Chapter 3 explores whether the haemodynamic response can indeed precede electrical activity, and whether a new HRF model made specifically for paediatric epilepsy patients (IED-HRF) will perform better than the standard canonical model in predicting seizure focus. To do this EEG-fMRI will be used to define the haemodynamic response function (HRF), which is necessary for localisation of the seizure onset zone to predict the fMRI BOLD response of epileptic events.

If haemodynamic changes as measured by BOLD fMRI are indeed seen prior to epileptic events, it would be beneficial to understand more fully their origin. To do this we aim to measure oxygenation changes prior to IEDs or seizures in addition to $CMRO_2$, CBF, and CBV, using NIRS. To perform EEG-NIRS measurements in our patient population, a system for NIRS measurements will be created and tested for the hospital environment (without interrupting standard clinical EEG protocol). The development of the NIRS-EEG recordings will be the subject of Chapter 4 and its application on paediatric focal epilepsy patients in Chapter 5. The differing haemodynamic response between seizures and IEDs in paediatric focal epilepsy patients will be further explored and compared to those found in EEG-fMRI analyses.

In conclusion this thesis aims to explore the change in haemodynamics involving epileptic events such as seizures and interictal epileptiform activity via EEG-fMRI and EEG-NIRS. The outcome of these studies will be discussed in the following chapters.

Chapter 2 Interictal Activity Contributes to Abnormal Connectivity in Paediatric Focal Epilepsy

2.1 Abstract

Patients with focal epilepsy have been shown to have reduced functional connectivity in intrinsic connectivity networks (ICNs) which has been related to neurocognitive development and outcome. However, the relationship between interictal epileptiform discharges (IEDs) and changes in ICNs remain unclear with evidence both for and against their influence.

EEG-fMRI data was obtained in 27 children with focal epilepsy (mixed localization and aetiologies) and 17 controls. A natural stimulus task (cartoon blocks verses blocks where the subject was told 'please wait') was used to enhance the connectivity within networks corresponding to ICNs while reducing potential confounds of vigilance and motion. Our primary hypothesis was that the functional connectivity within visual and attention networks would be reduced in patients with epilepsy. We further hypothesized that controlling for the effects of IEDs would increase the connectivity in the patient group.

The key findings were: 1) Patients with mixed epileptic foci showed a common connectivity reduction in lateral visual and attentional networks compared to controls. 2) Having controlled for the effects of IEDs there were no connectivity differences between patients and controls. 4) A comparison within patients revealed reduced connectivity between the attentional network and basal ganglia associated with interictal epileptiform discharges. We also found that the task activations were reduced in epilepsy patients but that this was unrelated to IED occurrence.

Unexpectedly, connectivity changes in ICNs were strongly associated with the transient effects of interictal epileptiform discharges. Interictal epileptiform discharges were shown to have a pervasive transient influence on the brain's functional organisation.

2.2 Objectives

The aims of the present chapter are to: 1) examine differences in networks between patients with focal epilepsy and controls during a controlled brain state via a natural stimulus paradigm. 2) To determine the impact of interictal activity on the networks investigated.

2.3 Introduction

The goal of treatment in epilepsy is seizure freedom. However, the benefits of interictal epileptiform discharge (IED) suppression are controversial as the evidence for the impact of IEDs on cognitive function is mixed (Binnie et al., 2003; Aldenkamp et al., 2004; Aldenkamp et al., 2005; Fonseca et al., 2007; Nicolai et al., 2012; Ebus et al., 2015). IED prevalence is not typically used as an indication for treatment modification. However questions remain as to how and whether IEDs impact cognitive and neural function.

Previous studies indicate IEDs accompany transitory cognitive impairment in cognitive behavioural tasks (Aarts et al., 1984; Kasteleijn-Nolst et al., 1987; Kasteleijn-Nolst et al., 1988; Ebus et al., 2012). The increased rate of epileptiform discharges has been associated with lower performance on cognitive functioning and attention-sensitive tasks (Kasteleijn-Nolst et al., 1987; Kasteleijn-Nolst et al., 1988; Ebus et al., 2012; Nicolai et al., 2012), which is dependent on when and where the activity occurs (Kleen et al., 2013). Non-transient effects of IEDs are less well characterised although there is some evidence that a worse cognitive outcome in the long term is related to increased frequency of epileptic discharges in focal epilepsies (Sánchez et al., 2015) and at onset of Lennox-Gastaut syndrome (Warren et al., 2016). Cognitive dysfunction initiated by IEDs would presumably reflect an impact on the underlying cellular network mechanisms. Due to neurovascular coupling such changes would also reflect alterations in haemodynamics (see section 1.2). These changes would be observed in neuroimaging techniques such as Blood Oxygen Level Dependent (BOLD) which makes fMRI a good tool to analyse the impact of IEDs on cognitive function.

Imaging studies have found that the brain is organised into intrinsic connectivity networks (ICNs) which can be investigated via BOLD signal correlations between brain regions. This is referred to as functional connectivity. Functional connectivity is beneficial in understanding the organisation of brain networks and cognitive function. It is chiefly used in the absence of an explicit task such as in resting state fMRI (RS-fMRI). The majority of findings concerning RS-fMRI and epilepsy suggest a reduction in functional connectivity within ICNs (reduced network integrity) as a feature of epilepsy. Previous research has demonstrated a relationship between within-network functional connectivity and cognitive performance in epilepsy (Widjaja et al., 2013; Ibrahim et al., 2014a), psychiatric and neurodevelopmental disorders (Venkataraman et al., 2012; Washington et al., 2014), and healthy subjects (Smith et al., 2009; Sadaghiani et al., 2014). However, very few studies have accounted for the impact of IEDs on these findings in epilepsy despite evidence that the IEDs are associated with changes to ICNs (Laufs et al., 2007; Chaudhary et al., 2013; Lopes et al., 2014).

A recent study by Ibrahim et al. (2014a) demonstrated reduced network connectivity in ICNs using resting state MEG over short timescales before and during IEDs. This suggests that some of the fMRI connectivity differences in ICNs compared to controls (e.g. Ibrahim et al., 2014b) may be related to IEDs. Simultaneous measurements of electrophysiology and fMRI allow the measurement of the impact of IEDs on these connectivity differences. This is also important because differences have been shown in epilepsy between fMRI and electrophysiology connectivity measurements (Bettus et al., 2011).

EEG-fMRI is most commonly used for localisation of seizure generation sites in focal epilepsies (Salek-Haddadi et al., 2006; Zhang et al., 2010). Surprisingly few studies have used the benefits of recording simultaneous EEG-fMRI to examine the relationship between IEDs and ICN connectivity. Previous studies have attempted to avoid IED effects by excluding patients or data periods with IEDs on EEG (Pittau et al., 2012) and still found differences in ICN connectivity (Mankinen et al., 2012) which suggests that there might be non-transient alterations to ICN connectivity unrelated to transient effects of IEDs which might be associated with disease duration (Morgan et al., 2011; Christodoulou et al., 2012).

An important limitation in most imaging studies with focal epilepsy patients using resting state fMRI are the potential confounds of movement (Satterthwaite et al., 2012) and vigilance (Tagliazucchi and Laufs, 2014). Both of these factors can be variable between control and epilepsy populations; epilepsy patients have a high incidence of sleep problems (Chan et al., 2011). An interesting alternative to the resting state for producing connectivity in networks similar to certain ICNs is a natural stimulus paradigm (e.g. watching movies, TV shows, etc.). These stimuli have been shown to produce highly reliable responses across subjects (Hasson et al., 2004; Hasson et al., 2010). In addition to reducing variability in vigilance we have shown in a previous study that this stimulus also attenuates motion within our patient population (Centeno et al., 2016).

The aim of the current study was to provide a detailed investigation on the impact of IEDs in paediatric focal epilepsy by measurements of network connectivity, a marker of cognitive performance, during a natural stimulus paradigm. Our main hypotheses were that 1) Epilepsy patients would have reduced functional connectivity within networks engaged by the natural stimulus task (in line with ICN connectivity reductions in previous studies). 2) Functional connectivity would increase in epilepsy patients when adjusted for the effects of IEDs but remain lower than in healthy controls indicating a non-transient effect of epilepsy on network connectivity that might be related to disease duration.

To test these hypotheses we performed simultaneous EEG-fMRI to measure connectivity within ICNs in a large group of focal paediatric epilepsy patients and age matched controls. Uniquely, we used a low-demand natural stimulus to modulate connectivity in networks similar to ICNs found in RS-fMRI while reducing motion and increasing vigilance that can confound the comparison of different groups using resting state fMRI. We therefore additionally tested the response of the patient and control group to the task to define the networks, and evaluated if this response was modulated by IEDs.

2.4 Methods

2.4.1 Subjects

53 children with drug-resistant focal epilepsy undergoing assessment for surgery at Great Ormond Street Hospital (GOSH), London, UK were recruited for this study. Inclusion criteria for the study were: the presence of frequent IEDs on EEG and ages between six and 18. Exclusion criteria were: large structural lesions (i.e. strokes, cortical malformations involving several lobes, large atrophic regions, and cysts; 13 subjects), or not completing the two task sessions (12 subjects), and one subject was excluded due to a technical problem with the RF head coil. Patients with focal cortical dysplasia or cortical abnormalities circumscribed to a region within a lobe were included. After which 27 patients remained (see Table 2.1) (for more details also see Centeno et al., 2016). 17 volunteer controls also participated in the study age range 9-16 years old (mean=11.64). These included 11 females. Subjects were recruited through advertisements to GOSH staff webpages advertising participation. The study was approved by the local research ethics committee. All participants/families provided informed consent.

Table 2.1 Patient Information: EEG-fMRI Connectivity

Patient	Gender	Age	IEDs	Age of Onset (years)	Epilepsy focus localisation	Lesion Type	IQ (FSIQ)	Medication (mg/day)
# 1	Female	14	0	4	Left Frontal	None	81	CBZ 800, LVT 2000
# 2	Male	11	255	0.25	Left Temporal	Hypothalamic Hamartoma	88	LVT 1625
# 3	Male	15	0	10	Left Temporal	None	108	CBZ 600
# 4	Female	11	66	1.3	Right Fronto-Temporal Junction	None	93	LCM 100 GAB 500 CLBZ 5
# 5	Male	15	44	10	Right Frontal	None	83	CBZ 1200
# 6	Male	14	478	8	Left Temporal Posterior	Focal Cortical Dysplasia	84	OXC 1200, LVT 1000
# 7	Female	14	181	2.5	Right Temporal	Cortical Abnormality Unknown Aetiology	N/A	LVT 2000, TPM 150
# 8	Female	11	265	6	Right Fronto-temporal	None	66	CBZ 800, LTG 250
# 9	Female	10	270	7	Right Fronto-Polar	Focal Cortical Dysplasia	115	OXC 1050
# 10	Female	16	168	10	Right Frontal	None	111	LTG 500, LVT 2000

# 11	Female	16	21	6	Left Frontal	None	83	VPA 2000, CBZ 400
# 12	Female	17	0	0.42	Left Temporal	Astrocytoma	44	TPM 500, OXC 2100
# 13	Female	15	200	13	Left Insula-deep	Focal Cortical Dysplasia	N/A	TPM 50, CBZ 800
# 14	Male	17	57	0.008	Right Precuneus	Focal Cortical Dysplasia	59*	PGB 200, LCM 400, LTG 300, TPM 200
# 15	Male	11	264	3	Right Frontal	None	56	CBZ 640
# 16	Male	15	234	9	Temporal-posterior quadrant	Hippocampal Sclerosis	91	LTG 575, ZNS 200
# 17	Female	17	134	3	Left Temporal	None	56	LVT 3000
# 18	Female	16	0	5	Left Frontal	None	109	OXC 1200
# 19	Male	15	160	8	Right Frontal	None	119	PMP 4
# 20	Male	12	44	3	Right Frontal	Focal Cortical Dysplasia	105	OXC 1950, CLBZ 6
# 21	Female	9	30	3	Right Frontal	None	88	LVT 1200, CBZ 280

# 22	Male	10	104	6	Left Frontal	None	87	OXC 375
# 23	Male	16	333	8	Right Parietal	None	87	LVT 2500, OXC 1800, CLBZ 20
# 24	Female	17	341	5	Bilateral Orbito-Frontal	Bilateral orbitofrontal cortex polymicrogyria	101	LVT 2000, VPA 800
# 25	Female	17	0	1	Right Fronto-Parietal	Focal Cortical Dysplasia	57	OXC 2100, TPM 200, RUF 2400
# 26	Female	11	692	5	Right Parietal	Focal Cortical Dysplasia	81	OXC 1500, CLBZ 10, VPA 1000
# 27	Female	16	146	12	Left Frontal Midline	None	102	VPA 1000

CBZ: Carbamazepine, CLBZ: Clobazam, GAB: Gabapentin, LCM: Lacosamide, LTG: Lamotrigine, LVT: Levetiracetam, OXC: Oxcarbazepine, PGB: Pregabalin, PMP: Perampanel, RUF: Rufinamide, TPM: Topiramate, VPA: Valproate, ZNS: Zonisamide.

** This patient IQ was gathered using the WASI while other patient IQ data was gathered from the WISC, though both are highly correlated r=0.91 (Wechsler, 2011).*

2.4.2 Data Acquisition

We acquired simultaneous EEG-fMRI in a 1.5T Siemens Avanto scanner (Erlangen, Germany) at the Great Ormond Street Hospital MRI Department with a 12 channel receive coil, using sequences with low Specific Absorption Rate (SAR) to minimise electrode heating risks. Subjects were fitted with a vacuum cushion during scanning to reduce head movement, and given headphones to dampen the noise from the MRI.

2.4.2.1 EEG Acquisition

Scalp EEG was recorded with a 64-channel MR compatible cap (BrainAmp MR plus, Brain Products, Gilching, Germany). EEG data were band-pass filtered at 0.016Hz-1 kHz, 16-bit digitalization (0.05μV resolution) and the sampling rate was 5 kHz.

2.4.2.2 MRI Acquisition

Subjects underwent four sessions of echo-planar imaging (EPI). The parameters of the experiment were as follows: a 3.3x3.3x4mm effective resolution with a field of view (FOV) =210mm, TR=2160ms, TE=30ms, flip angle=75 degrees, number of slices=30, slice thickness=3mm, slice gap=1mm, ascending order, matrix 64x64, 300 volumes (4 sessions of 300).

2.4.3 Paradigm

During the 2/4 fMRI sessions subjects were asked to rest with eyes closed and for the remaining two, to watch a video. Sessions of rest and video were alternated with the first session randomly assigned to be a rest or video session. During the video task subjects were asked to watch a ‘natural stimulus’ consisting of two periods (4 minutes each) with a cartoon clip of Tom and Jerry. This clip had sound, but no speaking lines and was chosen to avoid any possible language or age-related confounds. In-between the video clips a screen with the words ‘please wait’ (1minute 24seconds) was presented (see Figure 2.1). The goal of this video was to present a natural stimulus that would maintain attention with low cognitive demand while being accessible to a wide range of ages and IQ levels, therefore providing a relatively consistent brain state between individuals. Each session was 10minutes and 48seconds.

Figure 2.1 Task paradigm
The task involves a Tom and Jerry video (4min) with period of wait (1min 24sec).

2.4.4 Data Processing

2.4.4.1 EEG data

EEG data were corrected offline for scanner and pulse related artefacts using template artefact subtraction (Allen et al., 1998; Allen et al., 2000) implemented in BrainVision Analyzer2.0 (BrainProducts, Gilching, Germany). Interictal epileptiform activity was visually identified and categorized by two experts for each session by consensus between a clinical neurologist (Maria Centeno) and a physiologist (Kelly St Pier).

2.4.4.2 MRI data

For each session of 300 volumes, four volumes were removed to account for T1 equilibrium effects. Retrospective noise control was applied using FIACH (Tierney et al. 2016) to reduce motion and physiological effects in the fMRI data. The functional MRI data was preprocessed using SPM8 r4667 (www.fil.ion.ucl.ac.uk) running in Matlab (www.mathworks.com). The preprocessing steps were slice time correction, spatial realignment, FIACH, image normalisation, and smoothing. Realignment was performed relative to the mean image used as a reference in SPMs two-pass procedure. Normalisation was performed into Montreal Neurological Institute (MNI) space by registration to SPMs EPI template. Smoothing was performed with a full-width half maximum (FWHM) of 8x8x8mm.

2.4.5 Controlling for the Effect of IEDs

To remove the effect of IEDs from the data it was projected onto a space orthogonal to the IEDs. Where there were multiple IED types (based on morphology and distribution) each type was modelled separately within the same model. This was performed by multiplication of a copy of the original data (following slice time

correction, spatial realignment, FIACH) by the residual forming matrix (R) defined in Equation 2.1 and Equation 2.2 (Friston et al., 2006) using the pseudo function in the FIACH package (Tierney et al., 2016). The new model can be solved for via the maximum likelihood solution (Equations 2.3-2.5).

$$\boldsymbol{R = I - X_{IED} X_{IED}^{+}} \qquad \textit{Equation 2.1}$$

$$\boldsymbol{Y_{NEW} = RY} \qquad \textit{Equation 2.2}$$

$$\boldsymbol{\beta = (X^T X)^{-} X^T Y} \qquad \textit{Equation 2.3}$$

$$\boldsymbol{X^{+} = (X^T X)^{-} X^T} \qquad \textit{Equation 2.4}$$

$$\boldsymbol{\hat{Y} = X\beta} \qquad \textit{Equation 2.5}$$

Where I is the identity matrix, X is the design matrix, and X^{+} denotes the pseudo inverse of X. β represents the weight estimates for the maximum likelihood solution. $\hat{Y}$ represents the predicted signal.

2.4.6 Statistical Analysis

The statistical analysis consisted of: 1) a general linear model (GLM) used to define the networks activated by the task within and between groups (patients and controls). 2) Seeds were defined for the connectivity analysis based on group differences from analysis step '1'. 3) Seed-to-voxel connectivity analysis was performed within and between groups (patients and controls). 4) Analysis steps '1' and '3' were repeated controlling for the effects of IEDs (see Figure 2.2).

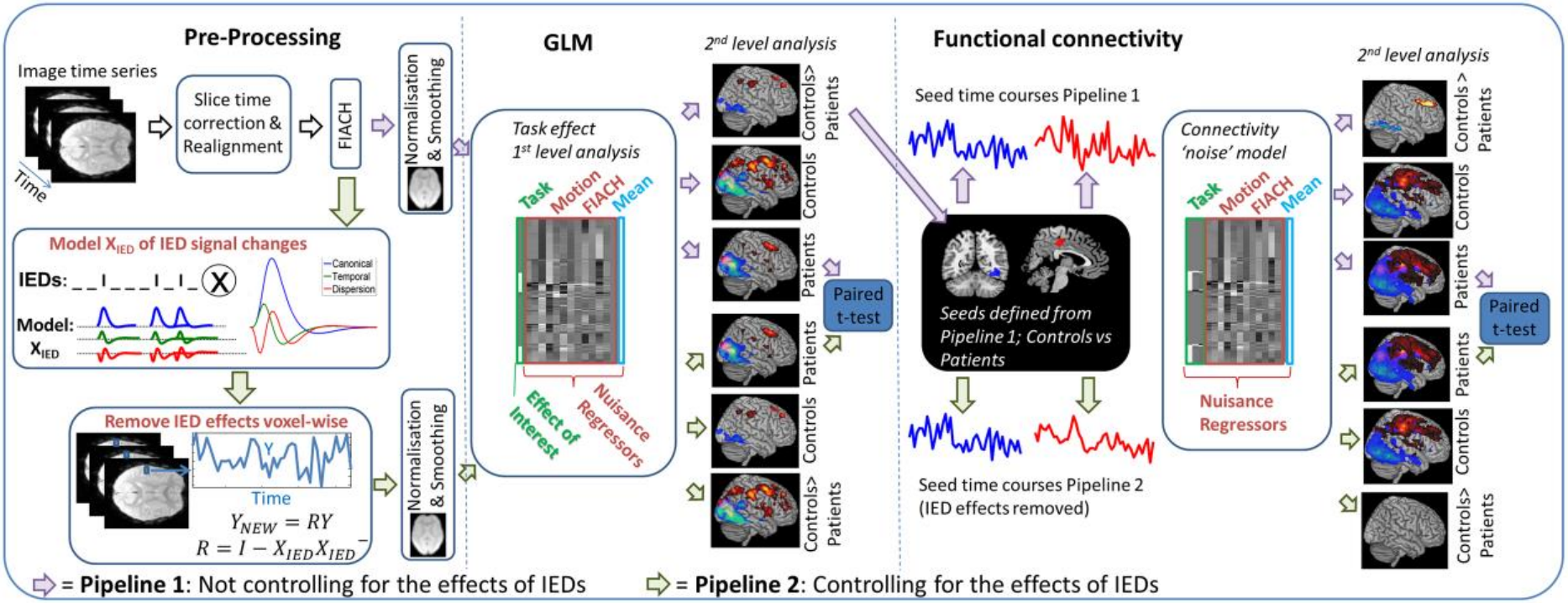

Figure 2.2 Overview of analysis approach

The steps of the analysis begin with pre-processing of the image time series (slice time correction; realignment; FIACH (Tierney et al., 2016)). After this the processing splits into two streams: Pipeline 1 (purple arrows) illustrates the processing pipeline that does not control for the effects of IEDs; Pipeline 2 (green arrow) illustrates the processing pipeline when controlling for the effects of IEDs where IED signal changes are modelled by convolving the IEDs with the canonical haemodynamic response function and its derivatives and projecting the data from each voxel into an orthogonal space before continuing to normalisation and smoothing. Both pipelines apply the same steps following pre-processing

that are a first level GLM analysis per subject followed by a second level GLM analysis which characterizes group task responses for controls and patients, and any differences related to pipeline (e.g. IEDs) using a paired t-test between the patients' task responses. Functional connectivity was then performed with the data from each pre-processing pipeline using seeds from the second level GLM. The first level functional connectivity analysis measured the correlation with the seed time courses while controlling for task and nuisance effects (connectivity noise model). The second level connectivity analysis then characterized connectivity within and between controls and patient groups for each pipeline. A paired t-test was then used to compare the IED effects on the patients' functional connectivity.

2.4.6.1 Task Response Analysis

Using the general linear model, and a mass univariate framework in SPM a first level analysis was performed for each subject in both patients and controls, where the task blocks (video and wait) were entered as conditions and convolved with the canonical haemodynamic response function. Six realignment parameters and 6 additional noise regressors were included as confounds (Tierney et al., 2016). The first-level analysis was performed with the original data and a projection of the data with the effect of IEDs removed.

Parameter estimates for each condition of interest were calculated for each voxel. For each subject statistically significant differences in activity during 'video' and 'wait' task blocks were assessed using a t-contrast. The task activated networks were compared to the intrinsic connectivity networks defined according to Smith et al.'s (2009) categorisation. The reported anatomical regions within these networks were based on the Automated Anatomical Labelling (AAL) atlas (Tzourio-Mazoyer et al., 2002).

A second-level group analysis was performed by taking t-contrast images generated from the single-subject level to test for commonalities in the task response. From this the task engaged brain regions were defined for both wait>video and video>wait contrasts in the control group SPMs at a significance level of $p<0.05$ FWE corrected. We further wanted to test if the response within these brain networks was different between patient and control groups. This was therefore tested with t-contrasts within the networks engaged by the natural stimulus task defined by a mask based on the average response of the control group (Friston, 1997). FWE was controlled using random field theory ($p<0.05$, one tailed).

To evaluate if any differences in task response within patients were due to IEDs a second level paired t-test was performed where each pair consisted of the patient task response of the GLM controlling versus not controlling for IEDs. A significance threshold of $p<0.05$ FWE correction was used.

2.4.6.1.1 Effect of Clinical Variables

To determine the effects of clinical variables in the task response, a multiple linear regression model was performed on patients. The defined explanatory variables (see below) were drug load, IQ, age, and epilepsy duration. The dependent variable was defined as the maximum patient response magnitude controlling for the transient effect of spikes within a 10mm radius surrounding the global maxima between group differences of controls versus patients obtained for both the video>wait (right fusiform/38, -58, -12) and wait>video (superior frontal/-28, 42, 42) contrasts (see Appendix Figure 8.1). Results were determined significant if $p<0.05$.

2.4.6.1.1.1 Drug Load

Drug load was defined based on administered patient dose relative to maximum recommended dosage requirements appropriate for patient age and weight, as defined by the Joint Formulary Committee (2016); these were summed over drug types per patient. Further analyses on subgroups of drug types were defined as either 'non-negative' for drugs that do not disrupt cognitive development or 'negative' for those known to disrupt cognitive development according to previous literature (Park and Kwon, 2008; Eddy et al., 2011; Beltramini et al., 2015).

2.4.6.1.1.2 Neuropsychological Testing - IQ

IQ was defined by the Full Scale IQ (FSIQ) score in the Wechsler Intelligence Scale for Children (WISC) (Wechsler, 2003) in 24 patients. One patient had an IQ score measured using the Wechsler Abbreviated Scale of Intelligence (WASI) (Wechsler, 1999) which is highly correlated to scores received in the WISC with r=0.91. Multiple imputation was conducted for two patients to account for missing IQ data (see Table 2.1). The method used for imputation was predictive mean matching (PMM) with number of imputations=10, maximum iterations=10, and seed=500 using the MICE package (van Buuren and Groothuis-Oudshoorn, 2011) in R (R Core Team, 2016).

2.4.6.2 Functional Connectivity Analysis

To study functional connectivity (FC) in patients with epilepsy we performed an analysis using the CONN toolbox (http://www.nitrc.org/projects/conn). A seed-to-voxel analysis was performed using the seed region defined as the largest clusters from group differences between patients and control found in the task-based GLM

analysis described above; namely the middle cingulate (part of the attention network and a region associated with the executive control network – ECN an ICN) and the right fusiform (part of the lateral visual network, an ICN). The seed region masks were created using SPM. The confounds used to remove noise effects from the connectivity consisted of within-subject realignment parameters and a noise model derived from FIACH (Tierney et al., 2016) as for the GLM. In addition to these confounds the main task effect was modelled as a confound by convolving the blocks with the canonical haemodynamic response function and its derivatives to remove the task modulation from the connectivity results. This analysis was performed for each subject with the original data and a projection of the data with the effect of IEDs removed (see Figure 2.2). Positive contrasts of a bivariate correlation were used in comparing the source ROI to every other voxel in the brain. The band-pass filter was set at 0.00125 and 0.09 (Hz). Results were thresholded at $p<0.05$ FWE correction (matching the GLM threshold).

Intra-network (voxels within the network that the seed belonged to) and inter-network (voxels from outside the network that the seed belonged to) connectivity differences were assessed at the group level between patients and controls using a voxel-wise t-test. A paired t-test was performed voxel-wise between the patient functional connectivity maps controlling and not controlling for IEDs. This approach was repeated for both middle cingulate and right fusiform seeds both for intra-network and inter-network connectivity.

2.4.6.3 Spatial Correspondence between Natural Stimulus and Resting State Networks

To determine the similarity between the resulting group maps from the GLM and functional connectivity analysis to previously defined ICNs, a semi-quantitative measure of network overlap was used. For the visual network, the corresponding Smith et al. (2009) ICN was compared to our results. For the attentional network the corresponding ICN (ECN) was derived from Seeley et al. (2007) and Smith et al. (2009), because of the variability of its definition in the literature. To circumvent this limitation we used an anatomical definition of the ECN using nodes from both of these papers (these nodes are listed in the Appendix Table 8.4-Table 8.9). To define the spatial correspondence, each reported region was visually compared to the AAL

atlas by outlining regional borders via the SPM toolbox WFU PickAtlas (Maldjian et al., 2003) and mricron (Rorden and Brett, 2000) respectively. If regions included multiple AAL regions, all regions were reported. An overlap for each node in our results was defined if an SPM contained a minimum of 10 voxels within the network nodes previously defined by the literature (Seeley et al., 20007; Smith et al., 2009). Due to the lack of consistency in anatomical labelling in previous studies, regions reported in the current study will be referenced in relation to the AAL atlas. This is necessary as Seeley et al. (2007) do not provide maps available for download and the network map of Seeley et al. (2007) and Smith et al. (2009) are displayed at different statistical thresholds (ours being the most conservative at $p<0.05$, FWE).

2.5 Results

2.5.1 Network More Activated by Waiting

The brain regions that were more active in the 'wait' condition in the control group included areas within an attentional network overlapping parts of the executive control network (ECN) previously defined by Seeley et al. (2007) and Smith et al. (2009) covering the medial-frontal, and parietal areas, anterior cingulate, and paracingulate regions. Additional regions also included the insula, putamen, piriform cortex, and the posterior cingulate (see Figure 2.3 first row in red, and Appendix Table 8.1). The patient group also activated some of the same network covering dorsal medial prefrontal, inferior parietal, middle cingulate, insula, caudate and cuneus (see Figure 2.3 second row in red, and Appendix Table 8.1). However the network response was less extensive and weaker compared to controls. Patients showed reduced activity compared to controls during the wait>video contrast in areas of the attention network associated with the ECN (frontal regions, middle cingulate, and inferior parietal) (see Figure 2.3 third row in red, and Appendix Table 8.1). Patients did not show any regions with significantly greater activity than controls. There was a high percentage of network overlap with the previously reported ECN (Seeley et al., 2007; Smith et al., 2009) (see Appendix Figure 8.2 and Appendix Table 8.4-Table 8.6).

2.5.2 Network More Activated by Video

The brain regions more active in the video condition for controls compared to the wait condition (video>wait contrast) included the fusiform gyrus, middle occipital, and middle temporal regions (Figure 2.3 first row blue regions, and Appendix Table 8.2). Patients also activated regions (fusiform gyrus, middle occipital, middle temporal) within this network and additional regions in the thalamus and calcarine sulcus (Figure 2.3 second row blue regions, and Appendix Table 8.2).

There was a significantly greater response in the controls compared to patients (controls>patients, Figure 2.3 third row blue regions, and Appendix Table 8.2) in the fusiform and middle occipital gyrus. This visual network has previously been associated with semantic processing (Price, 2012) and object recognition (Goodale and Milner, 1992). Patients did not show any regions of significantly greater activity than controls. There was network overlap with previously reported visual network (Smith et al., 2009) (see Appendix Figure 8.2 and Appendix Table 8.4-Table 8.6).

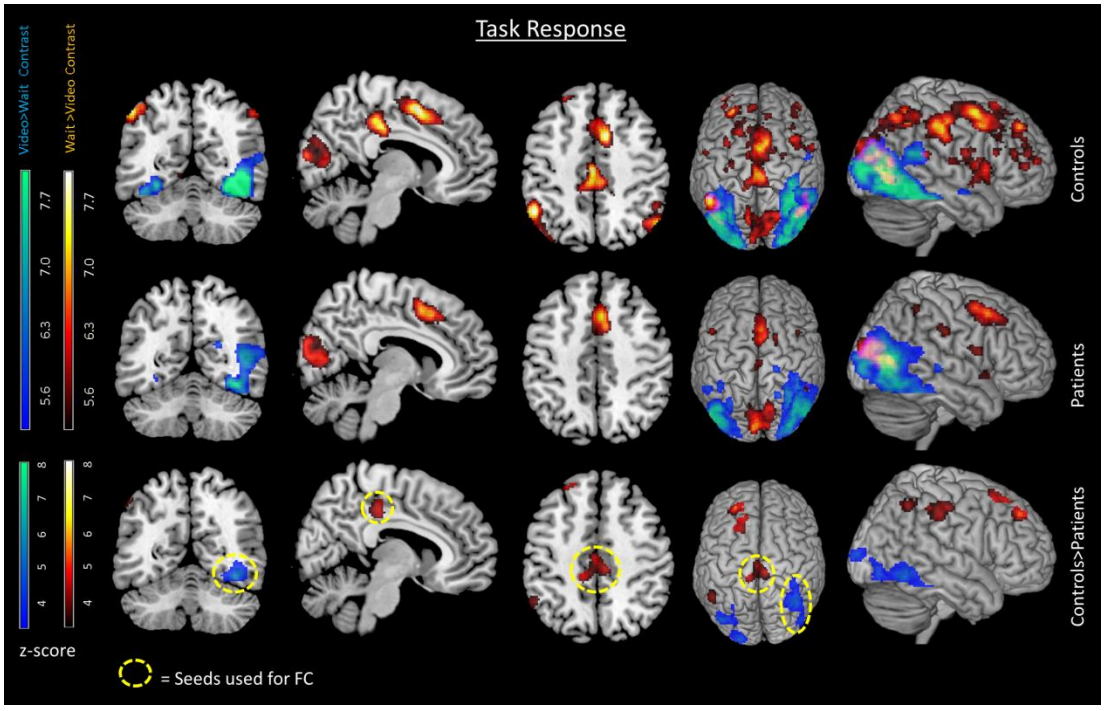

Figure 2.3 Task response
The task response for groups of controls (first row), patients (second row), and the differences between groups controls>patients (third row). The red regions are associated with the wait contrast and the blue regions are associated with the video

contrast. Circled yellow regions indicate seeds later used in the functional connectivity analysis. FC=functional connectivity.

2.5.2.1 Task Response Analysis Controlling for IEDs

Controlling for the effects of IEDs did not significantly change the patients' activations. There were no significant differences in the task responses with or without the effects of IEDs removed measured using a paired samples t-test and a threshold of $p<0.05$ FWE corrected.

2.5.2.2 Clinical Variables

The effect of clinical variables on patient response within regions driving group differences was tested using a multiple regression model including variables drug load, IQ, age, and epilepsy duration. Results indicate drug load (for medications that do not disrupt cognitive development) to be a significant factor with $t(19.2) = 2.46$, $p<0.05$ in the superior frontal region defined in the wait>video contrast. A greater response was associated with greater drug load. There were no significant effects of clinical variables when video was more active than the wait in the video>wait contrast.

2.5.3 Functional Connectivity

In this section, the functional connectivity from brain regions derived from the GLM task responses were explored. To determine the impact of IEDs, analyses were compared with and without controlling for the effects of interictal activity on the connectivity (see Figure 2.4). Note the contribution of the response to the task is modelled as a confound and so was effectively removed from the measurements of connectivity. In general, patients show decreased connectivity with respect to controls however they did not show significant increased connectivity.

2.5.3.1 Connectivity to the Attention Network Middle Cingulate Seed

Both control and patient groups had widespread connectivity within the attentional network when seeding from the middle cingulate (see Figure 2.4 first and second row in red). The middle cingulate was the region showing a greater task response in controls than patients in the GLM wait>video. However, connectivity from the middle cingulate gyrus was reduced in the patients relative to controls in the bilateral dorsal medial prefrontal cortex and the right middle frontal gyrus (see Table 2.2 and

Figure 2.4 third row in red). When accounting for the effect of interictal activity on connectivity there were no differences between groups within the attentional network (see Table 2.2 and Figure 2.4 fourth row). There were no regions of significantly altered inter-network connectivity from the middle cingulate to outside the attentional network. There was network overlap with the previously reported ECN (Seeley et al., 2007; Smith et al., 2009) (see Appendix Figure 8.3 and Appendix Table 8.7-Table 8.9).

Table 2.2. Seed middle cingulate functional connectivity controls > patients

Model	L/R	Label	Maxima (t-value)	XYZ
Not Controlling for IEDs	R	Middle Frontal	5.11	44, 36, 38
	L+R	Dorsal Medial Prefrontal	3.45	10, 14, 46
Controlling for IEDs	Not Significant			

IEDs: Interictal Epileptiform Discharges, L: Left, R: Right.

2.5.3.2 Connectivity to the Visual Network Right Fusiform Seed

Both control and patient groups had strong connectivity within the visual network when seeding from the right fusiform gyrus seed (see Figure 2.4 first and second row in blue). However, patients' connectivity was deceased compared to controls in the right inferior occipital region (see Table 2.3, and Figure 2.4 third row in blue). As with the middle cingulate seed, when the influence of interictal activity on the connectivity was accounted for there were no connectivity differences between patients and controls within the visual network (see Table 2.3 and Figure 2.4 fourth row). There were no significant regions of altered inter-network connectivity from the right fusiform to outside the visual network. There were overlaps with previously reported visual network (Smith et al., 2009) for functional connectivity in the fusiform seed (see Appendix Figure 8.3 and Appendix Table 8.7-Table 8.9).

Table 2.3. Seed right fusiform functional connectivity controls > patients

Model	L/R	Label	Maxima (t-value)	X, Y, Z
Not Controlling	R	Inferior Occipital	4.43	46, -78, -8
for IEDs	R	Inferior Occipital	4.32	34, -64, -8
Controlling for IEDs			Not Significant	

IEDs: Interictal Epileptiform Discharges, L: Left, R: Right.

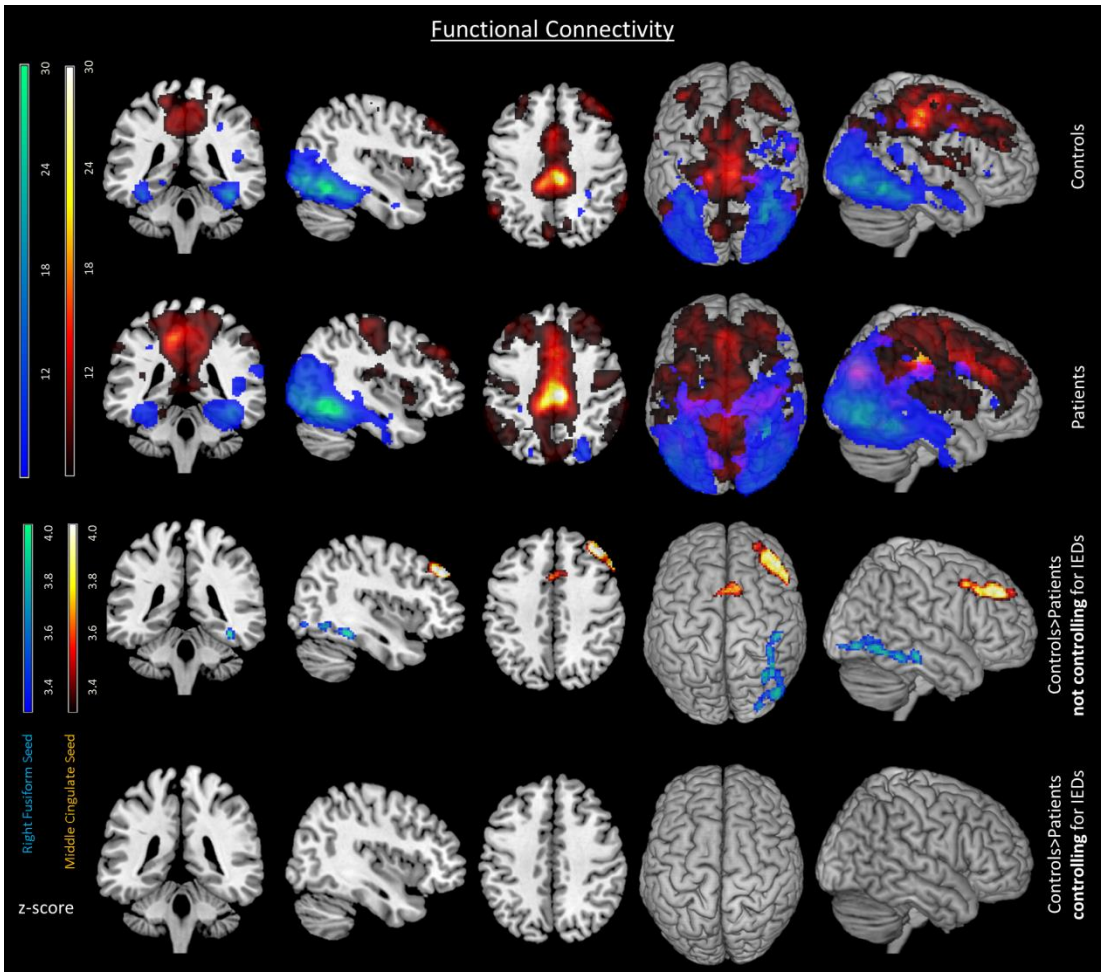

Figure 2.4 Functional connectivity

The functional connectivity for groups of controls (first row) and patients (second row). Group differences controls>patients indicate not controlling (third row) and controlling (fourth row) for IEDs. All comparisons include both middle cingulate and right fusiform seeds depicted in red and blue respectively. Differences between groups do not appear once IEDs are controlled for.

2.5.3.3 Functional Connectivity Controlling for IEDs

To understand the impact of the IEDs on the patients functional connectivity a paired samples t-test of functional connectivity with and without controlling for the effects of IEDs was performed (see Figure 2.5). The motivation for performing this additional test was due to the null result found when comparing controls versus patient maps controlling for the effects of IEDs (see Figure 2.4 fourth row).

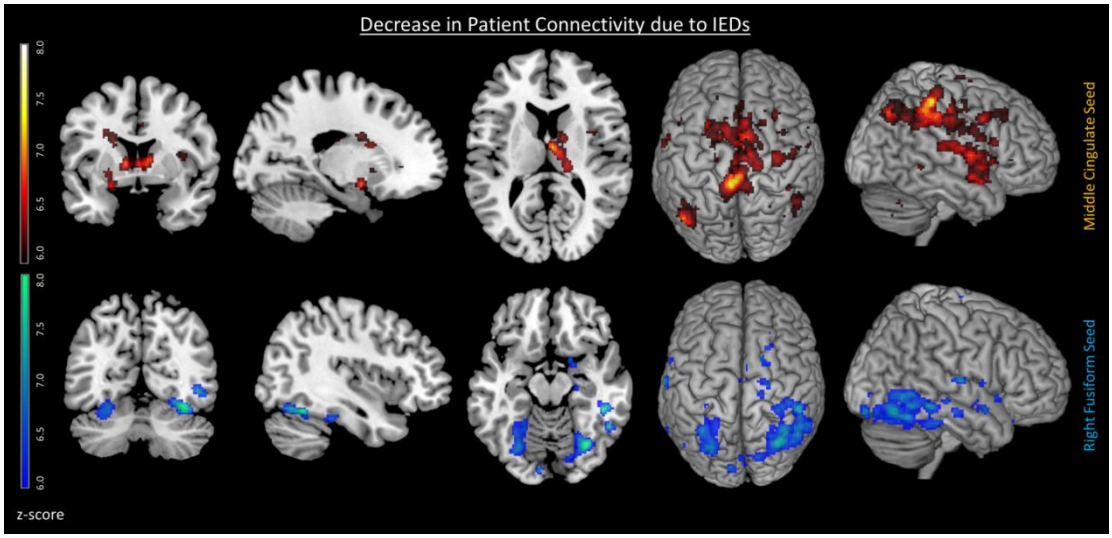

Figure 2.5 Changes in patient functional connectivity associated with IEDs
Decreased patient connectivity associated with IEDs for the middle cingulate seed (top row in red) and the right fusiform seed (bottom row in blue) $p<0.05$ FWE. Decreased connectivity can be seen between the basal ganglia and middle cingulate seed associated with IEDs.

The IEDs were associated with reduced intra-network connectivity for both the middle cingulate seed and right fusiform seed (see Figure 2.5 top row and bottom row respectively, and Appendix Table 8.3). For the middle cingulate seed an attentional network was found with regions including parts of the ECN such as the middle cingulate and inferior parietal (see Appendix Table 8.3) and additionally the basal ganglia regions such as the caudate, putamen, and also supplementary motor area, insula, cerebellum, and precuneus. For the right fusiform seed regions included the right fusiform, middle temporal, and middle occipital within the visual network (see Figure 2.5 bottom row, and Appendix Table 8.3). While patients consistently

show decreased connectivity with respect to controls they did not show significant increased connectivity.

2.6 Discussion

2.6.1 Summary

The natural stimulus elicited brain activity from two networks: 1) the attentional network, which was more active in the wait condition and is traditionally associated with active maintenance, and comprised of the parietal and prefrontal regions (Seeley et al., 2007) (see Appendix Table 8.4-Table 8.9), and 2) a lateral visual network (see Appendix Figure 8.2), which was more active in the video condition, and comprised of occipital and fusiform gyri (Goodale and Milner, 1992; Wandell et al., 2009). These responses to the stimulus were reduced in the patients with epilepsy (see Figure 2.3). However this was not associated with ongoing transient epileptic discharges. Drug load of medications known to have less impact on cognition was associated with greater response magnitude in these regions.

Our primary hypothesis was that we would find a reduction in connectivity within ICN-like networks in patients with epilepsy; to test this we evaluated the connectivity differences between groups within the attentional and visual networks (see Figure 2.4). This decreased within network connectivity was found in patients when compared to controls in both the attentional and the visual networks. Our secondary hypothesis was we would measure connectivity differences between control and epilepsy patients having controlled for the effects of scalp visible IEDs due to non-transient effects of epilepsy on the network that have been previously reported. We did not find evidence for this; once the effects of IEDs on connectivity were accounted for, there were not significant connectivity differences in the patients compared to the control group. Therefore, the transient effects of IEDs had a stronger influence on patient connectivity than was originally hypothesised and no non-transient connectivity changes were found.

2.6.2 Importance of IEDs and Compromised Network Connectivity

We have shown that even in a task that requires low cognitive demand there are significant differences found between patients and controls; patients have

compromised network connectivity. We have clearly demonstrated IEDs impact on cognitive network connectivity in this context which has been shown to be a marker of effective cognition in many studies of healthy subjects and patients (Smith et al., 2009; Venkataraman et al., 2012; Widjaja et al., 2013; Ibrahim et al., 2014a; Sadaghiani et al., 2014; Washington et al., 2014). Therefore the changes in connectivity associated with IEDs measured in this study are highly likely to be accompanied by impairments consistent with the transient performance changes measured by behavioural studies (Pressler et al., 2005). This provides a neurobiological measurement of the impact of IEDs that may call into question the prevailing view that IEDs are not important in the treatment of epilepsy (Sánchez et al., 2015). Furthermore, changes with neuropsychological correlates have been confirmed by a recent study (Glennon et al., 2016) who found an association between IEDs and cognitive dysfunction measured by IQ, academic skill, language and memory tasks.

The strong influence of IEDs on our functional connectivity results illustrates that functional connectivity is dynamic (Chang and Glover, 2010; Smith et al., 2012) and that dynamic changes due to IEDs must be accounted for in functional connectivity studies of epilepsy to interpret the results. Pathological transient activity (IEDs) was found to be strongly associated with compromised network connectivity in patients, and without these effects the networks were not significantly different to healthy controls. This common effect of IEDs on the integrity of the networks active in our task is more remarkable when considering the heterogeneous patient population (see Table 2.1) and consequently can be considered a very general finding. This suggests that there is a common pathway through which IEDs can impact cognitive networks and subsequently performance across focal epilepsy patients with different localisations.

2.6.3 Transient and Non-Transient Effects of IEDs

Our secondary hypothesis was that we would find evidence for both transient and more non-transient alterations in connectivity that would be related to disease duration. Transient and non-transient changes were separable by using simultaneous measurements of fMRI and EEG, which provided direct measurements of both the IEDs and the functional networks. Once the effects of transients were accounted for

there was no evidence for remaining non-transient differences in network connectivity. This is consistent with a recent MEG study that demonstrated reduced network integrity related to IEDs during rest in default mode, salience, dorsal attention, and motor networks (Ibrahim et al., 2014a). We have further demonstrated a direct link between this finding and changes in fMRI connectivity in ICNs. This is important because there is evidence of divergent connectivity results in electrophysiological and fMRI in epilepsy (Bettus et al., 2011).

Non-transient changes in ICNs have been frequently reported in patients with very infrequent IEDs (Mankinen et al., 2012). However, these previous studies have not used simultaneous EEG-fMRI and so cannot distinguish transient effects of IEDs from more non-transient effects. Pittau et al. (2012) found decreased connectivity in adult temporal lobe patients using simultaneous EEG-fMRI in sessions without IEDs. It is possible that because previous studies have predominantly focused on adults with mesial temporal lobe epilepsy there is limited sensitivity to IEDs in the scalp EEG. This could be further explored using intracranial EEG-fMRI where it is possible to more fully capture epileptic activity some of which cannot be seen in scalp EEG (Vulliemoz et al., 2011; Carmichael et al., 2012).

A clear distinction should be made between alterations in ICN connectivity and connectivity within the epileptic network itself. A recent study by Iannotti et al. (2016) suggest connectivity increases within the epileptic network are present even after controlling for the effect of scalp-visible IEDs. This may represent the impact of epileptic activity that is not visible in scalp EEG but is often revealed by intracranial recordings, and the influence of long term pathological processes. Furthermore, some resting state studies have found disease duration to have a significant impact on the connectivity (Morgan et al., 2011; Christodoulou et al., 2012), implying a long-term effect of epilepsy on networks.

A second potential explanation for the functional connectivity changes found in ICNs in patients with epilepsy that were independent of IEDs, is that they were driven by confounding factors. Recent work indicates that vigilance levels have a strong impact on functional connectivity results and epilepsy is frequently associated with sleep problems (Chan et al., 2011). This can lead to inaccurate conclusions concerning

differences between groups that could be driven by different groups falling asleep more frequently during resting state fMRI (Tagliazucchi and Laufs, 2014). To circumvent this potential confound we employed a natural stimulus paradigm to engage the patients and controls with the aim of reducing differences due to vigilance. The effectiveness of this approach is supported by the finding that no differences in functional connectivity were found once the effects of IEDs were controlled for (Figure 2.4).

2.6.4 The Impact of Drug Load on Patient Task Response

Due to the differences in the GLM task response that persisted even after controlling for the effects of IEDs we explored the factors that influenced the magnitude of the response. We looked at a number of clinical factors including drug load, age, epilepsy duration, and IQ. The significant factor explaining an increased response in the prefrontal cortex was drug load. This relationship might be expected when considering evidence from previous studies describing the influence of antiepileptic drugs (AEDs) on cognitive networks (Koepp, 2011; Beltramini et al., 2015). Our patient cohort was mainly given medication such as levetiracetam, valproate, and lamotrigine which are drugs that do not disrupt cognitive development (Eddy et al., 2011). Some antiepileptic drugs, such as topiramate are known to induce negative cognitive outcomes (Szaflarski et al. 2012), while levetiracetam and valproate have prompted normalisation of patient networks in temporal lobe and juvenile myoclonic epilepsy patients (Vollmar et al., 2011; Wandschneider et al., 2014).

The effects of drug load were not significant in the visual cortex, which may indicate sensory cortices are less susceptible to the effects of the medication used in our patients; although some anticonvulsive medications have adverse effects on visual perception (Steinhoff et al., 1997; Hilton et al., 2004).

2.6.5 Clinical Implications

2.6.5.1 Is IED Suppression Beneficial?

It has previously been shown that decreased connectivity within ICNs was predictive of behavioural performance (Smith et al., 2009; Venkataraman et al., 2012; Widjaja et al., 2013; Ibrahim et al., 2014a; Sadaghiani et al., 2014; Washington et al., 2014).

Cognitive network integrity has also been linked to neurocognitive outcome such as FSIQ in epilepsy (Ibrahim et al., 2014a). Our results also raise the question that if IEDs were supressed by treatment in the paediatric setting, would an improvement in cognition be possible via the restoration of cognitive network connectivity? The results presented here demonstrate that there are significant neurobiological changes known to predict brain function that were associated with IEDs even during a low-demand cognitive task. This suggests that cognitive performance may be generally improved by IED suppression and can be sensitively measured via cognitive network connectivity. In practice, the benefits of therapy for IED suppression would need to be balanced against any possible side effects.

2.6.5.2 Role of the Basal Ganglia in Maintaining Network Connectivity

The basal ganglia was found to have altered connectivity attributable to IEDs (see Figure 2.5). Our results also showed that IEDs affected the brain networks active during our task. This is consistent with studies demonstrating that epileptic discharges can affect the networks most active during rest, such as default mode network (Laufs et al., 2007). This makes it likely that the impact of IEDs is generalizable in terms of a disturbance to the 'active network'. Given the heterogeneity of epilepsy localisation in the patients, common structural connectivity abnormalities previously found (Zhang et al., 2011) are highly unlikely. Therefore we propose that the interaction between the core epileptic network generating IEDs and the active network is mediated by the basal ganglia, which provides a common pathway across the subjects. The basal ganglia is part of the epileptogenic network in generalised idiopathic epilepsy (Tyvaert et al., 2009), and is identified as a critical region for normal attentive consciousness (Paz et al., 2007; Motelow and Blumenfeld, 2009) however its role in focal epilepsy has been less well documented although it has been implicated in the modulation of epileptic activity in temporal lobe epilepsy (Rektor et al., 2012). This suggests that the IEDs from different locations may alter the function of the basal ganglia, which then cannot perform its role of coordinating the active networks (Luo et al., 2012) potentially explaining their reduced connectivity. Current efforts using DBS target the basal ganglia in epilepsy patients to decrease seizure burden (Cox et al., 2014). This raises the question if one could appropriately modify basal ganglia connectivity via deep brain

stimulation (DBS), whether this would decrease the occurrence or impact of epileptic activity.

2.6.6 Seizures and IEDs

The current study found consistent effects of IEDs on connectivity networks which were measured using correlations of BOLD signal from different brain regions. The neural origin of BOLD signal is still highly debated (Murta et al., 2015) however the effect of IEDs on BOLD signal insinuates concurrent changes in haemodynamics. Furthermore, differences in neural population and networks in IEDs versus seizure activity have been reported (De Curtis and Avanzini, 2001). Therefore, the possibility of differing haemodynamic changes in these two epileptic events should be further explored (see Chapter 3 and Chapter 5).

2.6.7 Future Works

Work from the current study suggests that IEDs (independent of focus location) can alter basal ganglia network function. Therefore it would be interesting for future works to explore functional connectivity within the basal ganglia network of children with focal epilepsy and its possible implications for treatment via stimulation techniques such as DBS or Transcranial Magnetic Stimulation (TMS).

Chapter 3 Finite Impulse Response and Quantifying the fMRI Response to Epileptic Spikes

3.1 Abstract

EEG-fMRI is a non-invasive technique used to map the generators of interictal epileptiform discharges (IEDs) in epilepsy patients to aid pre-surgical evaluation. This process requires the definition of an event on EEG and a model of the expected haemodynamic response. A number of studies have suggested that the canonical fMRI response to a stimulus may be altered in 1) epilepsy and 2) children. The HRF of IEDs in children is therefore unclear, and there is some evidence that fMRI changes may precede electrographic events (Hawco et al., 2007; Moeller et al., 2008; Jacobs et al., 2009; Rathakrishnan et al., 2010; Pittau et al., 2011; Rollings et al., 2016; Brevard et al., 2006).

Our main hypothesis was that we would find haemodynamic changes prior to epileptic events in children with epilepsy and that this could be better modelled with a basis set created by a smooth FIR deconvolution of epileptic events from the fMRI data of children with epilepsy (termed IED-HRF). This basis set, specifically for epilepsy patients, would therefore provide more accurate EEG-fMRI maps for pre-surgical evaluation.

This was achieved by using a smooth Finite Impulse Response (FIR) deconvolution in EEG-fMRI data from 16 children with focal epilepsy in whom the epileptogenic region was confirmed. An additional 11 patients were included in the study; these patients were post-surgical with good outcome (Engel outcome classification = 1) or had an MRI lesion; however they did not have concordant EEG-fMRI maps using a canonical HRF. They were included to test the performance of the smooth FIR basis set and to verify any potential improvement from the canonical HRF (cHRF).

The main findings were that the change in haemodynamics occurred up to ~20sec prior to epileptic events however the neurophysiological underpinning of these changes is unclear. Localisation improved in patients with non-concordant EEG-fMRI when using the new IED-HRF rather than the traditional cHRF as sensitivity

increased to 64% (7/11). The total sensitivity for all patients was 70% (19/27) for the IED-HRF and 59% (16/27) for the cHRF, thereby indicating the benefit of the IED-HRF model in patients with paediatric focal epilepsy, especially in those in whom the cHRF model fails.

3.2 Objectives

The goal of this chapter is to: 1) see if haemodynamic responses preceded IEDs, 2) construct a new model of haemodynamics with greater sensitivity than the cHRF, and 3) to indicate the efficacy of the new HRF model for future patient studies and provide a more accurate representation of patient focus in EEG-fMRI maps.

3.3 Introduction

Epilepsy is the most common neurological disorder in children affecting 1% of children (Harrison et al., 1976; Hauser et al., 1991), with up to 33% of affected children remaining resistant to medication. EEG-fMRI (functional magnetic resonance imaging) has proven useful in defining the epileptic network (Centeno et al., 2016) by providing data on haemodynamic and electrographic information simultaneously. However to obtain an accurate EEG-fMRI localisation map, a representative patient haemodynamic response function (HRF) must be defined.

The traditional way to model an HRF is using a canonical model (Buxton et al., 2004). The canonical HRF is a parsimonious fixed shape model extracted from healthy subjects (Boynton et al., 1996; Menon and Kim, 1999) however variations among individuals have been reported in several parameters including onset time, peak time, and amplitude (Aguirre et al., 1998; Miezin et al., 2000). Therefore, even in healthy subjects there is a certain amount of variability in haemodynamic response. Although some variation is natural, the canonical HRF may be inappropriate for groups whose metabolism is abnormal resulting in reduced sensitivity (Lu et al., 2006). Such reduced sensitivity might impair clinical inferences.

One example of differing cerebral metabolism is in children. Age-related changes in vasculature could lead to misinterpretation of the neurovascular response interpreted

by the BOLD signal. Changes in CBF have previously been reported by Hales et al. (2014), indicating increased blood flow in younger children compared to adults. As BOLD signal is a combination of physiological variables (including CBF), it is important to account for age related changes when interpreting fMRI results.

Morphological variations in the HRF have not only been seen in age, but for IED frequency as well. Increased spike frequency results in a peak amplitude decrease while younger children (age 0-2years) have longer peak times (Jacobs et al., 2008). Such changes in patient HRF include differences in time-to-peak observed in both focal and idiopathic generalised epilepsies, where the Blood Oxygen Level Dependent (BOLD) response can occur up to six seconds prior to event onset in adults and children (Hawco et al., 2007; Moeller et al., 2008; Jacobs et al., 2009). Therefore, there is uncertainty in the HRF model for children and epilepsy patients. In addition, this is accompanied by methodological issues that make interpreting fMRI data in children with epilepsy difficult.

These methodological issues arise from the definition of the HRF. Previous studies have recognized the importance of HRF model flexibility and have tried to account for this by using multi-peak functions (Jacobs et al., 2009; Rathakrishnan et al., 2010; Moeller et al., 2008), the canonical HRF with derivatives (Rollings et al., 2016), and the deconvolution of subject-specific HRFs (Lu et al., 2006; Hawco et al., 2007). Unfortunately all of these methods have their drawbacks, for example, though the multi-peak method is able to account for changes in time there is no accounting for changes in shape. Similarly, adding the time and dispersion derivatives to the canonical model expand its flexibility but only account for limited possible variations for example of a few seconds in the peak response; however a greater variability than this has been reported in response to IEDs (Lu et al., 2006). Unlike the multi-peak and canonical (with derivatives) models, the deconvolution method provides subject-specific HRFs at each voxel. Though its flexibility is a positive feature, it is highly sensitive to noise and can over-fit data. Therefore an attractive option is to utilise the deconvolution method, but instead of using a subject-specific approach to use an HRF representative of the group as a whole; thereby avoiding the issues of individual subject noise, over-fitting and circularity. Typically a FIR deconvolution is used for fMRI (van Houdt et al., 2010) however this is sensitive to noise and over-fitting,

which can be controlled for by the smooth FIR (Finite Impulse Response) deconvolution (Goutte et al., 2000). This provides all of the necessary requirements of flexibility while reducing the impact of noise.

To date, to our knowledge there are no studies using the smooth FIR on clinical data. Therefore, this will be the first study using smooth FIR deconvolution to extract a representative HRF basis set of an epilepsy patient group. The resulting basis set will be used to provide future EEG-fMRI studies with more sensitive localisation maps.

3.4 Methods

3.4.1 Participants

57 children with drug resistant focal epilepsy going through pre-surgical evaluation were recruited for simultaneous EEG-fMRI at Great Ormond Street Hospital, London, UK. After inclusion criteria were met (see below) a total of 27 children (14 female; mean age = 13.7 years) remained, and were used in the current study (see Table 3.1).

The patient data was split into two groups the first of which consisted of 16 patients (termed 'training data') that were used to calculate a paediatric epilepsy haemodynamic basis set. The second group was used to test the efficacy of the new basis set (termed 'testing data ') which included 11 patients.

Inclusion criteria for creating a basis set were 1) ages between 6-18years 2) presence of frequent interictal epileptiform discharges (IEDs) 3) a well-defined epileptogenic focus. A well-defined epileptogenic focus was classified as the resected region in patients with a good post-surgical outcome (Engel outcome = 1) or patients in whom the structural lesion was concordant with EEG-fMRI using a canonical HRF and time and dispersion derivatives. Clusters were categorised as concordant if they contained a cluster of significant BOLD changes within the presumed epileptogenic region (as defined in Centeno et al., 2016). The focus for these patients was defined as the concordant EEG-fMRI cluster derived from the dominant spike type. Inclusion criteria for testing the basis set were 1) between the ages of 6-18 and 2) patients with well-defined epileptogenic focus but non-concordant maps.

Table 3.1 Patient Information: EEG-fMRI haemodynamics

Patient	Group	Gender	Age	Surgery Type	Age of onset	Epilepsy focus	MR Lesion	Lesion type	Medication (daily dose [mg])
1	C	Female	11	Hemispherectomy	2.5 years	L Central Junction	Yes	Unknown; widespread	OXC 600
2	C	Female	13	Hipphocampectomy	12 years	R Temporal	Yes	DNET	Topiramate 150
3	C	Male	14	Hemispherectomy	3 years	L Hemisphere	Yes	Autoimmune/ inflammatory; hemispheric atrophy	Azathioprine 50, Epilim Chrono 700, CLBZ 15, Heminevrin 192, Chloral hydrate 1000, Prednisolone 40, Buccal Midazolam 10
4	C	Female	16	Hemispherectomy	2 years	L Hemisphere and deep cortex	Yes	Unknown	LEV 2000, CLNZ 2
5	C	Male	17	Resection	7 years	R Parietal	Yes	FCD	Levetiracetam 3000, CLBZ 15, Sodium Valproate 2400
6	C	Female	10	Lesionectomy	7 years	R Frontal	Yes	FCD	OXC 1050
7	C	Male	15	Hemispherectomy	7 years	L Occipital	Yes	Vascular	OXBZ 900, Gabapentin 1500
8	C	Male	12	NA	18 months	R Perysilvian	Yes	Polymicrogyria; widespread	VPA 800, LVT 250, CBZ 1000, CLBZ 30
9	C	Female	16	Resection	12 years	L Frontal	No	Unknown	Epilim Chrono 1000

10	C	Female	14	Resection	2.5 years	R Temporal	Yes	Vascular	Levetiracetam 1000, Topiramate 150
11	C	Female	8	Disconnection	4 years	L Frontal	Yes	Vascular	VPA 1200, LEV 600, ETHZ 1000
12	C	Male	17	NA	2 years	R Occipital	Yes	Vascular	OXC 1500, LMT 100, LVT 2000
13	C	Male	13	Disconnection	7 years	L Occipital	Yes	FCD	CBZ 800, TPM 325, CBLZ 30
14	C	Female	17	NA	5 years	Fronto-temporal/Orbito-frontal	Yes	Bilateral Orbito-Frontal abnormality; polymicrogyria	LVT 2000, VPA 800
15	C	Female	11	Lesionectomy	5 years	R Parietal	Yes	FCD	OXC 750, CLBZ 10, Sodium Valproate 1000
16	C	Female	13	NA	7 years	L Frontal	Yes	FCD	VPA 1200
17	T	Male	16	Resection	10 years	R Frontal	No	Unknown	Tegretol 1200
18	T	Male	17	Lesionectomy	3 years	L Temporal	No	Unknown	LEV 3000
19	T	Male	13	Lesionectomy	3 years	L Frontal	Yes	FCD	OXC 1950, CLBZ 6
20	T	Female	15	Lesionectomy	13 years	R Parietal	Yes	Tumor	LEV 2500, LMT 400
21	T	Female	11	NA	5 years	L Frontal	Yes	Unknown	OXC 900, CLBZ = 40
22	T	Male	18	NA	3 days	R Parietal	Yes	FCD	PGB 175 LCM 400 LTG 300 TPM 200
23	T	Female	16	NA	13 years	L Insula/ Perisylvian Fissure	Yes	FCD	TPM 50, CBZ 400

24	T	Female	8	NA	9 months	L Parietal	Yes	TS	LVT 1200 Nitrazepam 7.5
25	T	Male	11	NA	2 years	R Temporal	Yes	Unknown	CBZ 800 TPM 150
26	T	Male	18	NA	2.5 years	R Parietal/R Temporal	Yes	Unknown	LCM 400 LTG 400
27	T	Male	11	NA	3 months	L Frontal/ Hypothalamus	Yes	Hypothalamic Hamartoma	LVT 1600

C = training the basis set; T = testing the basis set; NA = not applicable; FCD = focal cortical dysplasia; TS = Temporal sclerosis; DNET = Dysembryoplastic Neuroepithelial Tumour; CBZ = Carbamazepine; CLBZ = Clobazam; GAB = Gabapentin; LCM = Lacosamide; LTG = Lamotrigine; LVT = Levetiracetam; OXC = Oxcarbazepine; PGB = Pregabalin; PMP = Perampanel; RUF = Rufinamide; TPM = Topiramate; VPA = Valproate; ZNS = Zonisamide.

3.4.2 Data Acquisition

We acquired simultaneous EEG-fMRI using a 1.5T Siemens Avanto scanner (Erlangen, Germany) at the Great Ormond Street Hospital MRI Department with a 12 channel receive coil, using sequences with low Specific Absorption Rate (SAR) to minimise electrode heating risks. Subjects were fitted with a vacuum cushion during scanning to reduce head movement, and given headphones to dampen the noise from the MRI.

3.4.2.1 EEG Acquisition

Scalp EEG was recorded with a 64-channel MR compatible cap (BrainAmp MR plus, Brain Products, Gilching, Germany). EEG data were band-pass filtered at 0.016Hz-1 kHz, 16-bit digitalization (0.05μV resolution) and the sampling rate was 5 kHz.

3.4.2.2 MRI Acquisition

Subjects underwent four sessions of echo-planar imaging (EPI). The parameters of the experiment were as follows: a 3.3x3.3x4mm effective resolution with a field of view (FOV) =210mm, TR=2160ms, TE=30ms, flip angle=75 degrees, number of slices=30, slice thickness=3mm, slice gap=1mm, ascending order, matrix 64x64, 300 volumes (4 sessions of 300).

3.4.3 Data Processing

3.4.3.1 EEG Processing

EEG data were corrected offline for scanner and pulse related artefacts using template artefact subtraction (Allen et al., 1998; Allen et al., 2000) implemented in BrainVision Analyzer2.0 (BrainProducts, Gilching, Germany). Interictal epileptiform activity was visually identified and categorized by two experts for each session by consensus between a clinical neurologist (Maria Centeno) and physiologists (Kelly St Pier and Charlotte Wilkinson).

3.4.3.2 MRI Processing

For each session of 300 volumes, four volumes were removed to account for T1 equilibrium effects. Retrospective noise control was applied using FIACH (Tierney et al. 2016) to reduce motion and physiological effects in the fMRI data. The

functional MRI data was preprocessed using SPM8 r4667 (www.fil.ion.ucl.ac.uk) running in Matlab (www.mathworks.com). The preprocessing steps were slice time correction, spatial realignment, FIACH, and smoothing. Realignment was performed relative to the mean image used as a reference in SPMs two-pass procedure. Smoothing was performed with a full-width half maximum (FWHM) of 8x8x8mm.

3.4.4 Finite Impulse Response Deconvolution

The smooth FIR deconvolution was tested using simulated data. There were two simulations conducted, one for method validation and another for smoothness optimisation. If its advantage is confirmed it will be used on patient data to extract a more accurate HRF basis set. The FIR performs a deconvolution to determine the shape of the HRF within a general linear model consisting of an impulse response for each time point where a response to an event is expected (see Equation 3.1). The main limitation of this approach is over-fitting of model parameters. Therefore an alternative is to use a constraint. This can be achieved using a smooth FIR (Goutte et al., 2000) where the nearest neighbouring points (in time) are assumed to be more highly correlated than those further away, decreasing the chance of sporadic signal change (see Equation 3.2). This is a sensible approach to haemodynamics as non-BOLD contributions to noise will be reduced via smoothing. The betas, representing the response of the system, are then obtained by the maximum likelihood regression adjusted for the smooth FIR (see Equation 3.3).

$$\hat{\boldsymbol{y}}(\boldsymbol{t}) = \sum_{\boldsymbol{i=1}}^{\boldsymbol{d}} \boldsymbol{w_i}\, \boldsymbol{x}(\boldsymbol{t}-\boldsymbol{i}) = \boldsymbol{w^T x}(\boldsymbol{t}) \qquad \textit{Equation 3.1}$$

Where $y(t)$ is the fMRI signal acquired with a stimulus of $x(t)$. The image index of t runs between 1 and T (counted in scans). The FIR filter order is described by d using the linear coefficients $w = (w_1, w_{2,\ldots}w_d)^T$. Where $x(t) = (x(t\text{-}1), x(t\text{-}2), \ldots x(t\text{-}d))^T$ is a vector of past values of the stimulus.

$$\boldsymbol{R} = \boldsymbol{\Sigma^{-1}}\ \boldsymbol{with}\ \boldsymbol{\Sigma_{ij}} = \boldsymbol{v}\ \boldsymbol{exp}\left(-\frac{\boldsymbol{h}}{\boldsymbol{2}}\right)(\boldsymbol{i}-\boldsymbol{j})^{\boldsymbol{2}} \qquad \textit{Equation 3.2}$$

Where R (inverse covariance matrix) implements the constraints put on the FIR model. It maintains that neighbouring points must be related, while points farther

away have limited associations. v is the strength of regularisation and h is the smoothness factor. $|\ i - j\ |$ is the non-negative decreasing function of distance between points.

$$\boldsymbol{w_{MAP} = \Sigma(\Sigma X^T X + \sigma^2 I)^{-1} X^T Y} \qquad \textit{Equation 3.3}$$

Where $X = [x(d+1), x(d+2), \ldots, x(\mathrm{T})]^{\mathrm{T}}$, which is a matrix containing the input vectors $x(t)$ for all values of t. $\mathrm{Y} = [y(d+1), y(d+2), \ldots, y(\mathrm{T})]^{\mathrm{T}}$, which is the vector of output measurements.

w_{MAP} represents the betas in result of our FIR filter. σ^2 represents noise level. The betas are obtained from the maximum likelihood regression model: $w_{\mathrm{ML}} = (\mathrm{X}^{\mathrm{T}}\mathrm{X})^{-1}\mathrm{X}^{\mathrm{T}}\mathrm{Y}$.

The original application of a smooth FIR to imaging data used a Bayesian approach where noise (σ^2) , strength of regularisation (v), and smoothness factor (h) were treated as hyper-parameters (Goutte et al., 2000). They found the noise level to be well determined by the data, such that the posterior distribution could be represented as a dirac delta function; implying that a fixed noise level value is a reasonable approach. The other hyper-parameters however were less well defined.

In the current study all hyper-parameters (including v and h) were defined using a frequentist approach considering knowledge from previous work and simulated data. The noise level was defined by the patient data, as previously suggested. However, the strength of regularisation was defined based on the resulting peak posterior distribution in Goutte et al. (2000). Finally, the smoothness level for patients was based on results from simulated data (see below).

3.4.5 Simulation

Two simulations were performed. The first aimed to assess smoothness optimisation and the other was done for method validation. Method validation was performed blinded to the simulated input response.

The first simulation study was done using a time series with a single event. The HRF was simulated according to the balloon model (Buxton et al., 1998) described by Friston et al. (2000) with the SPM default parameters for a canonical response: RT = 0.5, delay of response = 6sec, delay of undershoot = 16sec, dispersion of response = 1sec, dispersion of undershoot = 1sec, ratio of response to undershoot = 6sec, onset = 0, length of kernel = 32. A response for both standard and smooth FIR was extracted for a series of model scenarios with multiple smoothness and noise levels. Smoothness levels were tested from 0.9-0.1 with larger numbers representing less smoothness (see Equation 3.2). Random noise was added to obtain 179 SNR levels (see Equation 3.4). The responses were then averaged over 50 repetitions to depict the sensitivity of smooth FIR with changes in noise and smoothness.

$$\mathrm{SNR} = \frac{\sigma^2_{\mathrm{signal}}}{\sigma^2_{\mathrm{noise}}} = \{0.01 \dots 0.9\} \qquad \textit{Equation 3.4}$$

Where σ^2 is the variance of the signal and noise.

The second simulation was a set of simulated fMRI data with added randomised noise (created by David Carmichael). The only known information about the time series was the number of events (four) and their onsets, replicating the standard EEG-fMRI analyses in epilepsy. The response function was calculated using both the standard and smooth FIR deconvolution models for a comparison of the two methodologies. A smoothness level of 0.5 was used as it was thought to be optimal for our patient data, which has SNR values ranging from 0.3-0.9. Knowledge of the appropriate smoothness level was derived from the first simulation study explained above.

3.4.6 Training the IED Basis Set

3.4.6.1 Principal Components Analysis

To characterize the HRF of paediatric epilepsy patients we performed a principal components analysis (PCA) on the extracted BOLD response of the generators of the IEDs (see Figure 3.1). The BOLD response to epileptiform events was extracted using the smooth FIR deconvolution of 16 patients (see Table 3.1). The epileptic

focus was defined as the concordant EEG-fMRI cluster derived from the dominant spike type. This analysis was done to define the response across patients.

We extracted the number of components that cumulatively explain 90% of the variance in the data. Subsequently, to exclude components dominated by noise we applied a metric based on spectral frequency where only physiological data was considered. Data was determined to be physiological if the spectral density was between 0.02-0.05 Hz with a peak around 0.03 Hz as defined by previous literature (Maziero et al., 2015; Buxton et al., 2004). With these constraints, three components remained and were used for defining the HRF basis set.

PCA was done using prcomp from the stats package in R (R Core Team, 2016). Components were then smoothed using the functions scatter.smooth and loess from the stats package in R (R Core Team, 2016) with parameters: smoothness = 0.5, degree of local polynomial = 2 and Gaussian fitting by weighted least squares.

The new data driven basis set will be tested against the standard canonical HRF (with derivatives). The benefit of this basis set will be reported in patients with concordant clusters reported in training the basis set. To test whether there were significant differences in resulting F-values and distances (to foci) in IED-HRF to cHRF models a one-tailed test of proportions was performed in R (R Core Team, 2016). Subsequently, this smoothed basis set will be tested to confirm its efficacy on defining localisation in EEG-fMRI maps.

3.4.7 Testing the IED Basis Set

The main aim of the current study was to extract a representative HRF basis set of our paediatric epilepsy patient group to provide future EEG-fMRI studies with more sensitive localisation maps. To do so we tested the model sensitivity of various basis sets in patients with a well-defined epileptogenic region, but who had non-concordant maps when applying the canonical HRF (see Table 3.1).

The fMRI data was analysed using a General Linear Model (GLM) where IEDs were used as temporal regressors and convolved with the basis set. There were three basis sets which were tested (see Figure 3.2): the standard canonical HRF (cHRF) with

time and dispersion derivatives, the extracted smooth FIR for IEDs (IED-HRF) described previously and the nested model in which both are merged together (cHRF + IED-HRF). FMRI signal changes significantly related to IEDs were subsequently measured with an F-test (see Equation 3.5-3.9). The statistical threshold was defined based on previous work on EEG-fMRI localisation maps (Centeno et al., 2016) at $p<0.001$ uncorrected with a minimum of 5 continuous voxels, which provides a reasonable balance between specificity and sensitivity. Further work dealing with statistical thresholds in random field theory (RFT) have indicated overly conservative values (Tierney et al., 2016b), which supports the use of this threshold level in the context of this study.

The size of both the cHRF and IED-HRF basis sets was three, resulting in three regressors for each event type. However the nested model has double the number of regressors. Therefore, model comparisons could only be quantified in cHRF and IED-HRF models. A one-tailed test of proportions was done in R (R Core Team, 2016) to test whether there were significant differences in resulting F-statistics and distances (to foci) in cHRF and IED-HRF epileptogenic clusters.

The total yield of each model was also calculated. This was defined as the likelihood that each model would provide an accurate localisation map, which refers to the number of patients with significant SPMs over the total number of patients tested (where significant here means an SPM with a cluster of $p<0.001$, $k=5$). Finally, the sensitivity of each basis set to reveal signal changes in the epileptogenic zone. The epileptogenic zone was defined within subjects whose localisation in the EEG-fMRI maps was improved with the use of IED-HRF/nested basis sets in comparison to the standard cHRF. Sensitivity was defined as the proportion of true positives in defining the focus. In the current study this refers to the number of concordant patients over the number of patients with significant SPMs.

$$\boldsymbol{F_{df1,df2} = \frac{\widehat{B}^T c(H^T H)^- c^T \widehat{\beta}}{\frac{Rss_{Total}}{df_{Total}}}} \qquad \textit{Equation 3.5}$$

$$\boldsymbol{H = (X^T)^+ c} \qquad \textit{Equation 3.6}$$

Where F is the f-test output, $\hat{\beta}$ represents the predicted betas, c represents the contrast matrix, X represents the design matrix, and the $^{+}$ denotes a (Moore-Penrose) pseudo-inverse. This implementation is ideal for large data sets, as the alternative (Equation 3.7) can be computationally demanding.

The alternative to Equation 3.5 can also be described as the F-ratio, or the magnitude of difference between different conditions (see Equation 3.7-3.9). Both options will yield the same results.

$$\boldsymbol{F = \frac{explained\ variance}{unexplained\ variance} = \frac{\frac{Rss_{Reduced} - Rss_{Total}}{df_{Difference}}}{\frac{Rss_{Total}}{df_{Total}}}} \qquad \textbf{\textit{Equation 3.7}}$$

$$\boldsymbol{df_{Difference} = df_{Reduced} - df_{Total}} \qquad \textbf{\textit{Equation 3.8}}$$

$$\boldsymbol{Rss = \sum(Y - \hat{Y})} \qquad \textbf{\textit{Equation 3.9}}$$

Where Rss is the residual sum of squares, df refers to the degrees of freedom, Y refers to obtained data and $\hat{Y}$ refers to the predicted data. The Rss and df of both the reduced model (not including regressors of interest) and the total model (including regressors of interest) are calculated.

The global maxima of the SPM map derived from EEG-fMRI has been shown to be a relatively poor indicator of the epileptic focus (Dongmei et al., 2013; Centeno et al., 2016b). Here, the results are presented for both the global maxima as well as the local maxima within the concordant cluster (local maxima of the cluster within closest range of the epileptogenic region).

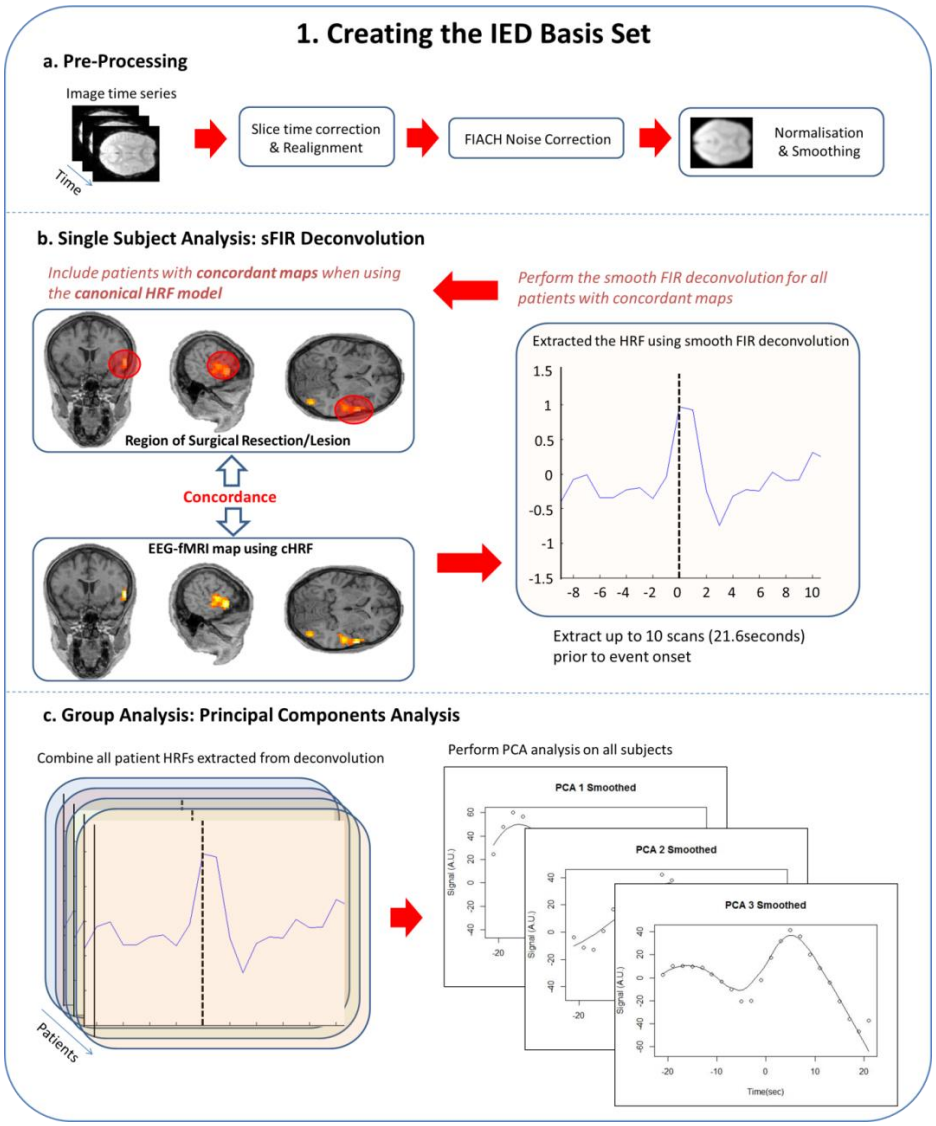

Figure 3.1 Methods for training the basis set

The first step in the analysis is training the basis set, which requires three processing steps: pre-processing the data (a), single subject analysis using smooth finite impulse response (sFIR) deconvolution (b) and group analysis using principal components analysis (c). Step 'a' involves slice time correction, realignment, and FIACH noise correction (see Tierney et al., 2016 for more details), and normalisation and smoothing. The single subject analysis step 'b' only uses patients with concordant maps (EEG-fMRI maps that have significant clusters in the focus) when using the canonical haemodynamic response function (cHRF). After which, a sFIR deconvolution is done for each patient to determine their HRF also including time prior to event onset. The group analysis step 'c' combines the patient HRFs extracted in step 'b' and performs a principal components analysis using three components as representatives HRFs for paediatric epilepsy patients.

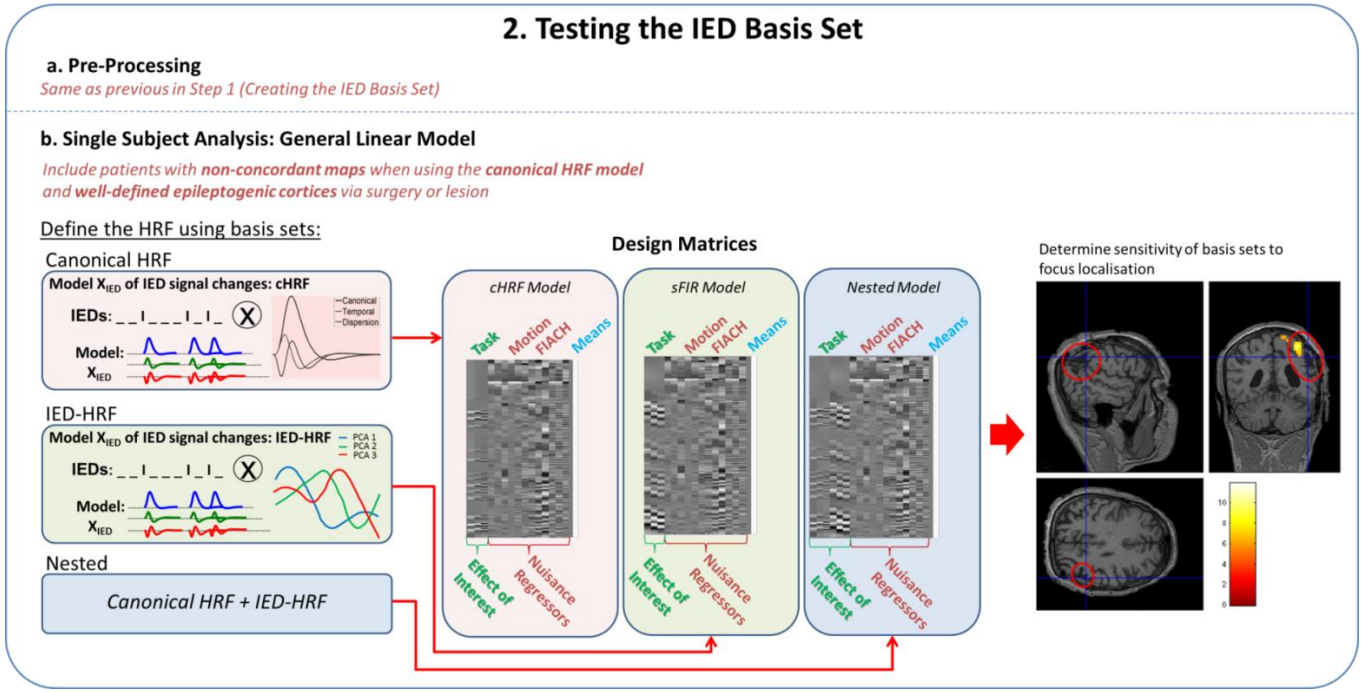

Figure 3.2 Methods for testing the basis set

The second step in the analysis is testing the IED basis set. This requires pre-processing the data (a) and performing a single subject analysis in the general linear model (b). The pre-processing in step 'a' is the same as in Step 1 for training the basis set. The single subject analysis is done in a general linear model (GLM) by defining three different types of basis sets (bottom panel, far left): the canonical haemodynamic response function (cHRF) in red, the IED-HRF (Interictal Epileptiform Discharge HRF) in green, and the nested model which includes both cHRF and IED-HRF in blue. These models are described in the design matrices (bottom panel, middle). Finally, a statistical parametric map can be used to identify the efficacy of each basis set in defining epileptogenic cortices.

3.5 Results

3.5.1 Simulations

3.5.1.1 Simulation 1: FIR Smoothness Optimisation

The results for the first simulation study for the standard FIR deconvolution method found a linear relationship between noise level and error, illustrating that an increased noise results in an increased error. The error ranged from 0-0.9 (see Figure 3.3 left panel).

The results for the smooth FIR deconvolution method were similar to the standard FIR, as an increase in noise resulted in an increase in error. However the range of error was substantially smaller (between 0-0.4). In general, a stronger smoothness level resulted in a decrease in error (see Figure 3.3 right panel, note that smaller values relate to stronger smoothness levels as stated in Equation 3.2) though the rate of error change was varied. For example, the smoothness level of 0.5 had less error across a wide range of noise levels and was thus considered optimum for most conditions.

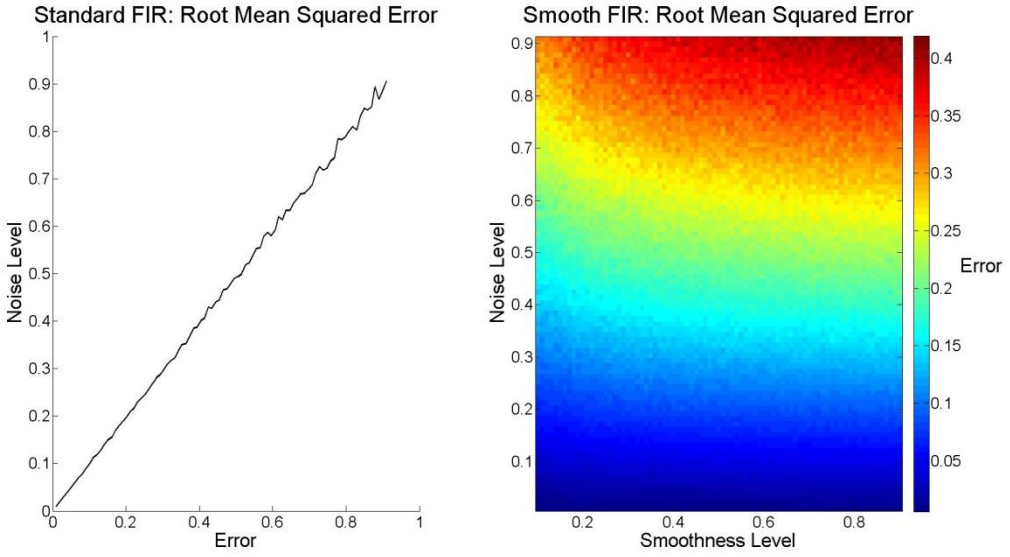

Figure 3.3 Smoothness optimisation simulation comparing standard and smooth FIR

Left) The root mean squared error for standard FIR deconvolution with different noise levels. The plot demonstrates a linear relationship between noise level and

error. Right) The root mean squared error for smooth FIR deconvolution with differing noise and smoothness levels. The linear relationship between noise and error described in left plot is also seen in right plot. However the additional factor of smoothness level illustrates that an increase in smoothness magnitude results in a decrease in error (with larger numbers representing less smoothness). The error rates are lower in smooth FIR compared to the standard FIR deconvolution.

3.5.1.2 Simulation 2: Method Validation

The second simulation was used to test the methodology/code using a predefined response function when performing the FIR deconvolution. Both standard and smooth FIR responses were extracted and compared to the original time course with and without noise (see Figure 3.5-Figure 3.6). Both methodologies extracted results similar to the response function that was used as input both in magnitude and shape. However, the smooth FIR is optimal in the presence of noise, and as expected, smooths abrupt transitions in the response which is appropriate for physiological data.

The input function contained a discontinuity and so due to the Gibbs phenomenon a ringing artefact was observed in the smooth FIR deconvolution response. The Gibbs phenomenon is known to occur at discontinuities such as square waves and is considered a fundamental problem of filtering algorithms (see Figure 3.4). In general, this 'ringing' artefact occurs when a non-oscillating input (such as a square wave) releases an oscillating output, and is caused by the superimposition of a finite number of smoothed functions to exactly reproduce a sharp border. The limit of magnitude change for this phenomenon is 9% (Gibbs, 1899), which is equivalent to the percent change seen in Figure 3.4 due to the ringing effect. However this effect would not be present in BOLD data as discontinuity would not occur in a haemodynamic response.

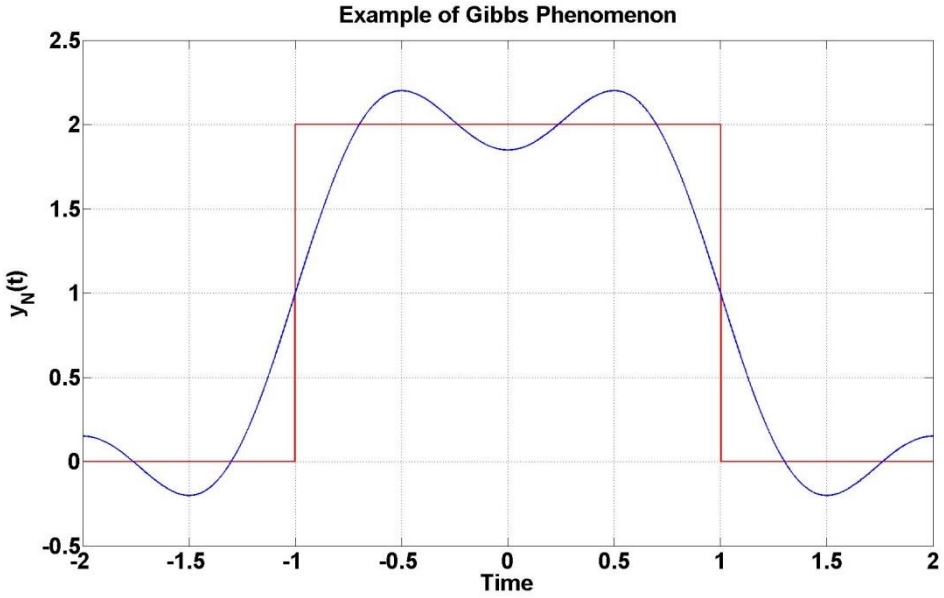

Figure 3.4 Example of Gibbs phenomenon.
Near the region of discontinuities of the square wave (red) the approximation (blue) overshoots and induces a ringing effect.

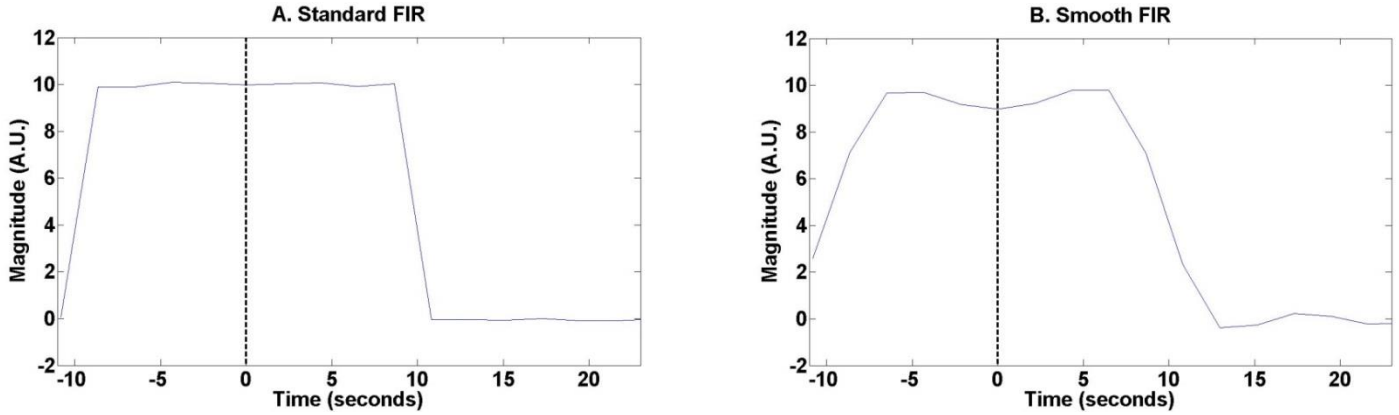

Figure 3.5 Extracted responses for both standard and smooth FIRs

A) The response to the onset of events extracted from standard FIR. B) The response to the onset of events extracted from smooth FIR. Responses were averaged over all voxels.

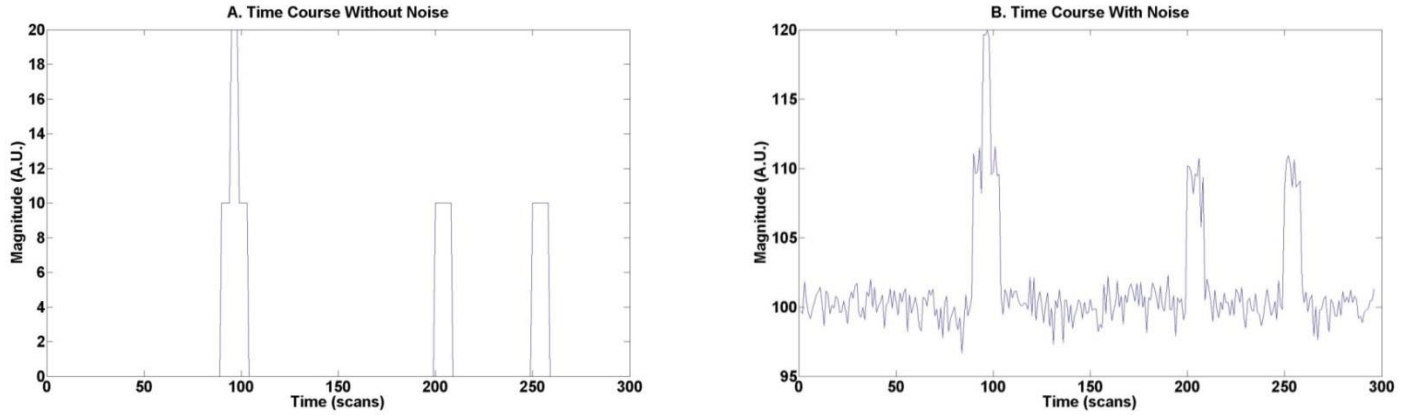

Figure 3.6 Time course of original data

A) Simulation data without noise. B) Simulation data with added noise.

3.5.2 Training the IED Basis Set

An HRF basis set was extracted using PCA. The three final smoothed components are illustrated in Figure 3.7. These three components explain 50% of the variance in the FIR derived HRFs. The remaining components were excluded due to noise, but can be viewed in the Appendix (Figure 8.4).

All three components evolve in a similar manner over time. There is an initial peak from baseline, followed by a large undershoot and a return to baseline. This follows the general shape of the previously described canonical response. However, the timing parameters (time to onset, time to peak, and time to baseline) for the first two components are different from those seen in the standard canonical model. For example, the third component is representative of the canonical model, while other components (such as component 1) are similar to the canonical but are time shifted.

The first component (see Figure 3.7, left) peaks at approximately 17seconds prior to the event onset. After which the response steadily declines until the time of onset and returns to baseline after approximately 10seconds.

The second component (see Figure 3.7, middle) peaks at approximately 3 seconds prior to the event onset, and similar to the first component, the response undershoots and returns to baseline. The return to baseline occurs approximately 20seconds after event onset.

The first two components have peak times well before the estimated peak from the canonical HRF however the third component (see Figure 3.7, right) is very similar to the canonical HRF in both shape and timing parameters. The response advances from baseline to an initial dip before peaking 5seconds after event onset.

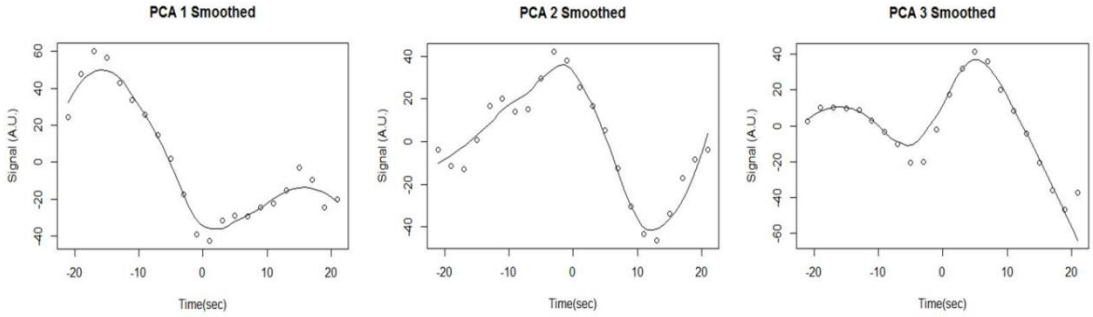

Figure 3.7 PCA Components
The top three components explaining the greatest amount of variance in the data are shown by PCA 1 (left), PCA 2 (middle), and PCA 3 (right) after smoothing was applied. The smoothing is illustrated by the black curve fitted line and the shape prior to smoothing is represented by circles.

Results show that there were no significant differences between using the cHRF model or the IED-HRF model in these patients (Table 3.2). However, there was a trend in IED-HRF predicting more accurate distances to epileptic foci (see Table 3.3-Table 3.4 and Figure 3.8).

3.5.2.1 Yield

There was 100% (16/16) yield in all SPMs for both cHRF (as this was a requirement of the inclusion criteria for patients involved in training the basis set) and IED-HRF models.

3.5.2.2 Sensitivity

For the IED-HRF there was a sensitivity of 75% (12/16) in the concordant cluster and 44% (7/16) for the IED-HRF in the global maxima.

All patients had a concordant cluster for the cHRF because this was the inclusion criteria for the patients involved in training the basis set. There was a sensitivity of 56% (9/16) for the cHRF in the global maxima. Therefore, the sensitivity in the global maxima was lower for both models.

Table 3.2 Patients included in training the basis set

		Concordant Cluster		Global Maxima	
		Canonical HRF	IED-HRF	Canonical HRF	IED-HRF
Patient #1					
	Region	L Postcentral	L Postcentral	L Postcentral	L Postcentral
	Coordinate	[-58, 11, 25]	[-52, 5, 26]	[-58,11,25]	[-52,3,26]
	F-value	**16.45**	6.85	**16.45**	6.85
	Distance	21	**16.03**	21.02	**17.12**
Patient #2					
	Region	R Hippocampus	**R Angular Gyrus**	**R Middle Temporal**	**R Middle Frontal**
	Coordinate	[33, 45, -26]	[56, -4, 9]	[63,-8,9]	[50,55,23]
	F-value	**7.74**	7.70	**12.23**	11.24
	Distance	**5**	45.92	73.63	**54.61**
Patient #3					
	Region	L Insula	L Insula	**R Superior Temporal**	**R Superior Temporal**
	Coordinate	[-22, 49, -17]	[-29, 49, -17]	[69,38,-3]	[72,29,6]
	F-value	**6.68**	6.42	15.56	**16.45**
	Distance	**3.16**	4.12	95.95	**95.91**
Patient #4					
	Region	L Caudate	L Caudate	L Caudate	L Caudate

	Coordinate	[-9, 30, -17]	[-3, 40, 2]	[-9,30,-17]	[-3,40,2]
	F-value	16.63	**16.89**	16.63	**16.89**
	Distance	5.39	**4.24**	5.39	**4.24**
Patient #5					
	Region	R Inferior Parietal	R Inferior Parietal	R Inferior Parietal	**R Superior Frontal**
	Coordinate	[38, 1, 13]	[38, 1, 13]	[38, 1, 13]	[12, 72, 24]
	F-value	**11.90**	10.50	11.90	**15.19**
	Distance	18.30	**10.18**	**18.30**	87.42
Patient #6					
	Region	R Superior Frontal	R Superior Frontal	**L Angular**	R Superior Frontal
	Coordinate	[30, 77, 15]	[30,77,15]	[-35,-44, 8]	[30,77,15]
	F-value	12.60	**15.94**	13.58	**15.94**
	Distance	**0**	**0**	137.53	**0**
Patient #7					
	Region	L insula-occipital	L Occipital	L Occipital	L Fusiform
	Coordinate	[-54, 48, -10]	[-44, -34, -13]	[-34,-26,-21]	[-31,-26,-21]
	F-value	6.60	**9.57**	**19.47**	11.32
	Distance	**0**	**0**	25.24	**25.06**
Patient #8					

	Region	R Perisylvian	**Middle Cingulate**	R Perisylvian	**L Calcarine**
	Coordinate	[60, 3, -25]	[7, -2, 20]	[59,2,-24]	[-5,-7,-12]
	F-value	**7.93**	6.42	7.93	**8.85**
	Distance	30.50	**23.09**	**30.50**	63.63
Patient #9					
	Region	R Superior Frontal	L Superior Frontal	**L Angular Gyrus**	**L Middle Temporal**
	Coordinate	[11, 34, 41]	[-26, 37, 21]	[-42, -25, 0]	[-42, -6, -23]
	F-value	7.46	**8.81**	12.33	**20.84**
	Distance	**11.85**	18.28	89.99	**72.49**
Patient #10					
	Region	R Middle Temporal	R Middle Temporal	R Middle Temporal	R Middle Temporal
	Coordinate	[64,20,-24]	[64,23,-20]	[64,20,-24]	[64,23,-20]
	F-value	**20.35**	11.45	**20.35**	11.45
	Distance	**0**	**0**	**0**	**0**
Patient #11					
	Region	L Inferior Frontal	L Middle Frontal	**R Inferior Frontal**	**R Middle Frontal**
	Coordinate	[-33, 40, -8]	[-33, 39, 33]	[52,37,-3]	[39,61,29]
	F-value	**17.20**	6.88	**55.24**	20.39
	Distance	13.60	**0**	65.74	**56.47**

Patient #12

Region	R Occipital	R Occipital	**L Occipital**	**L Occipital**
Coordinate	[54, 7, -13]	[44, -36, -33]	[-22,-45,-39]	[-21,-47,-43]
F-value	7.31	**7.78**	**12.64**	12.45
Distance	48.47	**0**	**16.12**	18.63

Patient #13

Region	L Occipital	L Occipital	L Inferior Parietal	L Inferior Parietal
Coordinate	[-56, -20, 18]	[-17, -17, 3]	[-43,-19,45]	[-43,-20,41]
F-value	7.15	**10.03**	17.91	**17.94**
Distance	8.06	**0**	21	**15.65**

Patient #14

Region	R Middle Temporal	R Inferior Temporal	R Middle Temporal	R Inferior Temporal
Coordinate	[50,7,-26]	[40,-21,-44]	[50,7,-26]	[40,-21,-44]
F-value	**20.30**	17.86	**20.30**	17.86
Distance	**0**	**0**	**0**	**0**

Patient #15

Region	R Inferior Parietal	**Middle Cingulate**	R Inferior Parietal	**Middle Cingulate**
Coordinate	[33,0,29]	[0,19,20]	[33,0,29]	[0,19,20]
F-value	**11.71**	6.58	**11.71**	6.58

	Distance	**0**	39.12	**0**	39.12
Patient #16					
	Region	L Inferior Frontal	**Middle Cingulate**	**R Insula**	**L Precentral**
	Coordinate	[-31, 69, 2]	[-5, 33, 34]	[28, 53, -21]	[-31, 24, 47]
	F-value	**10.43**	7.07	**10.78**	9.96
	Distance	**0**	62.71	**64.51**	71.46

Values with the 1) largest F-values and 2) closest distance to foci were bolded. Non-concordant regions were highlighted in red.

Table 3.3 Concordant Cluster

	cHRF	IED-HRF
F-value	10/16 (62.5%)	6/16 (37.5%)
Distance*	5/16 (31%)	7/16 (44%)

* The remaining values were tied between cHRF and IED-HRF.

Table 3.4 Global Maxima

	cHRF	IED-HRF
F-value	9/16 (56%)	7/16 (44%)
Distance*	5/16 (31%)	9/16 (56%)

* The remaining values were tied between cHRF and IED-HRF.

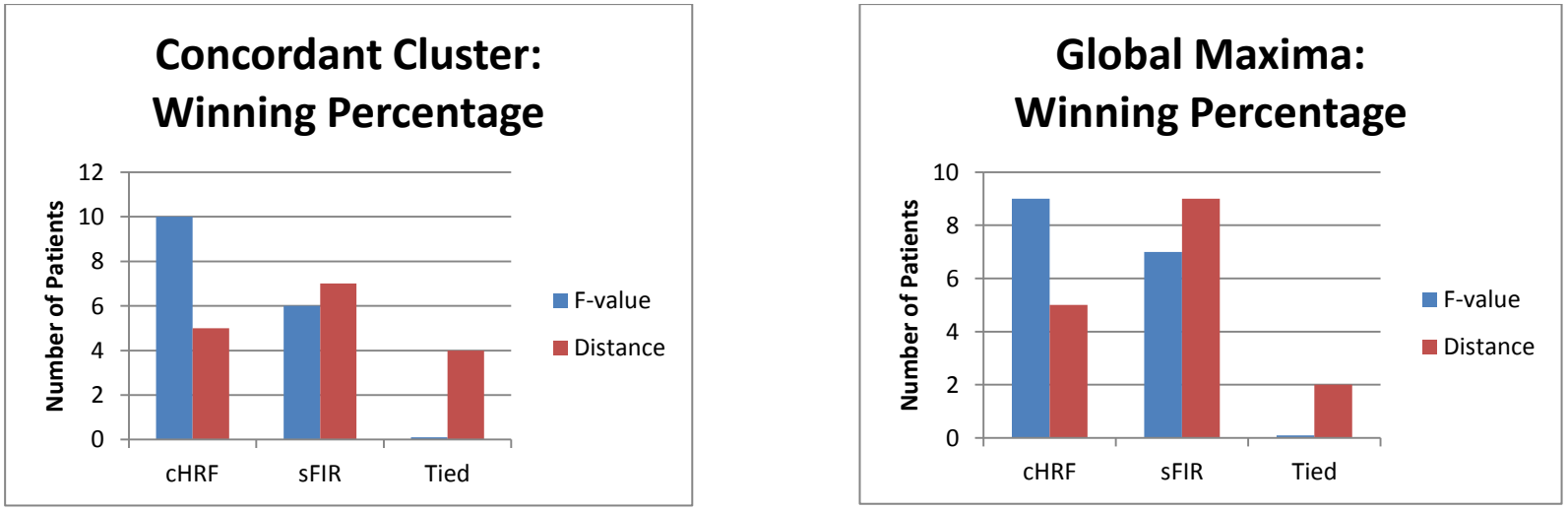

Figure 3.8 GLM Comparison for patients included in training the IED-HRF basis set

A bar chart displaying the number of patients with larger F-values and smaller distances to foci in the cHRF, and IED-HRF, and values in which both models are tied. F-values are displayed in blue while distances are displayed in red. These values are within the concordant cluster (left) and global maxina (right).

3.5.3 Testing the IED Basis Set

The primary goal of testing the basis sets was to determine which of the three models (cHRF, IED-HRF, and a combination of the two) was the most sensitive in defining the epileptogenic zone.

For patients in the testing of the basis set, there was significant difference between the cHRF and IED-HRF models for the distance to foci in the concordant cluster with $p<0.01$ with FWE correction; indicating a significantly better localisation in the IED-HRF model than cHRF within the concordant cluster (see Table 3.9 and Figure 3.10). There was also a significant difference between the cHRF and IED-HRF models for the F-values in the global maxima with $p<0.01$ with FWE correction; indicating significantly higher F-values in the IED-HRF model than in the cHRF within the global maxima (see Table 3.10 Figure 3.10).

There were a total of nine patients with a correct localisation (defined based on surgery or lesion) using the IED-HRF in the testing/training group (clusters within the presumed focus).

3.5.3.1 Yield

The yield of the cHRF model in the test group was 64% (7/11) this is because the failure of the cHRF model was used in defining this group. The yield of the IED-HRF model was 100% (11/11), and the yield of the nested model was 82% (9/11).

Taken together the yield of the cHRF group was 85% (23/27) and the IED-HRF was 100% (27/27) for the training and testing of the basis set.

3.5.3.2 Sensitivity

The sensitivity of the concordant cluster was 64% (7/11) in the test group of patients when using the IED-HRF (see Table 3.5-Table 3.6 and Figure 3.9). In contrast, when using the global maxima to select the cluster a 9% (1/11) increase in sensitivity was found (see Table 3.7-Table 3.8). The nested model was sensitive in defining the seizure focus in 11% (1/9) of patients within the concordant cluster and 0% in the global maxima. Due to the change in variance accounted for by the IED-HRF / IED-

HRF +cHRF regressors in the nested model, the cHRF model was improved in 14% (1/7) of patients in the concordant cluster and 0% in the global maxima.

Taken together (training and testing of the basis set) the sensitivity of the cHRF group was 59% (16//27) and 37% (10/27) in the concordant cluster and global maxima respectively. The IED-HRF was 70% (19/27) and 30% (8/27) in the concordant cluster and global maxima respectively.

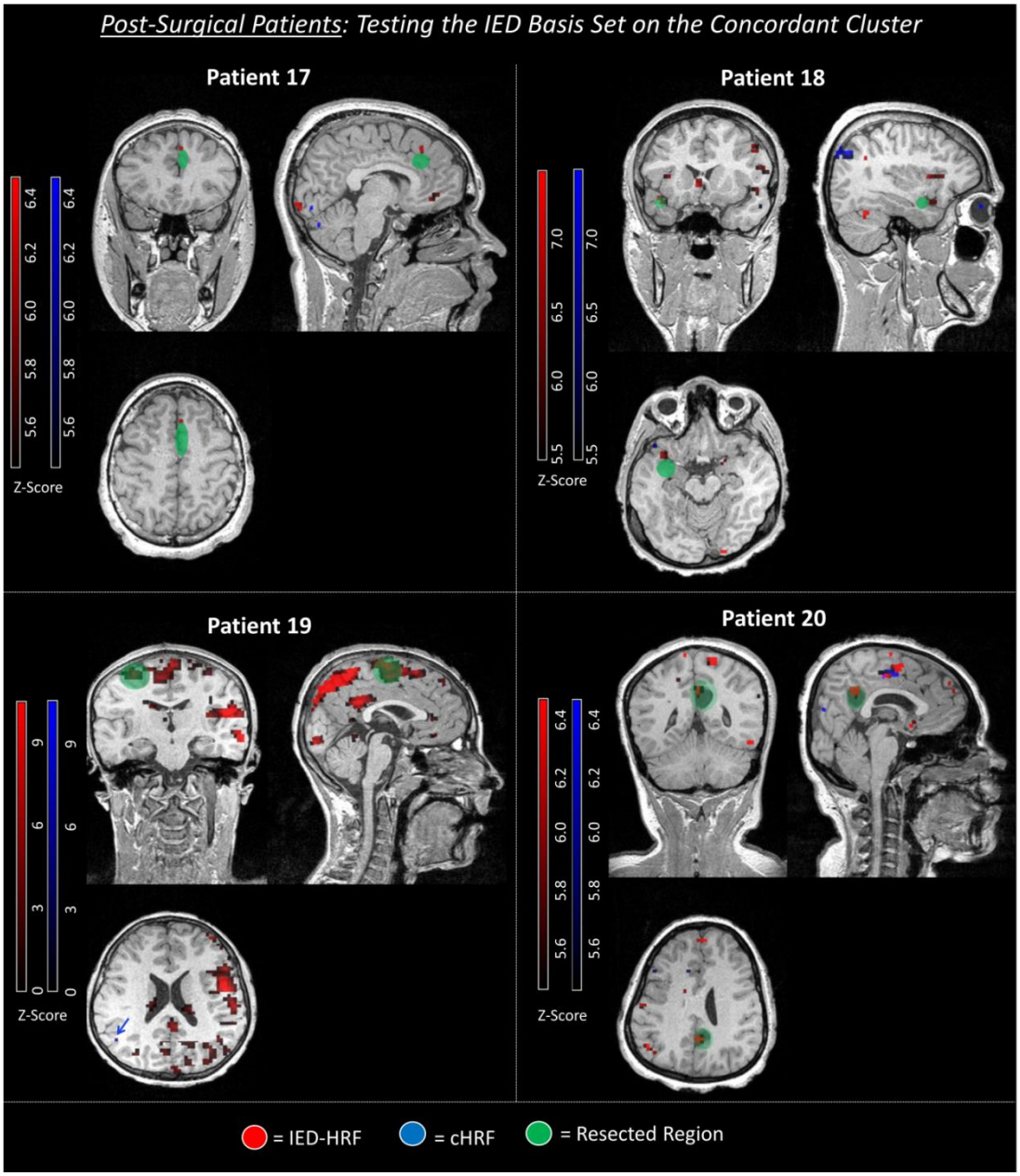

Figure 3.9 Post-surgical patients: testing the IED basis set on the concordant cluster

The comparison between EEG-fMRI maps using different basis sets for the haemodynamic response function (HRF). The concordant cluster for all four post-surgical patients (Patients 17-20) are depicted above with red indicating the IED-HRF result, blue indicating the cHRF result, and green indicating the resected region. However please note the resected region is an illustration and therefore a representation of surgery. In summary the IED-HRF basis set increases the sensitivity of EEG-fMRI maps to the resected region when compared to the cHRF. The blue arrow in the axial plane of patient 19 is pointing to a small (5 voxel) cluster for the cHRF.

Table 3.5 Post-surgical patients included in testing the basis set: Concordant Cluster

		Concordant Cluster				
		Canonical HRF	IED-HRF	Nested	Surgery	Concordance
Patient #17						
	Region	L Cuneus	R Middle Frontal	L Postcentral	R Frontal	IED-HRF
	Coordinate	[-7, -47, 20]	[42, 59, 16]	[-40, 20, 11]		
	F-value	8.04	**9.55**	4.06		
	Distance	79.29	**42.61**	59.60		
Patient #18						
	Region	L Caudate	L Temporal Pole/ L Insula	L Thalamus	L Temporal	IED-HRF
	Coordinate	[-1, 34, 25]	[-37, 40, 13]	[-14, 34, 21]		
	F-value	**7.64**	7.03	5.13		
	Distance	34.41	23.41	**22.89**		
Patient #19						
	Region	NA	L Superior Frontal	L Inferior Temporal	L Frontal	IED-HRF
	Coordinate	NA	[-16, 37, 73]	[-35, 8, 4]		
	F-value	NA	**6.57**	4.53		
	Distance	NA	**0**	77.55		

Patient #20

	Region	R Precuneus	R Posterior Cingulate	R Inferior Parietal	R Parietal/ Posterior Cingulate	IED-HRF
	Coordinate	[4, -53, 27]	[10, -27, 39]	[59, -45, 41]		
	F-value	**6.38**	5.69	4.84		
	Distance	21.11	**0**	27.75		

NA = not available; no clusters passed the significance threshold. Distance is described in millimetres.

Table 3.6 Lesion patients included in testing the basis set: Concordant Cluster

		Concordant Cluster				
		Canonical HRF	IED-HRF	Nested	Lesion	Concordance
Patient #21						
	Region	R Precuneus	L Inferior Frontal	R Anterior Cingulate	L Frontal	IED-HRF
	Coordinate	[9, -33, 31]	[-37, 62, 7]	[9, -62,-11]		
	F-value	7.46	**12.13**	4.89		
	Distance	105.86	**6.56**	43.09		
Patient #22						
	Region	L Precentral	R Precuneus	R Superior Temporal	R Parietal	None
	Coordinate	[-19, 16, 9]	[7.29, -25, -13]	[37, 22, -31]		
	F-value	6.64	6.06	**7.00**		
	Distance	41.80	**31.12**	59.05		
Patient #23						
	Region	R Inferior Parietal	L Superior Temporal/ Perisylvian Fissure	R Lingual Gyrus	L Insula/ Perisylvian Fissure	IED-HRF
	Coordinate	[30, -9, 8]	[-45, -14, -13]	[7, -61, -47]		

	F-value	**8.60**	7.76	4.75		
	Distance	61.97	**20.73**	85.51		
Patient #24						
	Region	NA	L Inferior Parietal	NA	L Parietal	IED-HRF
	Coordinate	NA	[-35, 1, 53]	NA		
	F-value	NA	**7.88**	NA		
	Distance	NA	**20.57**	NA		
Patient #25						
	Region	NA	L Lingual	NA	R Temporal	None
	Coordinate	NA	[-2, -47, 11]	NA		
	F-value	NA	**8.08**	NA		
	Distance	NA	**67.30**	NA		
Patient #26						
	Region	R Middle Temporal	L Calcarine	R Inferior Parietal	R Parietal/ R Temporal	cHRF, Nested
	Coordinate	[20, -36, 30]	[-3, -62, 24]	[7, -50, 41]		
	F-value	**9.85**	7.58	4.37		
	Distance	**0**	20.01	11.85		
Patient #27						

Region	NA	Thalamus	L Posterior Cingulate	L Frontal/ Hypothalamus	None
Coordinate	NA	[-9, 3, 36]	[-3, -21, 63]		
F-value	NA	**7.44**	5.29		
Distance	NA	**24.18**	56.44		

NA = not available; no clusters passed the significance threshold. Distance is described in millimetres.

Table 3.7 Post-surgical patients included in testing the basis set: Global Maxima

		Global Maxima				
		Canonical HRF	IED-HRF	Nested	Surgery	Concordance
Patient #17						
	Region	L Fusiform	R Middle Frontal	L Postcentral	R Frontal	IED-HRF
	Coordinate	[-26, -15, -35]	[46, 67, -15]	[-40, 20, 11]		
	F-value	9.18	**15.49**	4.06		
	Distance	89.47	66.84	**59.60**		
Patient #18						
	Region	L Cerebellum	R Insula	L Thalamus	L Temporal	None
	Coordinate	[-1, -13, -6]	[45, 50, 21]	[-14, 34, 21]		
	F-value	10.78	**13.15**	5.13		
	Distance	46.21	79.61	**22.89**		
Patient #19						
	Region	NA	R Superior Temporal	L Inferior Temporal	L Frontal	None
	Coordinate	NA	[70, 64, 9]	[-35, 8, 4]		
	F-value	NA	**48.20**	4.53		
	Distance	NA	110.22	**77.55**		
Patient #20						

Region	R Middle Cingulate	L Inferior Temporal	R Inferior Temporal	R Parietal/ Posterior Cingulate	None
Coordinate	[11, 12, 61]	[-49, -37, 10]	[53, -20, -16]		
F-value	7.57	**12.33**	6.52		
Distance	**36.51**	66.64	70.28		

NA = not available; no clusters passed the significance threshold. Distance is described in millimetres.

Table 3.8 Lesion patients included in testing the basis set: Global Maxima

		Global Maxima				
		Canonical HRF	IED-HRF	Nested	Lesion	Concordance
Patient #21						
	Region	R Precuneus	L Inferior Parietal	R Precuneus	L Frontal	None
	Coordinate	[9, -33, 31]	[-20, -46, 10]	[9, -33,27]		
	F-value	7.46	**24.94**	4.63		
	Distance	105.86	108.78	**55.18**		
Patient #22						
	Region	L Precentral	L Middle Occipital	R Superior Temporal	R Parietal	None
	Coordinate	[-19, 16, 9]	[-35, -35, -36]	[37, 22, -31]		
	F-value	6.64	**15.99**	7.00		
	Distance	**41.80**	74.60	59.05		
Patient #23						
	Region	R Inferior Parietal	L Middle Temporal	R Lingual Gyrus	L Insula/ Perisylvian Fissure	None
	Coordinate	[30, -9, 8]	[-55, -14, -25]	[7, -61, -47]		
	F-value	8.60	**15.86**	4.75		

	Distance	61.97	**36.49**	76.09		
Patient #24						
	Region	NA	R Supramarginal	NA	L Parietal	None
	Coordinate	NA	[53, -16, 19]	NA		
	F-value	NA	**47.46**	NA		
	Distance	NA	**87.65**	NA		
Patient #25						
	Region	NA	L Lingual	NA	R Temporal	None
	Coordinate	NA	[-2, -47, 11]	NA		
	F-value	NA	**8.08**	NA		
	Distance	NA	**67.30**	NA		
Patient #26						
	Region	L Inferior Parietal	L Lingual	L Posterior Cingulate	R Parietal/ R Temporal	None
	Coordinate	[-49, -47, 41]	[-6, -41, 9]	[-6, -34, -46]		
	F-value	**13.67**	8.75	5.31		
	Distance	66.36	30.58	**28.09**		
Patient #27						
	Region	NA	R Angular	L Posterior	L Frontal/	None

			Cingulate	Hypothalamus
Coordinate	NA	[47, -58, 68]	[-3, -21, 63]	
F-value	NA	**26.11**	5.29	
Distance	NA	99.03	**56.44**	

NA = not available; no clusters passed the significance threshold. Distance is described in millimetres.

Table 3.9 Concordant Cluster

	cHRF	IED-HRF	Nested
F-value	4/11 (36%)	6/11 (55%)	1/11 (9%)
Distance	1/11 (9%)	9/11 (82%)	1/11 (9%)

Table 3.10 Global Maxima

	cHRF	IED-HRF	Nested
F-value	1/11 (9%)	10/11 (91%)	0/11 (0%)
Distance	2/11 (18%)	3/11 (27%)	6/11 (55%)

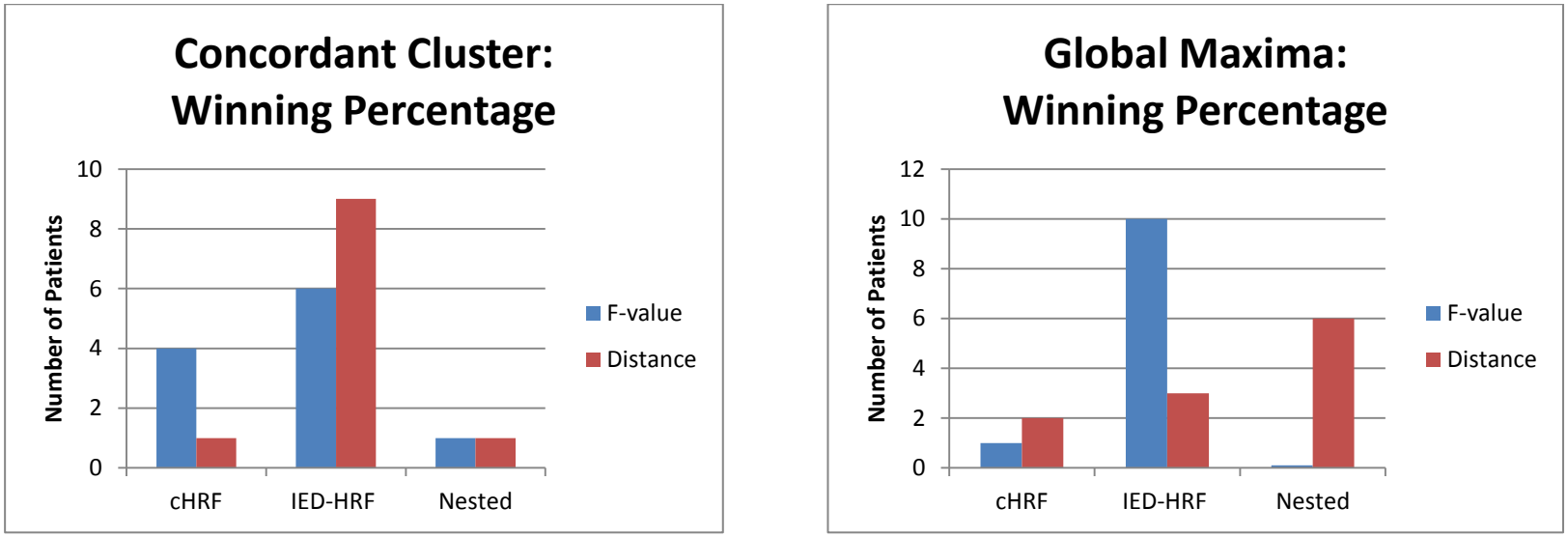

Figure 3.10 Comparison for patients included in testing the IED-HRF basis set

A bar chart displaying the number of patients with larger F-values and smaller distances to foci in the cHRF, IED-HRF, and nested models. F-values are displayed in blue while distances are displayed in red. These values are within the concordant cluster (left) and the global maxima (right).

3.6 Discussion

To extract a patient's epileptogenic network an accurate HRF must be defined. Previous studies have commented on the possible inaccuracies of the current canonical model especially in its temporal characteristics (Hawco et al., 2007; Moeller et al., 2008; Jacobs et al., 2009; Rathakrishnan et al., 2010; Pittau et al., 2011; Rollings et al., 2016; Brevard et al., 2006). The goal of the current study was to 1) to see if haemodynamic responses preceded IEDs and 2) to construct a new model of haemodynamics with greater sensitivity than the cHRF. However, prior to answering these questions method on patients, tests confirming the efficacy of the deconvolution method were implemented.

3.6.1 Simulations

Firstly, simulation data was used to 1) study the efficacy of the standard FIR and smooth FIR models at varying degrees of noise and 2) their ability to accurately predict a response without prior knowledge of shape or temporal parameters. Results showed that a stronger smoothness level resulted in decreased error therefore a smoothness level of 0.5 (see Figure 3.3) was a suitable for our fMRI data. Additionally, prior knowledge on temporal and morphological characteristics was not necessary to extract an accurate response. Therefore the efficacy of the smooth FIR deconvolution was confirmed and was subsequently applied to our patient data.

3.6.2 Smooth FIR Deconvolution

Previous studies have used deconvolution methods to extract patient-specific HRFs. Though this methodology is an improvement upon the standard canonical model due to its flexibility (Lu et al., 2006), it is also somewhat circular in that the extracted signal is subsequently reapplied to the same dataset increasing the chance of over-fitting the data and vastly inflating statistical significance. Therefore to improve upon this technique the current study provides a novel approach in combining subject-specific HRFs at a group level via PCA on a training dataset. The resulting basis set is then tested for efficacy in both the same and an independent group of patients, removing the issue of over-fitting and circularity in the latter case. Another novel aspect of the current study is the use of smooth FIR deconvolution. It has yet to be

applied to clinical epilepsy data even though it is the optimal way in providing a balance between model flexibility (of the FIR) and constraint (reducing the impact of noise on the fitted response).

The smooth FIR function was applied to the region of epileptogenic focus at a time window surrounding interictal events (between 20 seconds prior and 20 seconds after the event) to determine the likelihood of preceding BOLD changes. From this a series of patient HRFs was gathered and a PCA was performed. The purpose of the PCA was to characterise response parameters that behave similarly across patients. Results show that the shape of the HRFs resemble the standard canonical response however the peak times for two out of three components were prior to event onset. The third component resembled the canonical HRF in both shape and temporal characteristics. Results generated a basis set with varying peak times at approximately -17, -3, +5 seconds relative to event onset. This variability in the time to peak demonstrates a haemodynamic change prior to epileptic events confirming that the current canonical model is insufficient. However by combining the temporally distinct PCA components as an HRF basis we can account for these variations and provide more accurate EEG-fMRI localisation maps.

As a measure of face validity we first tested the IED-HRF on the training data (patients with concordant maps using the cHRF model) to determine any benefit the IED-HRF model in patients with already maps using the canonical model.

3.6.3 Testing the IED-HRF Basis Set

The main aim of testing the new IED basis set was to determine if it could increase the sensitivity and yield of EEG-fMRI maps delineating epileptogenic cortex in patients in whom the cHRF was ineffective. When applying this new basis set we found maps could correctly localise in 7/11 patients. Interestingly, combining both cHRF and IED-HRF is more beneficial than the cHRF model alone, even when the cHRF accounts for time and dispersion derivatives. This could possibly be due to the increase in variance explained. There were significant differences found between IED-HRF and cHRF models when using the concordant cluster (defined as containing significant BOLD changes within the presumed epileptogenic region), the IED-HRF was more likely to produce regions near the epileptogenic focus as was

expected. Furthermore, in the global maxima, the IED-HRF was more likely to produce larger F-values. This suggests that using the IED-HRF in an EEG-fMRI model is beneficial for defining the epileptogenic zone in future EEG-fMRI studies when the canonical model fails.

Both yield and sensitivity are measurements of model performance. When we combined these values in both the training and testing data set, we were able to estimate relative model efficacy. Results show that the overall yield of the IED-HRF model was 100% while the sensitivity of the IED-HRF in the concordant cluster was 70%, compared to 85% and 59% respectively in the cHRF model. Though these results indicate the benefit of using the IED-HRF model especially in cases where the cHRF model fails, it is important to note the limitation of using the training set, as it is defined based on the efficacy of the canonical model thus making it biased towards the cHRF. Ideally the testing of all models (cHRF versus IED-HRF) would be done on a new data set without any bias towards an HRF model. However, patients with well-defined epileptogenic networks are difficult to collect, especially in children with good post-operative outcome and clear lesions. Nevertheless, the PCA analysis showed equal weighting from each individual, therefore the results are likely to be representative.

3.6.4 Issues with Reporting the Global Maxima

In the current study, both the global maxima and concordant cluster (local maxima of the cluster within the closest range of the epileptogenic region) were reported due to the recent debate (Dongmei et al., 2013). Though the global maxima is easy to extract, it suffers from poor sensitivity as it is often located in regions remote from the epileptogenic cortex (Centeno et al., 2016b). This supports the findings of the current study, as the concordant cluster was unlikely to occupy the cluster within the global maxima. Though this is a secondary finding, it might improve the sensitivity of future EEG-fMRI findings.

3.6.5 Possible Reasons for Early Haemodynamic Change

Here, we found early haemodynamic responses preceding electrical events by up to 17 seconds. However, it is unclear what might be the driver of these changes preceding epileptic discharges. There are two possibilities that could explain this

phenomenon: 1) there is a change in neuronal activity prior to haemodynamic events that cannot be visually detected on the scalp or 2) the physiological events triggering changes in BOLD signal precede that of neuronal discharge.

In the first case, there are many ways in which this could happen. One pertains to invisible EEG changes prior to IEDs that are undetectable by a neurophysiologist. However, previous studies have tested this hypothesis by performing statistical analyses on the EEG power (Jacobs et al., 2009). However they could not find consistent relevant power changes in relation to the early HRF timings in a majority of their patients, making it an unlikely source for this phenomenon. Another refers to the possibility of measuring propagated electrical events. However, previously reported peaks which can occur up to 9 seconds prior to the event (Moeller et al., 2008; Jacobs et al., 2009) could not be attributed to spike propagation, as propagation occurs within milliseconds (Emerson et al., 1995).

It has also been hypothesized that the 'invisibility' of the scalp EEG to spikes could also be due to deep subcortical sources that are not visible on the scalp. However, haemodynamic changes prior to epileptic activity have also been measured in subcortical regions in idiopathic generalised epilepsy (Moeller et al., 2008). Furthermore, intracranial EEG recordings have confirmed that spikes invisible to scalp EEG are only responsible for a small proportion of early haemodynamic changes (Pittau et al., 2011), while others could be explained by metabolic changes not involved in synchronized neuronal discharges.

This brings us to the second case, in which non-neuronal mechanisms regulate changes in haemodynamics. Such mechanisms include astrocytes, which are thought to have a role in neurovascular coupling (and consequently related to BOLD signal changes) and possibly in preparing the synchronous neurological discharge of a spike (Schummers et al., 2008; Jacobs et al., 2009). In addition it might be that changes in the brain's connectivity, such as those measured in Chapter 2, play a facilitative role in IED generation. This could explain fMRI changes preceding events at these timescales.

Furthermore, focal seizures are thought to be the product of changes in neuromodulators and neurotransmitters such as extracellular potassium, oxygen, ATP consumption, and glucose supply, all of which occur on a slow time scale (Jirsa et al., 2014). Though interictal activity might not necessarily be the driving force behind seizures, their occurrence may similarly reflect the fluctuations of these processes within the epileptogenic network. However some of these parameters cannot be measured in EEG recordings, and would therefore require other forms of measurement to determine key biomarkers for seizure prediction (see below in future work).

Previous work (Chapter 2) demonstrates the role of IEDs in altering BOLD signal, and therefore interpretation of network connectivity. However, the question remained as to how these changes occur. Results from the current study answer this question, indicating early changes in haemodynamics preceding electrical events.

3.6.6 Limitations

Specificity is quite difficult to determine in EEG-fMRI localisation maps, for both cHRF and IED-HRF models. Specificity can be measured with great accuracy in Electrical Source Imaging (ESI) at the cost of sensitivity. Therefore, the combination of these two techniques could vastly improve both the specificity and sensitivity in defining epileptogenic cortex (Centeno et al., 2016b).

3.6.7 Future Work

In this study the possible interaction of antiepileptic drugs (AEDs) on the haemodynamic changes were not considered but may be a relevant factor to be considered in future studies, as they could have an influence on the underlying abnormal neurovascular coupling in epilepsy. However this is beyond the scope of the current study as the possible interaction effects of a patient's AED administration (see Table 1) would be highly complex. Especially considering paediatric epilepsy patients are on an average of two AEDs per day.

Another area of interest is the EEG correlates to the early changes found in the haemodynamic response relative to IED activity. For example, is EEG sensitive

enough to detect these changes via visual inspection? Or can these changes be seen in via frequency analysis? All of these questions warrant further investigation.

A more practical application if these results were confirmed is the possible detection of IEDs and seizures using measurements of haemodynamics given they seem to happen before electrical discharges. Changes in BOLD signal involve an interaction of various physiological variables including blood flow, blood volume, and oxygen content. While fMRI provides an indirect measurement of neuronal activity in relation to changes of deoxyhaemoglobin, Near Infrared Spectroscopy (NIRS) might be an interesting technique to further examine the neurovascular coupling of epileptic activity as it measures changes of both –oxy and –deoxy haemoglobin.

3.7 Conclusions

An early BOLD response to focal IEDs was derived to form an IED-HRF. This basis set had changes occurring well before the electrographic events. This early response may represent a pre-existing metabolic change in state that is predictive of the epileptiform activity. In subjects where the more standard cHRF basis set failed the IED-HRF was able to localise in 64% of patients, this could potentially increase the clinical yield of EEG-fMRI in children. Therefore, future work should consider the use of the IED-HRF basis set to increase sensitivity in detecting the epileptic focus in children with epilepsy.

Chapter 4 NIRS Optode Holder Design and Construction

4.1 Abstract

Near Infrared Spectroscopy (NIRS) is a promising technique for non-invasively measuring concentration changes in –oxy and –deoxy haemoglobin. Its role in the clinical setting has yet to be established, however the possibility of using NIRS for long-term recordings is desirable as it can determine whether haemodynamic changes can be seen prior to epileptic activity. Such preictal haemodynamic changes would be beneficial in determining seizure focus for surgical resection, but would require simultaneous EEG recordings. Unfortunately there are obstacles that need to be faced before simultaneous EEG-NIRS is applied in the clinical setting. Long term EEG-NIRS recordings require ease of application, stability over long recordings, reduced motion sensitivity and flexibility of optode arrangement to provide patient specific examinations.

To avoid these obstacles we developed, implemented, and optimised two optode holder designs for use in the Koala Ward at Great Ormond Street Hospital (GOSH) during clinical EEG telemetry. These included one traditional cap design embedded with NIRS optodes and one novel design using a flexible 3D printed grid. Efficacy of design was tested using a series of well-defined motor and numerical reasoning tasks using a 24-channel Hitachi ETG-100 system. Results showed that a flexible optode grid applied via clinical-grade collodion gel provided the most reliable measurements.

After the optimal optode holder was established, the new design was piloted on 14 healthy controls performing a motor task to confirm the holder efficacy in a hospital environment. Results indicate that the flexible optode grid overcomes difficulties found in previous methods and produces valid and reliable results in healthy participants. Therefore, this novel design is ideal for future work in measuring NIRS in the clinical paediatric setting.

4.2 Objectives

The goals of this chapter are to create an optode holder design that is compatible with the long-term recordings of clinical EEG video telemetry of paediatric epilepsy patients. To do so, two optode holder designs were manufactured and tested to determine which was most effective in reducing noise such as hair absorption and movement artefacts during simultaneous EEG-NIRS.

4.3 Introduction

The diagnostic potential of optical imaging functioning in the near infrared (NIR) range has been of interest since its first introduction by Jobsis (1977). The properties of near infrared light allow it to traverse biological tissue and bone to be absorbed by chromophores such as haemoglobin. Haemoglobin has specific absorption spectra dependent on its oxygenation state, making the application of certain wavelengths sensitive to particular chromophores.

Methods such as near infrared spectroscopy (NIRS) take advantage of this phenomenon and provide in-vivo measurements of changes in haemoglobin oxygenation. Studies using NIRS non-invasively have become increasingly popular in both adults and children (see reviews Obrig, 2014 and Gervain et al., 2011). However, hair, skin colour, motion, and fibre stability all have the potential to affect the fidelity of the recordings and consequently need to be taken into consideration (Strangman et al., 2002).

Different optode (optical fibre) application techniques have appeared in an attempt to decrease the influence of these artefacts. For example there are brush optodes threaded through hair (Khan et al., 2012), mechanical mounting structures (Coyle et al., 2007; Giacometti and Diamond, 2013), modified motorcycle helmets, thermoplastic moulds, fibres embedded in rubber, and spring-loaded fibres attached to a semi-rigid form (Strangman et al., 2002). However, many of these require advanced preparation or are inappropriate for the clinical setting.

Though there are many options to choose from, traditionally NIRS preparation is performed using a flexible fabric cap with embedded optodes allowing for a quick

application process and variability in head size. However, optode-skin contact is required for accurate measurements, which can be difficult using the cap design due to attenuation of light by hair (Lloyd-Fox et al., 2010). To avoid this issue spring-loaded optodes can be used, but are impractical for long-term recordings as they can cause subject discomfort and participation dropout (Lloyd-Fox et al., 2010; Suzuki et al., 2010; Cui et al., 2011).

An alternative to the spring-loaded optodes would be the more comfortable flat tip (prism based) NIRS optodes placed directly on the scalp. To secure the optodes a gel or adhesive paste must be used. In the past, clinical strength collodion has had great success in reducing motion artefact by 90% and generally increasing SNR during simultaneous EEG-NIRS (Yucel et al., 2014). The collodion-fixed optodes were placed in-between EEG electrodes as part of a concurrent clinical study, thereby recording simultaneous EEG-NIRS. The prism based fibres used for this study are beneficial for their ease of application. However they have potentially unstable structural integrity.

The structural integrity can be compromised by an unreliable connection between the prism and the coupling interface (i.e.: the prism could break away or become loose) leading to erroneous data collection. The alternative would be to bend the optical fibre making it perpendicular to the scalp. Also note, that the paired optode distance is crucial for signal feedback, therefore NIRS grids cannot be placed using proportions such as the 10-20 system frequently used in EEG. The collodion fixed optodes are a novel approach that can be practically used in the clinical setting. However improvements still need to be made in regards to the application and optode fibres used.

Another approach to simultaneous EEG-NIRS recordings is to physically insert the NIRS optode in the EEG electrode (Cooper et al., 2009) or to create a subject specific grid with both EEG and NIRS optodes embedded (Giacometti and Diamond, 2013). Unfortunately both of these techniques are impractical for clinical video telemetry of epilepsy patients that require standard montages of clinical EEG electrodes.

Therefore, the aims of the current study are to create a reliable optode design that is compatible with the recording of EEG video telemetry in our population of paediatric epilepsy patients. This was achieved by designing and manufacturing a subject-specific optode grid that could be placed in-between the clinical EEG electrodes and recorded simultaneously. New optode holders were designed and tested that by splitting into three parts allowing access to the scalp (by hair separation) prior to being secured with collodion allowing for good optical contact and stabilised the optodes to reduce artefact from movement.

4.4 Methods

In the following sections we describe the iterative process of optode holder design and testing. The first optode holder tested was a traditional NIRS cap design with reference to standardised EEG locations, and the second being a novel design with a flexible optode grid made specifically for paediatric epilepsy patients. The efficacy of each was tested through a series of well-defined motor, numerical reasoning, and blood occlusion tasks (see Figure 4.1). The methodological processes of each design is summarised in Figure 4.2.

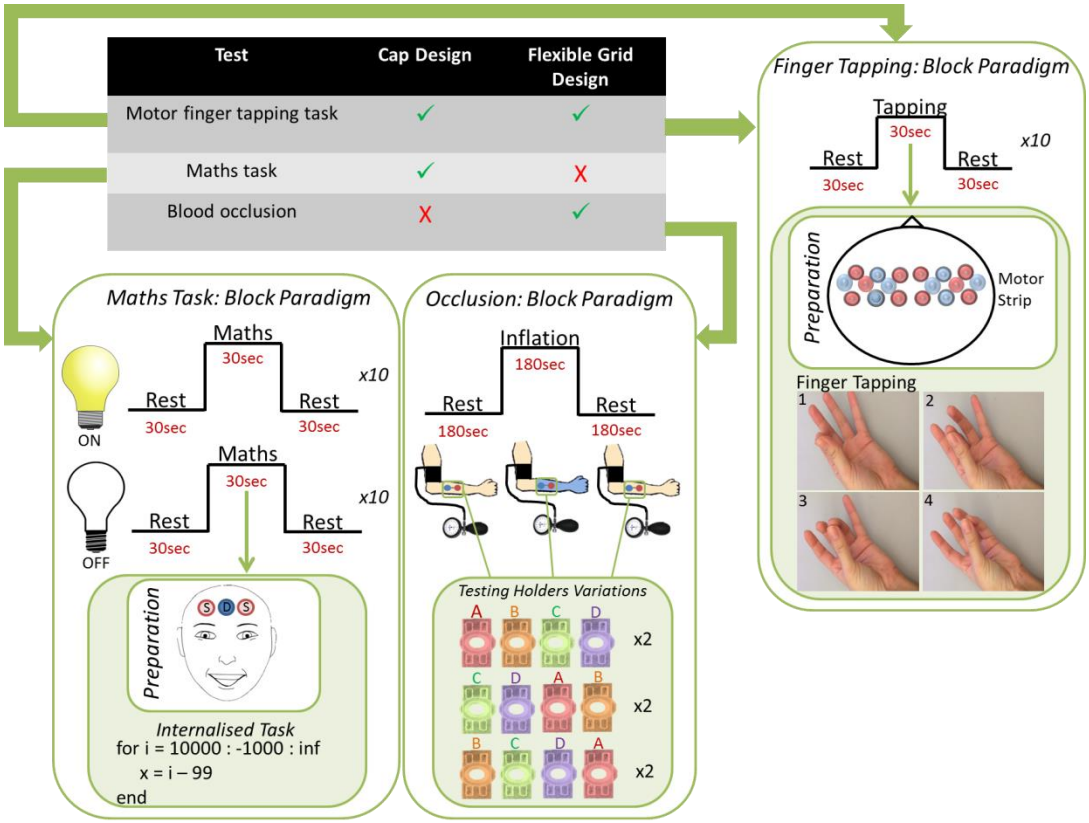

Figure 4.1 Summary of tasks performed to test efficacy of both cap and flexible grid designs

Both cap and flexible grid designs had tests done with a motor finger tapping task (right panel). The maths task was only tested in the cap design (left panel), in order to test the source of signal interference from hair and external light. The occlusion task was only tested in the flexible grid design (middle panel), which was done to determine the optimal holder dimensions for the flexible grid design.

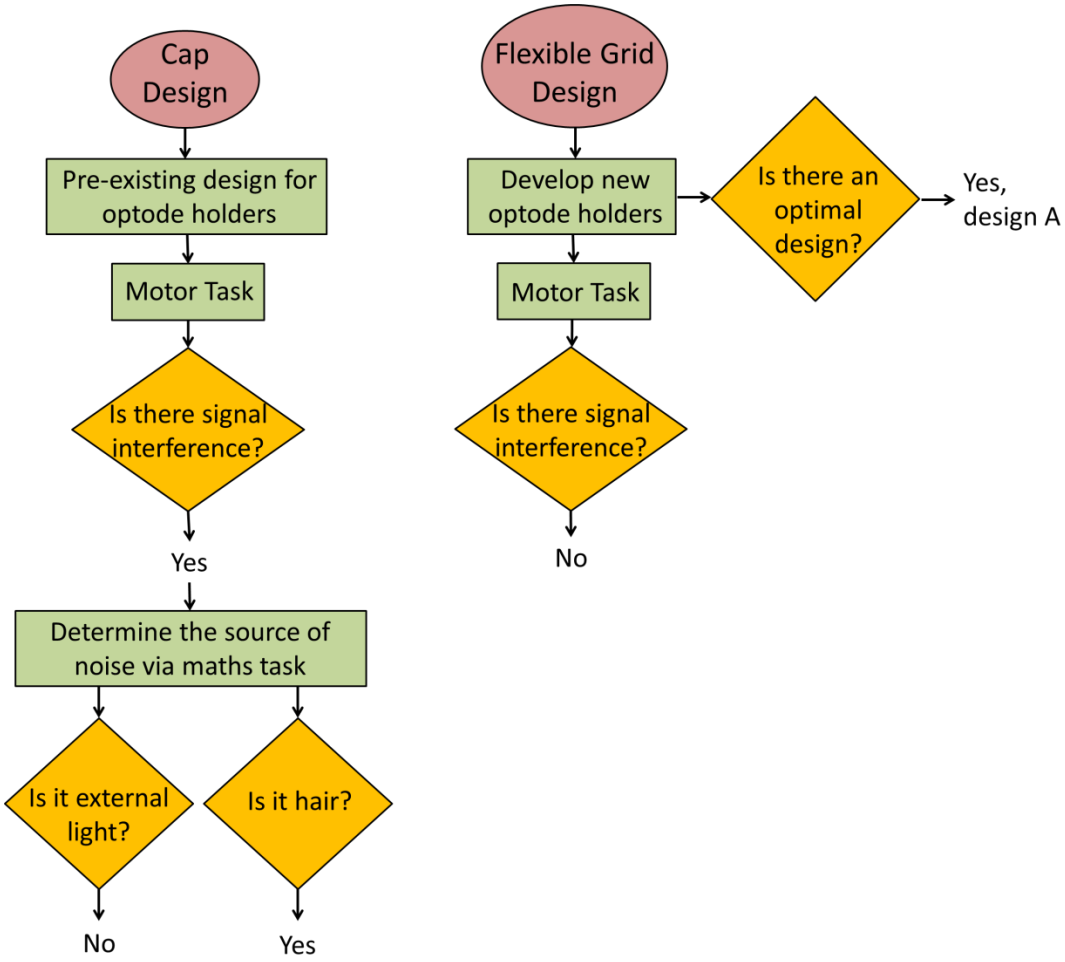

Figure 4.2 Flowchart of methodological steps taken for the cap and flexible grid designs

The left panel indicates the methodological steps taken to test the cap design. The pre-existing design was used for the motor task however there was signal interference from the hair as indicated by the results in the maths task which tested interference from both external light (from the room) and hair. The right panel indicates the methodological steps for the flexible grid design, in which new optode holder designs were created. Variations on the holders were tested, and the optimal design was determined to be holder A. The motor task was subsequently tested and

results were not contaminated by signal interference, thereby proving to be the superior design.

4.4.1 Data Acquisition

4.4.1.1 EEG Recordings for Both Cap and Flexible Grid Designs

EEG preparation was identical for both cap and flexible grid design testing. EEG placements were based on the international 10-20 system, simulating standard clinical procedure in the Koala Ward at Great Ormond Street Hospital (GOSH) (see Figure 4.3). EEG activity was recorded during both 'eyes open' and 'eyes closed' resting conditions, to confirm signal detection via visual inspection of alpha rhythms. When simultaneous EEG-NIRS was performed, the EEG electrodes were applied prior to NIRS optodes to reduce potential disturbance to the clinical routine.

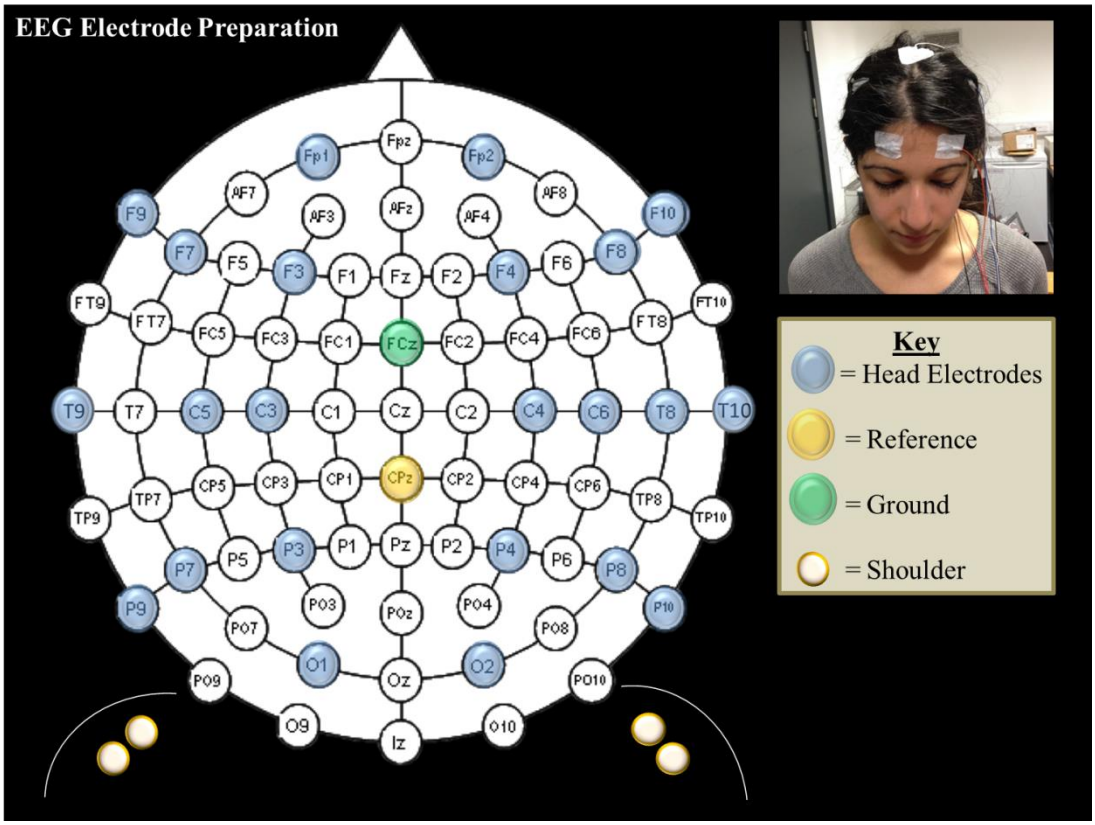

Figure 4.3 EEG electrode placement used for simultaneous EEG-NIRS
GOSH standard telemetry EEG placement. There are 33 electrodes which include 29 on the head and 4 on the shoulders (recording EMG and ECG). The reference electrode is highlighted in yellow, the ground electrode is highlighted in green, and the shoulder electrodes are highlighted in orange. The remaining head electrodes

are shaded in blue. The clinical single (discrete) EEG electrodes placed underneath NIRS cap as seen in the far right picture.

4.4.1.2 Cap Design Pilot on Healthy Adults

A pilot study using a NIRS cap design was applied on healthy controls from ages 22-37. Four controls (2 male, 2 female) were tested with NIRS exclusively, and 2 (1 male, 1 female) were tested with simultaneous EEG-NIRS (see Figure 4.3-Figure 4.4). The purpose of testing NIRS simultaneously with EEG was to confirm that there was no interference due to NIRS on the clinical EEG (and vice versa) and to test the efficacy of the cap design.

Neither mechanical nor signal interference was expected from simultaneous EEG-NIRS however interference checks were performed to demonstrate to the clinical staff that the clinical investigation would not be affected. Interference was determined through real time visual inspection from an expert neurophysiologist (Charlotte Wilkinson) and biomedical engineer (Ilias Tachtsidis) in EEG and NIRS respectively. Furthermore, a synchronisation test was performed to confirm that both EEG and NIRS were time locked. A time locked signal was generated with a button press on both EEG and NIRS systems. The efficacy of the synchronisation technique was confirmed by clinical scientist, Alan Worley.

4.4.1.2.1 NIRS Measurements during a Motor Task

The NIRS cap design used embedded optodes with reference to EEG electrode locations (see Figure 4.4). This design has been used in previous studies to ensure standardized optode placement relative to EEG mainly in infants and adults (Lloyd-Fox et al., 2014; Pinti et al., 2015). The cap optode holder buttons two parts together using one embossed and one extruding square, which then grip the optode. This holder slides into the cap using a circular foot base (see Figure 4.5). Data was collected using a Hitachi ETG-100 Optical Topography System (Hitachi Medical Co., Japan), with wavelengths at 780 and 830nm and 24 channels. A 3x3 grid was placed over the motor cortex on both hemispheres. Each optode array consisted of 5 source optodes and 4 detector optodes.

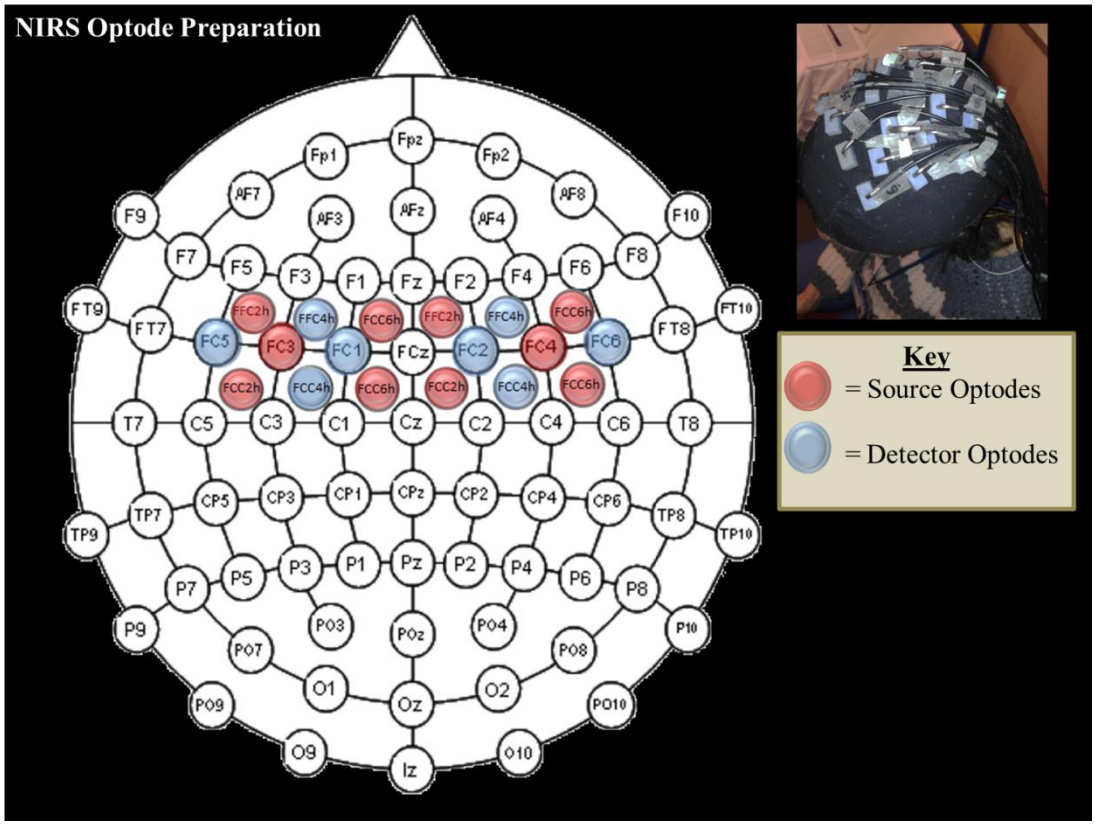

Figure 4.4 NIRS optode placement for motor task in simultaneous EEG-NIRS
The NIRS optodes were placed with reference to standardized EEG electrode locations. The bilateral 3x3 grid was placed over the motor cortex using 5 source electrodes (in red) and 4 detector optodes (in blue). The NIRS cap was placed on top of EEG electrodes as seen in the far right picture.

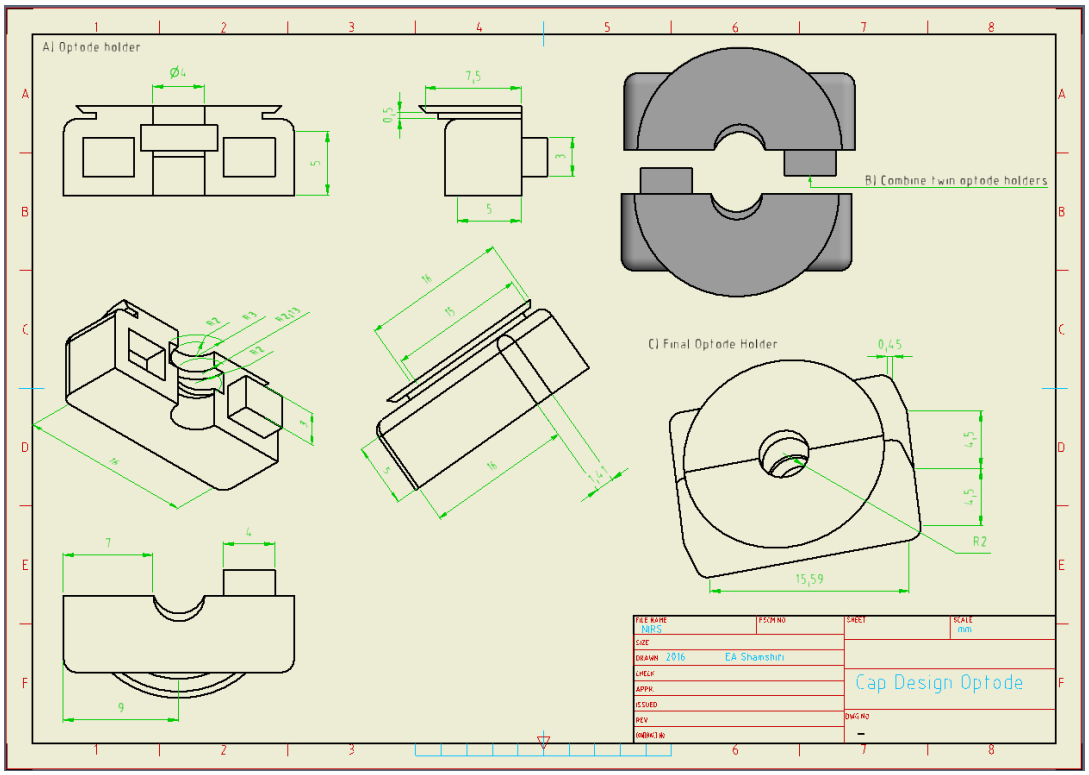

Figure 4.5 CAD drawing of optode holder used in cap design

CAD design of cap-embedded optode holders. The optode holder (A) is joined together with its twin (B) forming a finalised optode holder with an extruding ring (C) which is embedded in the EEG cap.

As in the EEG recordings, NIRS recordings tested blocks of 'eyes open' and 'eyes closed' resting conditions to confirm signal detection and baseline noise level (see Figure 4.6). Subsequently subjects were asked to perform a bilateral motor task in which they would tap their fingers to their thumb in serial order (fore finger, middle finger, ring finger, little finger, ring finger, middle finger fore finger, etc.). Subjects were seated in a comfortable chair with palms facing upwards. They were instructed to look ahead blankly and avoid making any movements other than those needed for the task. The tapping order was kept consistent and lasted for 30seconds followed by 30seconds of rest. This paradigm was repeated 10 times to ensure the validity of the response. Subjects were asked to keep at a steady pace from which they would not grow tired. Finally subjects were asked to perform three different types of movement to mimic possible motion artefact (heading nodding and natural movement) to determine the effect of movement on the signal. The finger-tapping task was done to confirm the sensitivity of the optical signal to changes in neuronal activity.

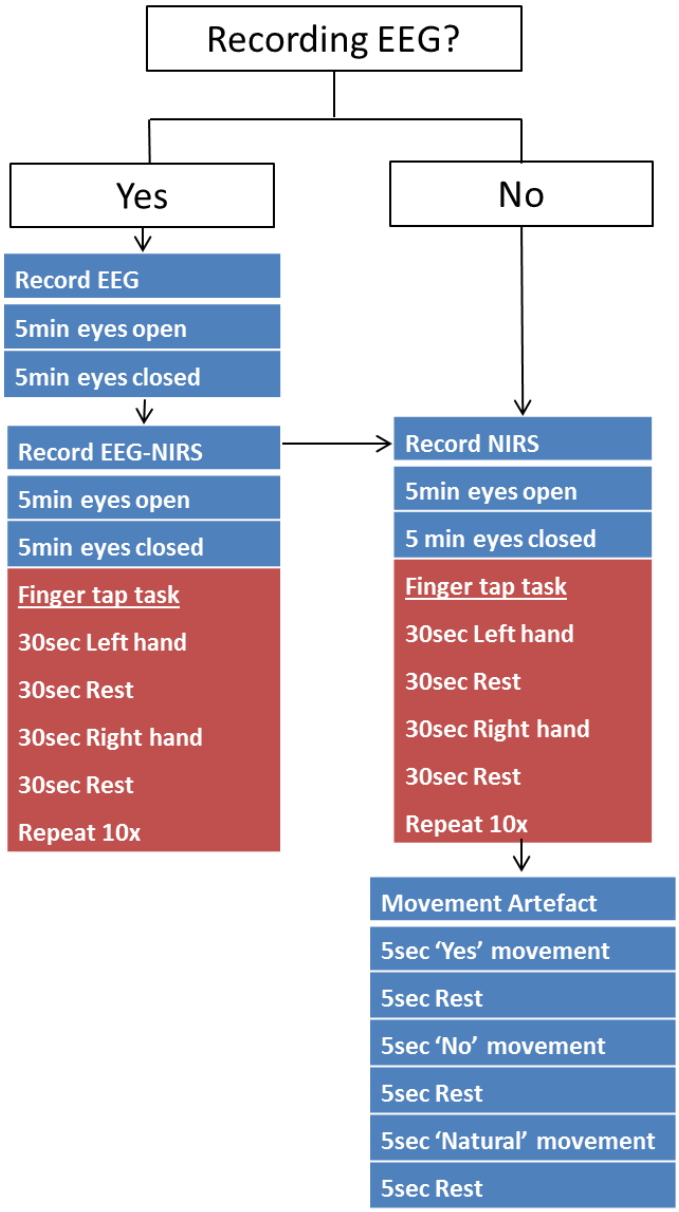

Figure 4.6 Recording conditions for the pilot NIRS cap design
Left panel illustrates the recording paradigm for the NIRS cap design when EEG is recorded. This includes lone EEG recordings followed by simultaneous EEG-NIRS recordings which include an eye opening paradigm and a finger tap task. The right panel illustrates the recording paradigm when only NIRS is recorded. This includes an eye opening task, a finger tap task, as well as a test for motion artefact.

4.4.1.2.2 Determining the Source of Noise

Results on the cap design showed signs of noise corruption in the data. To confirm the source of the artefact a separate analysis was done on the forehead of a participant (female, age 24), removing the likelihood of signal attenuation from the light absorption of hair. Additionally, the possible interference from an external light

source was verified. The paradigm involved 30seconds of rest and 30seconds of task interleaved with 10 repetitions. This was repeated with the room lights turned off to control for interference from external light sources. The task was an internally vocalized subtraction maths test, requiring the subject to subtract 99 from a starting point of 10,000. For each subsequent task block, the subject was to start at a number 1,000 less than the previous. Data was collected with 2 source optodes and 1 detector optode on the forehead of the participant. Optode holders described in Figure 4.5 were secured via self-adhesive paper tape.

4.4.1.3 Flexible Optode Design Pilot on Healthy Adult Controls

4.4.1.3.1 Development of Optode Holders for the Flexible Optode Design

The second optode holder tested was a novel design using a flexible optode grid applied via clinical-grade collodion gel. This design was created specifically for the current study, and therefore was aimed at testing paediatric epilepsy patients. Four variations of the optode holders in the flexible grid design were created using 3D printing. The efficacy of each variation was systematically tested with an occlusion task.

The occlusion task was used because it is well-established in NIRS (Cope and Delpy 1988; Cross and Sabapathy, 2015) and its changes are easily observable in real-time recordings, contrary to cognitive tasks whose haemodynamic changes occur on a much smaller level and are difficult to observe in real-time without online filtering. Therefore, any subtle differences between optode designs should be apparent in the occlusion task. Additionally, recordings were done on the forearm of the participant to evade noise associated with hair absorption as seen in the cap design (see Figure 4.7).

This alternative optode holder separates into three parts: two of which grip onto the optode as done in the original optode holder, and another which remains fixated on the head allowing for hair separation as done in EEG preparation (see Figure 4.8). The optode part fixed on the scalp is done so via collodion gel avoiding the use of the cap as an intermediary. One source and one detector optode was separated by a 30mm connector made from 100micron transparency film.

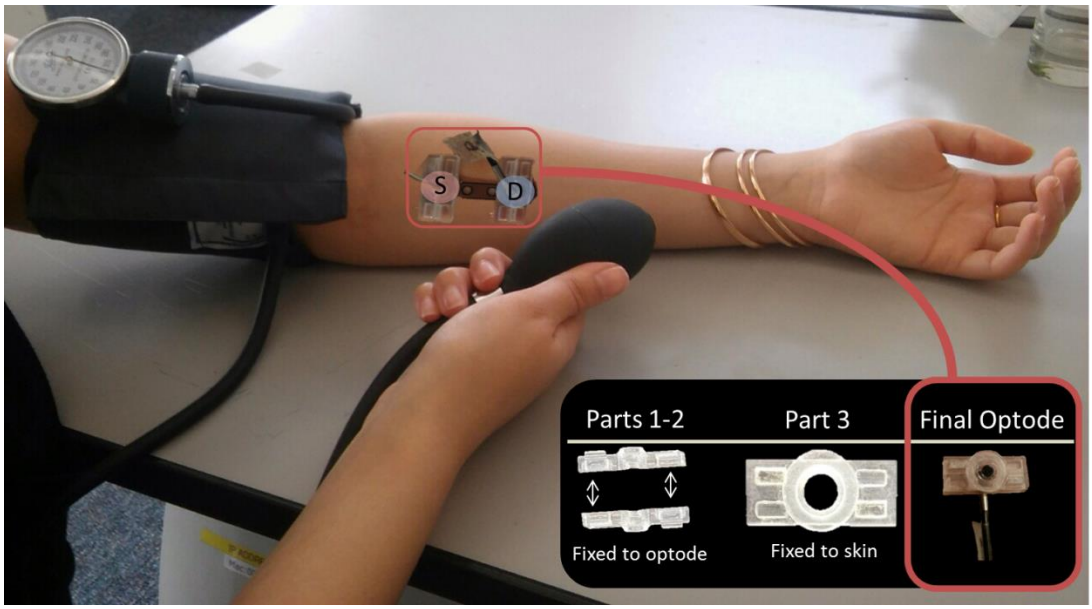

Figure 4.7 Testing variations of the flexible grid design
This figure illustrates testing the efficacy of variations of optode holders using the flexible grid design. The sphygmomanometer was used for blood vessel occlusion of the forearm measuring changes in –oxy and –deoxy haemoglobin concentrations. A NIRS source-detector pairing (circled in red and blue respectively) was connected with a flexible 3cm grid. The optode holder consisted of three parts: 1-2 were twin parts which were fixed onto the optode, and part 3 was fixed onto the skin using collodion gel. The combined parts 1 and 2 were subsequently buttoned to part 3, securely placing the laser onto the skin.

The task paradigm testing each optode holder design was separated into blocks of rest (180sec) and sphygmomanometer inflation to 160mmHg (180sec) and finally returning to rest (180sec). Variations of the optode holders A-D (see Table 4.1) were tested at two time points within the same session to confirm reproducibility. After the initial pilot test, the order in which optode holders were tested was randomised. The only constraint applied to the randomisation was that holders could not be tested in the same order position from previous pilot tests. The randomised order of optodes tested can be seen in Table 4.2.

Table 4.1 Testing optode holders: Holder dimensions

	Holder A	Holder B	Holder C	Holder D
Button Extrusion	1.5mm	1.5mm	2mm	2mm
Ring Extrusion	0.5mm	0.25mm	0.25mm	0.5mm

Variations of optode holders A-D were defined by the length of button extrusion and the ring extrusion from the base.

Table 4.2 Testing optode holders: Iterations

Pilot #1		Pilot #2		Pilot #3	
TP #1	TP #2	TP #1	TP #2	TP #1	TP #2
A	A	C	C	B	B
B	B	D	D	C	C
C	C	A	A	D	D
D	D	B	B	A	A

Variations of the optode holders A-D were tested for efficiency during a blood occlusion task. After pilot 1 the order of holders tested was randomized with a constraint on ordering of prior positions. Each holder was tested twice at two time points to confirm reproducibility of results. TP = time point.

Once the optimal optode holder was decided upon, a flexible grid using these optodes was tested on 14 healthy adult controls between the ages of 25-37. Of these participants 6 had simultaneous EEG-NIRS, and 6 had bilateral 3x3 optode grids (see Figure 4.9). The majority of controls had a unilateral right sided 3x3 optode grid placement, thereby only testing a left finger-tapping task. And again (as done in the cap design) interference between NIRS and EEG was checked via real time visual inspection.

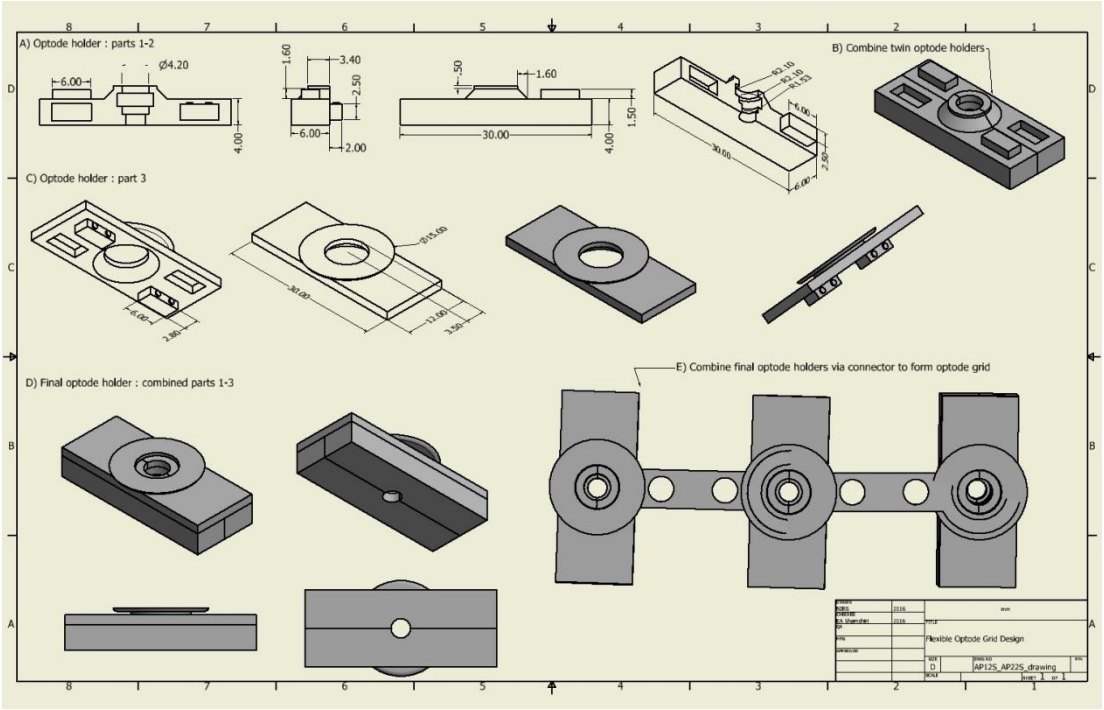

Figure 4.8 CAD drawing of optode holder used in flexible grid design

The final optode holder used in the flexible grid. Directions for assembly should be read from left to right, top to bottom. This design is composed of three parts. Parts 1-2 are twin pieces meant to hold the optode stable. Part 3 is placed on the scalp via collodion gel meant to allow for the clearing of hair within the circular rim. Firstly, parts 1-2 are attached together with the laser shining through the circular opening. Subsequently parts 1-2 are buttoned onto part 3, which remains stationary on the scalp after hair preparation, thus completing the optode holder design. Finally, connectors separating the optode holders at exactly 30mm will slide into the circular ring, attaching all optodes together thereby forming a grid of variable size.

Unilateral recordings were originally acquired to confirm the efficacy of the flexible optode grid design on the scalp. Once this was confirmed, bilateral recordings were done to practice NIRS application, as reduced application time is ideal for the clinical environment. In addition, the goal of testing NIRS simultaneously with EEG was to confirm that there was no equipment interference, though previous work indicated that inference between NIRS and EEG was unlikely. Therefore, it was not necessary for the purpose of this pilot to test all subjects with bilateral simultaneous recordings.

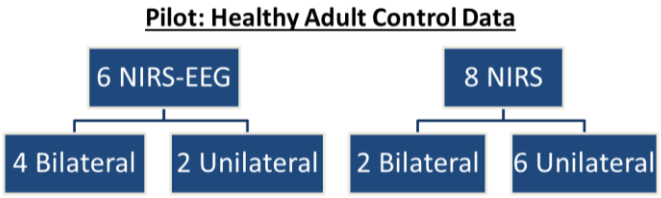

Figure 4.9 Recording paradigm for healthy adult controls in pilot data
Bilateral recordings included 3x3 grids over the motor strips of both left and right hemispheres. Unilateral recordings included 3x3 grids only over the right hemisphere, thereby testing motor movements of the left hand.

4.4.1.3.2 NIRS Measurements during a Motor Task

The grid was placed on the motor strip (see Figure 4.10) surrounding EEG electrodes C3 and C4 (see Figure 4.11), which are known to be sensitive to fine motor activity from tasks such as finger-tapping. An optional headband was offered to participants for comfort to secure wires in place. The finger-tapping paradigm for healthy controls included blocks of 30sec rest followed by 30sec of finger-tapping; this paradigm was repeated 10 times as done in the recording conditions for the cap design (see section 4.4.1.2).

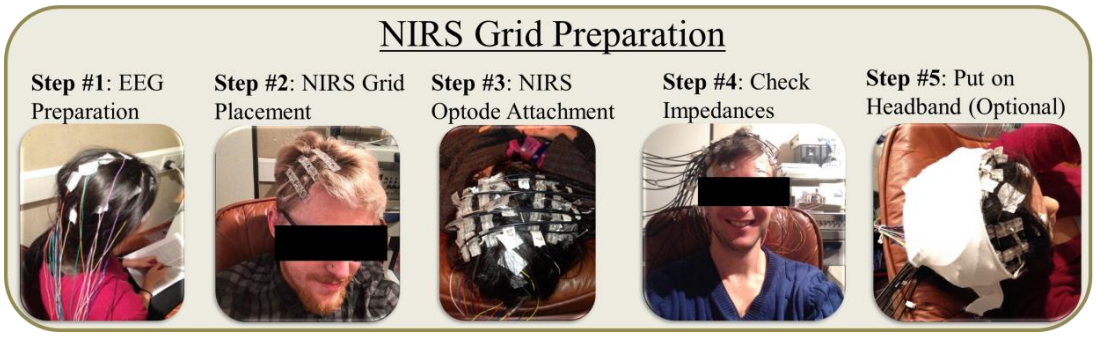

Figure 4.10 Steps for NIRS grid preparation
The first step for NIRS preparation of the novel flexible grid design is to prepare the EEG with the same GOSH protocol. The second step is to place the NIRS grid on top of the scalp using collodion gel. Hair must be parted for each optode exposing the scalp before applying collodion. The third step involves attaching the laser optode onto the grid. The fourth step is to check the impedance for both NIRS and EEG. Then an optional step 5 is to place a cotton headband on top of the grids. This is done mainly for comfort and to secure the wires. Once this is finished the NIRS preparation is complete.

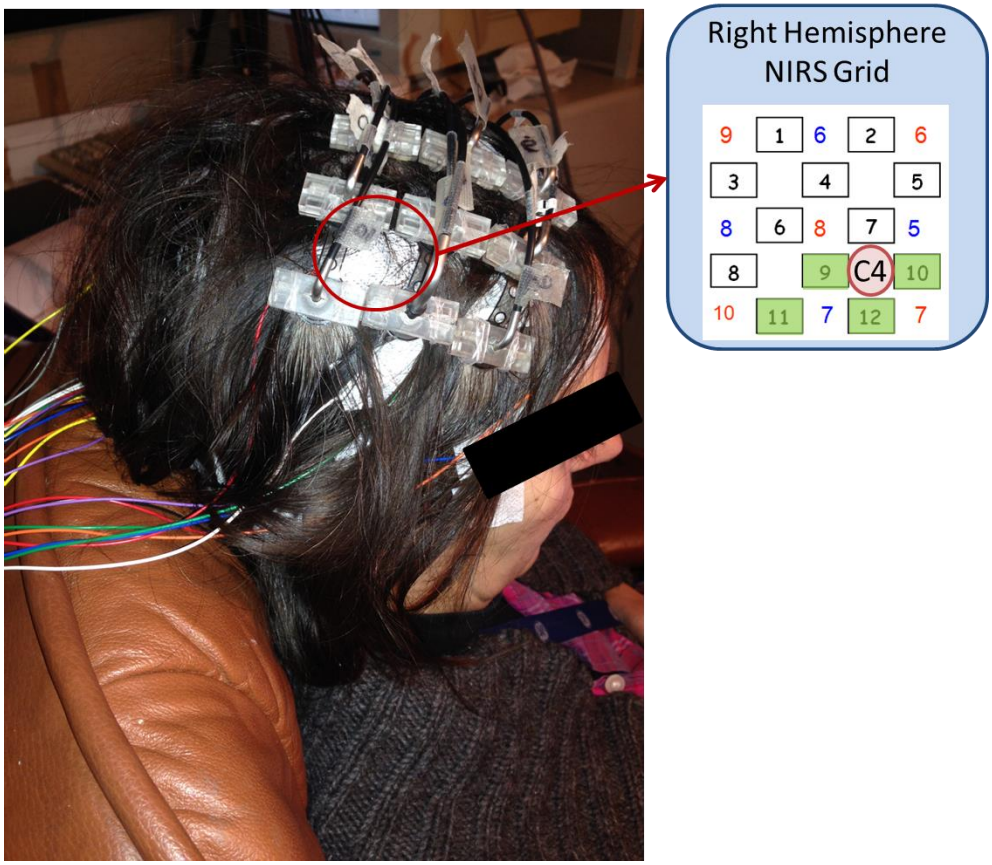

Figure 4.11 Example of NIRS grid placement during motor task
An example of how a NIRS optode grid is placed on the right hemisphere motor strip. The figure to the left shows a real-life example of optode placement, while the figure to the right is an illustration of a NIRS optode grid. Channels are defined by squares, sources are displayed in red, and detectors are displayed in blue. Channels surrounding the motor cortex are highlighted in green. A red circle indicates the position of electrode C4, a marker for the right hemisphere motor strip.

4.4.2 Data Processing

4.4.2.1 Cap Design on Healthy Adults

The pre-processing of NIRS signals will be done in software developed by Hitachi called POTATo (Platform for Optical Topography Analysis Tools) (Tokyo, Japan). All data will go through a standard pre-processing pipeline including 1) conversion of raw concentration values via Modified Beer-Lambert Law (MBLL), 2) baseline fitting which uses the period before and after the task to determine the signal's baseline (also known as detrending), 3) applying a bandpass filter between 0.01Hz and 0.08Hz and 4) blocking conditions. Blocking will only be used in pilot data, as it

is not applicable to seizure activity which is based on non-homogeneous epileptic events.

4.4.2.2 Flexible Optode Design Pilot on Healthy Adult Controls

Pre-processing steps were identical to those used for the cap design (section 4.4.2.1) however additional steps were applied including outlier detection and Hampel filtering. Both steps were done using the FIACH package (Tierney et al., 2016) in R (R Core Team, 2016) following the conversion of raw values. Outlier detection was performed to identify spurious observations replacing them with the median. Hampel filtering was defined with a window width of 10 and a threshold for median absolute deviations of 3.

After first-level pre-processing is completed, statistical analysis of the group data is performed for the right hemisphere as the majority of subjects tested had unilateral recordings (see Figure 4.9). The group average is calculated and a sample t-test is performed on all subjects of the finger-tapping task. Significance is thresholded at $p<0.05$ with family wise error correction.

4.5 Results

4.5.1 Cap Design on Healthy Adults

The cap design has been tested in both NIRS and EEG-NIRS however the signal was dominated by noise. There were two types of noise that appeared: 1) a flatline signal possibly caused by the complete absorption of light and 2) periodic oscillations due to partial absorption of light (see Figure 4.12). These periodic oscillations were beyond the range expected from a physiological response of a finger-tapping task (Sato et al., 2007). Consequently, the data gathered with the cap design did not represent changes in neuronal activity as light was not able to penetrate the cerebrum.

Following visual inspection from an expert neurophysiologist (Charlotte Wilkinson), it was confirmed that there was no interference from NIRS on the EEG data. Additionally, the synchronisation test confirmed that both the EEG and NIRS

equipment could be synchronised within 0.04ms accuracy, which is sufficient for monitoring haemodynamic changes.

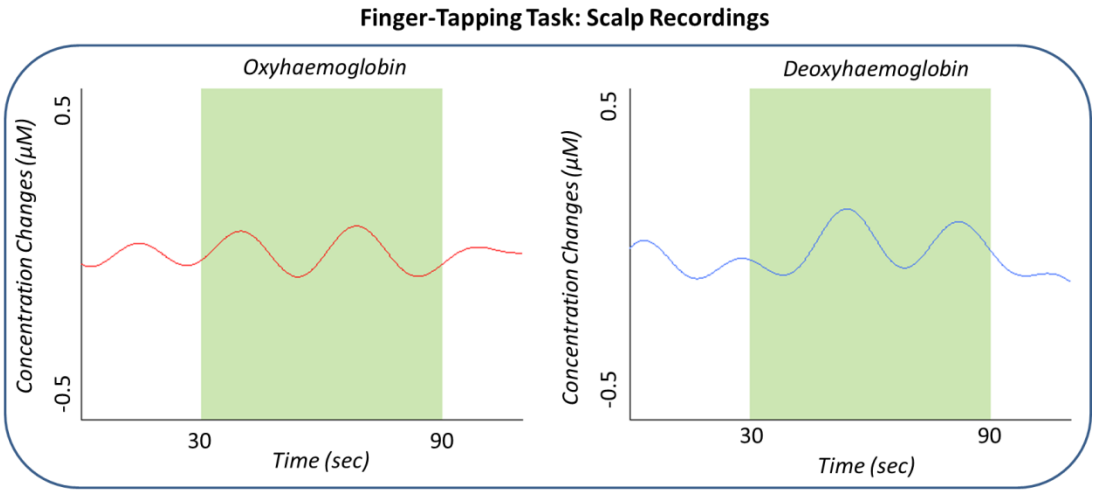

Figure 4.12 Changes in haemoglobin during finger-tapping task using cap design
Concentration changes in –oxy (red) and –deoxy (blue) haemoglobin during a task (green block) for single subject recordings. Haemoglobin changes recorded from the scalp show periodic oscillations that are possibly due to hair absorption in the cap design.

The external absorption of light was thought to originate from the hair. This was confirmed in the maths task acquired on the forehead, an area with little to no hair. Expected increases in oxyhaemoglobin with corresponding decreases in deoxyhaemoglobin were found during the maths task paradigm (see Figure 4.13). We additionally tested the influence of external light, but found that it was not a contributing factor. Results show that placing optodes in an area free from hair absorption allows for signal penetration to the cerebrum.

Though signal was able to penetrate the cerebrum, practical observations found that self-adhesive paper tape was not sufficient to hold the optode for extensive periods of time. Therefore, something with stronger adhesive capabilities must be used for future recordings.

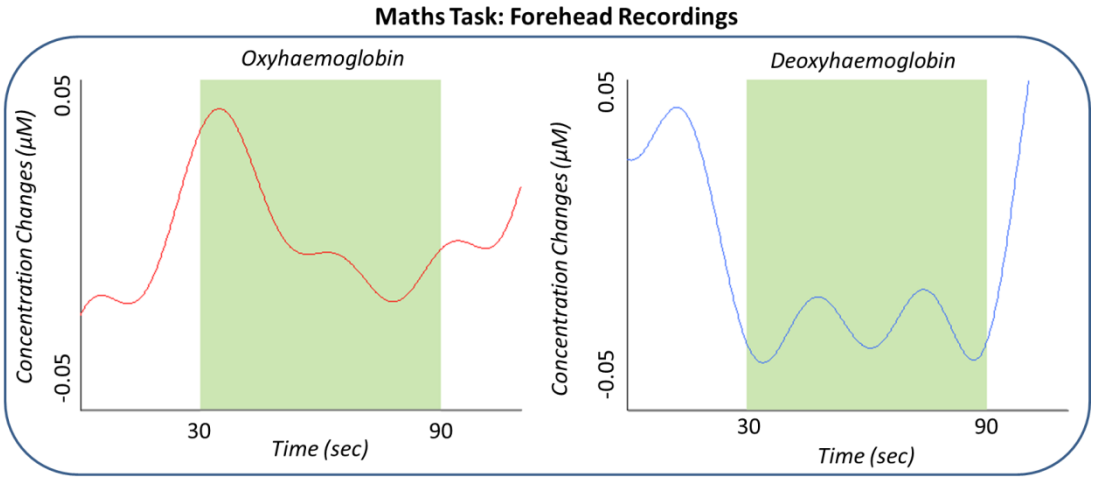

Figure 4.13 Changes in haemoglobin during maths task: forehead recordings
Concentration changes in –oxy (red) and –deoxy (blue) haemoglobin during a maths task (green block) for single subject recordings. Results illustrate haemoglobin changes recorded from the forehead showing an increase in oxyhaemoglobin and decrease in deoxyhaemoglobin during the task period.

4.5.2 Flexible Optode Design Pilot on Healthy Adults

Results for the flexible optode grid design were tested allowing for scalp exposure (to reduce the effects of light absorption from hair) and clinical-grade collodion gel (for securing the NIRS optodes on the scalp) were as expected. The arm occlusion task caused a dramatic decline of oxyhaemoglobin and a corresponding rise in deoxyhaemoglobin within the measured region (see Figure 4.14). There were no significant differences between optode holders, however practical observations found optode holder A to be the optimal design. Holders B and C had a ring extrusion (see Table 4.1) that was too sensitive and prone to breaking. Holder D was structurally robust, but the skin-to-laser contact was less than optode A, making A the optimal choice.

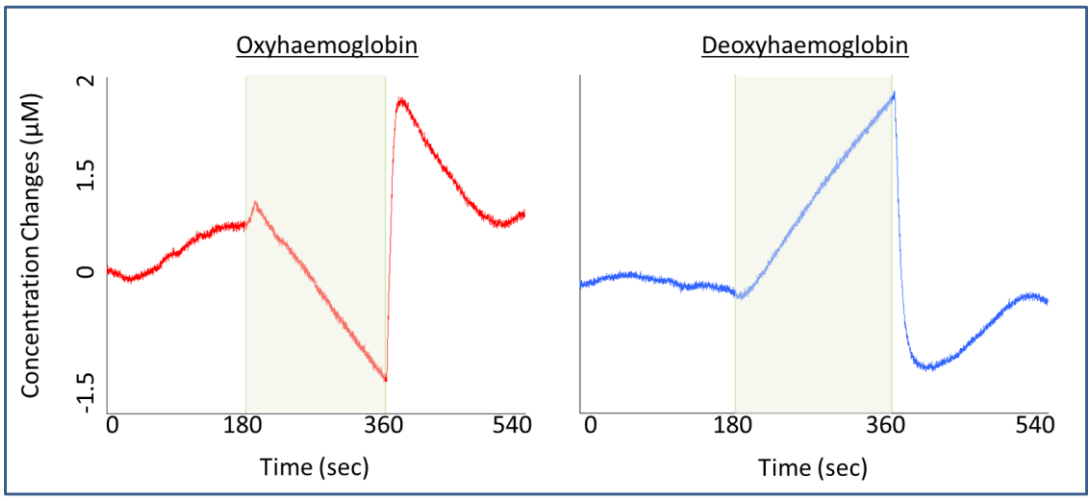

Figure 4.14 Haemoglobin concentration changes during blood occlusion
The NIRS concentration changes for both –oxy and –deoxy haemoglobin during rest (highlighted in white) and sphygmomanometer inflation (highlighted in green). During inflation there was a dramatic decrease in oxyhaemoglobin and an increase in deoxyhaemoglobin.

To test the viability for functional NIRS using flexible optode holder A (which was determined to be the optimal optode holder), a flexible grid using these optodes was tested on healthy adult controls. The group average was calculated, resulting in a general increase in oxyhaemoglobin (see Figure 4.15) and a decrease in deoxyhaemoglobin (see Figure 4.16) during periods of finger-tapping. No interference was seen between the NIRS and EEG.

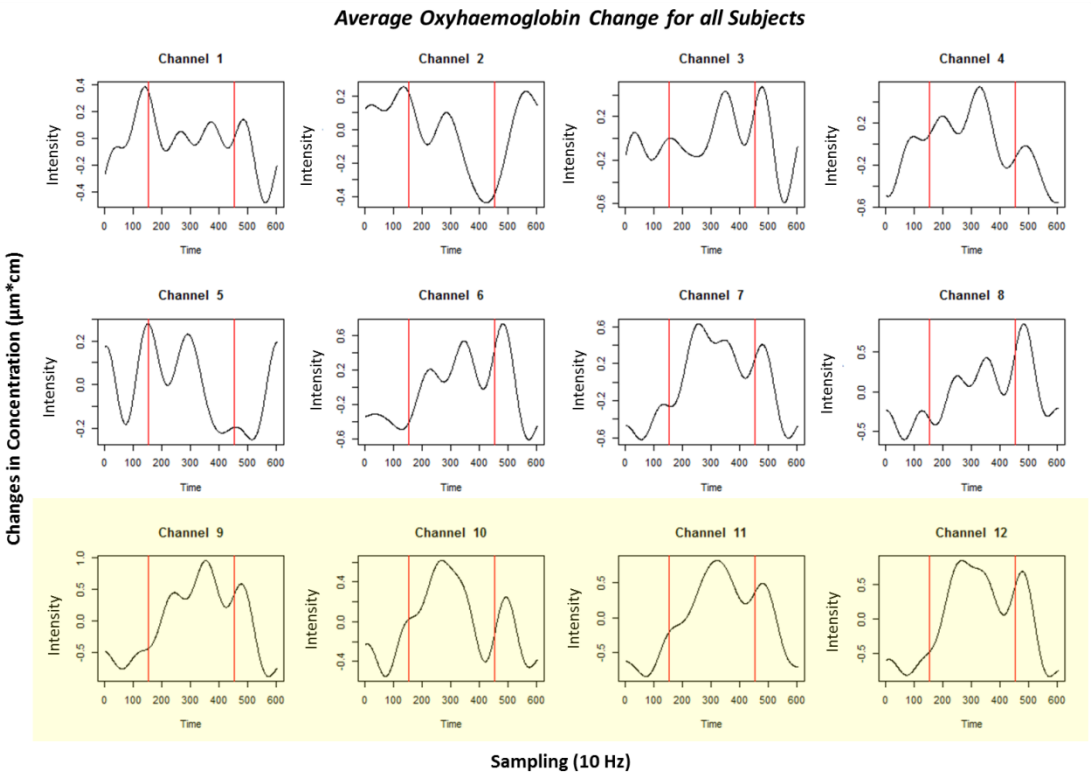

Figure 4.15 Average change in oxyhaemoglobin for all healthy subjects during finger-tapping motor task

The average oxyhaemoglobin change for all subjects is illustrated for twelve channels in the right hemisphere. A windowed period of 150Hz (15seconds) is displayed prior to the start of the finger-tapping task and again at the end of the task. The finger-tapping block is indicated by vertical red lines. Channels highlighted in yellow are those on the motor strip.

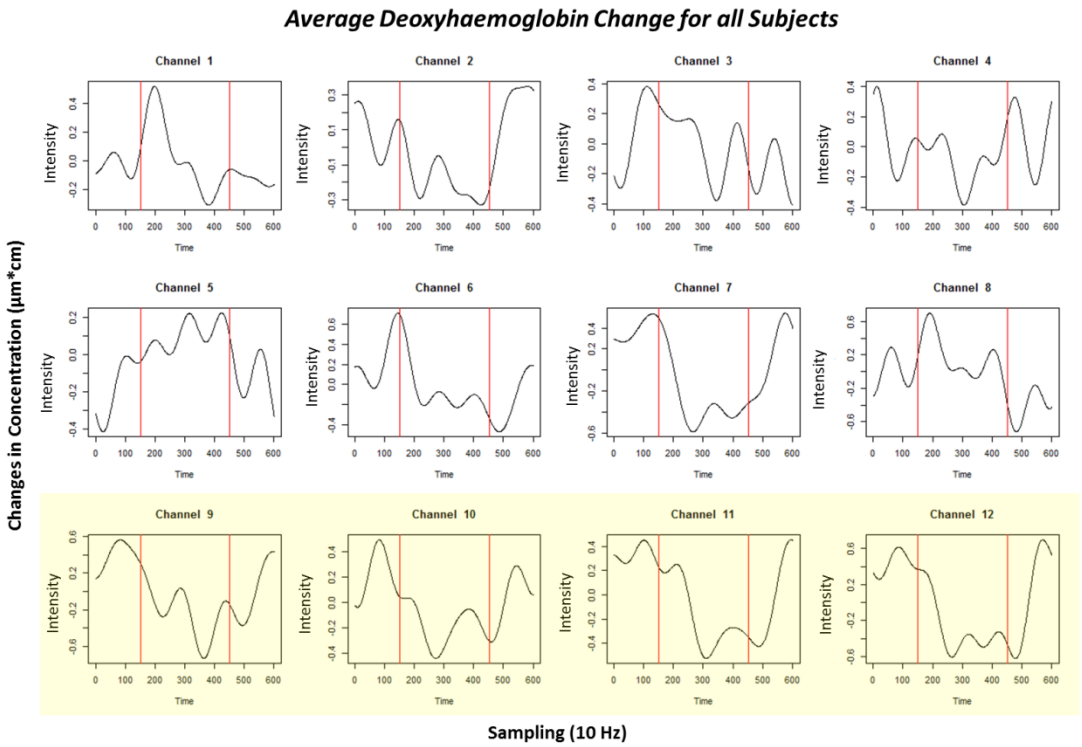

Figure 4.16 Average change in deoxyhaemoglobin for all healthy subjects during finger-tapping motor task

The average deoxyhaemoglobin change for all subjects is illustrated for twelve channels in the right hemisphere. A windowed period of 150Hz (15seconds) is displayed prior to the start of the finger-tapping task and again at the end of the task. The finger-tapping block is indicated by vertical red lines. Channels highlighted in yellow are those on the motor strip.

A sample t-test is performed on all subjects for the finger-tapping task. Changes in oxyhaemoglobin concentration are significant for the peaks in channels 9 and 12; both of which lie on the right hemisphere motor strip (see Figure 4.17). However, no significant changes in oxyhaemoglobin concentration were found in deoxyhaemoglobin (see Figure 4.18).

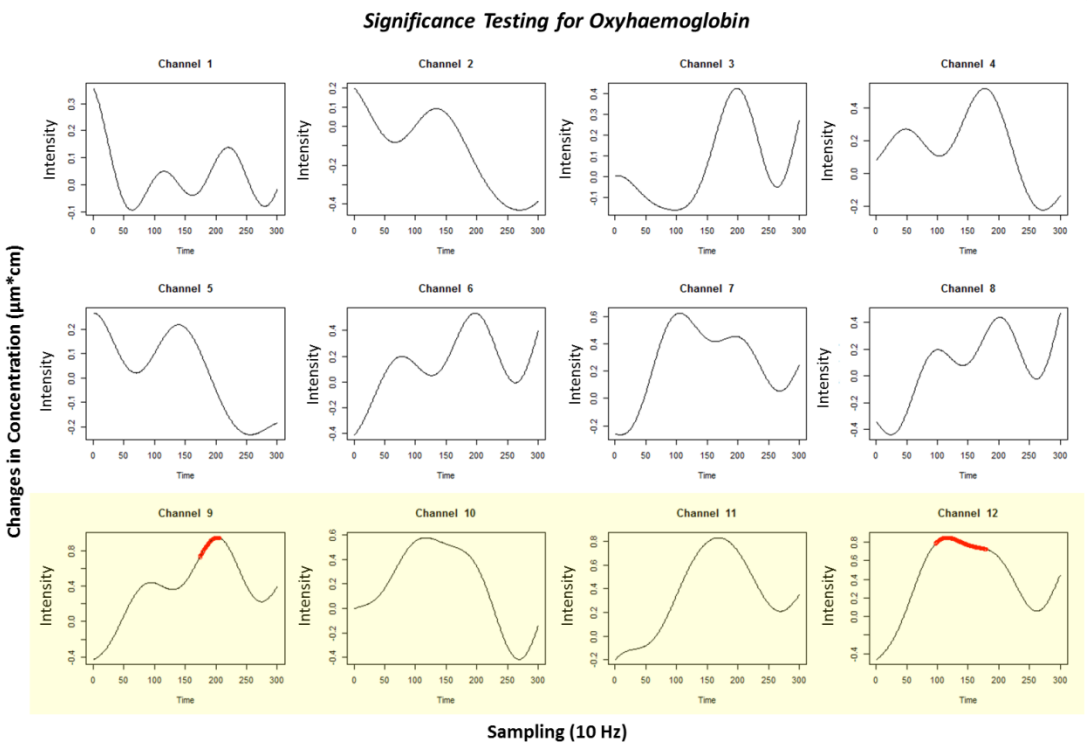

Figure 4.17 Significant differences in oxyhaemoglobin in healthy adults during finger-tapping motor task

Window of the finger-tapping task for channels 1-12 in the right hemisphere. Significant changes are displayed by red dots. Channels highlighted in yellow are those on the motor strip of the right hemisphere.

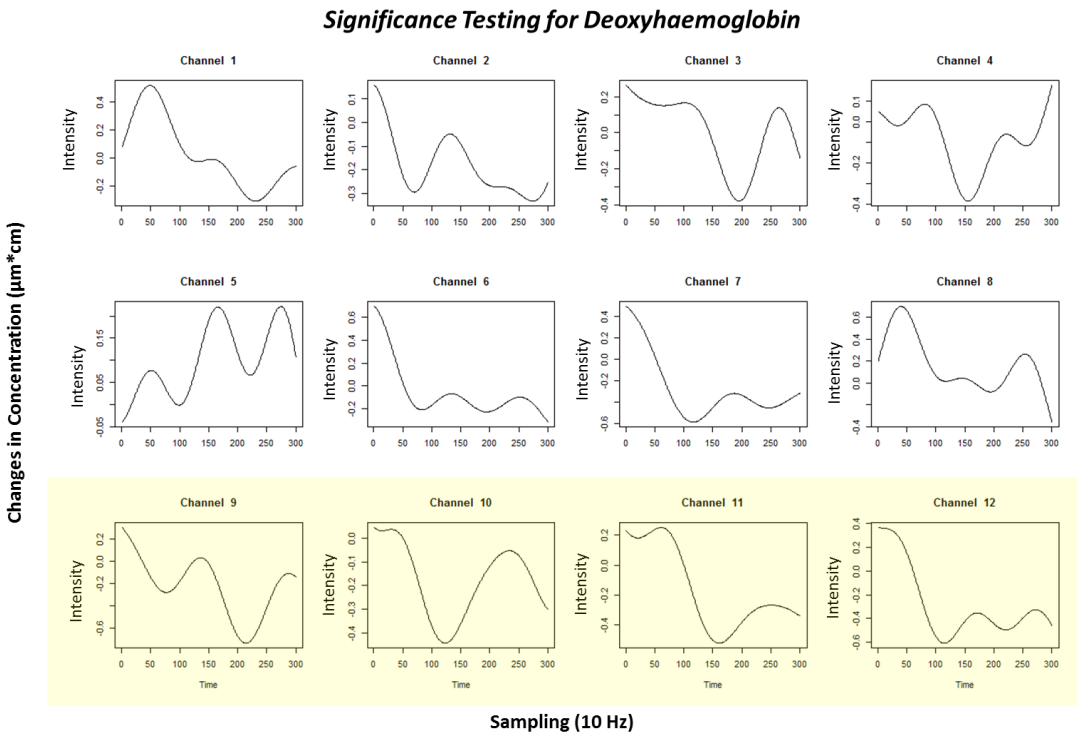

Figure 4.18 Significant differences in oxyhaemoglobin in healthy adults during finger-tapping motor task

Window of the finger-tapping task for channels 1-12 in the right hemisphere. There were no significant changes found. Channels highlighted in yellow are those on the motor strip of the right hemisphere.

4.6 Discussion

Optode holders and fixation systems were designed and tested for application in a clinical paediatric epilepsy setting. Two holder types were tested using well-defined functional tasks. Results show that the cap design causes light piping produced by light attenuation from hair, thereby generating noise (see Figure 4.12). This is a particularly interesting result considering this is currently the most popular form of optode preparation.

The second design involved a flexible optode grid which was applied via clinical grade collodion gel. This proved to be the optimal design, as it was not affected by artefact from hair absorption. This was due to the added step of hair preparation possible with the 3-part optode holder: part 1 allowing for hair separation, parts 2-3 applying the optode on the scalp. Additionally, the collodion application process is known to withstand motion artefacts (Yucel et al., 2014), which is especially problematic for a paediatric population.

Additionally, we were able to meet our objectives of providing an optode holder that 1) requires no interference with the standard clinical protocol while 2) providing subject specific preparation. Additionally we were also able to 4) reduce potential artefacts (such as hair absorption and motion) while 5) providing a NIRS optode preparation with mobile flexibility and comfort.

Due to the requirement of hair separation, NIRS optode preparation can range from 15-45 minutes depending on hair thickness and length. This is a relatively long period of preparation time when compared to clinical EEG preparation, which takes approximately 15minutes with compliant patients (29 channels). In comparison, EEG preparation performed via cap EEG (64 channels; EasyCap) can take approximately 30minutes. Therefore, the NIRS flexible grid design is ideal for children, however

preparation time is still significant when compared to EEG. This could be problematic for young toddlers if they are not entertained during preparation. This should be taken into account during future recordings. A general summary describing the benefits and disadvantages of each technique can be seen in Figure 4.19.

Benefits	Cap Design	Flexible Grid Design
Easy/quick preparation time (5-10min)	✓	X
Good for long term recordings	X	✓
Flexibility around clinical EEG	X	✓

Figure 4.19 Pro/Con list of optode holder designs
The flexible grid design proved to be more beneficial in the clinical environment than the cap design, as it was good for long term recordings and was flexible around the clinical EEG. However, the cap design has a faster preparation time.

In general, the flexible grid design is highly beneficial in the clinical environment when compared to the standard cap design traditionally used in simultaneous EEG-NIRS experiments. Though the cap design allows for quick preparation (between 5-10 minutes) and requires little preparatory training, it is not ideal for long term recordings and does not provide the flexibility necessary for application in the clinical EEG environment. In contrast, the flexible grid design has a longer preparation time (15-45 minutes) but is ideal for long term recording and is highly flexible thereby providing a patient-specific design ideal for the clinical environment.

Chapter 5 EEG-NIRS Recordings in Paediatric Epilepsy Patients during EEG Video-Telemetry

5.1 Abstract

Near Infrared Spectroscopy (NIRS) is a relatively new technique that could allow for the recording of haemodynamic changes related to epileptic activity. Previous work has shown the presence of haemodynamic changes prior to interictal epileptiform discharges (see Chapter 3) however the presence of preictal changes is less well known. The presence of such preictal haemodynamic changes would be beneficial in determining seizure focus for surgical resections in paediatric epilepsy patients.

The system for recording developed in Chapter 4 (flexible optode grids) was used to record focal epilepsy patients with a 24 channel Hitachi ETG-100. Recordings were successful in 10 children demonstrating tolerability and reliability of the NIRS optode system in a wide age range (4-17years) of children with focal onset seizures. The data obtained was analysed by smooth finite impulse response (sFIR) deconvolution of the interictal epileptiform discharges (IEDs) and visual inspection of seizure events. The main results showed a consistent change in HbDiff in all seizure events with a bimodal peak both prior and subsequent to seizure onset.

In conclusion, haemodynamic changes recorded via EEG-NIRS indicated a change prior to electrical activity in multiple event types including IEDs and seizures. Furthermore, the practicality of recording EEG-NIRS in children with epilepsy during clinical video telemetry has been demonstrated.

5.2 Objectives

The goal of the study reported in this chapter is to 1) determine the feasibility of NIRS recordings occurring simultaneously with clinical video-telemetry especially in regards to the tolerance level for paediatric epilepsy patients (4-17years) and 2) to demonstrate preictal haemodynamic events.

5.3 Introduction

Near Infrared Spectroscopy can measure changes in –oxy and –deoxy haemoglobin. Early studies testing NIRS in patients with epilepsy found heterogeneous patterns of oxygenation changes depending on seizure semiology (Villringer et al., 1993; Steinhoff et al., 1996; Adelson et al., 1999; Sokol et al., 2000; Munakata et al., 2004). Many studies found an increase in cerebral blood volume (CBV) accompanying seizure activity (Singh et al., 2014; Yucel et al., 2014; Watanabe et al., 2000; Haginoya et al., 2002) or dramatic concentration changes in deoxyhaemoglobin (deoxyHb) and oxyhaemoglobin (oxyHb) (Wallois et al., 2009; Slone et al., 2012; Rizki et al. 2015). Unfortunately, there is no consensus on the relationship between seizure activity and deoxyHb, as some studies report a dramatic increase in oxyHb (Rizki et al., 2015; Villringer et al., 1993) while others report a hypoxic event during the seizure (Peng et al., 2016). Furthermore, it should be noted that age-related CBF changes can also occur (Hales et al., 2014), and as many of these studies have been performed in adults, the changes in haemodynamics reported may not be applicable to the paediatric setting. Furthermore, many NIRS studies performed in children are grouped with adults (Watanabe et al., 2000; Watanabe et al., 2002; Nguyen et al., 2012; Peng et al., 2016b) making it difficult to interpret the effect of age on the haemodynamic response. Factors influencing the variability of results surrounding epileptic events could be due to the heterogeneity of epileptic syndromes, age, or the stability of the recordings measured.

One major limitation in some older studies is the small number of channels observed, which usually consisted of only one channel placed on the forehead to avoid hair contamination (Seyel et al., 2014; Villringer et al. 1993; Steinhoff et al. 1996; Sokol et al. 2000; Haginoya et al., 2002; Roche-Labarbe et al., 2008). For example, preictal changes in haemoglobin concentrations have been observed over the frontal lobe, but unfortunately it is difficult to interpret these changes considering the temporal lobe focus was remote from the area of measurement (Slone et al., 2012; Seyal et al., 2014). In recent years multi-channel human NIRS systems have been developed with 8-58 channels (Watanabe et al. 2000; Cooper et al., 2011; Singh et al., 2014). This has made it possible to cover much more of the cortex to try and use NIRS for imaging (Gervain et al., 2011).

With this increase in spatial coverage, NIRS has provided reports on the detection of seizure foci (Watanabe et al., 2000; Watanabe et al., 2002). This is an area of potential clinical benefit and suggests that NIRS could play a role in the evaluation of children for epilepsy surgery. NIRS is attractive in this context because it is minimally invasive and relatively portable when compared to other neuroimaging techniques such as SPECT, PET, or fMRI.

Very few studies have looked at paediatric epilepsy patients using NIRS, especially in the age range from toddlers to teenagers despite this being a clinically important age group for epilepsy. This is partially due to the difficulty of studying younger children, as they typically get bored and restless during long experimental paradigms leading to motion artefacts and limited tolerance compared to babies (who have little hair and tend to remain still, especially those in critical care) and adults where there is increased likelihood of tolerance. There are three studies measuring high-density NIRS in focal epilepsy patients, two of which included only one child (Watanabe et al., 2000; Sato et al., 2013). The third study was a seminal paper by Watanabe et al. (2002), which included 29 patients with focal epilepsy unfortunately these patients had their seizures induced by bemegride. This approach is not used in the UK due to ethical concerns, and the effect of bemegride on seizure activity is not well understood. Therefore it is difficult to determine if the haemodynamic changes reported during seizures are influenced by the direct effects of the medication. The only other cases of non-induced seizure were case studies (Gallagher et al., 2008; Sato et al., 2013).

In the following chapter, EEG-NIRS was used in patients between the ages of 4-17 years to explore its tolerability during clinical video-telemetry and to explore the neurovascular coupling between haemoglobin concentration changes and seizures. This is the first group study to use high-density NIRS recordings (up to 24 channels) to measure spontaneous focal epileptic seizures within this age group.

5.4 Methods

5.4.1 Patients

Ten patients, age range 4-17 years, were recruited from the Koala Ward of Great Ormond Street Hospital (GOSH), London, UK. Simultaneous EEG-NIRS was performed during the clinical video telemetry examinations. Inclusion criteria included a strong spatial hypothesis regarding the seizure onset zone (SOZ) based on current/previous clinical EEG recordings, tolerance of EEG preparation, and frequent epileptic activity. Patients with deep/subcortical foci were excluded as were patients with dense (and dark) hair due to previously reported issues in hair absorption (Orihuela-Espina et al., 2010; Wallois et al., 2010). Patients were tested in blocks of 45 minutes (with a maximum 4 blocks) in order to capture seizure activity. The number of blocks obtained was primarily based on the patient's tolerance and comfort in conjunction with their families, and the clinical team. Twenty four channel recordings were recorded in eight patients, and 12 channel recordings made ipsilateral to the SOZ in a further two patients. Unilateral recordings were made to reduce preparation time in patients who were not able to tolerate the bilateral hemisphere preparation. This study has been approved by the UK national research ethics committee. All participants/families provided informed consent and assent as appropriate and were free to stop the study at any time.

5.4.2 Data Acquisition:

5.4.2.1 EEG

Methodologies for acquiring simultaneous EEG-NIRS have been detailed previously in Chapter 4. Briefly, EEG placements were based on the standard clinical procedure at GOSH using the international 10-20 system. However, one patient (Patient 3) had extra fronto-polar electrodes for clinical purposes. The EEG electrodes were standard clinical Ag-AgCl cup electrodes (Ambu Ltd, Denmark). Recordings were bandpass filtered at 0.1Hz-400Hz with 16-bit digitalization (0.5μV) and sampling rate of 1024Hz. The EEG electrodes were applied prior to NIRS optodes to reduce disturbance to the clinical routine. Synchronised video telemetry was recorded for monitoring of concurrent behavioural changes.

5.4.2.2 NIRS

A flexible grid (see Chapter 4 for details) was applied via collodion gel to avoid artefact from hair absorption and movement. The inter-optode distance was kept consistently at 3cm. In all patients a grid was applied over the scalp proximal to the assumed epileptic focus. Grid size varied based on patient semiology; larger foci were given either 4x4 grids (8 sources, 8 detectors) or 3x5 grids (8 sources, 7 detectors), while smaller foci were given two 3x3 grids (10 sources, 8 detectors) that were placed bilaterally. NIRS measurements were acquired with the Hitachi ETG-100 (Hitachi Medical Ltd, Tokyo, Japan) operating at 780nm and 830nm with a sampling rate of 10Hz.

5.4.3 Data Analysis

5.4.3.1 NIRS Pre-processing

The raw values gathered from the NIRS system calculated relative changes in concentration from an arbitrary baseline set at the beginning of each recording period. The pre-processing of NIRS signals includes conversion of raw concentration values via Modified Beer-Lambert Law (MBLL) and baseline fitting which uses the period before and after the task to determine the signal's baseline (also known as detrending). Outlier detection and Hampel filtering were performed using the FIACH package (Tierney et al., 2016) in R (R Core Team, 2016). Outlier detection was performed to identify spurious observations replacing them with the median. Hampel filtering was defined with a window width of 10 and a threshold for median absolute deviations of 3. A bandpass filter between 0.008Hz and 0.2Hz was then applied to eliminate unwanted effects such as respiration (0.25Hz) and heart beat (1Hz).

5.4.3.2 EEG Marking

Interictal epileptiform activity was identified and manually marked on the EEG by clinical physiologists at the Koala Ward Telemetry Unit of Great Ormond Street Hospital (GOSH) which included Kelly St Pier, Charlotte Wilkinson, Emma Dean, Rui Silva, or Arjel Lejarde. In addition, a clinical neurophysiologist, Rachel Thornton, also assisted in the marking of several EEG cases (in particular those with seizures). The EEG traces were reviewed in both bipolar and average montages for the accurate identification of IEDs.

5.4.3.3 Seizure Analysis

Epochs corresponding to a window of 40 seconds (20 seconds prior to the event, and 20 seconds after the event) were visually inspected in both NIRS and EEG traces. This relatively small timescale was also chosen to make visual inspection possible between EEG and NIRS recordings, as EEG occurs at a much higher sampling frequency (1024Hz) compared to NIRS (10Hz). However, a larger window was used when viewing NIRS data independently; in this case, window size was up to 5 minutes (prior/after event onset) was applied as previous haemodynamic changes have been reported within this range in adults (Ronne-Engström et al., 1993; Seyal et al., 2012). Concentration changes in oxyHb, deoxyHb, total haemoglobin (HbT), and haemoglobin difference (HbDiff) were displayed for in channels closest to the focus. In cases in which bilateral grids were applied, the contralateral side to the focus was also examined. HbT was calculated as the sum of oxyHb and deoxyHb and is representative of regional cerebral blood volume. HbDiff was calculated as oxyHb minus deoxyHb and is representative of cerebral oxygenation (and saturation). Changes in haemodynamics are considered statistically significant if different from the baseline when p=0.05 (two-tailed t-test, FWE=0.05). This analysis was performed for three patients who had seizures or seizure build-up activity during EEG-NIRS recordings.

5.4.3.4 Interictal Epileptiform Discharge Analysis

The next step was to extract the haemodynamic response to IEDs to provide a complementary and potentially confirmatory result to those obtained in Chapter 3 using EEG-fMRI. Therefore we employed a similar methodology using a smooth FIR deconvolution to determine the shape of the haemodynamic response function (HRF) see section 3.6. As for Chapter 3 we used the following parameter values noise = 0.3, smoothness level=0.4, and regularisation. A two-tailed one-sample t-test (FWE corrected at 0.05) was performed to determine whether statistically significant changes occurred in the haemodynamic response.

5.5 Results

Of 10 children with focal epilepsy (see Table 5.1), two had seizures during NIRS recordings and 1 had electrographic build-up which resulted in a seizure directly after the removal of NIRS optodes. Nine patients showed interictal epileptiform

discharges (IEDs), while one (patient #10) was given medication just before NIRS recordings (on consultant recommendation) after a period of AED (antiepileptic drug) reduction, and had no interictal discharges during NIRS recordings.

There was a wide range of foci including frontal, temporal, occipital, and parietal regions. On average, patients were able to tolerate 2 sessions of 45 minutes each.

Table 5.1 Patient information sheet: EEG-NIRS

Patient Number	Events Recorded	Age (yrs)	Age of Onset (yrs)	Number of Channels	Number of Blocks	Grid Dimensions	Focus Region	Gender	Medication (daily dose [mg])
# 1	Seizure build-up; IEDs	13	6	24	4	2x(3x3)	Right Frontal	Male	CBZ 600, VPA 1600
# 2	Seizure; IEDs	4	1	12	2	3x3	Left Temporal	Male	LVT 1400, TPM 150
# 3	Seizure; IEDs	12	4	24	4	2x(3x3)	Right Frontal	Female	LVT 2000
# 4	IEDs	14	10	24	2	2x(3x3)	Left Frontal	Male	CBZ 17*, TPM 7*
# 5	IEDs	7	1.5	22	1	3x5	Left Temporal	Female	VPA 31*, CLBZ 0.6*
# 6	IEDs	17	0.6	24	1	4x4	Left Temporal	Female	CBZ 700, LCM 250, PMP 10
# 7	IEDs	7	3.5	22	1	3x5	Right Occipital	Female	CBZ 280, CLBZ 20
#8	IEDs	8	4	12	2	3x3	Right Parietal	Male	CBZ 600
# 9	IEDs	11	4	24	1	4x4	Left Frontal	Female	Nil
# 10	Nil	13	4	24	2	2x(3x3)	Left Parietal	Female	LVT 300, LTG 150

* Per kilogram per day

CBZ = Carbamazepine; CLBZ = Clobazam; LCM = Lacosamide; LTG = Lamotrigine; LVT = Levetiracetam; PMP = Perampanel; TPM = Topiramate; VPA = Valproate

5.5.1 Patients with Seizures

In the following section we provide case reports in the patients who had seizures during the simultaneous EEG-NIRS recordings.

5.5.1.1 Patient #1

Patient #1 was a 13 year old boy who was diagnosed with tuberous sclerosis and epilepsy at the age of six years. He is also considered within the range of autism spectrum disorder. His seizures manifested as vacant unresponsive episodes during wake, however the more prominent seizures are likely to occur during sleep. The frequency of these seizures at the time of hospital admittance was between 4-5/night. He had multifocal bilateral sub-cortical and cortical tubers visible on MRI. Most prominent changes during seizures were captured over the right fronto-polar region. Telemetry recordings for simultaneous EEG-NIRS occurred over four hours during drowsiness and sleep stages. Twenty-four NIRS channels were recorded over two hemispheres of the frontal lobe (12 channels on the left, 12 channels on the right). The channels showing increased electrical activity on the EEG were Fp2 and Fp1 in the fronto-polar regions with greater emphasis in the right hemisphere. Patient #1 had an electrographic seizure directly after NIRS optodes were removed; however we report the changes related with broad discharges during the preictal (before seizure) period.

Results for the 40sec time window show a dramatic increase in oxyHb and HbT in the right hemisphere (see Figure 5.1). In contrast, deoxyHb measurements remained at baseline. Additionally, HbDiff values had a slight increase around 15 seconds prior to event onset, with another more dramatic increase at approximately seven seconds after onset. The left hemisphere shows similar results in oxyHb and HbT, but not in deoxyHb and HbDiff. DeoxyHb has a steady decrease after event onset in the left hemisphere, while HbDiff only shows one peak approximately 15 seconds after onset. The 10min window shows haemodynamic changes similar to that seen in the 40sec window as oxyHb, HbT, and HbDiff have significant increases after the seizure onset (see Figure 5.2). DeoxyHb changes remain fairly stable throughout the recording. However, there was a trend of bilateral haemodynamic changes seen up to

2 minutes prior to the event that included increases in oxyHb, HbT, and HbDiff and decreases in deoxyHb.

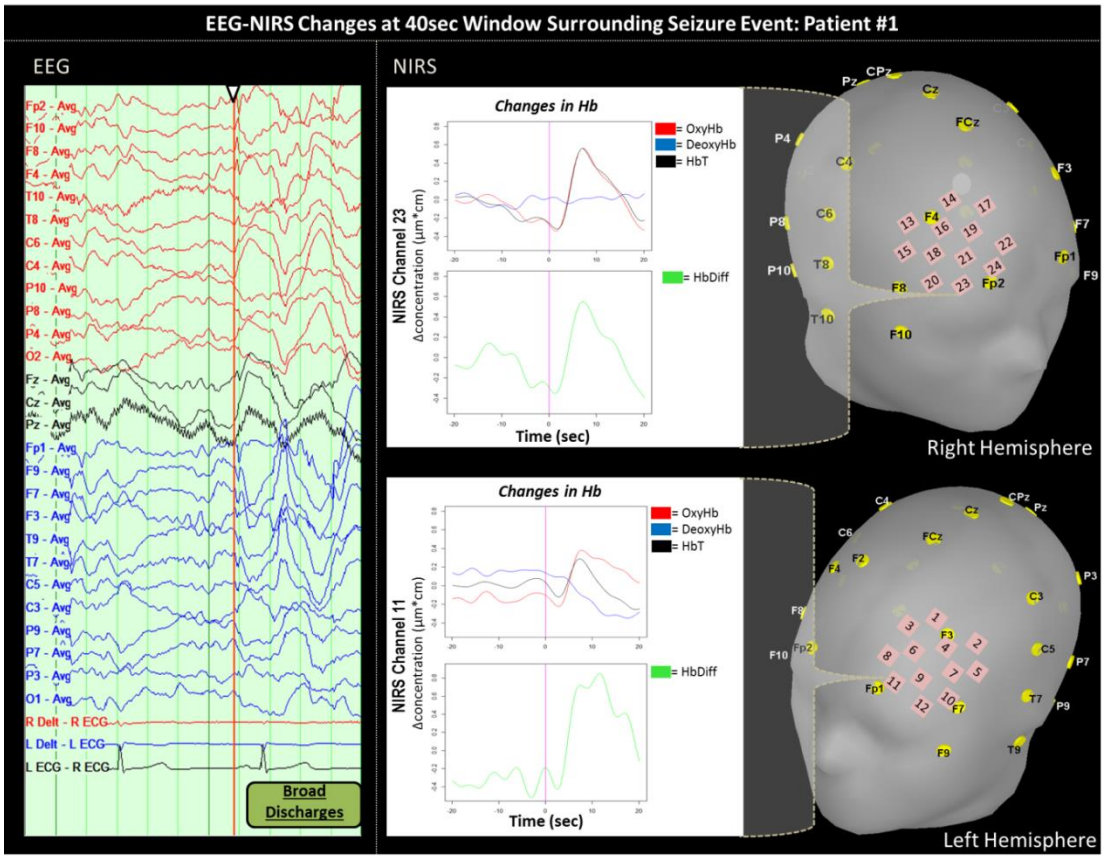

Figure 5.1 EEG-NIRS changes at 40sec window surrounding seizure event: Patient #1

Patient #1 had seizure build up in the right frontal cortex. The left panel shows the EEG trace with the onset of broad discharges shown by the red line (and black arrow at the top of the trace). The channels on the right hemisphere are displayed in red while the left is displayed in blue. Central regions are displayed in black. The behavioural manifestations are noted in green boxes in the bottom left panel. The right panel shows the bilateral NIRS results of oxyHb (red), deoxyHb (blue), HbT (black), and HbDiff (green) with reference to seizure onset (vertical magenta line). The right hemisphere (right panel, top) displays an increase in oxyHb and HbT after the event with a steady rate of deoxyHb. An HbDiff peak occurs both prior/after event onset. The left hemisphere (right panel, bottom) shows a similar relationship as the right hemisphere, with the exception of deoxyHb which shows a slight decrease after event onset, and HbDiff which displays an increase after event onset only.

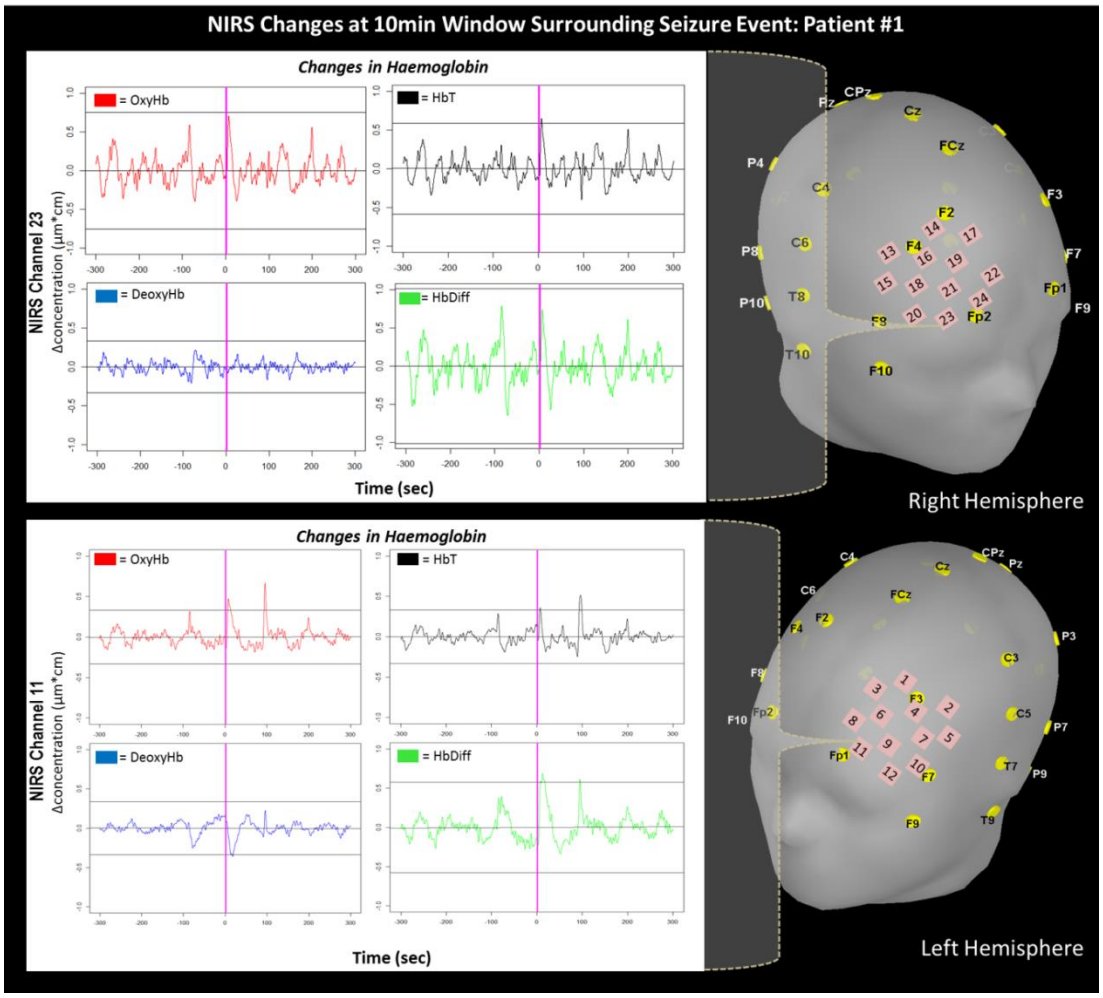

Figure 5.2 NIRS changes at 10min window surrounding seizure event: Patient #1
The top panel refers to the left hemisphere while the bottom panel refers to the right hemisphere. Changes in oxyHb (red), deoxyHb (blue), HbT (black), and HbDiff (green) can be seen both after/prior to the event onset (vertical magenta line). In the left hemisphere significant amplitude changes can be seen in oxyHb/HbT/HbDiff, however significant changes in the right hemisphere are seen in HbT. DeoxyHb continues to remain fairly stable throughout. Black lined boundaries signify the critical value required for significance (p=0.05, FWE=0.05).

5.5.1.2 Patient #2

Patient #2 was a four year old boy who was diagnosed with tuberous sclerosis and epilepsy. Age of onset of epilepsy was at one year, with delayed milestones and events characterised by standing still and shouting for approximately 5 seconds. He currently has two event types which include 1) head and eye deviation towards the left with slight jerking of the left arm and leg. These events can last from 10 seconds to three minutes. The frequency of these events is approximately 1/week. 2) His

second event type involved behavioural reactions that were distracted and slow, sometimes accompanied with a facial expression resembling a 'smile' (i.e. not a natural smile induced by the environment). These events were more frequent, occurring approximately 1-6/day. He showed multiple subependymal nodules and parenchymal tubers on MRI. Changes most prominently occur over the left temporal regions. Telemetry recordings for simultaneous EEG-NIRS occurred over two hours. Twelve NIRS channels were placed over the left temporal lobe. Patient #2 had a type 2 seizure during EEG-NIRS recordings.

Results for the 40sec time window indicate a large increase in oxyHb and HbT in the region of presumed focus (see Figure 5.3) however deoxyHb changes remained at baseline. HbDiff had a small increase approximately 15 seconds prior to event onset, with another more dramatic increase at approximately 13 seconds after onset. The 10min window shows changes in haemodynamics that confirm these results (see Figure 5.4), as significant peaks in HbT can occur 3 minutes after event onset.

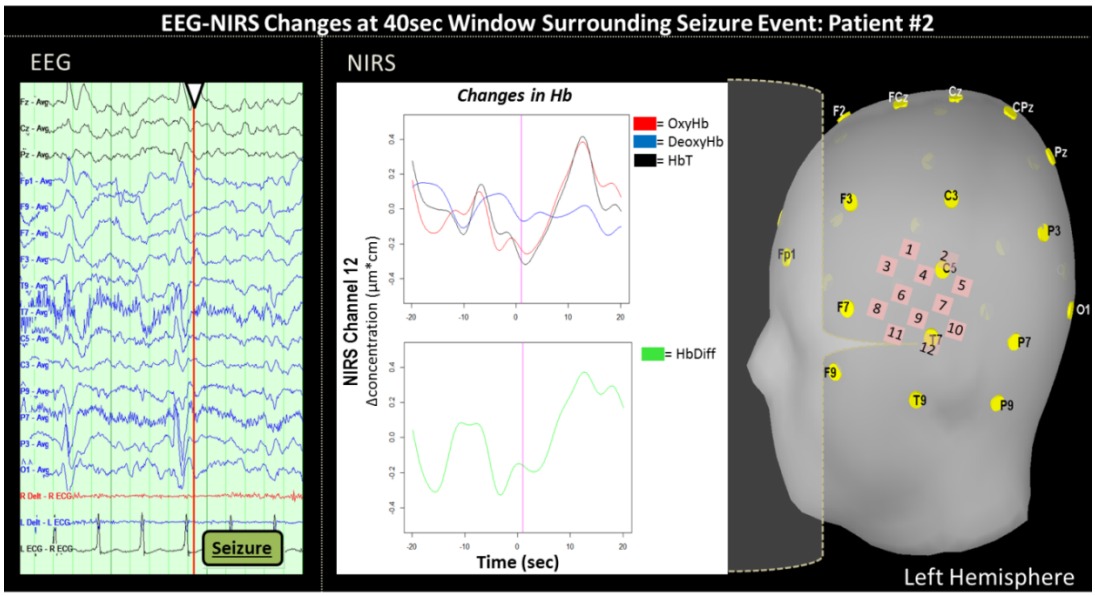

Figure 5.3 EEG-NIRS changes at 40sec window surrounding seizure event: Patient #2

Patient #2 had a seizure in the left temporal cortex. The left panel shows the EEG trace with the onset of broad discharges shown by the red line (and black arrow at the top of the trace). The left hemisphere is displayed in blue and central regions are displayed in black. The behavioural manifestations are noted in green boxes in the bottom left panel. The right panel shows the bilateral NIRS results of oxyHb (red),

deoxyHb (blue), HbT (black), and HbDiff (green) with reference to seizure onset (vertical magenta line). The left hemisphere (right panel) displays an increase in oxyHb and HbT after the event with a steady rate of deoxyHb. An HbDiff peak occurs both prior/after event onset.

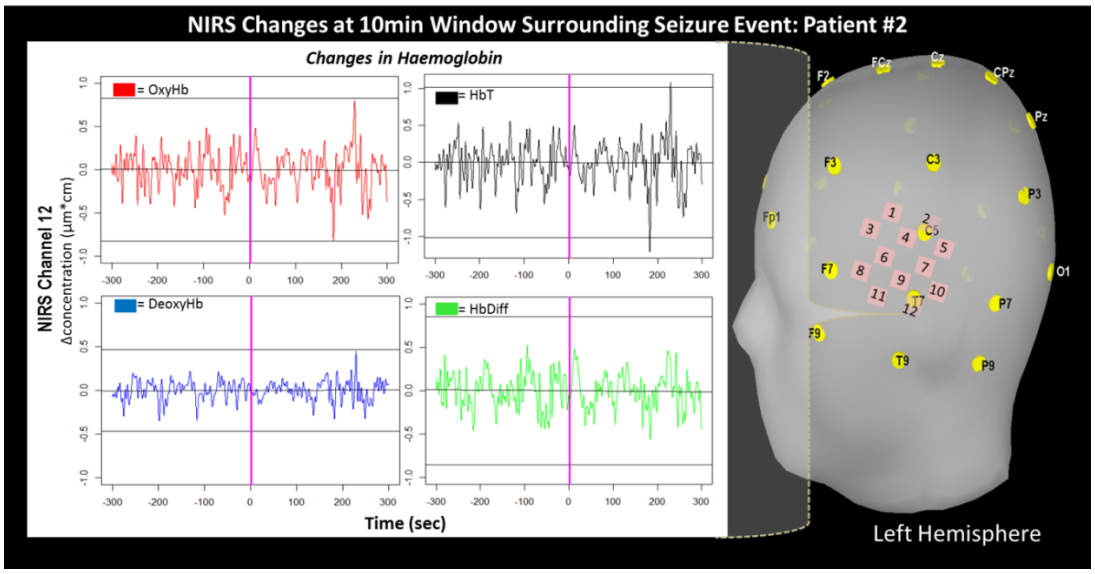

Figure 5.4 NIRS changes at 10min window surrounding seizure event: Patient #2
The recordings were done in the left hemisphere. Changes in oxyHb (red), deoxyHb (blue), HbT (black), and HbDiff (green) can be seen both after/prior to the event onset (vertical magenta line). Large amplitude changes are difficult to distinguish, however a significant peak in HbT can be seen after the seizure event. Black lined boundaries signify the critical value required for significance (p=0.05, FWE=0.05).

5.5.1.3 Patient #3

Patient #3 was a 12 year old girl with focal cortical dysplasia located in the right superior frontal gyrus. Age of epilepsy onset was four years old with episodes of vacant stares, lasting over a few seconds. Otherwise, early development consisted of normal milestones. Current events comprise of tonic clonic seizures with the right arm outstretching and facial grimacing with retained awareness. She experiences long periods of seizure freedom (up to six months), followed by periods of very frequent events (multiple per day). Twenty-four NIRS channels were placed over the presumed focus and its contralateral counterpart. NIRS recordings were performed prior to sleep as seizures were expected at night. Prominent changes in electrical activity were reported over the right frontal lobe which spread to the midline during

NIRS recording followed by a tonic clonic seizure which was captured during EEG-NIRS telemetry.

Results for the 40sec time window indicate a slight increase of deoxyhaemoglobin after the EEG recorded seizure event on the right hemisphere (see Figure 5.5). Both oxyHb and HbT remain at baseline, however values fluctuate after event onset. Additionally, there is an increase in HbDiff that occurs around seven seconds after event onset. The NIRS channel recorded over the left hemisphere (near the frontal midline region) shows a similar change in HbDiff, however the changes seen in oxyHb and HbT increase after event onset while deoxyHb fluctuates around baseline. Similarly, results for the 10min window show significant peak amplitude changes bilaterally in oxyHb and HbDiff within the first 1-3 minutes of seizure onset (see Figure 5.6).

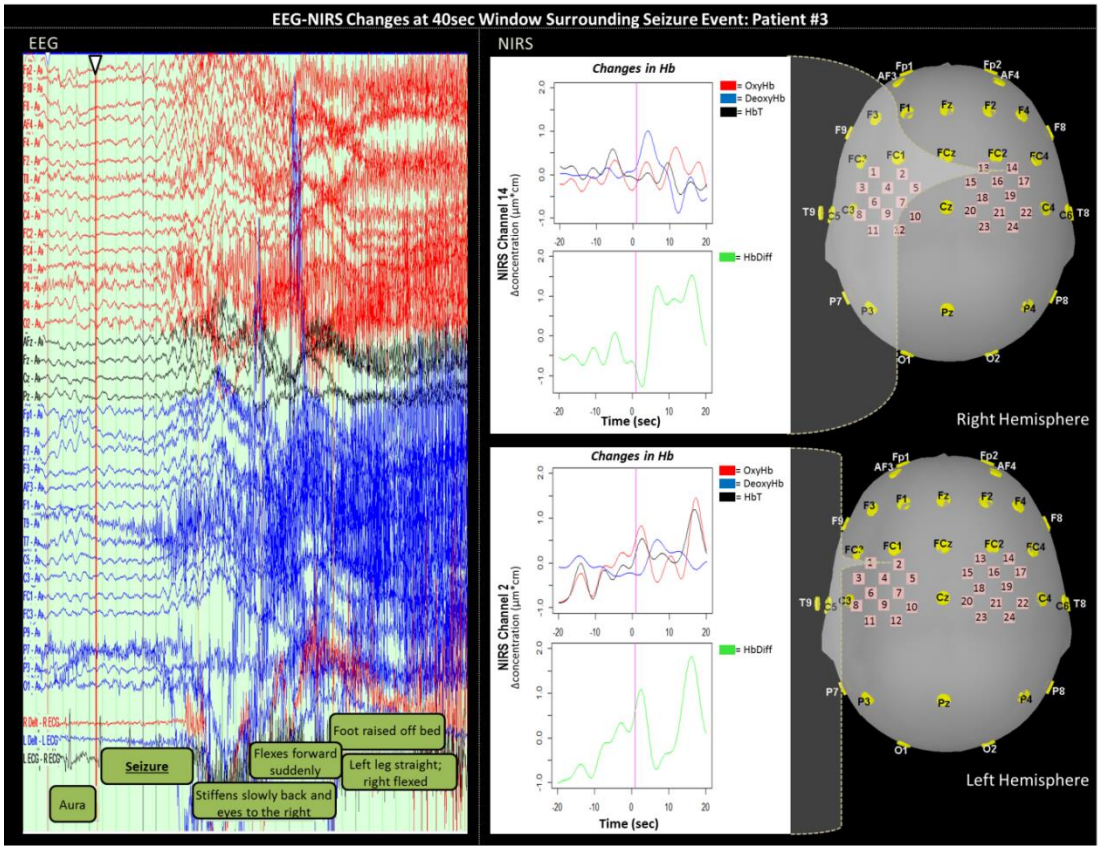

Figure 5.5 EEG-NIRS changes at 40sec window surrounding seizure event: Patient #3

Patient #3 had a seizure in the right frontal cortex. The left panel shows the EEG trace with the onset of broad discharges shown by the red line (and black arrow at the top of the trace). The right side of the head was displayed in red while the left

was displayed in blue. Central regions are displayed in black. The behavioural manifestations are noted in green boxes in the bottom left panel. The right panel shows the bilateral NIRS results of oxyHb (red), deoxyHb (blue), HbT (black), and HbDiff (green) with reference to seizure onset (vertical magenta line). The right hemisphere (right panel, top) displays an increase in oxyHb and HbT after the event with a steady rate of deoxyHb. An HbDiff peak occurs both prior/after event onset. The left hemisphere (right panel, bottom) shows a similar relationship as the right hemisphere, with the exception of deoxyHb which shows a slight decrease after event onset, and HbDiff which displays an increase after event onset only.

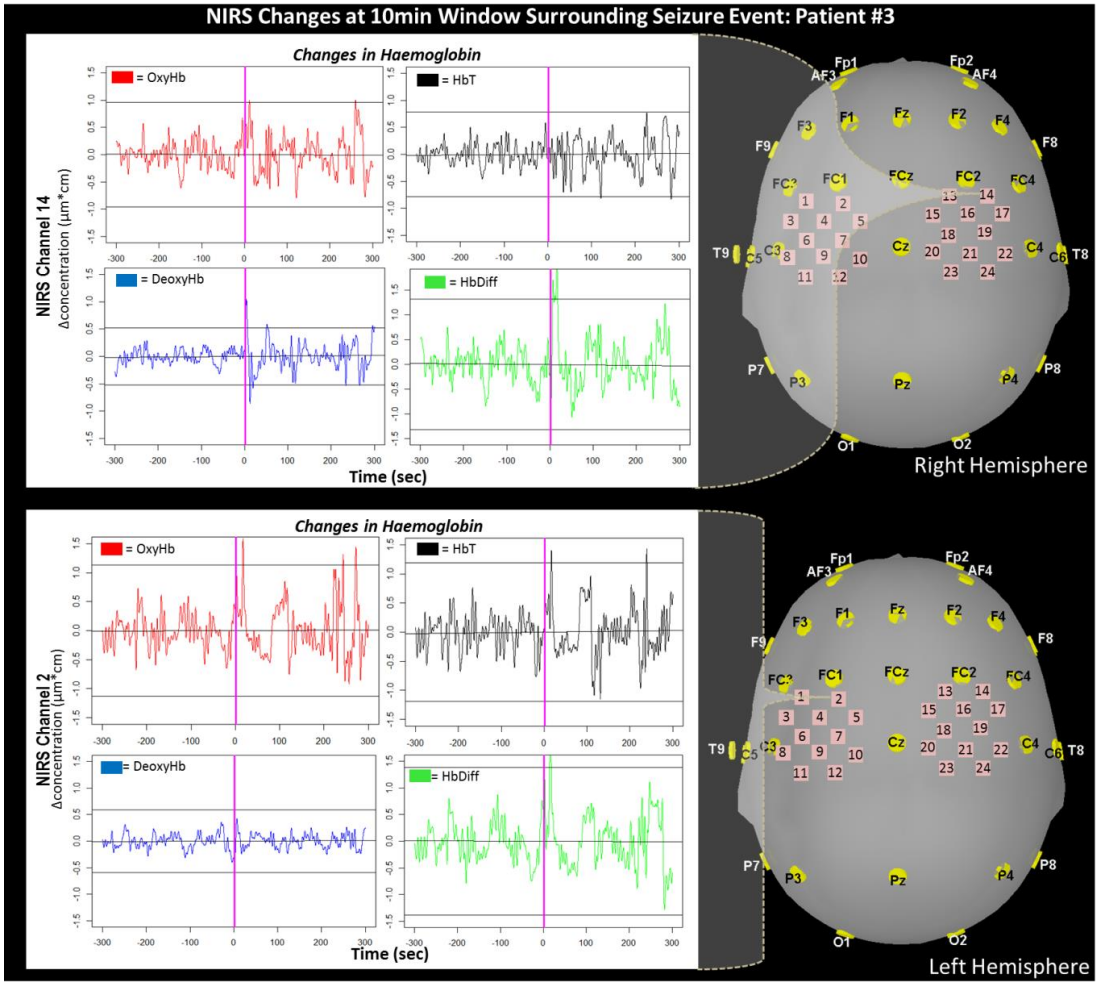

Figure 5.6 NIRS changes at 10min window surrounding seizure event: Patient #3
The top panel refers to the right hemisphere while the bottom panel refers to the left hemisphere. Changes in oxyHb (red), deoxyHb (blue), HbT (black), and HbDiff (green) can be seen both after/prior to the event onset (vertical magenta line), however the most dramatic changes are seen mainly after seizure onset in oxyHb and HbDiff bilaterally and deoxyHb in the right hemisphere and HbT in the left

hemisphere. Black lined boundaries signify the critical value required for significance (p=0.05, FWE=0.05).

5.5.2 Patients with Interictal Epileptiform Discharges

Significant haemodynamic changes in relation to IEDs were tested via a one-sample t-test (two-tailed; FWE corrected p=0.05). There were no statistically significant haemodynamic changes detected in relation to IEDs. All patient HRFs are displayed in Figure 5.7.

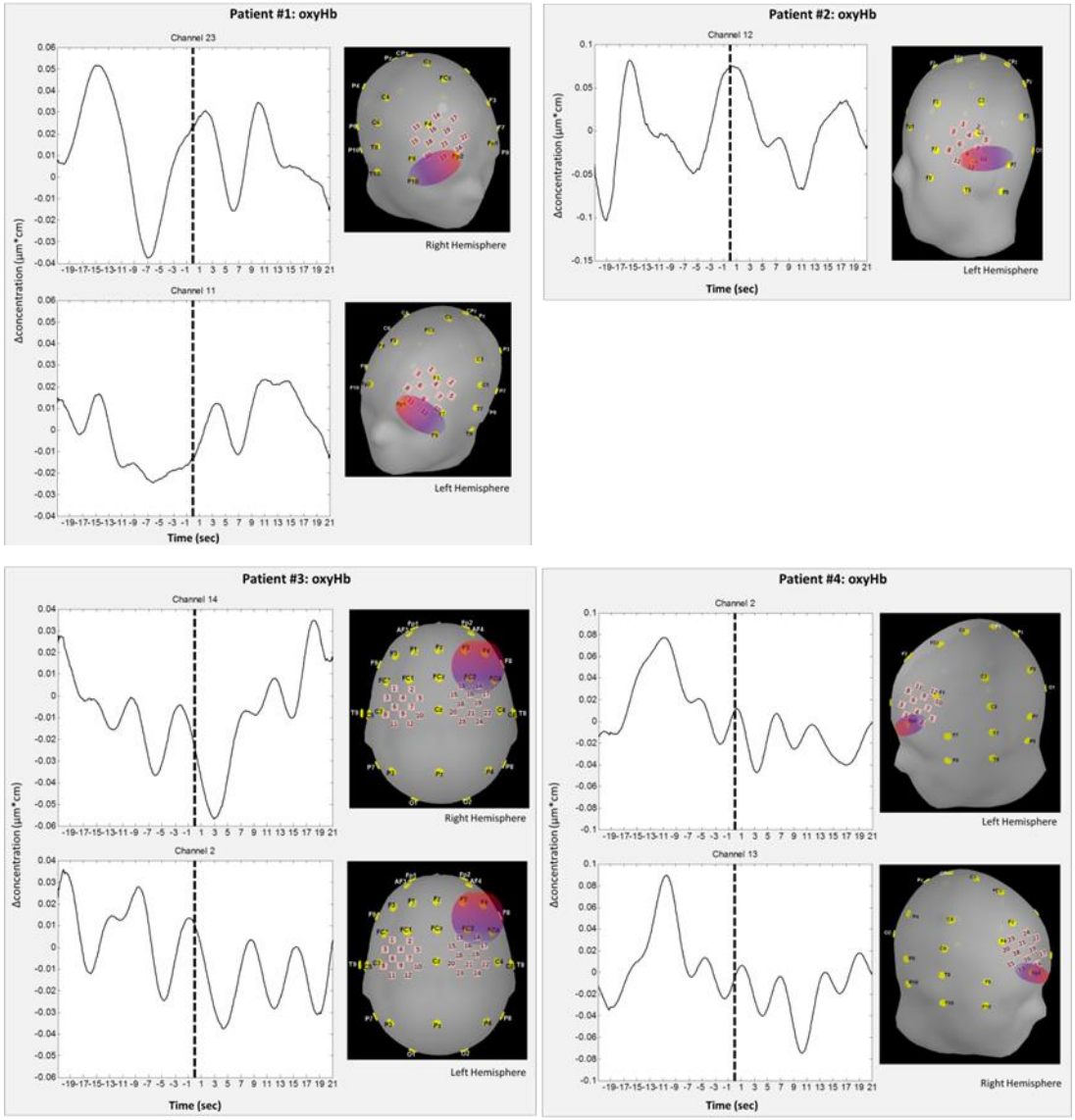

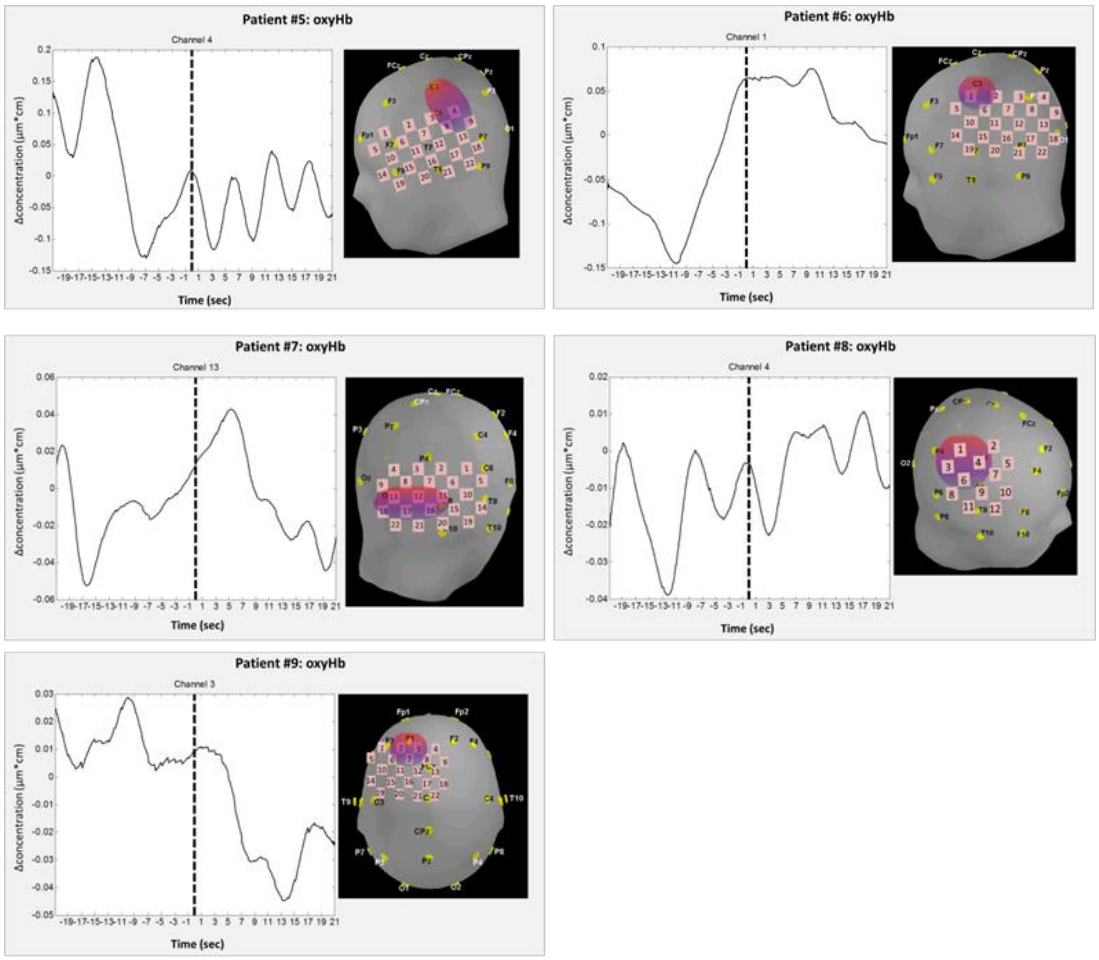

Figure 5.7 Patients: EEG and NIRS changes for IED events

The haemodynamic response for all patients (1-9) experiencing IEDs during EEG-NIRS recordings. The left panel displays oxyHb concentration changes in relation to the onset of IED event (displayed by lack dotted line). Only channels closest to the focus were displayed. The EEG channels (yellow circles) and NIRS channels (pink squares) are placed on top of the scalp and situated near the focus. The focus is highlighted by a colour-gradient ellipse with redder shades indicating higher rates of IEDs and purple/blue shades indicating lower rates of IEDs.

5.6 Discussion

The current study was able to record NIRS simultaneously with clinical video-telemetry and capture haemodynamic changes for both seizure and IED events in a wide age range of children with focal onset epilepsy, thereby achieving the overall goal of the study. Furthermore, we established that simultaneous EEG-NIRS recordings in parallel with video telemetry clinical evaluation were well tolerated among paediatric patients.

5.6.1 Haemodynamic Changes Related to Seizures

Simultaneous EEG-NIRS measurements were performed in paediatric epilepsy patients to measure heamodynamic changes related to spontaneous focal seizures. Simultaneous EEG-NIRS was performed during clinical video telemetry examinations, thereby allowing for minimal interference with the clinical protocol. The main findings were that in seizure events, HbDiff increases occurred up to 15 seconds prior to the event onset, indicating an increase in oxygen saturation. This was followed by another peak in HbDiff occurring 10 seconds after the onset and returning to baseline. The second peak had a larger amplitude change in comparison to the first peak in all seizures recorded; this implies a possible mechanism for identifying preictal changes. There was also a trend in increases in haemodynamic change up to 10 minutes prior to the seizure event however this was not statistically significant.

Significant increases in oxyHb and HbT were seen at optodes close to the presumed SOZ after the clinical onset of the seizure. This is consistent with some previous NIRS studies which also found increases in blood volume and oxygenated haemoglobin ipsilateral to the SOZ (Adelson et al., 1999; Gallagher et al., 2008; Steinhoff et al., 1996; Watanabe et al., 2000; Villringer et al., 1993). The CBV rise observed in the focus is congruent with the brain's attempt to meet the metabolic demand of epileptic neuronal activity with oxygenated haemoglobin (Suh et al., 2006).

Interestingly, deoxyHb concentration remained at baseline, with some patients showing a slight decrease after event onset. The relatively stable concentration of deoxyHb measured through the seizures recorded suggests adequate oxyHb supply while the slight decrease suggests oxyHb oversupply, thereby signifying that metabolic demand has been met in the seizure focus.

5.6.2 Haemodynamic Changes Related to Interictal Epileptiform Discharges

The haemodynamic responses to IED events derived from simultaneous EEG-NIRS were highly variable. Although some patients displayed oxyHb changes prior to discharge onset, there was no significant change detected from the baseline haemodynamic response. This can possibly be explained by the spatial extent of IED haemodynamic changes which are likely to be less widespread than seizures. Therefore the NIRS recordings may not often record the relatively small and localised haemodynamic changes

IEDs represent summations of thousands of neurons in hypersynchronous events. Neurons within epileptogenic tissue experience abnormally long depolarisations, followed by a train of action potentials also known as paroxysmal depolarisations shift (PDS; see section 1.1 for more details). During a seizure, PDS can spread due to failure of inhibitory mechanisms leading to large widespread changes in network function. Therefore an IED can represent smaller localised potentials of its larger seizure counterpart, making it more difficult to detect. It is possible that NIRS is best for picking up large changes in haemodynamics such as seizures, while subtle and more variable events such as IEDs are more difficult to capture. In this case, EEG-fMRI might be more sensitive to changes involving IED events (as seen in previous Chapters 2-3).

Nevertheless, in some subjects there was a clear increase in oxyhaemoglobin changes prior to the IED discharge which was consistent with previous results (Chapter 3) in which HRF peaks occurred up to ~20 seconds prior to IED onset in EEG-fMRI. This is particularly interesting considering that seizures did not display oxyHb changes prior to electrographic onset, suggesting that the haemodynamic response to IEDs is

inherently different to that of seizures. Future recording of both EEG-fMRI and EEG-NIRS in the same cohort would be advantageous to cross-validate the IED responses and spatial locations.

5.6.3 Deoxyhaemoglobin and Meeting Metabolic Demands of the Seizure Focus

Previous reports on changes in deoxyHb concentration are mixed. Studies found deoxyHb could decrease, remain unchanged, or increase during seizures (Buchheim et al., 2004; Wallois et al., 2009; Nguyen et al., 2012; Nguyen et al., 2013; Peng et al., 2016). Some suggest that the increase in deoxyHb could lead to hypoxic damage during ictal events (Wallois et al., 2009), while others show a stable deoxyHb concentration throughout the seizure indicating sufficient oxyHb supply to the tissue (Nguyen et al., 2013). These mixed results could be due to a number of factors involving seizure duration, spatial specificity, age, or reliability of measurements.

Seizure duration is highly variable, however longer seizures are generally thought of as being more toxic with increased likelihood of neuronal cell death (Dingledine et al., 2014). While animal models have demonstrated inadequate oxygenation during both status epilepticus (Meldrum and Brierly, 1973; Meldrum and Horton, 1973; Kreisman et al., 1984), as well as shorter-duration events (Bahar et al., 2006; Zhao et al., 2007; Zhao et al., 2009), work in humans has been more variable. Studies with long mesial temporal lobe seizures found deoxyHb increases (Nguyen et al., 2012), while short frontal lobe seizures demonstrated adequate oxygenation (Nguyen et al., 2013); however there were still individual variations reported within these samples. The current study was able to capture seizures of both frontal (n=2) and temporal lobe (n=1) onset, and found both to have adequate oxygen supply. Although it is difficult to compare these patients as they have differing seizure semiology; Nguyen et al. (2012) captures seizures from patients with mesial temporal focus while the current study has seizures from the middle temporal lobe in a patient with TS. Additionally, other neuroimaging techniques such as EEG-fMRI have reported similar results with positive BOLD changes (signal corresponding to decreases in deoxyHb; see section 1.3) in the seizure onset zone suggesting sufficient tissue oxygenation (Thornton et al., 2010; Chaudhary et al., 2013).

Another potential reason for heterogeneous reports of deoxyHb changes is that different brain regions associated with the seizures show differing deoxyHb changes. Any spatial variability is difficult to characterise due to the lack of spatial specificity of NIRS and the difficulty in identifying the spatial correspondence between the SOZ and the tissue interrogated by the NIRS optodes. This is further complicated by the typical clinical uncertainty in the SOZ which can range between 18-56% in children from routine clinical EEG (Wirrell et al., 2010). Additionally, as focal epilepsy is considered a network disease (Centeno and Carmichael, 2014; Laufs et al., 2014), it is possible that differing haemodynamic changes may be seen in different nodes of the network, specifically in propagated areas within the epileptogenic network. Finally, the haemodynamic changes seen in children may be different from those seen in adults. There are very few NIRS studies looking at children, and of those that do, many combine the results of both adults and children. For example, previous fMRI studies have previously shown differences in haemodynamic coupling dependent on age (Yamada et al., 2000; Jacobs et al., 2008) as has work in this thesis (see section 3.11). This stresses the importance of studying epilepsy during its development and changes associated with maturation.

Another point to consider is the mechanical properties of early NIRS optodes. In earlier NIRS studies, the wavelength sensitive to deoxyhaemoglobin was not well defined, and it wasn't until recently that the wavelength most sensitive to deoxyHb was determined to be 690nm (Sato et al., 2004). Therefore the measurements using the 780nm optodes, although are representative of deoxyHb concentrations, could be improved by using a more sensitive wavelength.

In summary, the current study shows consistent change in oxyHb, deoxyHb, HbT, and HbDiff, indicating that seizures are characterised by a preictal change in HbDiff followed by increases in both oxyHb and HbT. Despite mixed previous reports, in the three subjects studied here deoxyHb showed little change from baseline levels, however when interpreting these results the well-known instability of deoxyHb measurements should be taken into account.

5.6.4 Haemodynamics Contralateral to the Seizure Focus

In addition to haemodynamic changes over the epileptic focus, our study reveals modulations in contralateral homologous regions, which almost mirrored those seen ipsilaterally. This has been seen in previous studies in both animal (Schwartz and Bonhoeffer, 2001) and human work in adults (Nguyen et al., 2013). Therefore, this contralateral change does not seem to be dependent on age, and is a general finding.

5.6.5 Limitations

The limited number of patients participating in this study was due to a number of reasons: 1) not all patients that come through telemetry have a strong spatial hypothesis for SOZ, 2) patients with deep cortical foci could not participate due to the spatial restraints of NIRS, and 3) many patients with dense (and dark) hair were excluded due to the possibility of signal interference. Nevertheless, we were able to capture haemodynamic changes in a heterogeneous group of children with focal epilepsy. Furthermore, this is the largest multi-channel NIRS study done in this cohort (children with heterogeneous focal epilepsy) in a video telemetry environment.

5.6.6 Future Work

Determining a corresponding relationship between significant morphological changes in single subject HRFs with patient semiology would be an interesting topic for future work. However, for this to be realised, a large sample of patients must be collected with simultaneous clinical EEG recordings along with systemic physiological parameters such as CO_2 concentration, blood pressure, cerebral blood flow, and a measure of cellular oxidative metabolism (i.e.: cytochrome c oxidase) to disentangle the input of different physiological variables involved in the resulting patient HRF. The practicality of measuring all of these parameters simultaneously in patients on the ward is challenging but could be highly beneficial.

The EEG is rich in content and can provide information on the minute electrical changes surrounding epileptic events. Seizure progression can be subdivided into ictal phases such as 1) preictal, 2) ictal onset, 3) ictal established, and 4) late ictal, as done in Chaudhary et al. (2012) to define the evolution of the electrographic pattern

and clinical semiology. These electrographic changes can be analysed to determine their associated haemodynamic change using EEG-NIRS.

Another question regarding haemodynamics and children which has yet to be fully answered is the accurate modelling of seizures in EEG-fMRI data. It would be interesting to apply the results acquired in the current study to create a valid haemodynamic response function applicable for seizure events, as EEG-fMRI has been used for SOZ localisation.

5.6.7 Conclusion

Changes in haemodynamics can be reliably recorded by EEG-NIRS recordings during focal seizures in children and young people in a clinical ward setting. We found a consistent change in HbDiff in all seizure events, with a peak both prior to and after seizure onset. The haemodynamic responses to focal IEDs were inconsistent potentially due to the lack of sensitivity, spatial specificity and coverage of EEG-NIRS. Therefore this study suggests EEG-NIRS may be a useful tool for measuring seizures, but may have less potential for the mapping of characterisation of changes associated with IEDs.

Chapter 6 Laser Doppler Flowmetry in Surgical Paediatric Epilepsy Patients

6.1 Abstract

Invasive monitoring via intracranial EEG (iEEG) is sometimes required for epilepsy patients in order to better determine the epileptogenic cortex prior to surgical resection. Other measurements can be recorded simultaneously with the iEEG, such as Laser Doppler (LD), with the benefit of better spatial specificity and sensitivity to neuronal and vascular changes in the cortex. LD measures cerebral blood flow (or flux) by applying Doppler shift to quantify the rate of moving blood cells within the cerebrum. The simultaneous measurement of iEEG and LD relates epileptic activity to blood flow surrounding the seizure event. This chapter uses historical LD measurements to determine blood flow changes surrounding epileptic events with Ad-Tech intracranial grids imbedded with LD probes. Two LD probes were monitored for the duration of invasive EEG recording. However LD measurements were unstable after 24 hours of recording. The original goal was to record simultaneous LD-iEEG using new more reliable designs on implanted patients, however due to practical constraints simultaneous LD-iEEG recordings were not performed.

6.2 Objectives

fMRI, NIRS and LD have all detected haemodynamic changes prior to seizure onset (Hawco et al., 2007; Patel et al., 2013; Schwartz et al., 2011; Seyal 2014; Ronne-Engstrom et al., 1993). However, the timescale at which changes are detected can vary from 3 minutes to 13 hours prior to seizure (Ronne-Engström et al., 1993; Seyal, 2014). It is a goal of the current chapter to further explore this issue by 1) determining whether or not microvascular changes occur prior to seizure events, 2) identifying the time at which microvascular changes occur, 3) deriving the shape of the HRF and determine how it differs for patients, 4) exploring how we can apply this knowledge to aid current non-invasive imaging techniques and prevent invasive techniques in the future.

6.3 Introduction

Laser Doppler (LD) is an optical technique used to measure blood flow, which was originally described by Bonner and Nossal in 1981. It uses the backscattered laser light to measure the Doppler shift from moving particles (see Figure 6.1). The Doppler shift was originally described by Christian Doppler in 1842 and is described previously (Conroy, 1996). The movement of objects causes the backscattered light to be frequency shifted. Subsequently, the velocity of the moving objects can then be determined based on this frequency shift observed by the detector, making it possible to predict blood flow non-invasively. A critical difference in measurements from Near Infrared Spectroscopy (NIRS) and LD is that NIRS measurements are based on haemodynamics and changes in oxygenation, while LD measures blood flow or 'flux'.

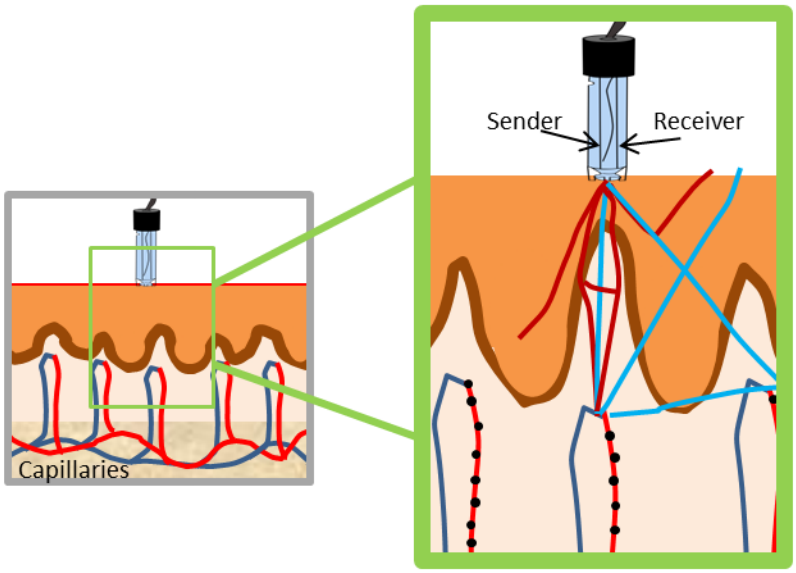

Figure 6.1 Laser Doppler measures the microvascular blood flow in capillaries
The Laser Doppler probe measures the blood flow in the capillary bed (left panel, green box). Each Doppler probe has a sending fibre and a receiving fibre (right panel) from which the backscattered light can measure the movement of blood within the capillaries. Note however, that not all of the backscattered light is received.

The motivation for the specification of blood 'flux', is that Laser Doppler cannot measure absolute flow values (i.e.: ml/min/100 gram tissue), and therefore must be expressed in arbitrary units called Perfusion Units (PU). PU can be described as the

number of moving blood cells in a measured volume (ratio of shifted light and non-shifted light) multiplied by the mean velocity of moving blood cells (magnitude of the light shift). The reasoning behind PU arbitrary units is that the volume of tissue and tissue depth among varying regions is unknown.

The variations between regional measurements are influenced by regional capillary density. Blood-rich organs have a considerably lower measuring depth (< 1mm), as the increase of blood prohibits the passage of light. This inconsistency is also applicable to structures within the central nervous system, as vascular density and geometry vary (Frerichs & Reuerstein, 1990). While taking these concerns into consideration, cerebral LD flow measurements have been reliably made since its initial introduction in both animal and human studies (Riva et al., 1972; Chen et al., 1986; Eyre et al., 1988; Winkler et al., 2012). However, there have been very few studies focusing on Laser Doppler in cerebral monitoring of epilepsy patients. A study by Ronne-Engström et al. (1993) tested six adult pre-surgical epilepsy patients with simultaneous subdural EEG and Laser Doppler. Results showed haemodynamic changes in the cortex during seizures, occurring up to four minutes before seizure activity, and returning to basal levels within 10 minutes of seizure termination. Both ictal hyperperfusion and hypoperfusion can be seen depending on the individual focus, possibly due to regional foci differences in blood flow. Another study has suggested changes in CBF 20 minutes prior to seizure onset (Wallsted et al., 1995). A more recent study has been conducted by Zhao et al. (2011) using a rat model inducing seizures with potassium channel blocker injections. They predict differences in relative CBF caused by the centre-surround phenomenon, where preictal vasoconstriction around the seizure focus shunts blood to the focus leading to a local metabolic drop-off of hypoperfusion. This model agrees with previous findings indicating an early vascular response by active vasoconstriction in arterioles preceding ictal onset surrounding the focus, leading to changes in cerebral blood flow prior to seizure onset.

However, Laser Doppler is unique in that it measures blood flux, or estimated changes in flow. Laser Doppler exploits the Doppler shift, which varies linearly with the mean velocity of flowing cells (see Equation 6.1). Unfortunately, photons from the incident laser can suffer several collisions before interacting with a moving blood

cell. Therefore, in order to accurately represent local blood flow, other biological bodies must be accounted for. This can be done using an Equation 6.2 derived from Bonner and Nossal (1981).

$$\Delta f = \frac{v}{c} V_o \qquad \textit{Equation 6.1}$$

Where v is the velocity of the source with respect to the observer, c is the velocity of the carrier wave motion, and V_o is the un-shifted observed frequency (Öberg, 1990).

$$\langle \omega \rangle = \frac{\langle V^2 \rangle^{1/2\beta}}{(12\xi)^{\frac{1}{2}} a} f(\bar{m}) \qquad \textit{Equation 6.2}$$

Where <ω> represents the normalised first moment of the spectrum, $<V^2>^{\frac{1}{2}}$ is the root mean squared (RMS) speed of moving particles, a is the radius of the average spherical scatterer, ξ is an empirical factor related to the shape of the cell body, β is an instrumental factor or the optical coherence of the signal at the detector surface, $\bar{m}$ is the average number of collisions which a detected photon makes with a moving cell, and f($\bar{m}$) is a linear function of the hematocrit of tissue.

6.3.1 Historical Laser Doppler Design

The original LD probe design for simultaneous LD-iEEG can be seen in Figure 6.2 (Perimed, Sweden). The main benefit of this design was the ease at which it could be placed on the standard clinical iEEG grid used in GOSH from Ad-Tech (Wisconsin, USA). As seen below, the LD fibres from perimed (Stockholm, Sweden) were glued on top of the grid surface and hung jointly with the external iEEG fibres, making it easily recordable with no added inconvenience for either the patient or the surgeon. There were five possible placements for the LD probe recordings; depending on epileptic focus the recording probes would change. Traditionally, one probe would be placed within predicted focus and one outside of the focus region (see Figure 6.3, and Figure 6.4). For example in Figure 6.3 only probes 1 and 2 were recorded from, as probe 1 was thought to be closest to the epileptogenic region, and probe 2 was outside seizure focus. It should be noted, that the purpose of implanting iEEG grids

in the patient is that the region of focus has not yet been delineated. Therefore, the placement of recording LD will not necessarily be inside/outside the focus as predicted prior to the intracranial investigation.

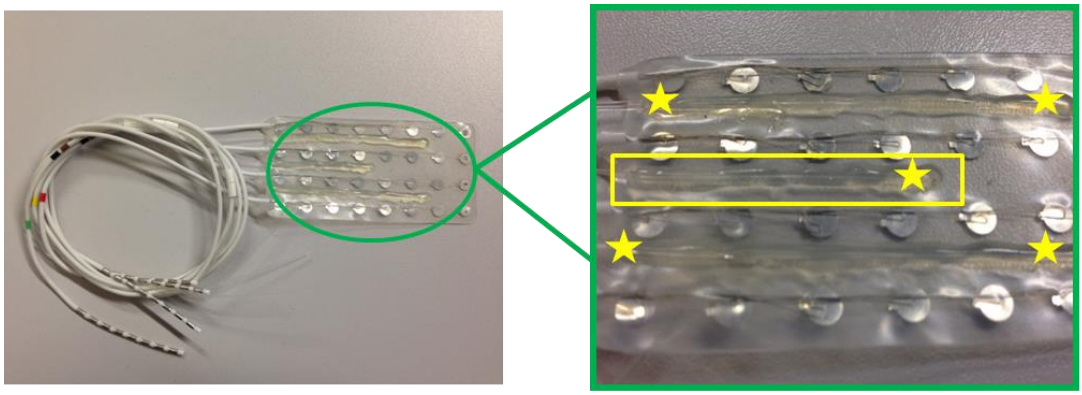

Figure 6.2 Historical LD-iEEG grid
The yellow border on the far right image illustrates the border for one of the Laser Doppler fibres. There are a total of five LD probes placed on this grid, which are represented by yellow stars.

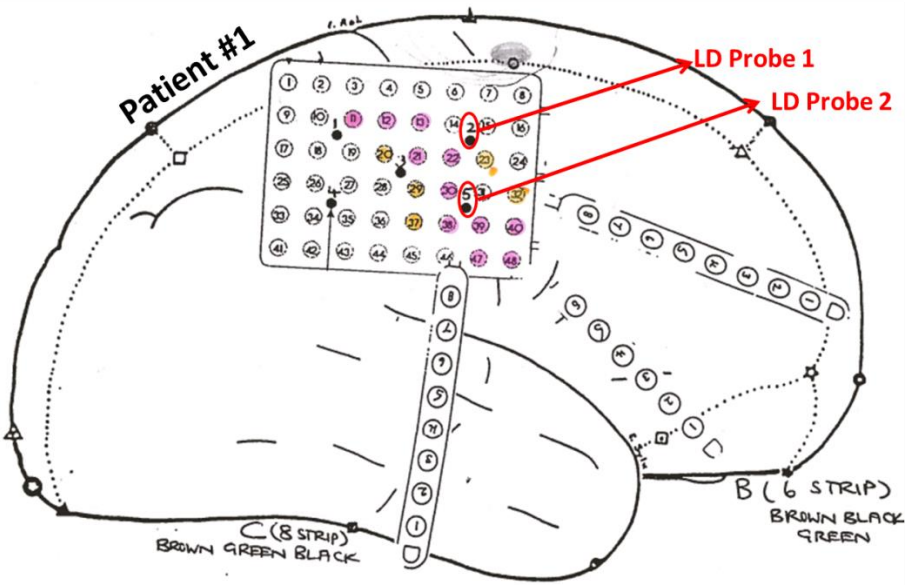

Figure 6.3 Historical data: Patient #1 LD-iEEG grid placement
Simultaneous recordings of iEEG grids (rectangle) and strips (oblong) can be seen with their embedded electrodes (black circles) and LD probes (black dots). Two Laser Doppler probes (red circles) were embedded in the grid. The EEG electrodes measuring increased epileptic activity are highlighted in pink and orange for higher and lower IED frequency respectively.

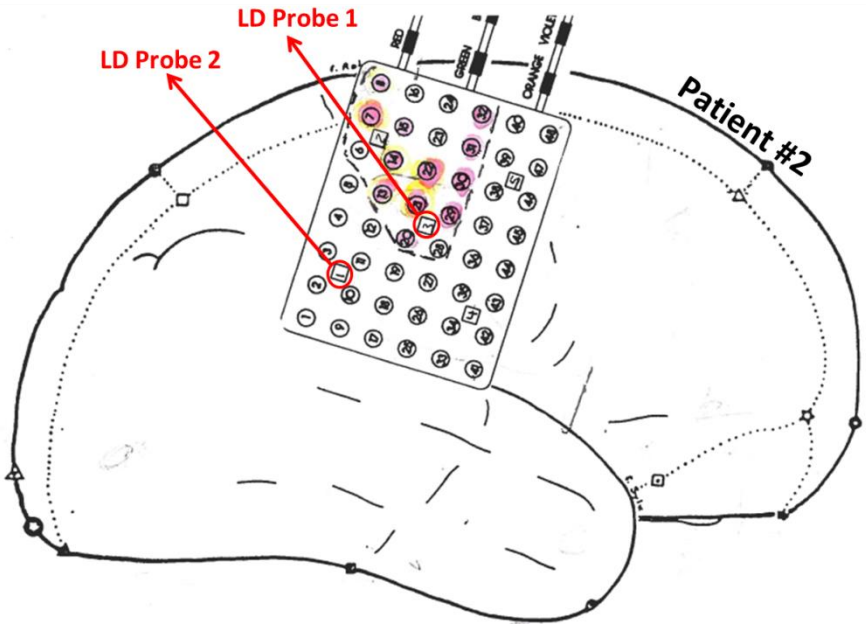

Figure 6.4 Historical data: Patient #2 LD-iEEG grid placement
Simultaneous recordings of iEEG grids (rectangle) and strips (oblong) can be seen with their embedded electrodes (black circles) and LD probes (black dots). Two Laser Doppler probes (red circles) were embedded in the grid. The EEG electrodes measuring increased epileptic activity are highlighted in pink and orange for higher and lower IED frequency respectively. The subsequent area of resection is marked by the dotted line.

6.3.2 Current Laser Doppler Design

The new design by Perimed has resolved most of the issues associated with the previous LD probe design (see Figure 6.5). The clotting problem was addressed by strengthening the outer sheath, which also allowed for the fibre to descend perpendicular to the surface. Additionally, the bending of fibres was eliminated by using a protective wire casing.

These new advancements in the LD probe design are highly encouraging. The example given in Figure 6.5 is designed specifically for an EEG strip (Winkler et al., 2012). However, in the current study, we will be using LD within an EEG grid. The initial concern for using LD on a standard iEEG grid was the probe protrusion, which is approximately 5mm. However, this protrusion is not sufficient to cause any additional risk, which was confirmed by the GOSH paediatric epilepsy

neurosurgeon, Martin Tisdall. As a result of these beneficial advancements, the new probe design will be used for future Laser Doppler data collection.

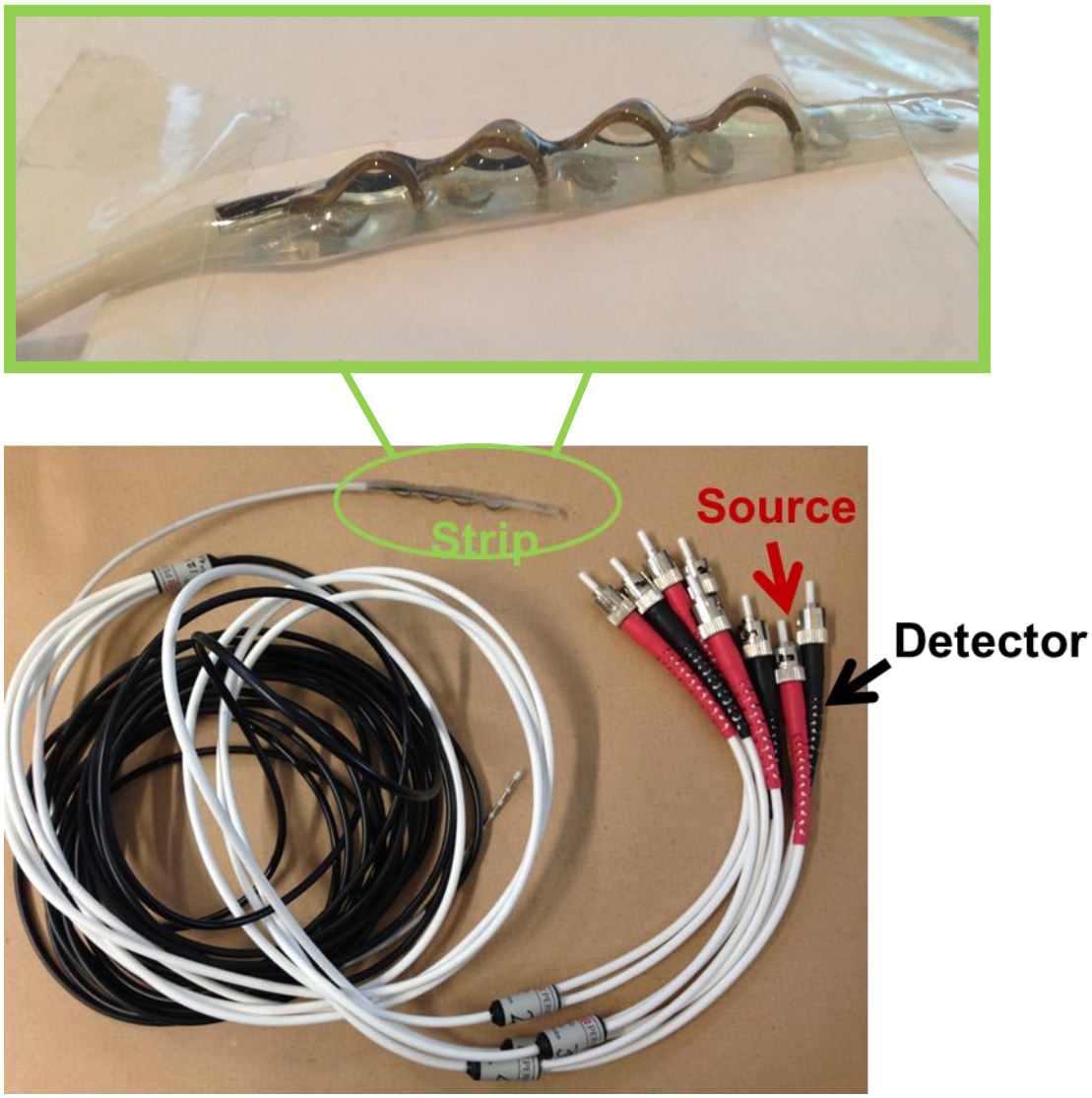

Figure 6.5 Modern Laser Doppler-iEEG strip design
The top panel displays the iEEG strip which includes both EEG (circles) and Laser Doppler probes (curved platinum wires) and is placed on the cerebrum by the surgeon. The bottom panel shows the source (red) and detector (black) fibres from the strip are then transferred through protected cables preventing damage or fibre bending.

6.4 Results

There are two sets of data that will be analysed. The first is a set of historical simultaneous LD-iEEG data gathered approximately 10 years ago at GOSH from

paediatric pre-surgical patients with focal epilepsy (n = 3) with a wavelength of 780nm. Continuous LD-iEEG recordings were integrated with clinical protocol to find seizure focus. The second dataset, which has yet to be gathered, will be LD-iEEG from current pre-surgical patients using an updated LD probe.

6.4.1 Historical Laser Doppler Data

Though the ease of implantation is attractive for this older probe design, the measurement output is not accurate due to design flaws. These include blood clotting, angle of penetration, and fibre bending. The first issue of blood clotting occurs at the LD probe tips due to insufficient cladding. This leads to abnormal changes in the refractive index and inaccurate measurements of flow. The second issue involves the angle of penetration as older probes lie flat on the cerebral surface instead of perpendicular, which would be more efficient in capturing backscattered light. Finally, the exposed fibres are prone to bending at the coupler, thus disturbing measurements. Therefore, results of the historical LD data are dominated by erroneous measurement. Additionally, dropout occurred after approximately 24 hours, possibly caused by the blood coagulation or peripheral wire movement. However, even with these issues, blood flow changes can be seen up to one minute before epileptic events occur with maximum blood flux at 90 PU within the first three hours of recording (see Figure 6.6).

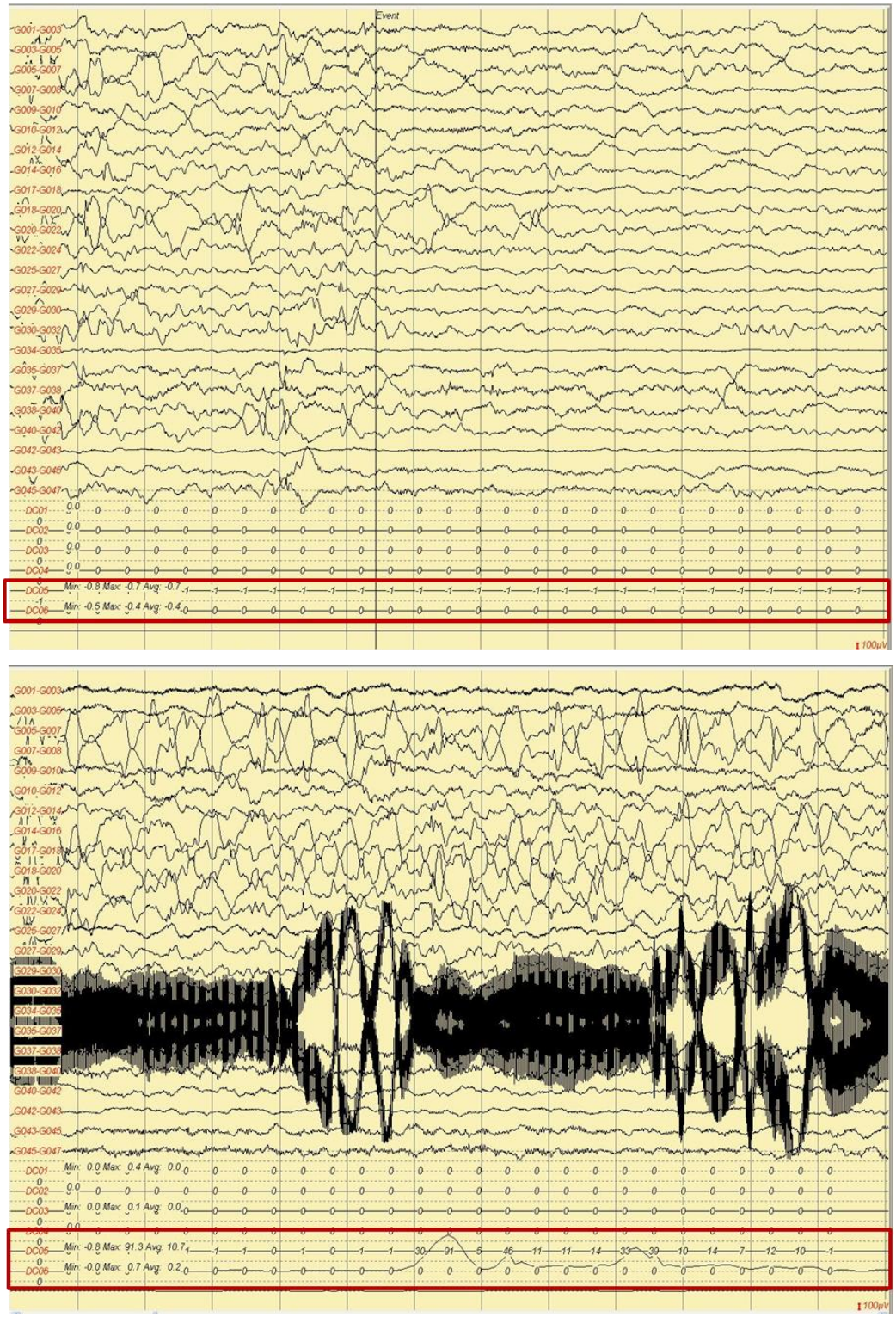

Figure 6.6 Historical Data: Patient #1 LD-iEEG recording

The marking 'Event' represents the start of a seizure. Recorded laser doppler probes are in bottom red panel. The top panel shows LD probe recordings of erroneous measurement between 0-1 during seizure. The bottom panel shows changes in blood flow 1 minute and 20seconds prior to epileptic run with maximum measurements at 90 PU.

6.4.2 Current Laser Doppler Data in Humans

Previously, the LD-iEEG grids were produced in a partnership between GOSH, Perimed, and Ad-Tech. Unfortunately Ad-Tech is currently under investigation by the Federal Drug Administration (FDA) and will not be able to produce any non-standardized grids until the investigation is completed. Other potential EEG grid companies have been contacted, for example DIXI (Besancon, France). However the novel nature of the probes has caused reluctance for advancement on DIXI's behalf for the following reasons:

1. Modified grids must go through a lengthy and expensive testing period to validate process changes.
2. Production is restricted to individual 8x8 grids.
3. Approval of re-sterilization after initial modification is a lengthy and expensive process.

6.5 Discussion

The BOLD signal (described in Chapters 2-3) is a combination of changes in blood flow, blood volume, and oxygen consumption. Therefore, it would be highly beneficial to know the independent effect of blood flow in relation to epileptic activity; this can be measured using simultaneous iEEG-LD. However due to unforeseen difficulties the human iEEG-LD project was not able to continue during the time course of this project. However, if the production restrictions continue, it might be of interest for future studies to work within an animal model. The benefit of this would be greater control of the environment (as is common in animal studies in comparison to humans), and cooperation from the medical instrument companies mentioned above.

Chapter 7 Discussion

7.1 Objectives and General Summary of Results

Neuroimaging techniques such as fMRI are used in pre-surgical evaluations to aid in the characterisation of the epileptogenic zone however they require an understanding of neurovascular coupling during epileptic events. To describe this interaction, I applied multi-modal imaging in a group of paediatric focal epilepsy patients via simultaneous EEG-fMRI (Chapters 2-3) and EEG-NIRS (Chapters 4-5), thereby allowing for both electrical and haemodynamic changes to be measured.

7.1.1 Network Connectivity Reductions are Due to IEDs

Epilepsy is increasingly considered to be a network disease with multi-nodal representations of epileptogenic cortex. In turn, the areas with increased epileptic activity seem to interact with intrinsic connectivity networks, as changes have been reported in large scale resting state networks that can be measured using fMRI. However the impact of IEDs on these networks has yet to be fully explored.

The results presented in Chapter 2 give us a better understanding of the impact of interictal epileptiform activity on these network abnormalities. Uniquely a natural stimulus task was used to target executive control and visual networks while controlling for age differences, patient movement and wakefulness.

EEG-fMRI results showed that intra-network connectivity was decreased in patients with epilepsy, which is likely to be associated with poorer network function and in turn cognitive behavioural performance. Interictal activity seemed to be a major driver of these functional connectivity differences in patients versus controls; this result is particularly relevant as epilepsy can be conceptualised as a network disease. This indicates a pervasive impact of IEDs on network connectivity and subsequently cognition. Therefore, connectivity changes in relation to clinically relevant factors such as seizures or disease duration can only be accurately investigated when controlling for IEDs. This can be achieved by recording and modelling the IEDs as done here.

However, this raises concerns with previous resting state studies and their inferences on network connectivity because, without simultaneous haemodynamic-electrical recordings, there is no way to confirm that differences between groups of patients and controls are not altered by the transient effects of IEDs.

Furthermore, the transient effects of IEDs may progress to more permanent changes, however, if and when this occurs is still unknown. Therefore an interesting topic of study for future work would be to determine whether development from childhood to adulthood promotes the evolution from transient to permanent changes prompted by the loss of brain plasticity. Another question that remains is how IEDs transform over different brain regions, and how this relative transformation impacts network connectivity? For example, what is the impact of IEDs on the epileptogenic network and how does the strength of connectivity from the SOZ to other brain regions compare to controls when IEDs are accounted for? Finally, from a more clinical perspective the pervasive influence of IEDs in a heterogeneous cohort raises questions about whether IED suppression should be included in treatment plans of future focal epilepsy patients. Though it is beyond the scope of this thesis, it is of interest for future clinical work to explore the effects of IED suppression and its subsequent effects on connectivity networks and cognition.

7.1.2 FIR and Quantifying the fMRI Response to Epileptic Spikes

EEG-fMRI has traditionally been reliant on an assumption regarding the relationship between IEDs and haemodynamics: that it is similar to the canonical response to a stimulus. However recent works have raised doubts about applying the canonical HRF in children with epilepsy in response to epileptic activity. Other approaches such as individual HRFs, multi-peak functions, and canonical HRFs with derivatives, have been attempted (Lu et al., 2006; Hawco et al., 2007; Moeller et al., 2008; Jacobs et al., 2009; Rathakrishnan et al., 2010; Rollings et al., 2016), unfortunately all of these methods have their drawbacks such as lack of flexibility, sensitivity, and over-fitting.

Therefore in Chapter 3 we aimed to determine the validity of the canonical model in paediatric patients with focal epilepsy. We found an early haemodynamic response in relation to electrical activity, thereby confirming the need for a new HRF model. The

current canonical HRF was tested against a new model (IED-HRF) to determine the most representative HRF model for a group of paediatric epilepsy patients.

Results for the IED-HRF model showed that haemodynamic responses preceded IED onset. These results indicated that a new basis set should be applied taking this into account. Once this new IED-HRF basis set was tested, a 64% improvement in sensitivity was found in defining the focus from EEG-fMRI maps of the epileptogenic cortex, where previously the canonical model had failed. Therefore, this observed haemodynamic change prior to IED onsets should be taken into account in the future.

The reason for this early response is unclear but could be influenced by neuromodulators and neurotransmitters such as extracellular potassium, oxygen, ATP consumption, and glucose supply. As many of these events cannot be measured by traditional neuroimaging methods such as EEG, it would be interesting for future studies to determine the impact of these components via animal models or invasive measurement techniques.

7.1.3 NIRS Identifying Oxygenation Changes in Seizure Focus

In Chapter 3 a new shape for the IED-HRF was defined. This shape was highly unusual in that the time to peak was much earlier than observed in previous studies. We therefore set out to gain a greater understanding of the underlying physiological responses to IEDs.

Though the BOLD response measured in Chapter 3 is representative of local changes in haemodynamics involving CBF, CBV and $CMRO_2$, the occurrence of oxygenation changes (oxyHb and deoxyHb) prior to epileptic events are better characterised by EEG-NIRS. Therefore, the aim of Chapter 4 was to adapt optical imaging to the clinical environment to extract a haemodynamic response more sensitive to oxygenation changes. The popular cap design for measuring NIRS was not practical for use in paediatric epilepsy patients during clinical video-telemetry. A new flexible grid optode holder design was created and tested (using a series of well-defined tasks in a group of healthy adults) and proven to be more beneficial in the clinical setting

than the standard cap design. After the NIRS holder design was established, the feasibility of using this technique on video-telemetry in-patients was also tested.

The new flexible grid design was able to reliably determine changes in haemodynamics via EEG-NIRS recordings during focal seizures (Chapter 5). Out of a group of 10 paediatric focal epilepsy patients, three had seizure events during simultaneous EEG-NIRS recordings. Results are consistent with previous studies in that there is an increase in oxyHb and HbT after seizure onset. Furthermore, changes prior to seizure onset can also be seen in HbDiff representing cerebral oxygen saturation thereby confirming efficacy of the flexible grid design, and its ability to measure changes in haemodynamics both prior/after the onset of seizure events.

Though pre-ictal/pre-IED changes were seen, results were inconsistent between patients. This was because results were confounded by both physiological and motion artefact. Therefore, future work should correct for systemic physiological parameters such as CO_2 concentration, blood pressure, cerebral blood flow, and a measure of cellular oxidative metabolism (i.e.: cytochrome c oxidase), as well as prospective (motion sensors) and retrospective (FIACH) motion artefact corrections. This will hopefully allow for interpretation of patient semiology and morphological changes seen in single subject HRFs.

7.1.4 The Potential for Invasive Blood Flow Measurements

The fMRI BOLD signal (Chapters 2-3) and the NIRS –oxy and –deoxy haemoglobin changes (Chapters 4-5) describe a combined effect of blood flow, blood volume, oxygen consumption, and changes in the oxygenation state of haemoglobin. However, the independent effect of blood flow in relation to epileptic activity can be better measured by simultaneous iEEG-LD.

Unfortunately, the historical LD-iEEG data was corrupted by noise due to design flaws of the probe (Chapter 6). Since then, the probe design has advanced and most of these defects have been repaired. The goal was to re-test the Laser Doppler in humans, but due to unforeseen difficulties this project could not advance within the time scale of this thesis. Therefore, a possible alternative for future work is to

investigate blood flow using simultaneous iEEG and LD in an animal model, which should prevent the barriers associated with testing paediatric focal epilepsy patients.

7.2 Summary

This thesis includes a wide breadth of research topics under the general theme of understanding the relationship between regional haemodynamic changes and focal epileptic events in children. The use of multi-modal imaging answers questions regarding neurovascular coupling that would otherwise be impossible when using single imaging modalities. The overall outcome illustrated that by utilizing both EEG-fMRI and EEG-NIRS a greater understanding of the haemodynamic changes surrounding epileptic events in children can be obtained. Furthermore, the haemodynamic response from epileptic events is not equivalent to the canonical response to a stimulus described in healthy controls. Therefore epileptic events (i.e.: IEDs) need to be carefully modelled to allow appropriate inference regarding the brain regions showing associated responses to them and interactions between ongoing brain activity and IEDs.

Chapter 8 Appendix

8.1 Connectivity Networks and the Effect of IEDs

Table 8.1 Group Activations for 'Wait' > 'Video'

Group	L/R	Label	Maxima (t-value)	X, Y, Z
Controls	L	Inferior Parietal	8.56	-50, -54, 48
	L	Superior Frontal	8.28	-28, 42, 42
	L+R	Dorsal Medial Prefrontal*	8.14	10, 10, 44
	R	Inferior Parietal	7.57	50, -64, 48
	L+R	Cuneus	7.23	12, -80, 18
	R	Insula	6.94	40, 12, 4
	L	Middle Frontal	6.81	-36, 56, 12
	L	Caudate	6.75	-8, -4, 20
	L	Superior Frontal	6.68	-20, 20, 60
	L	Insula	6.50	-32, 8, 12
	L	Anterior Cingulate	6.41	-4, 48, 8
	R	Anterior Cingulate	6.32	12, 38, 18
	L	Middle Frontal	6.17	-34, 48, 24
	R	Middle Frontal	6.15	44, 50, 16
	L	Putamen	6.09	-28, -14, 12
	R	Piriform cortex	6.07	14, 0, -8
	L	Rolandic Operculum	5.96	-56, -2, 14
	R	Caudate	5.86	18, 0, 22
	R	Putamen	5.70	28, -4, 14
	L	Precentral	5.58	-34, -20, 50
	R	Middle Frontal	5.58	38, 26, 50
	L	Posterior Cingulate	5.41	-10, -41, 15
	L	Cuneus	5.28	-8, -72, 34
	R	Anterior Cingulate	5.27	6, 30, 24
	R	Cuneus	5.26	10, -64, -4
	L	Superior Medial Frontal	5.25	-4, 34, 40
Patients	L+R	Dorsal Medial Prefrontal*	7.50	2, 16, 48

	L+R	Cuneus	6.76	10, -88, 22
	L	Insula	6.20	-50, 14, -6
	R	Caudate	6.08	18, 8, 14
	L+R	Middle Cingulate	6.04	0, -20, 30
	R	Inferior Parietal	5.94	52, -46, 50
	R	Insula	5.60	42, 12, -6
Group	L	Superior Frontal	6.13	-28, 42, 42
Differences	L+R	Middle Cingulate	4.97	-12, -30, 44
	L	Middle Frontal	4.64	-26, 20, 54
	L	Inferior Parietal	4.39	-52, -54, 50

L: Left, R: Right.

**Also consisting middle cingulate*

Table 8.2 Group Activations for 'Video' > 'Wait'

Group	L/R	Label	Maxima (t-value)	X, Y, Z
Controls	R	Fusiform	12.76	38, -60, -12
	L	Middle Occipital	10.87	-22, -98, 6
	R	Middle Occipital	10.48	40, -76, 8
	L	Fusiform	10.25	-36, -78, -12
	L	Middle Temporal	6.59	-50, -46, 16
	R	Middle Temporal	6.20	54, -4, -16
Patients	L	Middle Occipital	9.36	-40, -84, 8
	R	Middle Temporal	9.31	48, -70, 6
	R	Fusiform	8.01	38, -60, -14
	R	Calcarine	6.74	22, -56, 18
	R	Thalamus	6.54	20, -28, 0
	L	Fusiform	6.27	-42, -46, -18
	L	Middle Temporal	6.12	-56, -48, 14
Group	R	Fusiform	5.81	38, -58, -12
Differences	L	Middle Occipital	5.25	-20, -100, 6
	L	Fusiform	5.17	-42, -78, -14

L: Left, R: Right.

Table 8.3 Paired t-test for FC Controlling vs Not Controlling for IEDs

Seed	L/R	Label	Maxima (t-value)	X, Y, Z
Middle	L+R	Middle Cingulate	8.18	0, -34, 50
Cingulate	L	Inferior Parietal	6.20	-46, -56, 44
	R	Caudate	7.50	10, -16, 14
	R	Middle Cingulate	6.87	4, 10, 36
	R	Postcentral Gyrus	6.06	58, -6, 36
	R	Inferior Parietal	6.43	48, -56, 38
	R	Insula	6.14	36, 4, 10
	L	Rolandic Operculum	6.36	-60, 0, 4
	R	Caudate	6.16	18, -8, 26
	R	Insula	6.14	36, 4, 10
	L	Supplementary Motor Area	6.09	-2, 0, 68
	R	Supplementary Motor Area	6.08	6, -8, 70
	L	Caudate	6.08	-20, -18, 26
	L	Precuneus	6.07	-6, -74, 40
	R	Postcentral Gyrus	6.06	58, -6, 36
	L	Caudate	6.06	-12, 16, 16
	L	Superior Temporal Pole	6.06	-48, 16, -16
	R	Caudate	6.01	14, 10, 22
	L	Paracentral Lobule	5.97	-6, -26, 72
	R	Putamen	5.97	22, 22, 0
	R	Precentral Gyrus	5.93	58, 8, 32
	L	Cerebellum	6.13	-34, -60, -32
	R	Cerebellum	5.94	38, -66, -44
Right	R	Fusiform	8.66	32, -66, -16
Fusiform	R	Fusiform	8.37	48, -38, -12
	L	Fusiform	7.74	-36, -56, -24
	L	Lingual	7.39	-10, -88, -16
	L	Superior Temporal	7.28	-66, -12, 8
	L	Parahippocampal	6.80	22, -16, -18
	R	Putamen	6.67	22, 16, -6
	R	Inferior Temporal	6.39	52, -60, -18

L	Rolandic Operculum	6.37	-62, 4, 6
L	Middle Temporal	6.28	-64, -56, -4
L	Inferior Occipital	6.28	-50, -70, -12
L	Paracentral Lobule	6.15	-2, -12, 74
R	Inferior Orbital Frontal	6.13	24, 28, -24
L	Calcarine	6.04	2, -86, -2
R	Supplementary Motor Area	6.00	4, -12, 74
R+L	Cerebellar Vermis	6.50	0, -80, -22

IEDs: Interictal Epileptiform Discharges, L: Left, R: Right.

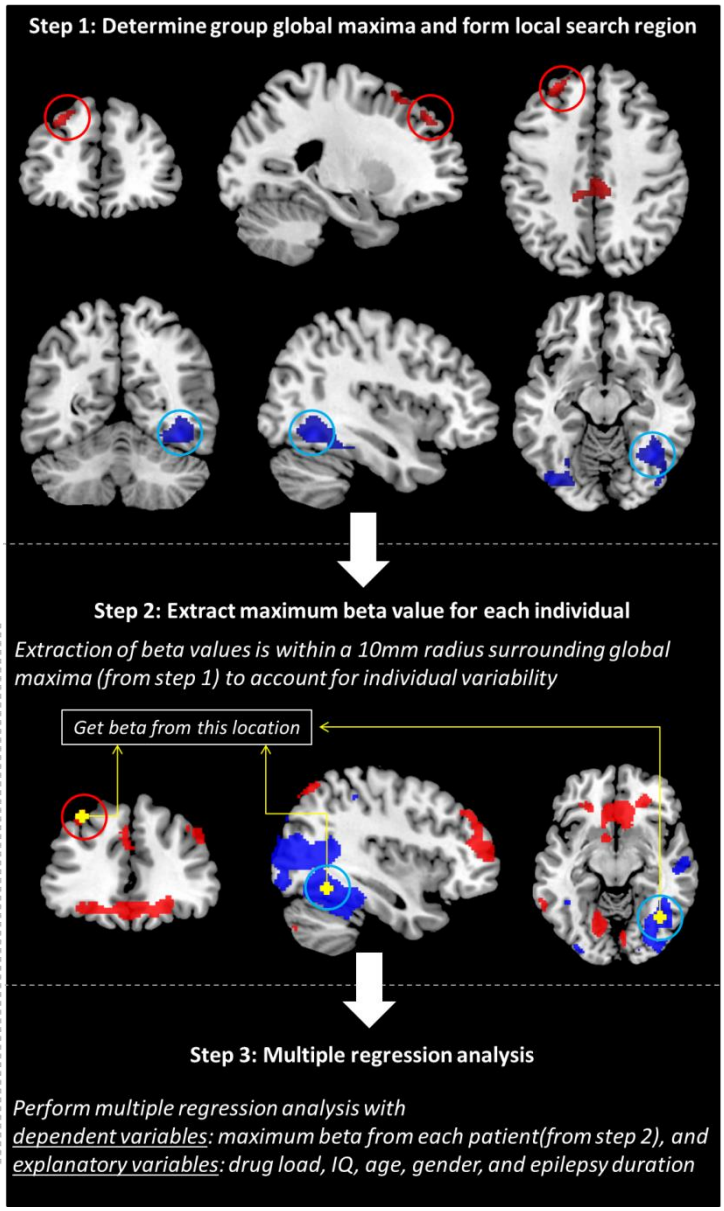

Figure 8.1 Spatial Definition for ROI determining Effect of Clinical Variables
Defining the effect of clinical variables by extracting the maximum patient response magnitude. Step 1) Determining the global maxima in group differences. Step 2) Extracting the maximum beta value within 10mm of the global maxima determined in Step 1. Step 3) Performing a multiple regression analysis with clinical variables and patient betas.

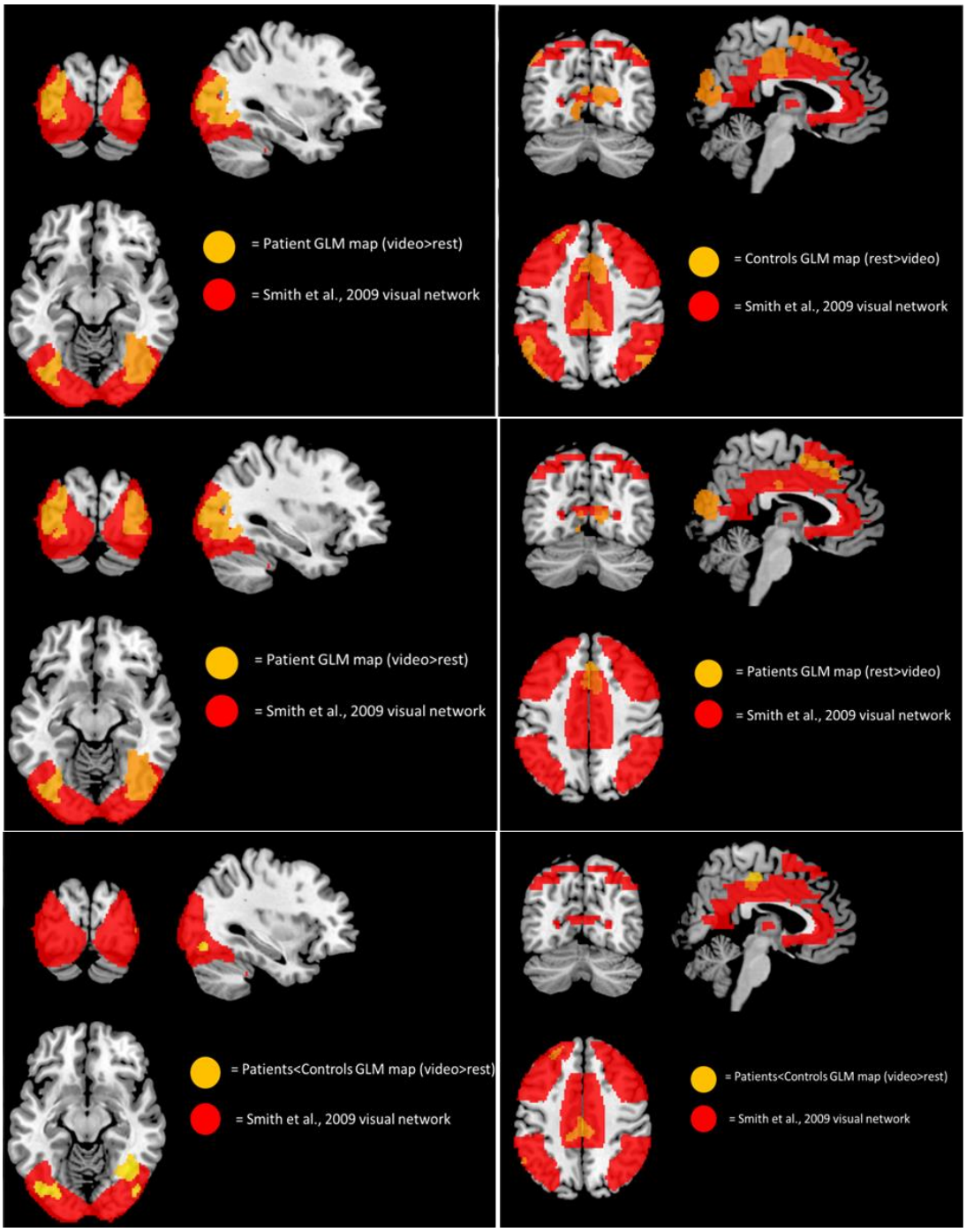

Figure 8.2 Network overlays of the General Linear Model
Overlay of resulting group difference maps in the general linear model analysis (orange) against the networks defined by Seeley et al. (2007) and Smith et al. (2009) (red). Visual and executive control network ICNs are displayed in the left and right panels respectively.

Table 8.4 Control Network Overlap with Previous Studies: GLM

Network	Reference Regions	AAL Atlas Regions	Concordant
Executive Control			
Seeley et al. (2007) &	Dorsolateral Frontal/Middle Frontal†‡	Superior Frontal/Middle Frontal	Yes
Smith et al. (2009)		Precentral	Yes
	Anterior Thalamus†	Thalamus	No
	Lateral Parietal†	Inferior Parietal	Yes
	Precuneus‡	Precuneus	Yes
	Dorsal Caudate Nucleus†	Caudate	Yes
	Anterior Cingulate‡	Anterior Cingulate	Yes
	Paracingulate‡	Anterior Cingulate/Middle Cingulate/Posterior Cingulate	Yes
	Ventrolateral Prefrontal Cortex†	Right Inferior Frontal Gyrus	Yes
		Insula	Yes
		Cuneus	No
		Putamen	No
		Dorsal Medial Prefrontal	Yes
		Rolandic Operculum	No
			Network Overlap = 71%

Visual			
Smith et al. (2009)	Occipital Pole‡	Calcarine	Yes
	Lateral Visual‡	Middle Occipital/Middle Temporal	Yes
	V1‡	Lingual/Calcarine	Yes
	V2‡	Lingual/Inferior Occipital	Yes
	V3‡	Fusiform /Inferior Occipital	Yes
			Network Overlap = 100%

† Region defined in Seeley et al. (2007)

‡ Region defined in Smith et al. (2009)

Table 8.5 Patient Network Overlap with Previous Studies: GLM

Network	Reference Regions	AAL Atlas Regions	Concordant
Executive Control			
Seeley et al. (2007) &	Dorsolateral Frontal/Middle Frontal†‡	Superior Frontal/Middle Frontal	No
Smith et al. (2009)		Precentral	No
	Anterior Thalamus†	Thalamus	No
	Lateral Parietal†	Inferior Parietal	Yes
	Precuneus‡	Precuneus	No
	Dorsal Caudate Nucleus†	Caudate	Yes
	Anterior Cingulate‡	Anterior Cingulate	No
	Paracingulate‡	Anterior Cingulate/Middle Cingulate/Posterior Cingulate	Yes
	Ventrolateral Prefrontal Cortex†	Right Inferior Frontal Gyrus	No
		Insula	Yes
		Cuneus	No
		Putamen	No
		Dorsal Medial Prefrontal	No
		Rolandic Operculum	No
			Network Overlap = 29%

Visual			
Smith et al. (2009)	Occipital Pole‡	Calcarine	Yes
	Lateral Visual‡	Middle Occipital/Middle Temporal	Yes
	V1‡	Lingual/Calcarine	Yes
	V2‡	Lingual/Inferior Occipital	Yes
	V3‡	Fusiform /Inferior Occipital	Yes
			Network Overlap = 100%

† Region defined in Seeley et al. (2007)

‡ Region defined in Smith et al. (2009)

Table 8.6 Group Difference Network Overlap with Previous Studies: GLM

Network	Reference Regions	AAL Atlas Regions	Concordant
Executive Control			
Seeley et al. (2007) &	Dorsolateral Frontal/Middle Frontal†‡	Superior Frontal/Middle Frontal	Yes
Smith et al. (2009)		Precentral	No
	Anterior Thalamus†	Thalamus	No
	Lateral Parietal†	Inferior Parietal	Yes
	Precuneus‡	Precuneus	No
	Dorsal Caudate Nucleus†	Caudate	No
	Anterior Cingulate‡	Anterior Cingulate	No
	Paracingulate‡	Anterior Cingulate/Middle Cingulate/Posterior Cingulate	Yes
	Ventrolateral Prefrontal Cortex†	Right Inferior Frontal Gyrus	Yes
		Insula	No
		Cuneus	No
		Putamen	No
		Dorsal Medial Prefrontal	Yes
		Rolandic Operculum	No
			Network Overlap = 36%

Visual			
Smith et al. (2009)	Occipital Pole‡	Calcarine	No
	Lateral Visual‡	Middle Occipital/Middle Temporal	Yes
	V1‡	Lingual/Calcarine	Yes
	V2‡	Lingual/Inferior Occipital	Yes
	V3‡	Fusiform /Inferior Occipital	Yes
			Network Overlap = 80%

† Region defined in Seeley et al. (2007)

‡ Region defined in Smith et al. (2009)

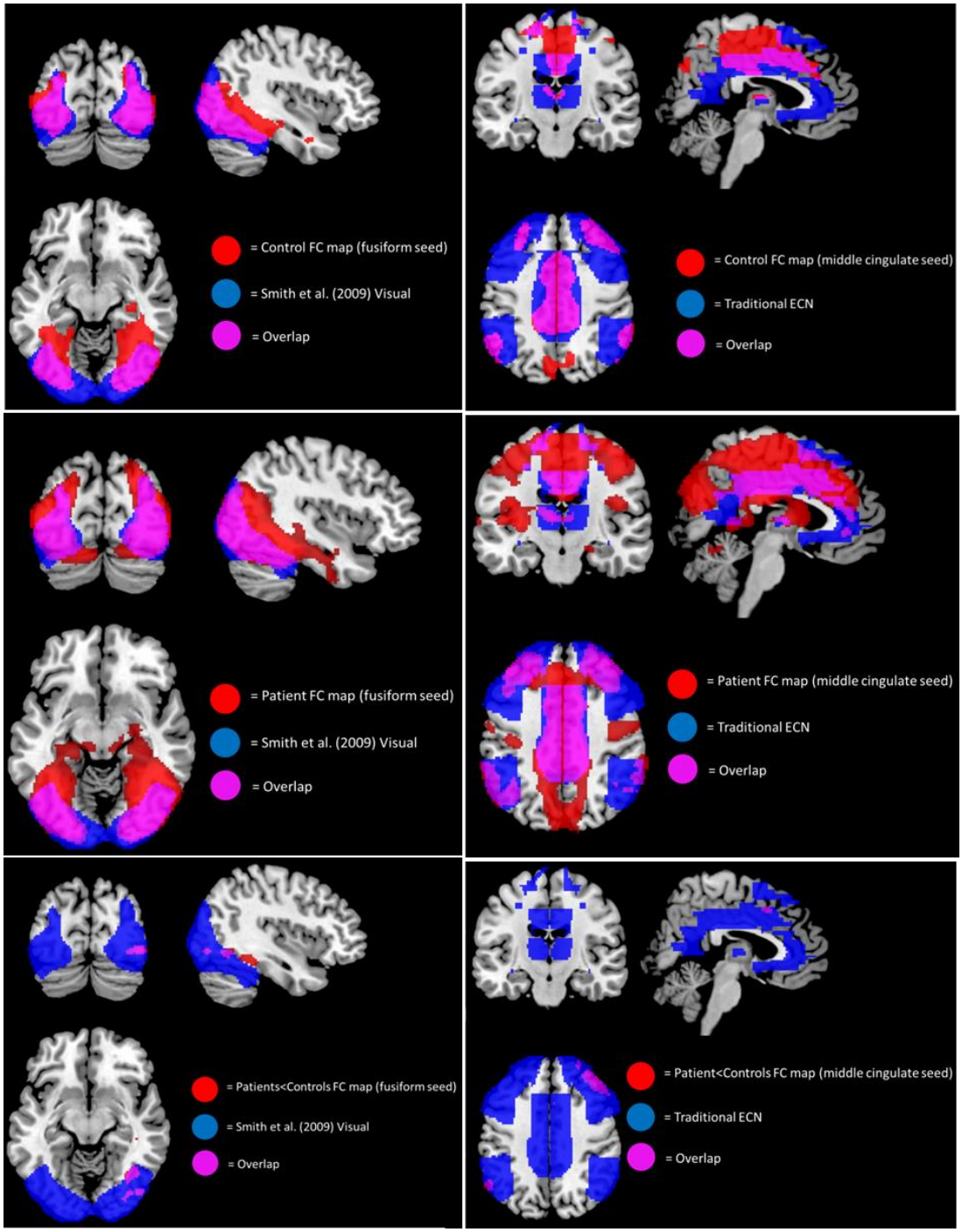

Figure 8.3 Network overlays of the functional connectivity map
Results in the current study for control groups are presented in red, while the traditional representations of ICNs are presented in blue (Seeley et al., 2007; Smith et al., 2009). The resulting overlap is shown in magenta. Networks from the fusiform (left panel) and middle cingulate (right panel) seeds are displayed.

Table 8.7 Control Network Overlap with Previous Studies: FC

Network	Reference Regions	AAL Atlas Regions	Concordant
Executive Control			
Seeley et al. (2007) &	Dorsolateral Frontal/Middle Frontal†‡	Superior Frontal/Middle Frontal	Yes
Smith et al. (2009)		Precentral	Yes
	Anterior Thalamus†	Thalamus	Yes
	Lateral Parietal†	Inferior Parietal	Yes
	Precuneus‡	Precuneus	Yes
	Dorsal Caudate Nucleus†	Caudate	Yes
	Anterior Cingulate‡	Anterior Cingulate	Yes
	Paracingulate‡	Anterior Cingulate/Middle Cingulate/Posterior Cingulate	Yes
	Ventrolateral Prefrontal Cortex†	Right Inferior Frontal Gyrus	Yes
		Insula	Yes
		Cuneus	No
		Putamen	No
		Dorsal Medial Prefrontal	Yes
		Rolandic Operculum	No
			Network Overlap = 79%

Visual			
Smith et al. (2009)	Occipital Pole‡	Calcarine	Yes
	Lateral Visual‡	Middle Occipital/Middle Temporal	Yes
	V1‡	Lingual/Calcarine	Yes
	V2‡	Lingual/Inferior Occipital	Yes
	V3‡	Fusiform /Inferior Occipital	Yes
			Network Overlap = 100%

† Region defined in Seeley et al. (2007)

‡ Region defined in Smith et al. (2009)

Table 8.8 Patient Network Overlap with Previous Studies: FC

Network	Reference Regions	AAL Atlas Regions	Concordant
Executive Control			
Seeley et al. (2007) &	Dorsolateral Frontal/Middle Frontal†‡	Superior Frontal/Middle Frontal	Yes
Smith et al. (2009)		Precentral	Yes
	Anterior Thalamus†	Thalamus	Yes
	Lateral Parietal†	Inferior Parietal	Yes
	Precuneus‡	Precuneus	Yes
	Dorsal Caudate Nucleus†	Caudate	Yes
	Anterior Cingulate‡	Anterior Cingulate	Yes
	Paracingulate‡	Anterior Cingulate/Middle Cingulate/Posterior Cingulate	Yes
	Ventrolateral Prefrontal Cortex†	Right Inferior Frontal Gyrus	Yes
		Insula	Yes
		Cuneus	No
		Putamen	No
		Dorsal Medial Prefrontal	Yes
		Rolandic Operculum	No
			Network Overlap = 79%

Visual			
Smith et al. (2009)	Occipital Pole‡	Calcarine	Yes
	Lateral Visual‡	Middle Occipital/Middle Temporal	Yes
	V1‡	Lingual/Calcarine	Yes
	V2‡	Lingual/Inferior Occipital	Yes
	V3‡	Fusiform /Inferior Occipital	Yes
			Network Overlap = 100%

† Region defined in Seeley et al. (2007)

‡ Region defined in Smith et al. (2009)

Table 8.9 Group Difference Network Overlap with Previous Studies: FC

Network	Reference Regions	AAL Atlas Regions	Concordant
Executive Control			
Seeley et al. (2007) &	Dorsolateral Frontal/Middle Frontal†‡	Superior Frontal/Middle Frontal	Yes
Smith et al. (2009)		Precentral	No
	Anterior Thalamus†	Thalamus	No
	Lateral Parietal†	Inferior Parietal	Yes
	Precuneus‡	Precuneus	No
	Dorsal Caudate Nucleus†	Caudate	Yes
	Anterior Cingulate‡	Anterior Cingulate	No
	Paracingulate‡	Anterior Cingulate/Middle Cingulate/Posterior Cingulate	Yes
	Ventrolateral Prefrontal Cortex†	Right Inferior Frontal Gyrus	Yes
		Insula	Yes
		Cuneus	No
		Putamen	No
		Dorsal Medial Prefrontal	Yes
		Rolandic Operculum	No
			Network Overlap = 50%

Visual			
Smith et al. (2009)	Occipital Pole‡	Calcarine	No
	Lateral Visual‡	Middle Occipital/Middle Temporal	Yes
	V1‡	Lingual/Calcarine	No
	V2‡	Lingual/Inferior Occipital	Yes
	V3‡	Fusiform /Inferior Occipital	Yes
			Network Overlap = 60%

† Region defined in Seeley et al. (2007)

‡ Region defined in Smith et al. (2009)

8.2 Principal Components Analysis

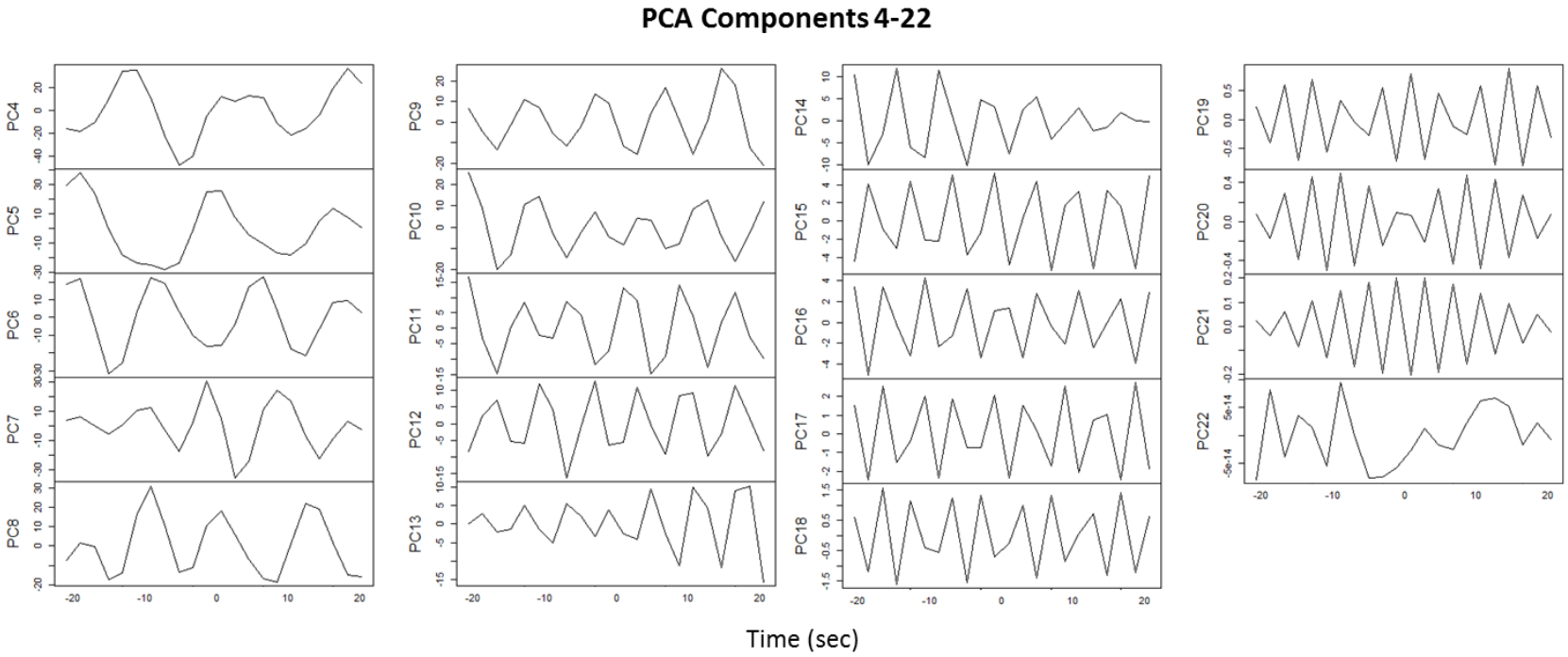

Figure 8.4 Principal components characterised as noise

The remaining components that were identified as noise (components 4-22) are illustrated above. 'PC' stands for principal component. Each principal component is defined from 20 seconds prior to onset (time point 0) and 20 seconds after onset.

References

Adelson PD, Nemoto E, Scheuer M, Painter M, Morgan J, Yonas H (1999): Noninvasive continuous monitoring of cerebral oxygenation periictally using near-infrared spectroscopy: a preliminary report. Epilepsia 40:1484–1489.

Aguirre GK, Zarahn E, D'esposito M (1998): The variability of human, BOLD hemodynamic responses. Neuroimage 8:360–9.

Allen PJ, Josephs O, Turner R (2000): A method for removing imaging artifact from continuous EEG recorded during functional MRI. Neuroimage 12:230–239.

Allen PJ, Polizzi G, Krakow K, Fish DR, Lemieux L (1998): Identification of EEG events in the MR scanner: the problem of pulse artifact and a method for its subtraction. Neuroimage 8:229–239.

Babb TL, Brown WJ (1987): Pathological Findings in Epilepsy. Surgical Treatment of the Epilepsies. New York: Raven Press: 511-540.

Bahar S, Suh M, Zhao M, Schwartz TH (2006): Intrinsic optical signal imaging of neocortical seizures: the "epileptic dip". Neuroreport 17:499–503.

Bale G, Mitra S, Meek J, Robertson N, Tachtsidis I (2014): A new broadband near-infrared spectroscopy system for in-vivo measurements of cerebral cytochrome-c-oxidase changes in neonatal brain injury. Biomed Opt Express 5:3450–66.

Banaji M, Mallet A, Elwell CE, Nicholls P, Tachtsidis I, Smith M, Cooper CE (2010): Modelling of mitochondrial oxygen consumption and NIRS detection of cytochrome oxidase redox state. Adv Exp Med Biol 662:285–291.

Berkovic SF, Heron SE, Giordano L, Marini C, Guerrini R, Kaplan RE, Gambardella A, Steinlein OK, Grinton BE, Dean JT, Bordo L, Hodgson BL, Yamamoto T, Mulley JC, Zara F, Scheffer IE (2004): Benign Familial Neonatal-Infantile Seizures: Characterization of a New Sodium Channelopathy. Ann Neurol 55:550–557.

Bettus G, Ranjeva J-P, Wendling F, Bénar CG, Confort-Gouny S, Régis J, Chauvel P, Cozzone PJ, Lemieux L, Bartolomei F, Guye M (2011): Interictal functional connectivity of human epileptic networks assessed by intracerebral EEG and BOLD signal fluctuations. PLoS One 6:e20071.

Bloch F (1946): Nuclear induction. Phys Rev 70:460–474.

Bloembergen N, Purcell EM, Pound R V (1947): Relaxation Effects in Nuclear Magnetic Resonance Absorption 73.

Bonner R, Nossal R (1981): Model for laser doppler measurments of blood flow in tissue. Appl Opt 20:2097–2107.

Boynton GM, Engel SA, Glover GH, Heeger DJ (1996): Linear systems analysis of functional magnetic resonance imaging in human V1. J Neurosci 16:4207–4221.

Brevard ME, Kulkarni P, King J a., Ferris CF (2006): Imaging the neural substrates involved in the genesis of pentylenetetrazol-induced seizures. Epilepsia 47:745–754.

Bromfield EB, Cavazos JE, Sirven JL (2006): An introduction to epilepsy. West Hartford (CT): American Epilepsy Society. Chapter 1, Basic Mechanisms Underlying Seizures and Epilepsy.

Brown CD, Davis HT, Ediger MN, Fleming CM, Hull EL, Rohrscheib M (2005): Clinical assessment of near-infrared spectroscopy for noninvasive diabetes screening. Diabetes Technol Ther 7:456–66.

Buchheim K, Obrig H, Pannwitz W V., Müller A, Heekeren H, Villringer A, Meierkord H (2004): Decrease in haemoglobin oxygenation during absence seizures in adult humans. Neurosci Lett 354:119–122.

Buxton RB (2001): The elusive initial dip. Neuroimage 13:953–958.

Buxton RB (2002): Coupling between CBF and CMRO2 during neuronal activity. Int Congr Ser 1235:23–32.

Buxton RB, Frank LR (1997): A model for the coupling between cerebral blood flow and oxygen metabolism during neural stimulation. J Cereb Blood Flow Metab 17:64–72.

Buxton RB, Uludağ K, Dubowitz DJ, Liu TT (2004): Modeling the hemodynamic response to brain activation. Neuroimage 23 Suppl 1:S220-33.

Buxton RB, Wong EC, Frank LR (1998): Dynamics of blood flow and oxygenation changes during brain activation: the ballon model. Magn Reson Med 39:855–864.

Caddick SJ, Hosford DA (1996): The Role of GABA B Mechanisms in Animal Models of Absence Seizures Thalamocortical Circuitry : Extrinsic and Intrinsic Mechanisms Underlying. Mol Neurobiol 13:23–32.

Carmichael DW, Vulliemoz S, Rodionov R, Thornton JS, McEvoy a W, Lemieux L (2012): Simultaneous intracranial EEG-fMRI in humans: protocol considerations and data quality. Neuroimage 63:301–9.

Cauli B (2004): Cortical GABA Interneurons in Neurovascular Coupling: Relays for Subcortical Vasoactive Pathways. J Neurosci 24:8940–8949.

Centeno M, Carmichael DW (2014): Network Connectivity in Epilepsy: Resting State fMRI and EEG-fMRI Contributions. Front Neurol 5:93.

Centeno M, Perani S, Tierney,TM, Shamshiri EA, StPier K, Konn D, Banks T, Vulliemoz S, Lemieux L, Pressler RM, Clark CA, Cross JH, Carmichael DW (2016b). EEG-fMRI and ESI together improve localization accuracy and predict surgery outcome in focal epilepsy. Annals of Neurology (submitted).

Centeno M, Tierney TM, Perani S, Shamshiri E a, StPier K, Wilkinson C, Konn D, Banks T, Vulliemoz S, Lemieux L, Pressler RM, Clark C a, Cross JH, Carmichael DW (2016): Optimising EEG-fMRI for Localisation of Focal Epilepsy in Children. PLoS One 11:e0149048.

Chaudhary UJ, Carmichael DW, Rodionov R, Thornton RC, Bartlett P, Vulliemoz S, Micallef C, McEvoy AW, Diehl B, Walker MC, Duncan JS, Lemieux L (2012): Mapping preictal and ictal haemodynamic networks using video-electroencephalography and functional imaging. Brain a J Neurol 135:3645–3663.

Chaudhary UJ, Centeno M, Carmichael DW, Vollmar C, Rodionov R, Bonelli S, Stretton J, Pressler R, Eriksson SH, Sisodiya S, Friston K, Duncan JS, Lemieux L, Koepp M (2013): Imaging the interaction: epileptic discharges, working memory, and behavior. Hum Brain Mapp 34:2910–7.

Chaudhary UJ, Duncan JS, Lemieux L (2013): Mapping hemodynamic correlates of seizures using fMRI: A review. Hum Brain Mapp 34:447–466.

Chen ST, Hsu CY, Hogan EL, Maricq H, Balentine JD (1986): A model of focal ischemic stroke in the rat: reproducible extensive cortical infarction. Stroke 17:738–743.

Chohan MO, Moore H (2016): Interneuron Progenitor Transplantation to Treat CNS Dysfunction. Front Neural Circuits 10:1–10.

Cohen MS (1997): Parametric analysis of fMRI data using linear systems methods. Neuroimage 6:93–103.

Colasante G, Lignani G, Rubio A, Medrihan L, Yekhlef L, Sessa A, Massimino L, Giannelli SG, Sacchetti S, Caiazzo M, Leo D, Alexopoulou D, Dell'Anno MT, Ciabatti E, Orlando M, Studer M, Dahl A, Gainetdinov RR, Taverna S, Benfenati F, Broccoli V (2015): Rapid Conversion of Fibroblasts into

Functional Forebrain GABAergic Interneurons by Direct Genetic Reprogramming. Cell Stem Cell 17:719–734.

Conroy, P. (1996): Definitions and Formulae. Folens, 22.

Cooper R, Winter A., Crow H, Walter WG (1965): Comparison of subcortical, cortical and scalp activity using chronically indwelling electrodes in man. Electroencephalogr Clin Neurophysiol 18:217–228.

Cooper RJ, Everdell NL, Enfield LC, Gibson a P, Worley A, Hebden JC (2009): Design and evaluation of a probe for simultaneous EEG and near-infrared imaging of cortical activation. Phys Med Biol 54:2093–102.

Cooper RJ, Hebden JC, O'Reilly H, Mitra S, Michell AW, Everdell NL, Gibson AP, Austin T (2011): Transient haemodynamic events in neurologically compromised infants: A simultaneous EEG and diffuse optical imaging study. Neuroimage 55:1610–1616.

Cope M, Delpy DT (1988): System for long-term measurement of cerebral blood and tissue oxygenation on newborn infants by near infra-red transillumination. Med Biol Eng Comput 26:289–294.

Coyle SM, Ward TE, Markham CM, Ward E, Markham CM (2007): Brain-computer interface using a simplified functional near-infrared spectroscopy system. J Neural Eng 4:219–26.

Cross TJ, Sabapathy S (2015): The impact of venous occlusion per se on forearm muscle blood flow: Implications for the near-infrared spectroscopy venous occlusion technique. Clin Physiol Funct Imaging:1–6.

Cui X, Bray S, Bryant DM, Glover GH, Reiss AL (2011): A quantitative comparison of NIRS and fMRI across multiple cognitive tasks. Neuroimage 54:2808–2821.

Davis TL, Kwong KK, Weisskoff RM, Rosen BR (1998): Calibrated functional MRI: mapping the dynamics of oxidative metabolism. Proc Natl Acad Sci U S A 95:1834–9.

De Curtis M, Avanzini G (2001): Interictal spikes in focal epileptogenesis. Prog Neurobiol 63:541–567.

Delpy DT, Cope M, van der Zee P, Arridge S, Wray S, Wyatt J (1988): Estimation of optical pathlength through tissue from direct time of flight measurement. Phys Med Biol 33:1433–1442.

Dingledine R, Varvel NH, Dudek FE (2014): When and How Do Seizures Kill Neurons, and Is Cell Death Relevant to Epileptogenesis? Adv Exp Med Biol 813:109–122.

Donahue MJ, Juttukonda MR, Watchmaker JM (2016): Noise concerns and post-processing procedures in cerebral blood flow (CBF) and cerebral blood volume (CBV) functional magnetic resonance imaging. Neuroimage.

Dongmei An, Firas Fahoum, Jeffery Hall, André Olivier, Jean Gotman and F, Dubeau (2013): Electroencephalography/functional magnetic resonance imaging responses help predict surgical outcome in focal epilepsy. Disabil Rehabil 54:2184–2194.

Doucet G, Osipowicz K, Sharan A, Sperling MR, Tracy JI (2012): Extratemporal functional connectivity impairments at rest are related to memory performance in mesial temporal epilepsy. Hum Brain Mapp.

Ebus S, Arends J, Hendriksen J, van der Horst E, de la Parra N, Hendriksen R, Santegoeds E, Boon P, Aldenkamp B (2012): Cognitive effects of interictal epileptiform discharges in children. Eur J Paediatr Neurol 16:697–706.

Edvinsson L, Krause DN (2002): Cerebral blood flow and metabolism (pp. 191-211). New York: Lippincott Williams and Wilkins.

Emerson RG, Turner CA, Pedley TA, Walczak TS, Forgione M (1995): Propagation patterns of temporal spikes. Electroencephalogr Clin Neurophysiol 94:338–348.

Engel J, Pedley TA, Aicardi J, Dichter MA, Moshe S (2007): Epilepsy: A Comprehensive Textbook. New York: Lippincott, Williams and Wilkins.

Escayg A, MacDonald B, Meisler M, Baulac S, Huberfeld G, An-Gourfinkel I, Brive A, LeGuern E, Moulard B, Chaigne D (2000): Mutations of SCN1A, encoding a neuronal sodium channel, in two families with GEFS+2. Nat Genet 24:343–345.

Eunson LH, Rea R, Zuberi SM, Youroukos S, Panayiotopoulos CP, Liguori R, Avoni P, McWilliam RC, Stephenson JBP, Hanna MG, Kullmann DM, Spauschus A (2000): Clinical, genetic, and expression studies of mutations in the potassium channel gene KCNA1 reveal new phenotypic variability. Ann Neurol 48:647–656.

Everitt AD, Sander JW (1998): Incidence of epilepsy is now higher in elderly people than children. BMJ 316:780.

Eyre JA, Essex TJH, Flecknells PA, Bartholomew PH (1988): A comparison of measurements of cerebral blood flow in the rabbit using laser Doppler

spectroscopy and radionuclide labelled microspheres. Clin Phys Meas 65:65–74.

Figaji AA, Zwane E, Tieggen G, Argent AC, Le Roux PD, Siesjo P, Peter JC (2009): Pressure autoregulation, intracranial pressure, and brain tissue oxygenation in children with severe traumatic brain injury. J Neurosurg Pediatr 70:420–428.

Fisher R (2016): Operational Classification of Seizure Types by the International League Against Epilepsy. J Chem Inf Model 53:1689–1699.

Fisher RS, Acevedo C, Arzimanoglou A, Bogacz A, Cross JH, Elger CE, Engel J, Forsgren L, French JA, Glynn M, Hesdorffer DC, Lee BI, Mathern GW, Moshé SL, Perucca E, Scheffer IE, Tomson T, Watanabe M, Wiebe S (2014): ILAE Official Report: A practical clinical definition of epilepsy. Epilepsia 55:475–482.

Fox MD, Snyder AZ, Vincent JL, Corbetta M, Essen DC Van, Raichle ME (2005): The human brain is intrinsically organized into dynamic, anticorrelated functional networks. Proc Natl Acad Sci U S A 102:9673–9678.

Frerichs K.U. and Feuerstein G.Z. (1990): Platelet-activating factor--key mediator in neuroinjury Cerebrovasc. Brain Metab. Rev. 2, 148- 160

Friston KJ, Jezzard P, Turner R (1994): Analysis of functional MRI time-series. Hum Brain Mapp 1:153–171.

Friston KJ, Josephs O, Rees G, Turner R (1998): Nonlinear event-related responses in fMRI. Magn Reson Med 39:41–52.

Friston KJ, Mechelli A, Turner R, Price CJ (2000): Nonlinear responses in fMRI: the Balloon model, Volterra kernels, and other hemodynamics. Neuroimage 12:466–77.

Frostig RD, Lieke EE, Ts'o DY, Grinvald a (1990): Cortical functional architecture and local coupling between neuronal activity and the microcirculation revealed by in vivo high-resolution optical imaging of intrinsic signals. Proc Natl Acad Sci U S A 87:6082–6086.

Gallagher A, Lassonde M, Bastien D, Vannasing P, Lesage F, Grova C, Bouthillier A, Carmant L, Lepore F, Béland R, Nguyen DK (2008): Non-invasive pre-surgical investigation of a 10 year-old epileptic boy using simultaneous EEG-NIRS. Seizure 17:576–582.

García-Peñas JJ (2011): [Interictal epileptiform discharges and cognitive impairment in children]. Rev Neurol 52 Suppl 1:S43–52.

Gervain J, Mehler J, Werker JF, Nelson C a, Csibra G, Lloyd-Fox S, Shukla M, Aslin RN (2011): Near-infrared spectroscopy: a report from the McDonnell infant methodology consortium. Dev Cogn Neurosci 1:22–46.

Giacometti P, Diamond SG (2013): Compliant head probe for positioning electroencephalography electrodes and near-infrared spectroscopy optodes. J Biomed Opt 18:1–11.

Gibbs JW (1899): Fourier's Series. Nature. 59(1539): 606-606.

Glennon JM, Weiss-Croft L, Harrison S, Cross JH, Boyd SG, Baldeweg T (2016): Interictal epileptiform discharges have an independent association with cognitive impairment in children with lesional epilepsy. Epilepsia:1–7.

Glover GH (1999): Deconvolution of impulse response in event-related BOLD fMRI. Neuroimage 9:416–429.

Goutte C, Nielsen FÅ, Hansen LK (2000): Modeling the Haemodynamic Response in fMRI Using Smooth FIR Filters 19:1188–1201.

Grant AC, Donnelly KM, Chubb C, Barr WB, Kuzniecky R, Devinsky O (2008): Temporal lobe epilepsy does not impair visual perception. Epilepsia 49:710–3.

Greicius M (2008): Resting-state functional connectivity in neuropsychiatric disorders. Curr Opin Neurol 21:424–30.

Greicius MD, Krasnow B, Reiss AL, Menon V (2003): Functional connectivity in the resting brain: a network analysis of the default mode hypothesis. Proc Natl Acad Sci U S A 100:253–8.

Grubb RL Jr, Raichle ME, Eichling JO T-PM (1974): The effects of changes in PaCO_2 on cerebral blood volume, blood flow, and vascular mean transit time. Stroke 5:603–609.

Haginoya K, Munakata M, Kato R, Yokoyama H, Ishizuka M IK (2002): Ictal cerebral haemodynamics of childhood epilepsy measured with near-infrared spectrophotometry. Brain 125:1960–1971.

Hales PW, Kawadler JM, Aylett SE, Kirkham FJ, Clark C a (2014): Arterial spin labeling characterization of cerebral perfusion during normal maturation from late childhood into adulthood: normal "reference range" values and their use in clinical studies. J Cereb Blood Flow Metab 34:776–84.

Hall CN, Howarth C, Turner R, Hamel E, Kleinfeld D, Montague R, Behrens T, Devor A, Gagnon L, Hillman E (2016): Interpreting BOLD : a dialogue between

cognitive and cellular neuroscience Discussion. Philos Trans R Soc B Biol Sci:15–16.

Ham T, Leff A, Boissezon X de, Joffe A, Sharp DJ (2013): Cognitive Control and the Salience Network: An Investigation of Error Processing and Effective Connectivity. J Neurosci 33:7091–7098.

Hamel E (2004): Cholinergic modulation of the cortical microvascular bed. Prog Brain Res 145:171–178.

Harper AM, Jennett S (1990): Cerebral blood flow and metabolism. Manchester: Manchester University Press.

Harrison R., Taylor D. (1976): Childhood Seizures: a 25-Year Follow-up: Social and Medical Prognosis. Lancet 307:948–951.

Hasson U, Malach R, Heeger DJ (2010): Reliability of cortical activity during natural stimulation. Trends Cogn Sci 14:40–8.

Hasson U, Nir Y, Levy I, Fuhrmann G, Malach R (2004): Intersubject synchronization of cortical activity during natural vision. Science 303:1634–40.

Hauser W a, Annegers JF, Kurland LT (1991): Prevalence of epilepsy in Rochester, Minnesota: 1940-1980. Epilepsia 32:429–445.

Hawco CS, Bagshaw AP, Lu Y, Dubeau F, Gotman J (2007): BOLD changes occur prior to epileptic spikes seen on scalp EEG. Neuroimage 35:1450–1458.

Heiss W-D, Turnheim M, Vollmer R, Rappelsberger P (1979): Coupling between neuronal activity and focal blood flow in experimental seizures. Electroencephalogr Clin Neurophysiol 47:396–403.

Heron SE, Crossland KM, Andermann E, Phillips HA, Hall AJ, Bleasel A, Shevell M, Mercho S, Seni MH, Guiot MC, Mulley JC, Berkovic SF, Scheffer IE (2002): Sodium-channel defects in benign familial neonatal-infantile seizures. Lancet 360:851–852.

Hoge R, Atkinson J, Gill B, Crelier G, Marrett S (1999): Investigation of BOLD signal dependence on cerebral blood flow and oxygen consumption: The …. Magn Reson Med 863:849–863.

Holmes GL, Ben-Ari Y (2001): The neurobiology and consequences of epilepsy in the developing brain. Pediatr Res 49:320–325.

Holmes M, Folley BS, Sonmezturk HH, Gore JC, Kang H, Abou-Khalil B, Morgan VL (2012): Resting state functional connectivity of the hippocampus associated with neurocognitive function in left temporal lobe epilepsy. Hum Brain Mapp.

Hughes, J (1994): EEG in Clinical Practice. Oxford: Butterworth-Heinemann.

Hyder F, Shulman RG, Rothman DL (1998): A model for the regulation of cerebral oxygen delivery. J Appl Physiol 85:554–564.

Iadecola C (2004): Neurovascular regulation in the normal brain and in Alzheimer's disease. Nat Rev Neurosci 5:347–360.

Iannotti GR, Grouiller F, Centeno M, Carmichael DW, Abela E, Wiest R, Korff C, Seeck M, Michel C, Pittau F, Vulliemoz S (2016): Epileptic networks are strongly connected with and without the effects of interictal discharges. Epilepsia 57:1086–1096.

Ibrahim GM, Cassel D, Morgan BR, Smith M Lou, Otsubo H, Ochi A, Taylor M, Rutka JT, Snead OC, Doesburg S (2014): Resilience of developing brain networks to interictal epileptiform discharges is associated with cognitive outcome. Brain:1–13.

Ibrahim GM, Cassel D, Morgan BR, Smith M Lou, Otsubo H, Ochi A, Taylor M, Rutka JT, Snead OC, Doesburg S (2014a): Resilience of developing brain networks to interictal epileptiform discharges is associated with cognitive outcome. Brain:1–13.

Ibrahim GM, Morgan BR, Lee W, Smith M Lou, Donner EJ, Wang F, Beers C a, Federico P, Taylor MJ, Doesburg SM, Rutka JT, Carter Snead O (2014b): Impaired development of intrinsic connectivity networks in children with medically intractable localization-related epilepsy. Hum Brain Mapp 00:1–15.

Ingvar M (1986): Cerebral blood flow and metabolic rate during seizures. Relationship to epileptic brain damage. Ann N Y Acad Sci 462:194–206.

Ives JR, Warach S, Schmitt F, Edelman RR, Schomer DL (1993): Monitoring the patient's EEG during echo planar MRI. Electroencephalogr Clin Neurophysiol 87:417–420.

Jacobs J, Hawco C, Kobayashi E, Boor R, LeVan P, Stephani U, Siniatchkin M, Gotman J (2008): Variability of the hemodynamic response as a function of age and frequency of epileptic discharge in children with epilepsy. Neuroimage 40:601–614.

Jacobs J, LeVan P, Moeller F, Boor R, Stephani U, Gotman J, Siniatchkin M (2009): Hemodynamic changes preceding the interictal EEG spike in patients with focal epilepsy investigated using simultaneous EEG-fMRI. Neuroimage 45:1220–1231.

Jaeger M, Soehle M, Schuhmann MU, Meixensberger J (2012): Clinical significance of impaired cerebrovascular autoregulation after severe aneurysmal subarachnoid hemorrhage. Stroke 43:2097–2101.

Jirsa VK, Stacey WC, Quilichini PP, Ivanov AI, Bernard C (2014): On the nature of seizure dynamics. Brain 137:2210–2230.

Jöbsis FF (1977): Noninvasive, infrared monitoring of cerebral and myocardial oxygen sufficiency and circulatory parameters. Science 198:1264–1267.

Kastrup A, Krüger G, Neumann-Haefelin T, Glover GH, Moseley ME (2002): Changes of cerebral blood flow, oxygenation, and oxidative metabolism during graded motor activation. Neuroimage 15:74–82.

Khan B, Wildey C, Francis R, Tian F, Delgado MR, Liu H, Macfarlane D, Alexandrakis G (2012): Improving optical contact for functional near infrared brain spectroscopy and imaging with brush optodes. Biomed Opt Express 3:878–98.

Kleen JK, Scott RC, Holmes GL, Roberts DW, Rundle MM, Testorf M, Lenck-Santini P-P, Jobst BC (2013): Hippocampal interictal epileptiform activity disrupts cognition in humans. Neurology 81:18–24.

Koike S, Nishimura Y, Takizawa R, Yahata N, Kasai K (2013): Near-infrared spectroscopy in schizophrenia: A possible biomarker for predicting clinical outcome and treatment response. Front Psychiatry 4:12–17.

Kreisman NR, Sick TJ, Rosenthal M (1984): Concepts of brain oxygen surficiency during seizures Adv Exp Med Biol 180: 381-392.

Laufs H (2012): A personalized history of EEG–fMRI integration. Neuroimage 62:1056–1067.

Laufs H, Rodionov R, Thornton R, Duncan JS, Lemieux L, Tagliazucchi E (2014): Altered FMRI connectivity dynamics in temporal lobe epilepsy might explain seizure semiology. Front Neurol 5:175.

Lauterbur PC (1973): Image formation by induced local interactions. Examples employing nuclear magnetic resonance. Nat (London, United Kingdom) 242:190–191.

Lemieux L, Salek-Haddadi a, Josephs O, Allen P, Toms N, Scott C, Krakow K, Turner R, Fish DR (2001): Event-related fMRI with simultaneous and continuous EEG: description of the method and initial case report. Neuroimage 14:780–787.

Liao W, Zhang Z, Pan Z, Mantini D, Ding J, Duan X, Luo C, Wang Z, Tan Q, Lu G, Chen H (2011): Default mode network abnormalities in mesial temporal lobe epilepsy: A study combining fMRI and DTI. Hum Brain Mapp 32:883–895.

Lloyd-Fox S, Blasi A, Elwell CE (2010): Illuminating the developing brain: The past, present and future of functional near infrared spectroscopy. Neurosci Biobehav Rev 34:269–284.

Lloyd-Fox S, Papademetriou M, Darboe MK, Everdell NL, Wegmuller R, Prentice AM, Moore SE, Elwell CE (2014): Functional near infrared spectroscopy (fNIRS) to assess cognitive function in infants in rural Africa. Sci Rep 4:4740.

Logothetis NK, Pauls J, Augath M, Trinath T, Oeltermann A (2001): Neurophysiological investigation of the basis of the fMRI signal. Nature 412:150–157.

Lopes da Silva F (2010): EEG: Origin and measurement. In: Mulert C, Lemieux L, editors. EEG-fMRI Physiological Basis, Technique, and Applications. Berlin: Springer.

Lopes da Silva F, van Rotterdam A (2005): Biophysical aspects of EEG and magnetoencephalographic generation. In: Niedermeyer E, Lopes da Silva F, editors. Electroencephalography: basic principles, clinical applications and related fields. New York: Lippincott, Williams and Wilkins.

Lossin C, Rhodes TH, Desai RR, Vanoye CG, Wang D, Carniciu S, Devinsky O, George AL (2003): Epilepsy-associated dysfunction in the voltage-gated neuronal sodium channel SCN1A. J Neurosci 23:11289–11295.

LoTurco JJ, Owens DF, Heath MJS, Davis MBE, Kriegstein AR (1995): GABA and glutamate depolarize cortical progenitor cells and inhibit DNA synthesis. Neuron 15:1287–1298.

Lu Y, Bagshaw AP, Grova C, Kobayashi E, Dubeau F, Gotman J (2006): Using voxel-specific hemodynamic response function in EEG-fMRI data analysis. Neuroimage 32:238–247.

Luo C, Li Q, Lai Y, Xia Y, Qin Y, Liao W, Li S, Zhou D, Yao D, Gong Q (2011): Altered functional connectivity in default mode network in absence epilepsy: a resting-state fMRI study. Hum Brain Mapp 32:438–49.

Luo C, Yang T, Tu S, Deng J, Liu D, Li Q, Dong L, Goldberg I, Gong Q, Zhang D, An D, Zhou D, Yao D (2014): Altered intrinsic functional connectivity of the salience network in childhood absence epilepsy. J Neurol Sci 339:189–95.

Ma H, Zhao M, Schwartz TH (2013): Dynamic neurovascular coupling and uncoupling during ictal onset, propagation, and termination revealed by simultaneous in vivo optical imaging of neural activity and local blood volume. Cereb Cortex 23:885–899.

Mankinen K, Jalovaara P, Paakki J-J, Harila M, Rytky S, Tervonen O, Nikkinen J, Starck T, Remes J, Rantala H, Kiviniemi V (2012): Connectivity disruptions in resting-state functional brain networks in children with temporal lobe epilepsy. Epilepsy Res 100:168–78.

Marrett, S, Gjedde, A (1997): Changes of blood flow and oxygen consumption in visual cortex of living humans. Adv. Exp. Med. Biol. 413, 205–208

Mathern GW, Babb TL, Pretorius JK, Leite JP (1995): Reactive synaptogenesis and neuron densities for neuropeptide Y, somatostatin, and glutamate decarboxylase immunoreactivity in the epileptogenic human fascia dentata. J Neurosci 15:3990–4004.

Maziero D, Sturzbecher M, Velasco TR, Rondinoni C, Castellanos AL, Carmichael DW, Salmon CEG (2015): A Comparison of Independent Component Analysis (ICA) of fMRI and Electrical Source Imaging (ESI) in Focal Epilepsy Reveals Misclassification Using a Classifier. Brain Topogr 28:813–831.

Meldrum BS, Brierly JB (1973): Prolonged epileptic seizures in primates: ischemic cell change and its relation to ictal physiological events. Arch Neurol 28: 10-17.

Meldrum BS, Horton RW (1973): Physiology of status epilepticus in primates. Arch Neurol 28:1-9.

Menon RS, Kim SG (1999): Spatial and temporal limits in cognitive neuroimaging with fMRI. Trends Cogn Sci 3:207–216.

Miezin FM, Maccotta L, Ollinger JM, Petersen SE, Buckner RL (2000): Characterizing the hemodynamic response: effects of presentation rate, sampling procedure, and the possibility of ordering brain activity based on relative timing. Neuroimage 11:735–59.

Moeller F, Siebner HR, Wolff S, Muhle H, Boor R, Granert O, Jansen O, Stephani U, Siniatchkin M (2008): Changes in activity of striato-thalamo-cortical network precede generalized spike wave discharges. Neuroimage 39:1839–1849.

Mraovitch S, Sercombe R (1996): Neurophysiological basis of cerebral blood flow control. Leicester: John Libbey & Co Ltd.

Munakata M, Haginoya K, Ishitobi M, Sakamoto O, Sato I, Kitamura T, Hirose M, Yokoyama H, Iinuma K (2004): Dynamic cortical activity during spasms in three patients with west syndrome: A multichannel near-infrared spectroscopic topography study. Epilepsia 45:1248–1257.

Murta T, Leite M, Carmichael DW, Figueiredo P, Lemieux L (2015): Electrophysiological correlates of the BOLD signal for EEG-informed fMRI. Hum Brain Mapp 36:391–414.

Nguyen DK, Tremblay J, Pouliot P, Vannasing P, Florea O, Carmant L, Lepore F, Sawan M, Lesage F, Lassonde M (2012): Non-invasive continuous EEG-fNIRS recording of temporal lobe seizures. Epilepsy Res 99:112–126.

Nguyen DK, Tremblay J, Pouliot P, Vannasing P, Florea O, Carmant L, Lepore F, Sawan M, Lesage F, Lassonde M (2013): Noninvasive continuous functional near-infrared spectroscopy combined with electroencephalography recording of frontal lobe seizures. Epilepsia 54:331–40.

Nicholson C (1973): Theoretical Analysis of Field Potentials in Anisotropic Ensembles of Neuronal Elements. IEEE Trans Biomed Eng BME-20:278–288.

Niedermeyer E (2005): The normal EEG in the waking adult. In: Niedermeyer E, Lopes da Silva F, editors. Electroencephalography: basic principles, clinical applications and related fields. New York: Lippincott, Williams and Wilkins.

Novotny E (1995): Overview-The Role of NMR Spectroscopy in Epilepsy. Magn Reson Imaging 13:1171–1173.

Öberg Å (1990): Review - Laser Doppler Flowmetry. Critical Reviews in Biomedical Engineering.

Obrig H (2014): NIRS in clinical neurology - a “promising” tool? Neuroimage 85:535–546.

Ogawa S, Lee TM, Kay AR, Tank DW (1990): Brain magnetic resonance imaging with contrast dependent on blood oxygenation. Proc Natl Acad Sci U S A 87:9868–9872.

Olejniczak P (2006): Neurophysiologic basis of EEG. J Clin Neurophysiol 23:186–189.

Orihuela-Espina F, Leff DR, James DRC, Darzi AW, Yang GZ (2010): Quality control and assurance in functional near infrared spectroscopy (fNIRS) experimentation. Phys Med Biol 55:3701–3724.

Patel KS, Zhao M, Ma H, Schwartz TH (2013): Imaging preictal hemodynamic changes in neocortical epilepsy. Neurosurg Focus 34:E10.

Penfield, von Santha, Kalman, Cipriani A (1939): Cerebral flow during seizures animals and man. J Neurophysiol 2:257–267.

Peng K, Pouliot P, Lesage F, Nguyen DK (2016): Multichannel continuous electroencephalography-functional near-infrared spectroscopy recording of focal seizures and interictal epileptiform discharges in human epilepsy: a review. Neurophotonics 3:31402.

Peng K, Nguyen DK, Vannasing P, Tremblay J, Lesage F, Pouliot P (2016b): Using patient-specific hemodynamic response function in epileptic spike analysis of human epilepsy: a study based on EEG–fNIRS. Neuroimage 126:239–255.

Pinti P, Aichelburg C, Lind F, Power S, Swingler E, Merla A, Hamilton A, Gilbert S, Burgess P, Tachtsidis I (2015): Using Fiberless, Wearable fNIRS to Monitor Brain Activity in Real-world Cognitive Tasks. J Vis Exp:1–13.

Pittau F, Grova C, Moeller F, Dubeau F, Gotman J (2012): Patterns of altered functional connectivity in mesial temporal lobe epilepsy. Epilepsia 53:1013–1023.

Pittau F, Levan P, Moeller F, Gholipour T, Haegelen C, Zelmann R, Dubeau F, Gotman J (2011): Changes preceding interictal epileptic EEG abnormalities: Comparison between EEG/fMRI and intracerebral EEG. Epilepsia 52:1120–1129.

Pressler RM, Robinson RO, Wilson GA, Binnie CD (2005): Treatment of interictal epileptiform discharges can improve behavior in children with behavioral problems and epilepsy. J Pediatr.

Purcell E, Torrey H, Pound R (1946): Resonance Absorption by Nuclear Magnetic Moments in a Solid. Phys Rev 69:37–38.

R Core Team (2016): R: A language and environment for statistical computing. R Foundation for Statistical Ccomputing. Vienna. http://www.R-project.org/.

Raichle ME, MacLeod a M, Snyder a Z, Powers WJ, Gusnard D a, Shulman GL (2001): A default mode of brain function. Proc Natl Acad Sci U S A 98:676–82.

Rathakrishnan R, Moeller F, Levan P, Dubeau F, Gotman J (2010): BOLD signal changes preceding negative responses in EEG-fMRI in patients with focal epilepsy. Epilepsia 51:1837–1845.

Riva C, Ross B, Benedek GB (1972): Laser Doppler measurements of blood flow in capillary tubes and retinal arteries. Invest Ophthalmol 11:936–944.

Rizki EE, Uga M, Dan I, Dan H, Tsuzuki D, Yokota H, Oguro K, Watanabe E (2015): Determination of epileptic focus side in mesial temporal lobe epilepsy using long-term noninvasive fNIRS/EEG monitoring for presurgical evaluation. Neurophotonics 2:25003-1–13.

Roche-Labarbe N, Zaaimi B, Mahmoudzadeh M, Osharina V, Wallois A, Nehlig A, Grebe R, Wallois F (2010): NIRS-measured oxy- and deoxyhemoglobin changes associated with EEG spike-and-wave discharges in a genetic model of absence epilepsy: The GAERS. Epilepsia 51:1374–1384.

Rogawski MA (1996): Epilepsy. In: Pullan L, Patel J, Totowa NJ, editors. Neurotherapeutics: Emerging Strategies, New Jersey: Humana Press Inc.

Rogawski MA (2011): Revisiting AMPA receptors as an antiepileptic drug target. Epilepsy Curr 11:56–63.

Rollings DT, Assecondi S, Ostwald D, Porcaro C, McCorry D, Bagary M, Soryal I, Bagshaw AP (2016): Early haemodynamic changes observed in patients with epilepsy, in a visual experiment and in simulations. Clin Neurophysiol 127:245–253.

Ronne-Engström E, Carlson H, Blom S, Flink R, Gazelius B, Spännare B, Hillered L (1993): Monitoring of cortical blood flow in human epileptic foci using laser Doppler flowmetry. J Epilepsy 6:145–151.

Rothman DL, Behar KL, Hyder F, Shulman RG (2003): In vivo NMR studies of the glutamate neurotransmitter flux and neuroenergetics: implications for brain function. Annu Rev Physiol 65:401–27.

Roy CS, Sherrington CS (1890): On the Regulation of the Blood-supply of the Brain. J Physiol 11:85–158.17.

Sato N, Hagihara B, Kamada T, Abe H (1976): A sensitive method for the quantitative estimation of cytochromes a and a3 in tissues 74:105–117.

Sato T, Ito M, Suto T, Kameyama M, Suda M, Yamagishi Y, Ohshima A, Uehara T, Fukuda M, Mikuni M (2007): Time courses of brain activation and their implications for function: A multichannel near-infrared spectroscopy study during finger tapping. Neurosci Res 58:297–304.

Sato Y, Fukuda M, Oishi M, Shirasawa A, Fujii Y (2013): Ictal near-infrared spectroscopy and electrocorticography study of supplementary motor area seizures. J Biomed Opt 18:76022.

Satterthwaite TD, Wolf DH, Loughead J, Ruparel K, Elliott M a, Hakonarson H, Gur RC, Gur RE (2012): Impact of in-scanner head motion on multiple measures of functional connectivity: relevance for studies of neurodevelopment in youth. Neuroimage 60:623–32.

Schmuel, A (2010): EEG: Origin and measurement. In: Mulert C, Lemieux L, editors. EEG-fMRI Physiological Basis, Technique, and Applications, Berlin: Springer.

Schummers J, Yu H, Sur M (2008): Tuned responses of astrocytes and their influence on hemodynamic signals in the visual cortex. Science (80-) 320:1638–1643.

Schwartz TH, Bonhoeffer T (2001): In vivo optical mapping of epileptic foci and surround inhibition in ferret cerebral cortex. Nat Med 7:1063–7.

Schwartz TH, Hong S-B, Bagshaw AP, Chauvel P, Bénar C-G (2011): Preictal changes in cerebral haemodynamics: review of findings and insights from intracerebral EEG. Epilepsy Res 97:252–266.

Seeley WW, Menon V, Schatzberg AF, Keller J, Glover GH, Kenna H, Reiss AL, Greicius MD (2007): Dissociable Intrinsic Connectivity Networks for Salience Processing and Executive Control. J Neurosci 27:2349–2356.

Seitz RJ, Roland PE (1992): Vibratory stimulation increases and decreases the regional cerebral blood flow and oxidative metabolism: a positron emission tomography (PET) study. Acta Neurol Scand 86:60–67.

Seyal M (2014): Frontal hemodynamic changes precede EEG onset of temporal lobe seizures. Clin Neurophysiol 125:442–448.

Shamshiri EA, Tierney TM, Centeno M, St Pier K, Pressler RM, Sharp DJ, Perani S, Cross JH, Carmichael DW (2016): Interictal activity is an important contributor to abnormal intrinsic network connectivity in paediatric focal epilepsy. Hum Brain Mapp 236:221–236.

Shen Q, Ren H, Duong TQ (2008): CBF, BOLD, CBV, and CMRO2 fMRI signal temporal dynamics at 500-msec resolution. J Magn Reson Imaging 27:599–606.

Singh H, Cooper RJ, Wai Lee C, Dempsey L, Edwards A, Brigadoi S, Airantzis D, Everdell N, Michell A, Holder D, Hebden JC, Austin T (2014): Mapping

cortical haemodynamics during neonatal seizures using diffuse optical tomography: A case study. NeuroImage Clin 5:256–265.

Slone E, Westwood E, Dhaliwal H, Federico P, Dunn JF (2012): Near-infrared spectroscopy shows preictal haemodynamic changes in temporal lobe epilepsy. Epileptic Disord Int epilepsy J with videotape 14:371–378.

Sloviter RS, Zappone CA, Harvey BD, Bumanglag A V., Bender RA, Frotscher M (2003): "Dormant basket cell" hypothesis revisited: Relative vulnerabilities of dentate gyrus mossy cells and inhibitory interneurons after hippocampal status epilepticus in the rat. J Comp Neurol 459:44–76.

Sokol DK, Markand ON, Daly EC, Luerssen TG, Malkoff MD (2000): Near infrared spectroscopy (NIRS) distinguishes seizure types. Seizure 9:323–327.

Song M, Du H, Wu N, Hou B, Wu G, Wang J, Feng H, Jiang T (2011): Impaired resting-state functional integrations within default mode network of generalized tonic-clonic seizures epilepsy. PLoS One 6:e17294.

Spampanato J, Escayg A, Meisler MH, Goldin AL (2001): Functional effects of two voltage-gated sodium channel mutations that cause generalized epilepsy with febrile seizures plus type 2. J Neurosci 21:7481–7490.

Speckmann EJ, Elger CE (2005). Introduction to the neurophysiological basis of EEG and DC potentials. In: Niedermeyer E, Lopes da Silva F, editors. Electroencephalography: basic principles, clinical applications and related fields. New York: Lippincott, Williams and Wilkins.

Spencer SS (2002): Neural Networks in Human Epilepsy : Evidence of and Implications for Treatment 43:219–227.

Steinhoff BJ, Herrendorf G, Kurth C (1996): Ictal near infrared spectroscopy in temporal lobe epilepsy : a pilot study:97–101.

Strangman G, Boas DA, Sutton JP (2002): Non-invasive neuroimaging using near-infrared light. Biol Psychiatry 52:679–693.

Suh M, Ma H, Zhao M, Sharif S, Schwartz TH (2006): Neurovascular Coupling and Oximetry During Epileptic Events. Mol Neurobiol 33:1559–1182.

Suzuki S, Harashima F, Furuta K (2010): Human control law and brain activity of voluntary motion by utilizing a balancing task with an inverted pendulum. Adv Human-Computer Interact 2010.

Tagliazucchi E, Laufs H (2014): Decoding wakefulness levels from typical fMRI resting-state data reveals reliable drifts between wakefulness and sleep. Neuron 82:695–708.

Terry JR, Benjamin O, Richardson MP (2012): Seizure generation: The role of nodes and networks. Epilepsia 53:166–169.

Thomas RH, Berkovic SF (2014): The hidden genetics of epilepsy-a clinically important new paradigm. Nat Publ Gr 10:283–292.

Thomsen K, Offenhauser N, Lauritzen M (2004): Principal neuron spiking: neither necessary nor sufficient for cerebral blood flow in rat cerebellum. J Physiol 560:181–9.

Thornton RC, Rodionov R, Laufs H, Vulliemoz S, Vaudano A, Carmichael D, Cannadathu S, Guye M, McEvoy A, Lhatoo S, Bartolomei F, Chauvel P, Diehl B, De Martino F, Elwes RDC, Walker MC, Duncan JS, Lemieux L (2010): Imaging haemodynamic changes related to seizures: Comparison of EEG-based general linear model, independent component analysis of fMRI and intracranial EEG. Neuroimage 53:196–205.

Tierney TM, Clark CA, Carmichael DW (2016b): Is Bonferroni correction more sensitive than Random Field Theory for most fMRI studies? arXiv 44.

Tierney TM, Weiss-Croft LJ, Centeno M, Shamshiri EA, Perani S, Baldeweg T, Clark CA, Carmichael DW (2016): FIACH: A biophysical model for automatic retrospective noise control in fMRI. Neuroimage 124:1009–1020.

Turnbull J, Lohi H, Kearney JA, Rouleau GA, Delgado-Escueta A V., Meisler MH, Cossette P, Minassian BA (2005): Sacred disease secrets revealed: The genetics of human epilepsy. Hum Mol Genet 14:2491–2500.

Turner R, Howseman A, Rees GE, Josephs O, Friston K (1998): Functional magnetic resonance imaging of the human brain: data acquisition and analysis. Exp Brain Res 123:5–12.

Vadlamudi RK, Sahin AA, Adam L, Wang RA, Kumar R (2003): Heregulin and HER2 signaling selectively activates c-Src phosphorylation at tyrosine 215. FEBS Lett 543:76–80.

van Houdt PJ, de Munck JC, Zijlmans M, Huiskamp G, Leijten FSS, Boon P a JM, Ossenblok PPW (2010): Comparison of analytical strategies for EEG-correlated fMRI data in patients with epilepsy. Magn Reson Imaging 28:1078–1086.

Van Kuilenburg ABP, Dekker HL, Van Den Bogert C, Nieboer P, Van Gelder BF, Muijsers AO (1991): Isoforms of human cytochrome-c oxidase. Eur J Biochem 199:615–622.

Vaudano AE, Carmichael DW, Salek-Haddadi A, Rampp S, Stefan H, Lemieux L, Koepp MJ (2012): Networks involved in seizure initiation. A reading epilepsy case studied with EEG-fMRI and MEG. Neurology 79:249–253.

Villringer A, Planck J, Stodieck S, Botzel K, Schleinkofer L, Dirnagl U (1994): Noninvasive assessment of cerebral hemodynamics and tissue oxygenation during activation of brain cell function in human adults using near infrared spectroscopy. Adv. Exp. Med. Biol. 345: 559-565.

Vitko I (2005): Functional Characterization and Neuronal Modeling of the Effects of Childhood Absence Epilepsy Variants of CACNA1H, a T-Type Calcium Channel. J Neurosci 25:4844–4855.

Voets NL, Adcock JE, Stacey R, Hart Y, Carpenter K, Matthews PM, Beckmann CF (2009): Functional and structural changes in the memory network associated with left temporal lobe epilepsy. Hum Brain Mapp 30:4070–4081.

Vulliemoz S, Carmichael DW, Rosenkranz K, Diehl B, Rodionov R, Walker MC, McEvoy AW, Lemieux L (2011): Simultaneous intracranial EEG and fMRI of interictal epileptic discharges in humans. Neuroimage 54:182–90.

Wallois F, Patil a, Héberlé C, Grebe R (2010): EEG-NIRS in epilepsy in children and neonates. Neurophysiol Clin 40:281–292.

Wallois F, Patil a., Kongolo G, Goudjil S, Grebe R (2009): Haemodynamic changes during seizure-like activity in a neonate: A simultaneous AC EEG-SPIR and high-resolution DC EEG recording. Neurophysiol Clin 39:217–227.

Wallsted L, Gazelius G, Lind B, Meyerson A, Linderoth B (1995): Chronic multifocal recording of cerebral microcirculation and subdural EEG during epileptic seizures in humans. Epilepsia S3: S146-147.

Wansapura JP, Holland SK, Dunn RS, Ball WS (1999): NMR relaxation times in the human brain at 3.0 Tesla. J Magn Reson Imaging 9:531–538.

Watanabe E, Maki A, Kawaguchi F, Yamashita Y, Koizumi H (2000): Noninvasive cerebral blood volume measurement during seizures using multichannel near 5:287–290.

Watanabe E, Nagahori Y, Mayanagi Y (2002): Focus diagnosis of epilepsy using near-infrared spectroscopy. Epilepsia 43 Suppl 9:50–5.

Widjaja E, Zamyadi M, Raybaud C, Snead OC, Smith ML (2013): Abnormal Functional Network Connectivity among Resting-State Networks in Children with Frontal Lobe Epilepsy. AJNR Am J Neuroradiol 34:2386–92.

Winkler MKL, Chassidim Y, Lublinsky S, Revankar GS, Major S, Kang E-J, Oliveira-Ferreira AI, Woitzik J, Sandow N, Scheel M, Friedman A, Dreier JP (2012): Impaired neurovascular coupling to ictal epileptic activity and spreading depolarization in a patient with subarachnoid hemorrhage: possible link to blood-brain barrier dysfunction. Epilepsia 53 Suppl 6:22–30.

Wirrell EC (2010): Prognostic significance of interictal epileptiform discharges in newly diagnosed seizure disorders. J Clin Neurophysiol 27:239–48.

Worsley KJ, Liao C, Grabove M, Petre V, Ha B, Evans AC (2002): A general statistical analysis for fMRI data. Neuroimage 15:1–15.

Yacoub E, Shmuel A, Pfeuffer J, Van De Moortele PF, Adriany G, Ugurbil K, Hu X (2001): Investigation of the initial dip in fMRI at 7 Tesla. NMR Biomed 14:408–412.

Yamada H, Sadato N, Konishi Y, Muramoto S, Kimura K, Tanaka M, Yonekura Y, Ishii Y, Itoh H (2000): A Milestone for Normal Development of the Infantile Brain Detected by Functional MRI. Neurology 55:218–223.

Yamaguchi S ichi, Donevan SD, Rogawski MA (1993): Anticonvulsant activity of AMPA/kainate antagonists: comparison of GYKI 52466 and NBQX in maximal electroshock and chemoconvulsant seizure models. Epilepsy Res 15:179–184.

Yücel M a, Selb J, Boas D a, Cash SS, Cooper RJ (2014): Reducing motion artifacts for long-term clinical NIRS monitoring using collodion-fixed prism-based optical fibers. Neuroimage 85 Pt 1:192–201.

Zhang Z, Lu G, Zhong Y, Tan Q, Chen H, Liao W, Tian L, Li Z, Shi J, Liu Y (2010): fMRI study of mesial temporal lobe epilepsy using amplitude of low-frequency fluctuation analysis. Hum Brain Mapp 31:1851–61.

Zhang Z, Lu G, Zhong Y, Tan Q, Liao W, Chen Z, Shi J, Liu Y (2009): Impaired perceptual networks in temporal lobe epilepsy revealed by resting fMRI. J Neurol 256:1705–13.

Zhao M, Ma H, Suh M, Schwartz TH (2009): Spatio-temporal dynamics of perfusion and oxymetry during ictal discharges in the rat neocortex. J Neurosci 29:2814–2823.

Zhao M, Suh M, Ma H, Perry C, Geneslaw A, Schwartz TH (2007): Focal increases in perfusion and decreases in hemoglobin oxygenation precede seizure onset in spontaneous human epilepsy. Epilepsia 48:2059–2067.

Zhao, M., Nguyen, J., Ma, H., Nishimura, N., Schaffer, C. B., & Schwartz, T. H. (2011): Preictal and ictal neurovascular and metabolic coupling surrounding a seizure focus. The Journal of Neuroscience: The Official Journal of the Society for Neuroscience, 31(37), 13292–13300.

Zonta M, Angulo MC, Gobbo S, Rosengarten B, Hossmann K-A, Pozzan T, Carmignoto G (2003): Neuron-to-astrocyte signaling is central to the dynamic control of brain microcirculation. Nat Neurosci 6:43–50.

Zuberi S, Eunson L, Spauschus A, De Silva R, Tolmie J, Wood N, McWilliam R, Stephenson J, Kullmann D, Hanna M (1999): A novel mutation in the human voltage-gated potassium channel gene (Kv1.1) associates with episodic ataxia type 1 and sometimes with partial epilepsy. Brain 122:817–825.